CRANFIELD UNIVERSITY

Marco Bonesi

CHARACTERIZATION OF FLOW DYNAMICS IN VESSELS WITH COMPLEX GEOMETRY USING DOPPLER OPTICAL COHERENCE TOMOGRAPHY

Cranfield Health

Ph.D. Thesis

CRANFIELD UNIVERSITY

Cranfield Health

Ph.D. Thesis

Academic Year 2007-2008

Marco Bonesi

CHARACTERIZATION OF FLOW DYNAMICS IN VESSELS WITH COMPLEX GEOMETRY USING DOPPLER OPTICAL COHERENCE TOMOGRAPHY

Supervisor: Dr. Igor V. Meglinski

January 2008

This thesis is submitted in partial fulfillment of the requirements
for the degree of Doctor of Philosophy

Abstract

The study of flow dynamics in complex geometry vessels is highly important in many biomedical applications where the knowledge of the mechanic interactions between the moving fluid and the housing media plays a key role for the determination of the parameters of interest, including the effect of blood flow on the possible rupture of atherosclerotic plaques. Doppler Optical Coherence Tomography (DOCT) is an optic, non-contact, non-invasive technique able to achieve detailed analysis of the flow/vessel interactions, allowing simultaneously high resolution imaging of the morphology and composition of the vessel and of the flow velocity distribution along the measured cross-section. DOCT system was developed to image high-resolution one-dimensional and multi-dimensional velocity distribution profiles of Newtonian and non-Newtonian fluids flowing in vessels with complex geometry, including Y-shaped and T-shaped vessels, vessels with aneurism, bifurcated vessels with deployed stent and scaffolds. The phantoms were built to study the interaction of the flow dynamics with different channel geometries and to map the related velocity profiles at several inlet volume flow rates. Feasibility studies for quantitative observation of the turbulence of flows arising within the complex geometry vessels are discussed. In addition, optical clearing of skin tissues has been utilized to achieve DOCT imaging of human blood vessels *in vivo*, at a depth up to 1.7 *mm*. Two-dimensional OCT images of complex flow velocity profiles in blood vessel phantom and *in vivo* subcutaneous human skin tissues are presented. The effect of optical clearing on *in vivo* images is demonstrated and discussed. DOCT was also applied for imaging scaffold structures and for mapping flow distributions within the scaffold.

To a great woman, very important in my life

Eleonora Morandini

Acknowledgements

I would like to express my gratitude to Professor Tony Turner who has offered to me the chance to further my Ph.D. studies at Cranfield University. Also I would like to express my appreciation to Professor Ricky Wang, who is managing my Ph.D. studies and project, and to Dr. Laurie Ritchie, my second supervisor, for offering me the possibility to work on the design and realization of a Polarization Sensitive Optical Coherence Tomography (PS-OCT) system. In addition I owe to Laurie that I had the opportunity to spend one very interesting week working in collaboration with the group of Professor Piotr Targowski (Institute of Physics, Nicolaus Copernicus University, Poland). I thank the Institute of Bio-Science and Technology (now Cranfield Health) for exposing me to their respective research activities. I would like to thank all my colleagues with whom I worked during my Ph.D. studies, especially to Dr. Dmitry Churmakov, Dr. Sergey Proskurin, Mr. Dave Pitts and Mr. Florian Bazant-Hegemark. I would also thank Dr. James Brighton and the staff of his department for making my stay in Silsoe campus a very enjoyable time and Mr. Ignacio Salan, friend and colleague, who has given me an invaluable support during the writing of this thesis. I must also thank Professor Seamus Higson, Dr. Sam Tothill, Professor Naresh Magan and particularly Professor Joe Lunec (Head of Cranfield Health), for their vital administrative support during my studies and staying in Silsoe campus

Finally, more importantly, I would like to express my sincere gratitude to Dr. Igor Meglinski, my supervisor, who has really helped me with his guidance, encouragement and support during the last part of my Ph.D. period.

Table of contents

ABSTRACT iii

ACKNOWLEDGEMENTS v

TABLE OF CONTENTS VI

LIST OF FIGURES ix
LIST OF TABLES xiii
LIST OF ACRONYMS xiv
LIST OF SYMBOLS xvi
SYSTÈME INTERNATIONAL D'UNITÉS xviii
SI units xviii
SI prefixes xviii
SI derived units xix
CGS UNITS xxi

CHAPTER 1

INTRODUCTION AND LITERATURE REVIEW OF OPTICAL IMAGING IN BIOMEDICINE AND FLOW DYNAMIC MEASUREMENTS 1

1.1 OPTICAL IMAGING IN BIOMEDICINE 2
1.2 AIMS OF THE THESIS 8
1.3 THESIS ORGANIZATION 8
Chapter 1 8
Chapter 2 9
Chapter 3 9
Chapter 4 9
Chapter 5 9
Chapter 6 10
1.4 MOTIVATIONS AND BACKGROUND 10
1.4.1 The need for flow measurements 14
1.5 BIOMEDICAL APPLICATIONS 16
1.5.1 Blood flow characterization 17
1.5.2 Tissue engineering 19
1.5.3 Others 20

CHAPTER 2

PRINCIPLES OF TIME-DOMAIN LOW COHERENCE IMAGING: THEORY OF OPTICAL COHERENCE TOMOGRAPHY AND DOPPLER OPTICAL COHERENCE TOMOGRAPHY 23

2.1 INTRODUCTION 24

2.2 PRINCIPLES OF TIME-DOMAIN OCT 25
2.3 APPLICATIONS OF OCT IN BIOMEDICINE 35
2.4 PRINCIPLES OF DOCT 36
2.4.1 Concepts of DOCT imaging 41
2.4.2 Sensitivity and resolution 42
2.5 OTHER IMPLEMENTATIONS OF DOCT IMAGING 44
2.5.1 Phase-resolved DOCT 44
2.5.2 Doppler Amplitude OCT 45
2.6 SUMMARY 46

CHAPTER 3

ELEMENTS AND PRINCIPLES OF FLUID MECHANICS 49

3.1 INTRODUCTION 50
3.2 MECHANICAL PROPERTIES OF FLUIDS 51
3.2.1 Shear stress in a moving fluid 51
3.2.2 Newtonian and non-Newtonian fluids 53
3.2.3 Density 54
3.2.4 Viscosity 55
3.3 CONCEPTS OF FLUID FLOW 55
3.3.1 Continuity equation 58
3.3.2 Momentum equation 59
3.3.3 Laminar and turbulent flow 60
3.4 EXAMPLES OF FLUID FLOW IN DUCTS 63
3.4.1 Flow in circular pipes 63
3.4.2 Blood flow 65
3.5 MODELLING AND NUMERICAL COMPUTATION OF FLUID FLOW 73
3.6 SUMMARY 75

CHAPTER 4

DEVELOPMENT OF THE DOCT EXPERIMENTAL SYSTEM 77

4.1 INTRODUCTION 78
4.2 LOW COHERENCE BROADBAND LIGHT SOURCE 79
4.3 CORE OF THE SYSTEM 82
4.3.1 Reference arm delay line 83
4.4 BEAM DELIVERY 89
4.5 SIGNAL TREATMENT AND DATA ANALYSIS 92
4.6 TD-DOCT WITH IMPROVED RSDL 95
4.7 PHANTOMS DESIGN 102
4.8 SUMMARY 108

CHAPTER 5

RESULTS AND DISCUSSION 111

5.1 INTRALIPID 112
5.3 HAEMOGLOBIN AND RBC 121
5.4 FLOW IN COMPLEX GEOMETRY VESSELS 124
5.4.1. Phantom studies 124
5.4.2. Application for skin tissues measurements in vivo 145
5.5 POROUS SCAFFOLDS FOR TISSUE ENGINEERING 147
5.7 SUMMARY 152

CHAPTER 6

CONCLUSIONS AND FUTURE WORK 155

LIST OF PUBLICATIONS 159

Journals – refereed 159
Conference proceedings 159
Conference presentations 160

REFERENCES 162

BIBLIOGRAPHY 190

List of figures

2.1	Schematic representation of a time-domain OCT system.	27
2.2	Typical shape of the cross-correlation interferometric signal.	31
2.3	Low and high numerical aperture focusing limits.	33
2.4	Low-coherence interferometry detection technique in OCT.	34
2.5	Schematic representation of the Doppler effect for EM waves.	39
2.6	Effect of the interaction of the probing radiation with a moving particle on the cross-correlation interferometric OCT signal.	40
2.7	Schematic representation of DOCT flow velocity data analysis.	42
3.1	Variation of shear stress with velocity gradient.	54
3.2	Reynolds's experimental apparatus for investigating the transition from laminar to turbulence in pipe flow.	61
3.3	Reynolds's experimental apparatus for investigating the transition from laminar to turbulence in pipe flow (details).	62
3.4	Examples of flow velocity profiles in pipe.	63
3.5	Examples of transitions from laminar to turbulent flow.	65
3.6	Blood flow in vessel (from *Encyclopædia Britannica Online*)	66
3.7	Scanning electron microscopy images of human blood constituent.	67
3.8	Anatomy of human heart.	69
3.9	Vesalius, The vein man (1554).	70
3.10	Leonardo da Vinci anatomy sketches.	72
4.1	Schematic representation of the built fibre-based time-domain DOCT system.	78
4.2	SLD intensity emission spectrum.	80
4.3	Variations of the absorption coefficient μ_a in function of the wavelength λ in the NIR region for several turbid media typically involved in OCT and DOCT measurements.	81
4.4	Variation of the absorption coefficient μ_a of water in function of the wavelength λ in the region 200-2000 *nm*.	81

4.5	Reference arm components implemented in the DOCT system.	83
4.6	Ideal position and velocity of the reference arm scan motor.	86
4.7	Comparison of the driving signal measured at the output of the function generator with the "position monitor" output of the motor driver.	87
4.8	Comparison of ideal and real motor driving signals.	88
4.9	Sample arm components configuration implemented in the DOCT system.	91
4.10	Schematics of the electronic circuitry for the optic-to-electronic transduction and signal conditioning.	93
4.11	GUI of the *LabVIEW* script to perform DOCT data acquisition.	94
4.12	Schematic representation of Doppler OCT experimental set-up.	96
4.13	Schematic of the Rapid Scan Delay Line (view from above).	98
4.14	Schematic representation of flow velocity measurement with Doppler OCT.	100
4.15	Design of a Y-shaped complex geometry vessel with circular cross-section.	103
4.16	Complex geometry vessel with circular cross-section built using metal rods as negative (photo).	104
4.17	Complex geometry vessels with circular cross-section built using wax as negative (photo).	106
4.18	Schematic representation of complex geometry vessels with square cross-section building technique	106
4.19	Complex geometry vessels with square cross-section (photo).	107
5.1	Particles of *Intralipid™10%.*	113
5.2	Optical properties of water solution of *Intralipid™10%* at [10%] volume concentration.	114
5.3	Measured backscattered light intensity of intralipid water solution at different volume concentrations.	115
5.4	OCT measurements of media with different refractive index.	116
5.5	Estimation of the refractive index of RO water and 1% stock solution of intralipid in RO water.	117

5.6	The wavelength dependence of the optical parameters of *Intralipid™ 20%.*	119
5.7	Measurement of the absorption coefficient μ_a of intralipid water solution at [1%] in volume.	120
5.8	Typical shape of a normal red blood cell "erythrocyte".	121
5.9	Particles of bovine haemoglobin diluted in RO water at 20%.	122
5.10	Backscattered intensity recorded from bovine haemoglobin diluted in PBS at different concentrations in weight.	123
5.11	Y-shaped phantom vessel used in the experiments (photo).	124
5.12	Velocity profiles of flow acquired across the inlet and outlet arms.	125
5.13	Turbulent flow velocity profiles acquired across the Y-shaped junction at the position T, T3, T4 and T5.	126
5.14	Flow velocity profiles acquired at the cross-sectional midpoint of the Y-shaped sample at the inlet arm, about 20 *mm* from the junction; at the junction and at the outlet left arm at about 20 *mm* after the junction.	127
5.15	Cross-sectional velocity profiles taken across the junction of the T-shaped sample.	128
5.16	Cross-sectional velocity profiles taken across the junction of the Y-shaped sample.	129
5.17	Longitudinal cross-sectional velocity profiles acquired through the junction of the T-shaped sample, Y-shaped sample and Y-shaped sample with aneurism.	130
5.18	Y-shaped phantom with deployed stent at the junction used in the experiment.	132
5.19	Cross-sectional flow velocity mapping from the Y-shaped phantom as illustrated in Figure 5.18, with no stent deployed inside the vessel.	134
5.20	Cross-sectional flow velocity mapping from the Y-shaped phantom as illustrated in Figure 5.18, with no stent deployed inside the vessel.	135
5.21	Cross-sectional flow velocity mapping from the Y-shaped phantom as illustrated in Figure 5.18, with stent deployed inside the vessel and associated structural OCT images (inlet arm).	137
5.22	Cross-sectional flow velocity mapping from the Y-shaped phantom as illustrated in Figure 5.18, with stent	138

	deployed inside the vessel and associated structural OCT images (at the junction).	
5.23	Cross-sectional flow velocity mapping from the Y-shaped phantom as illustrated in Figure 5.18, with stent deployed inside the vessel and associated structural OCT images (left outlet arm).	139
5.24	Cross-sectional flow velocity mapping from the Y-shaped phantom as illustrated in Figure 5.18, with stent deployed inside the vessel and associated structural OCT images (right outlet arm).	140
5.25	Flow dynamic cross-sectional mapping using 11% stock bovine haemoglobin solution at $\theta = 80°$.	143
5.26	Flow dynamic cross-sectional mapping using 11% stock bovine haemoglobin solution at $\theta = 90°$.	144
5.27	*In vivo* subcutaneous blood vessels of a human finger taken close to Y-junction: 1.3 μm SLD, 1.5 μm SLD.	145
5.28	OCT images of superficial blood vessel of a human finger *in vivo.*	146
5.29	OCT imaging of the scaffold structure.	149
5.30	Image of the internal structure of scaffold embedded in plastic tube.	150
5.31	Cross-sectional flow velocity distribution of non-filtered 1% stock solution of intralipid through the scaffold.	150
5.32	Microstructure of scaffold obtained with ISI ABT-55 low-vacuum scanning electron microscope.	151
5.33	Cross-sectional flow velocity distribution of filtered 1% stock solution of intralipid.	152

List of tables

4.1	Broadband light source specifications.	80
4.2	Reference arm translational stage technical data.	84
4.3	Scan motor driving signal parameters.	87
4.4	Sample arm translational stage technical data.	90
4.5	Properties of silicone rubber Q Sil-215.	104
5.1	Constituent of Intralipid10%.	112
5.2	Estimation of refractive index of RO water and 1% stock solution of intralipid.	118

List of abbreviations

1D	One-Dimensional, monodimensional
2D	Two-Dimensional
3D	Three-Dimensional
μTAS	Micro Total Analysis Systems
A/D	Analog-to-Digital
BS	Beam Splitter
CBF	Cerebral Blood Flow
CCD	Charged Coupled Device
CFD	Computational Fluid Dynamics
CL	Collimating Lens
CLSM	Confocal Laser Scanning Microscopy
CM	Confocal Microscopy
CMOS	Complementary Metal-Oxide Semiconductor (transistor type)
CT	Computed Tomography
DAQ	Data acquisition card
DC	Direct Current
DNA	Deoxyribonucleic Acid
DLS	Dynamic Light Scattering
DOCT	Doppler Optical Coherence Tomography
DWS	Diffusing Wave Spectroscopy
EM	Electromagnetic
FD-OCT	Fourier Domain Optical Coherence Tomography
FL	Focusing Lens
FWHM	Full Width Half Maximum
GR	Diffraction grating
I/O	Input-Output
IR	Infrared
IVUS	Intravascular Ultrasounds
L	Lens
LDS	Laser Doppler Flowmetry
LSCM	Laser Scanning Confocal Microscopy
M	Mirror

MRI	Magnetic Resonance Imaging
NA	Numerical Aperture
NIR	Near infrared
OCDR	Optical Coherence Domain Reflectometry
OCT	Optical Coherence Tomography
ODT	Diffuse Optical Tomography
OPD	Optical Path Difference
OPL	Optical Path Length
PBS	Phosphate Buffered Saline
PC	Personal Computer
PD	Photodetector
PIV	Particle Imaging Velocimetry
PS-OCT	Polarization-Sensitive Optical Coherence Tomography
PVC	Poly-vinyl chloride
RA	Reference Arm
RBC, RBCs	Red Blood Cells
RF	Radio Frequency
RO	Reverse Osmosis
RSDL	Rapid Scan Delay Line
SA	Sample Arm
SD-OCT	Spectral Domain Optical Coherence Tomography
SEFD-OCT	Spatially Encoded Fourier Domain Optical Coherence Tomography
SEM	Scanning Electron Microscopy
SI	*Système International d'unités*
SLD	Superluminescent diode
SM	Scanning Mirror
SNR	Signal-to-Noise Ratio
SS-OCT	Swept Source Optical Coherence Tomography
TD-OCT	Time Domain Optical Coherence Tomography
TEFD-OCT	Time Encoded Fourier Domain Optical Coherence Tomography
WBC, WBCs	White Blood Cells
a.u.	Arbitrary units

List of symbols

Symbol	*Description*	*Dependencies*	*S.I. units*
^{o}C	centigrade degree		$[K]$
∇p	pressure gradient		$[m^{-1} \cdot Pa]$
$\nabla \cdot \mathbb{F}$	shear forces		[N]
$\Delta\lambda$	light source spectral bandwidth		$[m]$
Φ	shear strain	x/y	adim
ε	eddy viscosity		$[Pa \cdot s]$
η	dynamic viscosity		$[Pa \cdot s]$
κ	permeability of the medium		$[m^2]$
λ	wavelength		$[m]$
μ_a	absorption coefficient		$[m^{-1}]$
μ_s	scattering coefficient		$[m^{-1}]$
μ'_s	reduced scattering coefficient	$\mu_s(1-g)$	$[m^{-1}]$
ρ	mass density		$[m^{-3} \cdot kg]$
σ	relative density		adim
τ	shear stress		$[N \cdot m^{-2}]$
υ	kinematic viscosity	η/ρ	$[m^2 \cdot s^{-1}]$
ω	angular frequency		$[rad \cdot s^{-1}]$
ω_D	angular Doppler shift		$[rad \cdot s^{-1}]$
A	area		$[m^2]$
D/Dt	substantive derivative		
F	force		$[N]$
$I(t)$	interferometric signal		a.u.
L_{ax}	axial resolution		$[m]$
L_f	focal length		$[m]$
L_{tr}	transverse resolution		$[m]$
N	ST-FFT time-window size		
P	Cauchy principle value		
Q	volume flow rate	$A \cdot u$	$[m^3 \cdot s^{-1}]$
R	resistance (fluid dynamics)	$\frac{8}{\pi} \cdot \frac{\upsilon l}{r^4}$	$[m^{-2} \cdot Pa \cdot s]$

Re	Reynolds number	$\frac{\rho u l}{\mu}$	adim
T_s	Sampling interval		$[s]$
$V_{p\text{-}p}$	peak-to-peak voltage		$[V]$
$V_m(t)$	scan motor instantaneous velocity		$[m \cdot s^{-1}]$
a	acceleration	$\frac{du}{dt}$	$[m \cdot s^{-2}]$
b	confocal parameter		$[m]$
d	diameter		$[m]$
d	diffraction grating pitch		$[m]$
d/dt	derivative		
$\mathbf{f}$	force		[N]
f	frequency		$[Hz]$
f_D	Doppler shift		$[Hz]$
f_s	sampling frequency		$[Hz]$
g	anisotropy factor		adim
$\boldsymbol{g}$	gravitational acceleration		$[m \cdot s^{-2}]$
l	distance, characteristic length		$[m]$
m	mass		$[kg]$
$\dot{m}$	mass rate of flow	$\rho A \bar{u}$	$[kg \cdot s^{-1}]$
p	static pressure		$[N \cdot m^{-2}]$
$\boldsymbol{p}$	momentum (mechanics)	$m \cdot \boldsymbol{u}$	$[m \cdot kg \cdot s^{-1}]$
$p(t)$	scan motor instantaneous position		$[m]$
r	radius of curvature		$[m]$
t	time		$[s]$
u	velocity (module)		$[m \cdot s^{-1}]$
$\bar{u}$	average velocity (module)		$[m \cdot s^{-1}]$
$\boldsymbol{u}$	velocity (vector)		$[m \cdot s^{-1}]$
$u_m(t)$	scan motor instantaneous velocity		$[m \cdot s^{-1}]$
w	specific weight	$\rho \cdot g$	$[m^{-2} \cdot kg \cdot s^{-2}]$
x, y, z	distance, Cartesian coordinates		$[m]$
z_R	Rayleigh range		$[m]$

Système International d'unités

SI units

Symbol	*Name*	*Quantity*
m	metre[1]	length
kg	kilogram	mass
s	second	time
A	ampere	electric current
K	kelvin	thermodynamic temperature
mol	mole	amount of substance
cd	candela	luminous intensity

SI prefixes

Prefix	*Symbol*	*Factor*
Y	yotta	10^{24}
Z	zetta	10^{21}
E	exa	10^{18}
P	peta	10^{15}
T	tera	10^{12}
G	giga	10^{9}
M	mega	10^{6}
K	kilo	10^{3}
h	hecto	10^{2}
da	deca	10^{1}
d	deci	10^{-1}
c	centi	10^{-2}
m	milli	10^{-3}
μ	micro	10^{-6}
n	nano	10^{-9}

[1] The correct English spelling of the unit is *metre*, but the variant *meter* is frequently used in the United States.

p	pico	10^{-12}
f	femto	10^{-15}
a	atto	10^{-18}
z	zepto	10^{-21}
y	yocto	10^{-24}

SI derived units

Symbol	*Name*	*Quantity*	*SI units*
Hz	hertz	frequency	s^{-1}
N	newton	force	$m \cdot kg \cdot s^{-2}$
Pa	pascal	pressure, stress	$N \cdot m^{-2} = m^{-1} \cdot kg \cdot s^{-2}$
J	joule	energy, work, quantity of heat	$N \cdot m = m^{2} \cdot kg \cdot s^{-2}$
W	watt	power, radiant flux	$J \cdot s^{-1} = m^{2} \cdot kg \cdot s^{-3}$
C	coulomb	quantity of electricity, electric charge	$A \cdot s$
V	volt	electric potential	$W \cdot A^{-1} = m \cdot kg \cdot s^{-2} \cdot A$
F	farad	capacitance	$C \cdot V^{-1} = m^{-2} \cdot kg^{-1} \cdot s^{4} \cdot A^{2}$
Ω	ohm	electric resistance	$V \cdot A^{-1} = m^{2} \cdot kg \cdot s^{-3} \cdot A^{-2}$
S	siemens	conductance	$V^{-1} \cdot A = m^{-2} \cdot kg^{-1} \cdot s^{3} \cdot A^{2}$
Wb	weber	magnetic flux	$V \cdot s = m^{2} \cdot kg \cdot s^{-2} \cdot A^{-1}$
T	tesla	magnetic flux density, magnetic induction	$Wb \cdot m^{-2} = kg \cdot s^{-2} \cdot A^{-1}$
H	henry	inductance	$Wb \cdot A^{-1} = m^{2} \cdot kg \cdot s^{-2} \cdot A^{-2}$
lm	lumen	luminous flux	$cd \cdot sr$
lx	lux	illuminance	$m^{-2} \cdot lm = m^{-2} \cdot cd \cdot sr$
Bq	becquerel	activity (ionizing radiation)	s^{-1}
Gy	gray	absorbed dose	$J \cdot kg = m^{2} \cdot s^{-2}$

$Pa \cdot s$	pascal second	dynamic viscosity	$m \cdot kg^{-1} \cdot s^{-1}$
$N \cdot m$	metre newton	moment of force	$m^2 \cdot kg \cdot s^{-2}$
$N \cdot m^{-1}$	newton per metre	surface tension	$kg \cdot s^{-2}$
$W \cdot m^{-2}$	watt per square metre	heat flux density, irradiance	$kg \cdot s^{-3}$
$J \cdot K^{-1}$	joule per kelvin	heat capacity, entropy	$m^2 \cdot kg \cdot s^{-2} \cdot K^{-1}$
$J \cdot kg^{-1} \cdot K^{-1}$	joule per kilogram kelvin	specific heat capacity, specific entropy	$m^2 \cdot s^{-2} \cdot K^{-1}$
$J \cdot kg^{-1}$	joule per kilogram	specific energy	$m^2 \cdot s^{-2}$
$W \cdot m^{-1} \cdot K^{-1}$	watt per metre kelvin	thermal conductivity	$m \cdot kg \cdot s^{-3} \cdot K^{-1}$
$J \cdot m^{-3}$	joule per cubic metre	energy density	$m^{-1} \cdot kg \cdot s^{-2}$
$V \cdot m^{-1}$	volt per metre	electric field strength	$m \cdot kg \cdot s^{-3} \cdot A$
$C \cdot m^{-3}$	coulomb per cubic metre	electric charge density	$m^{-3} \cdot s \cdot A$
$F \cdot m^{-1}$	farad per metre	permittivity	$m^{-3} \cdot kg^{-1} \cdot s^4 \cdot A^2$
$H \cdot m^{-1}$	henry per metre	permeability	$m \cdot kg \cdot s^{-2} \cdot A^{-2}$
$J \cdot mol^{-1}$	joule per mole	molar energy	$m^2 \cdot kg \cdot s^{-2} \cdot mol^{-1}$
$J \cdot mol^{-1} \cdot K^{-1}$	joule per mole kelvin	molar entropy, molar heat capacity	$m^2 \cdot kg \cdot s^{-2} \cdot K^{-1} \cdot mol^{-1}$
$C \cdot kg^{-1}$	coulomb per kilogram	exposure (ionizing radiations)	$kg^{-1} \cdot s \cdot A$
$Gy \cdot s^{-1}$	gray per second	absorbed dose rate	$m^2 \cdot s^{-3}$

CGS units

Symbol	*Name*	*SI equivalent unit*
erg	erg	1 $erg = 10^{-7}\ J$
dyn	dyne	1 $dyn = 10^{-5}\ N$
P	poise	1 $P = 1\ dyn{\cdot}s{\cdot}cm^{-2} = 0.1\ Pa{\cdot}s$
St	stokes	1 $St = 1\ cm^{2}{\cdot}s^{-1} = 10^{-4}\ m^{2}{\cdot}s^{-1}$
G	gauss	1 $G = 10^{-4}\ T$
Oe	oersted	1 $Oe = 1000{\cdot}(2\pi)^{-1}{\cdot}\ m^{-1}{\cdot}A$
Mx	maxwell	1 $Mx = 10^{-8}\ Wb$
sb	stilb	1 $sb = 1\ cd{\cdot}cm^{-2} = 10^{4}\ cd{\cdot}m^{-2}$
ph	phot	1 $ph = 10^{4}\ lx$

Chapter 1

Introduction and Literature Review of Optical Imaging in Biomedicine and Flow Dynamic Measurements

1.1 Optical imaging in biomedicine

Being actively developed from the mid 1980s (Udupa and Gabor 1999, Splinter and Hooper 2006), the methods of non-invasive optical diagnostics and imaging techniques are widely used today in various fields of medicine and biophysics (Tuchin 2000, Tuchin 2004).

The most common biomedical imaging modalities include X-ray radiography, ultrasound imaging (ultrasonography), X-ray computed tomography (CT), Magnetic Resonance Imaging (MRI) and confocal microscopy (CM). The discovery of X-rays in 1895, for which Wilhelm Conrad Röntgen[2] (1845-1923) received the first Nobel Prize in Physics in 1901, marked the advent of medical imaging. Ultrasonography, another very common imaging technique which is based on sonar, was introduced into medicine in 1940s after World War II. The invention of X-ray computed tomography in the 1970s, for which Allan McLeod Cormack (1924-1998) and Godfrey Newbold Hounsfield (1919-2004) received the Nobel Prize in Medicine in 1979, initiated digital cross-sectional imaging (tomography). The invention of MRI also in the 1970s, for which Paul Christian Lauterbur (1929-2007) and Peter Mansfield (b.1933) received the Nobel Prize in Medicine in 2003, enabled functional imaging with high spatial resolution.

The recent rapid progress in novel photonic technologies, on the basis of diode lasers, broadband femtosecond lasers (Ti:Sapphire or Cr:Försterite) and superluminescent diodes (SLD), allowed optical imaging currently emerging as a promising new addition to medical imaging (Unterhuber *et al.* 2004, Tuchin 2004, Wang and Wu 2007). As a result, several new original techniques have been suggested in the past. Diffusing wave spectroscopy (DWS) (Harden and Viasnoff 2001, Meglinski 2003), an extension of conventional Dynamic Light Scattering (DLS) (Cummins and Pike 1973), became an important tool in applications such as non-invasive quantitative monitoring of blood microcirculation for diabetes (Jaap and Tooke 1995) and port wine stains studies (Kelly *et al.* 2005), pharmacological intervention for failing surgical skin flaps or replants

[2] Röntgen's name is usually given as “Roentgen” (an alternative German spelling) in English; therefore most English scientific and medical references to him are found under this spelling.

(Neligan 1993), to assess burn depth (Niazi *et al.* 1993), to diagnose atherosclerotic diseases (Regar *et al.* 2007) and for investigation mechanisms of photodynamic therapy at cancer treatments (Korbelik and Krosl 1994). Laser speckle imaging is applied for dynamic, high-resolution monitoring of cerebral blood flow (CBF), which is crucial for studying the normal and pathophysiologic conditions of brain metabolism (Dunn *et al.* 2001, Haiying *et al.* 2004). By illuminating the cortex with laser light and imaging the resulting speckle pattern, relative CBF images with tens of microns spatial and millisecond temporal resolution were obtained (Luo *et al.* 2004). Laser interferometry of random phase (light scattering) methodology is used for describing of spatially-modulated laser beam transportation through thin tissue layers or turbid thin films. This technique is applied for random object inspection (Angelsky and Maksimyak 1990, Angelsky *et al.* 1999), for surface roughness measurements (Taganov and Toporets 1976, Ohlidal *et al.* 1995), and for retinal visual acuity determination at cataract (Saleh 1982, Enoch *et al.* 1995, Radchenko *et al.* 1999) and monitoring of scattering properties of blood during sedimentation and aggregation of erythrocytes (Gandjbakhche *et al.* 1994, Tuchin *et al.* 2002). Confocal Laser Scanning Microscopy (CLSM or LSCM) is a technique for obtaining high-resolution optical images. The key feature of confocal microscopy is its ability to produce in-focus images of thick specimens, a process known as *optical sectioning*. Images are acquired point-by-point and reconstructed with a computer, allowing three-dimensional reconstructions of topologically-complex objects. The principle of confocal microscopy was originally patented by Marvin Minsky in 1957 (US patent 3013467), but it took another thirty years and the development of lasers for CLSM to become a standard technique toward the end of the 1980s (Pawkey 2006). CLSM is widely-used in numerous biological science disciplines, from cell biology and genetics to microbiology and developmental biology. Clinically, CLSM is used in the evaluation of various eye diseases, and is particularly useful for imaging, qualitative analysis, and quantification of endothelial cells of the cornea (Patel and McGhee 2007, Pawkey 2006). It is used for localizing and identifying the presence of filamentary fungal elements in the corneal stroma in cases of keratomycosis, enabling rapid diagnosis and thereby early institution of definitive therapy. Research into CLSM techniques for endoscopic procedures is also showing

promise (Hoffman *et al.* 2006). This technique has a limited depth of view, typically in the range of hundred of microns. Optical heterodyne detection characterized by phase-sensitive measurements of light fields with a high signal-to-noise ratio (SNR) and large dynamic range is a relatively new and fast growing coherent-domain optical method. The technique, in its basic principles, is known as Optical Coherence Tomography (OCT) (Huang *et al.* 1991, Schmitt 1999, Fercher *et al.* 2003, Drexler 2004) and has found important applications in medicine, biology and material studies (Bouma and Tearney 2002, Tuchin 2004, Brezinski 2006, Regar *et al.* 2007).

Optical Coherence Tomography is a fundamentally new type of optical imaging modality. OCT performs high resolution (Brezinski and Fujimoto 1999, Drexler 2004), cross-sectional tomographic imaging of the internal microstructure in materials (Chinn and Swanson 2002, Dunkers 2002) and biological systems (Fujimoto *et al.* 1995) by measuring backscattered or backreflected light. Image resolutions of 1-15 μm can be achieved, which is one to two orders of magnitude higher than with conventional ultrasound (Brezinski *et al.* 1997). Imaging can be performed *in situ*, non-invasively and in real time (several frames per second for 200-500 pixel images) (Bouma and Tearney 2002, Brezinski 2006). The unique features of this technology enable a broad range of research and clinical applications; it is successfully applied in ophthalmology, for example, to obtain high-resolution images of the retina (Fercher *et al.* 1988, Swanson *et al.* 1993, Wojtkowski *et al.* 2002, Longmuir *et al.* 2008). OCT can be interfaced with a wide range of imaging delivery systems (Schmitt *et al.* 2005) and imaging probes (Li *et al.* 2000, Hwang *et al.* 2005). OCT technology is based on fiber optics and uses components developed for the telecommunications industry. Image information is generated in electronic form, which is amenable to image processing, and analysis, as well as electronic transmission, storage and retrieval. OCT systems can be engineered to be compact and low cost, suitable for applications in research, manufacturing or the clinic.

The imaging engine, intended as any optical detection device that performs high resolution and high sensitivity ranging and detection of backreflected or backscattered optical echoes, is the heart of the OCT system. Most time-domain OCT (TD-OCT)

systems have employed a reference delay scanning interferometer, such as a Michelson[3] interferometer (Born and Wolf 1999), in combination with a low coherence light source. There are many different embodiments of the interferometer and imaging engine for specific applications such as polarization diversity (insensitive) imaging, polarization-sensitive imaging and Doppler flow imaging. Polarization-sensitive detection techniques have been demonstrated using a dual channel interferometer (Hee *et al.* 1992, de Boer *et al.* 1997, Everett *et al.* 1998). These techniques permit imaging of the birefringence properties of structures. Collagen and other tissues are strongly birefringent, and polarization-sensitive OCT (PS-OCT) can be a sensitive indicator of the tissue microstructural organization (Bagnaninchi *et al.* 2008, Ugryumova *et al.* 2008a, Ugryumova *et al.* 2008b).

In *frequency domain OCT* the broadband interference is acquired with spectrally separated detectors (either by encoding the optical frequency in time with a spectrally scanning source or with a dispersive detector, like a grating and a linear detector array). Due to the Fourier relation (Wiener-Khintchine theorem between the autocorrelation and the spectral power density) the depth scan can be immediately calculated by a Fourier-transform from the acquired spectra, without movement of the reference arm. (Schmitt 1999, Fercher *et al.* 1995). This feature improves imaging speed dramatically, while the reduced losses during a single scan improve the signal-to-noise ration proportional to the number of detection elements. The parallel detection at multiple wavelength ranges limits the scanning range, while the full spectral bandwidth sets the axial resolution. Fourier Domain OCT (FD-OCT), also known as Spectral Domain OCT (SD-OCT) or Spatially Encoded Frequency Domain OCT (SEFD-OCT), extracts spectral information by distributing different optical frequencies onto a detector stripe (*e.g.* line-array CCD or CMOS) via a dispersive element. Thereby the information of the full depth scan can be acquired within a single exposure. However, the large signal-to-noise ratio advantage of FD-OCT is reduced due the lower dynamic range of stripe

[3] The Michelson interferometer is the most common configuration for optical interferometry and was invented by Albert Abraham Michelson (1852-1931). Michelson was a Polish-born American physicist known for his work on the measurement of the speed of light and especially for the Michelson-Morley experiment. In 1907 he received the Nobel Prize in Physics.

detectors in respect to single photosensitive diodes, resulting in an SNR advantage of ~10 *dB* at much higher speeds. The drawbacks of this technology are found in a strong fall-off of the SNR, which is proportional to the distance from the zero delay and a *sinc*-type[4] reduction of the depth dependent sensitivity because of limited detection linewidth (one pixel detects a quasi-rectangular portion of an optical frequency range instead of a single frequency, the Fourier transform leads to the *sinc* behaviour). Additionally the dispersive elements in the spectroscopic detector usually do not distribute the light equally spaced in frequency on the detector, but mostly have an inverse dependence. Therefore the signal has to be resampled before processing, which cannot take care of the difference in local (pixelwise) bandwidth, which results in further reduction of the signal quality. Time Encoded Frequency Domain OCT (TEFD-OCT), also known as Swept Source OCT (SS-OCT), tries to combine some of the advantages of standard TD-OCT and SEFD-OCT. Here the spectral components are not encoded by spatial separation, but they are encoded in time. The spectrum is either filtered or generated in single successive frequency steps and reconstructed before Fourier transformation. By accommodation of a frequency scanning light source (*i.e.* frequency scanning laser) the system optical setup becomes simpler than SEFD, but the problem of scanning is essentially translated from the TD-OCT reference arm into the TEFD-OCT light source. Here the advantage lies in the proven high SNR detection technology, while swept laser sources achieve very small instantaneous bandwidths (*i.e.* linewidth) at very high

[4] The sinc function, also called the sampling function and denoted by *sinc(x)* and sometimes by *Sa(x)*, is a function that arises frequently in signal processing and the theory of the Fourier transforms. The full name of the function is *sine cardinal*, but is commonly referred to by its abbreviation, sinc. In mathematics, the historical *sinus cardinalis* is defined by

$$\mathrm{Sa}(x) = \mathrm{sinc}(x) = \begin{cases} 1 & \text{for } x = 0 \\ \dfrac{\sin(x)}{x} & \text{otherwise} \end{cases}.$$

A plot of sinc(x) is illustrated below:

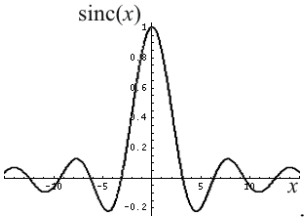

Let $\Pi(x)$ be the rectangular function, then the Fourier transform of $\Pi(x)$ is the sinc function

$$\mathcal{F}_x\left[\Pi(x)\right] = \mathrm{sinc}(\pi x).$$

frequencies (20-200 *kHz*). Drawbacks are the nonlinearities in the wavelength, especially at high scanning frequencies, the broadening of the linewidth at high frequencies and a high sensitivity to movements of the scanning geometry or the sample (below the range of nanometers within successive frequency steps). Flow imaging based on (colour) *Doppler Optical Coherence Tomography* (DOCT) (Izatt *et al.* 1996, Izatt *et al.* 1997, Yazdanfar *et al.* 1997, Chen *et al.* 1997a, Chen *et al.* 1997b, Chen *et al.* 1998, Barton *et al.* 1998, Yazdanafar *et al.* 1998, Yazdanafar *et al.* 2000) is an emerging technique and is still under investigation. The advantage of this technique is its very high spatial resolution (1-10 μm), which, however, limits the penetration depth to around 1 *mm* due to the wavelengths range of the light sources typically employed in OCT systems (NIR and IR regions, 800-1300 *nm*). Its application *in vitro* experiments has shown the possibility to measure parabolic and non parabolic velocity profiles (Proskurin *et al.* 2003a) and distribution of red blood cells (RBCs) concentrations (Moger *et al.* 2004). From these velocity profiles the local shear rate[5] can be derived, as has been shown by van Leeuwen and co-workers (van Leeuwen *et al.* 1999). *In vivo* applications were described in subsurface vessels of laboratory animals (Barton *et al.* 1999, Rollins *et al.* 2002, Wong *et al.* 2002, Chang and Hou 2003, Satomura *et al.* 2004). DOCT in human vessels concerned blood flow measurements in sub-superficial skin vessels (Proskurin and Meglinski 2007), which allowed more advanced diagnosis and therapeutic control of cutaneous disorders (Tearney *et al.* 2003, Pierce *et al.* 2004, Gambichler *et al.* 2005). Furthermore, OCT allows the assessment of the retinal blood flow dynamics and seems a promising technique for diagnosis of diabetic retinopathy and glaucoma (Yazdanafar *et al.* 2003). Although the technique is still in development, including needle-based DOCT (Yaqoob *et al.* 2006, Yang *et al.* 2005) and real-time flow assessment (Rollins *et al.* 2002, Schaefer *et al.* 2004, Leitgeb *et al.* 2004), OCT application for coronary flow measurements has not yet been shown. However, the use

[5] Shear rate is a measure of the rate of shear deformation:

$$\dot{\gamma}_{xy} = \frac{\partial u_x}{\partial y} + \frac{\partial u_y}{\partial x}.$$

For the simple shear case, it is just a gradient of velocity in a flowing material. The SI unit of measurement for shear rate is s^{-1}. For a Newtonian fluid, the wall shear stress τ can be related to the shear rate by $\tau = \dot{\gamma}_x \eta$, where η is the dynamic viscosity of the fluid.

of OCT for research on the flow-related changes in atherosclerotic plaque is promising, because of its demonstrated capacity to differentiate plaque constituents *ex vivo* and *in vivo* (Regar *et al.* 2003, Tearney *et al.* 2003, Patel *et al.* 2005, van der Meer *et al.* 2005a, van der Meer *et al.* 2005b, Regar *et al.* 2007).

1.2 Aims of the thesis

The ***aim*** of present research is the development of an optical device based on DOCT technology for non-invasive investigation of flow dynamics in vessels with complex geometry. In many practical situations involving flow dynamic measurements, the nature of the flow can be very complex and difficult to model or analyze using numerical methods. The presented DOCT system overcomes some of these limitations, enabling the mapping of complex flow dynamics. ***Specific objectives*** of this works include the development *ad hoc* of vessels with bifurcations and vessels with aneurysm[6] for the characterization of flow dynamics across the junction or along vessel irregularities using DOCT technique.

1.3 Thesis organization

Chapter 1

An overview and background of OCT and DOCT is presented, in conjunction with the motivations and aims of the presented work. Applications and important developments in several sectors of biomedicine which can benefit from non-invasive flow measurements are also discussed.

---

[6] An aneurysm (or aneurism) is a localized, blood-filled dilation (balloon-like bulge) of a blood vessel caused by disease or weakening of the vessel wall. Aneurysms most commonly occur in arteries at the base of the brain (the circle of Willis) and in the aorta (the main artery coming out of the heart), a so-called aortic aneurysm. The bulge in a blood vessel can burst and lead to death at any time. The larger an aneurysm becomes, the more likely it is to burst.

Chapter 2

The underlying theory of OCT and DOCT is summarized. The theory of time-domain optical coherence tomography systems and its functional extension, Doppler optical coherence tomography is presented. The results from flow dynamic measurement presented later in this thesis rely upon the theory presented in this chapter and in Chapter 3.

Chapter 3

A review of flow mechanics principles is presented. The basic concepts of flow dynamics described in this chapter represent the fundamental knowledge of flow dynamic measurements which, in conjunction with the theory exposed in Chapter 2, enable the correct interpretation of the results presented later in this thesis. The definitions of laminar and turbulent flow are discussed. Concepts of computational flow dynamic modeling are also introduced.

Chapter 4

In this chapter, a detailed description of the developed Doppler optical coherence tomography system is reported.

Chapter 5

Detailed description of the optical and mechanical properties of the media utilized in the experiments is reported. Results of flow dynamic measurements obtained from the custom developed complex geometry vessels – T-shaped, Y-shaped and vessel with aneurism – are illustrated and discussed. Application of the DOCT technique for mapping flow in scaffolds for tissue engineering is discussed. Finally, a further improvement of DOCT system is reported, which enabled the imaging of sub-cutaneous blood vessels *in vivo*.

Chapter 6

The main conclusions are discussed in this chapter. The fundamental importance of flow dynamic measurements in complex geometry vessels is demonstrated. A low-coherence interferometer based on Doppler optical coherence tomography technique was developed to perform non-invasive flow measurements in custom developed complex geometry vessels. This work has arisen as a consequence of the need to access complex flow information in quasi real-time or real-time processing. Original results of turbulent flow in complex geometry vessels, such as T-shaped, Y-shaped junctions and vessels with aneurism are reported.

1.4 Motivations and background

One of the motivations for these studies arose by observing that cardiovascular diseases are the leading cause of mortality in many countries worldwide (Mackay and Mensah 2004). Myocardial infarction[7] occurs due to intracoronary thrombosis, the ultimate step in a complex mechanism that leads to acute vessel occlusion. At least 50% of patients experiencing a myocardial infarction do so without previously experiencing any cardiac symptoms (Naghavi *et al.* 2003, Virmani *et al.* 2006, Falk 2006); atherosclerotic plaques prone to rupture do not necessarily limit the blood flow and thus do not cause any symptoms. These plaques, called vulnerable plaques, are characterized by their specific morphology and composition: a large lipid pool covered by a fibrous cap infiltrated by macrophages (Moreno *et al.* 1994) and expansive remodeling within the *lumen* of the vessel (Pasterkamp *et al.* 1998, Burke *et al.* 1997). Among the current imaging techniques characterizing plaque constituents, the application of intravascular

[7] The term *myocardial infarction* focuses on the heart muscle, which is called the myocardium,and the changes that occur in it due to the sudden deprivation of circulating blood. This is usually caused by arteriosclerosis with narrowing of the coronary arteries, the culminating event being a thrombosis (clot). The main change is death (necrosis) of myocardial tissue. The word *infarction* comes from the Latin *infarcire* meaning *to plug up* or *cram*. It refers to the clogging of the artery, which is frequently initiated by cholesterol piling up on the inner wall of the blood vessels that distribute blood to the heart muscle.

coherence domain optical diagnostic techniques allows visualization of the fibrous cap thickness, its infiltration with macrophages (Tearney *et al.* 2003) and the determination of major plaque components (Regar *et al.* 2003, Patel *et al.* 2005).

In the presence of cardiovascular risk factors, being systemic in nature, atherosclerotic plaques develop predominantly at certain locations in the arterial tree, including bifurcations and near the junction sites of side branches (van der Laan *et al.* 2004). These predilection sites are associated with deviations of the normal blood flow pattern (flow velocity field). In consequence, flow-induced shear stress – tangential drag force induced by blood flow acting on a certain luminal wall area – acting on the endothelial cells has been recognized as a key player in plaque localization and plaque growth (Zarins *et al.* 1983, Gnasso *et al.* 1997, Stone *et al.* 2003, Krams *et al.* 1997). Shear stress is linearly related to the flow and thus, for the determination of the local shear stress, the knowledge of blood flow velocity profile distribution is required. A normal shear stress range of 0.68±0.21 *Pa* was derived from Doppler-based blood flow measurements in angiographically normal coronary arteries of 21 patients (Doriot *et al.* 2000).

In human coronary arteries, the relationship between shear stress and plaque composition is under investigation. The study of the influence of shear stress on atherosclerotic plaque development and destabilization requires simultaneous assessment of shear stress and vessel wall internal microstructure. Potential techniques used for shear stress determination are external ultrasounds, intravascular ultrasounds (IVUS), magnetic resonance imaging and Doppler optical coherence tomography. The externally applied ultrasound transducers, which are placed in contact with the skin of the patient, enable measuring shear rate at the posterior wall of the carotid arteries or femoral arteries derived from the Doppler-based velocity profile (Reneman *et al.* 1986, Brands *et al.* 1995, Brands *et al.* 1999). Diagnostic sonographic scanners generally operate in the frequency range of 2 to 18 *MHz*. The choice of frequency is a trade-off between spatial resolution of the image and imaging depth: lower frequencies produce less resolution but image deeper into the body. Typical spatial resolution in soft tissues is ~100 μm. Unfortunately, to date only coronary flow reserve measurements have been

successful (Gadallah *et al.* 1998, Coletta *et al.* 1999), but no velocity profile measurements in coronary arteries have been reported. In principle, this technique might provide details on the wall geometry simultaneously with the shear rate.

Intravascular ultrasound technique is applied to measure blood velocity profiles based on the decorrelation of the radiofrequency (RF) signal (Li 1997, Lupotti *et al.* 2003). In clinical practice, an intravascular catheter is advanced distal to the area of interest. A slow pullback, either manual or automatic (0.5 to 1 $mm \cdot s^{-1}$) with verbal commentary is then performed from the distal vessel back into the guiding catheter. If necessary, the pullback may be repeated several times, or particular area of interest interrogated in greater detail. Present day catheters are less than 1 *mm* in diameter (having started from 2.5 *mm*), operate at 30 to 40 *MHz* and use either phased array or single rotating transducers. From the obtained velocity profiles the local blood flow can be estimated (Carlier *et al.* 1998). However, the presence of the catheter in the lumen disturbs the blood flow (Krams *et al.* 1999) and therefore precludes the possibility of obtaining physiological velocity profiles *in vivo*. Furthermore, although this technique would allow simultaneous assessment of vessel wall structure and blood flow, its application is limited to the study of the relationship between the shear stress and vessel wall averaged over a longitudinal segment rather than variations in this relationship over the vessel circumference. Typical spatial resolution is ~100 μm.

Starting from 1980s, quantitative flow measurements based on MRI were used in phantoms and in the major arteries of the cardiovascular system. Currently, phase contrast MRI is used clinically for imaging congenital heart disease and heart valves, and is still an emerging technique for assessment of myocardial perfusion, coronary flow reserve and flow-mediated dilatation in brachial or femoral arteries (Gatehouse *et al.* 2005, Silber *et al.* 2005). In MRI, the velocity profiles are measured throughout the entire geometry of the artery and combined with blood viscosity values to derive the local shear stress at the vessel wall (Moore *et al.* 1994, Oyre *et al.* 1997, Cheng *et al.* 2003a, Cheng *et al.* 2003b, Cheng *et al.* 2003c, Cheng *et al.* 2003d, Papathanasopoulou *et al.* 2003). MRI allows simultaneous measurement of both vessel wall and shear stress, thereby accounting for individual and local variations in both parameters. The

application of this technique in the abdominal aorta and thoracic aorta (Moore *et al.* 1994, Pedersen *et al.* 1999, Wentzel *et al.* 2005) shows an agreement between the areas of oscillatory, low shear stress and the location of atherosclerotic plaques. The application of this technique for velocity profile measurements in human coronary arteries, however, has not been achievable until now. Major limitations are its limited spatial and temporal resolution.

DOCT, as a functional extension of OCT, has the capability to simultaneously perform cross-sectional imaging of sample structure and fluid flow velocity profile distributions in turbid media. It offers high spatial resolution (1-15 μm) and good velocity resolution, down to 10 $\mu m \cdot s^{-1}$ (Wang 2004, Proskurin *et al.* 2004). The spatial resolution is generally an order of magnitude better than the ultrasound technique whilst the velocity resolution depends on the minimum detectable Doppler frequency shift and on the method used to evaluate it. Several groups have reported the capability of the DOCT technique to image flow velocity profiles in phantoms and blood vessels *in vivo* (Izatt *et al.* 1997, Yazdanfar *et al.* 1997, Proskurin *et al.* 2003a, Moger *et al.* 2004, Wang 2004, Proskurin *et al.* 2004). Izatt and co-workers described DOCT system improvements for blood flow velocity profile detection in biological tissues (Izatt *et al.* 1997, Kulkarni *et al.* 1998) and reported results from measurements of blood flow cardiac dynamics *in vivo* (Yazdanfar *et al.* 1997). Matcher and Moger studied blood flow dynamics in glass capillaries (Moger *et al.* 2004) and in addition, how multiple scattering can affect the quality of the DOCT signal (Moger *et al.* 2005). Wang and Proskurin studied flow dynamics in converging die entries (Proskurin *et al.* 2003a, Proskurin *et al.* 2003b, Wang 2004, Proskurin *et al.* 2004).

In this thesis, the results of extended studies of flow dynamics in vessel with complex geometry are reported. In particular, T- and Y-shaped junctions and bifurcations with aneurism were investigated. These studies offer the possibility to access a more detailed analysis, compared to the one offered by the actual clinical practice, of the flow/vessel interactions. The presented results clearly show the capability of DOCT to image at high resolution the morphology of vessels and the associated flow velocity regime along the measured cross-section. The possibility to image flow patterns in the vessels with

complex geometry represents a very useful tool for clinicians and can be applied to evaluate the velocity distribution around vessel's irregularities – such as an atherosclerotic plaque in human artery – and to derive the shear stress acting on the walls. This information is highly requested by clinicians to estimate the risk of plaque rupture with potentially consequent heart attack.

1.4.1 The need for flow measurements

Interest in fluid mechanics by scientist and engineers continues to increase. Fluid flow is important in a number of engineering fields, in many sectors of medicine and industry and in many practical studies related to oceanography, meteorology, astronomy, chemistry, geology and physics (Goldstein 1996, Yang 2001). Advances in sophisticated numerical methods (Drikakis and Geurts 2002) to study and predict fluid flows has not diminished the requirements of measurements and experimental quantitative and qualitative observations are still necessary to increase our understanding of the physical processes in flowing systems and for validation of numerical models. Flow measurements are particularly required in the characterization of turbulent flow (Lourenco 1998, Andreeva and Durtin 2002, Celata *et al.* 2005, Real *et al.* 2006) and three-dimensional flows (Berg and Torp 1998, Chao *et al.* 2005), as well as to determine specific flow quantities, needed in a variety of medical and industrial applications (Tatam 1997).

In practice, many different flow parameters are often required. These include the instantaneous magnitude of velocity, the vector velocity itself, spatial and temporal correlations, turbulent shear stress and overall volume or mass flow. The constant need for more complete and more accurate information is leading to the design of new variations on classical instrumentation as well as the development of relatively new instrumentation and techniques (Miller 1996, Baker 2002, Boyes 2002).

A very broad variety of flow measurements exists, which leads to many different applications, which can substantially differ a lot from each other according to the

particular need or wanted information. However, an overall methodology and philosophy of fluid measurements can be found among these diversities.

In a macroscopic scale, where the smallest geometric dimension of the container or duct is large in comparison to physical length scales (such as diffusion lengths, mean free paths or molecular dimensions), the analysis of the behaviour of fluids is based upon the fundamental laws of applied mechanics which relate to the conservation of mass-energy and the force-momentum equation. The motion of fluid substances can be described by the Navier-Stokes equations, named after Claude-Louis Marie Henri Navier[8] and George Gabriel Stokes[9] (1819-1903). These equations establish that changes in momentum in infinitesimal volumes of fluid are simply the sum of dissipative viscous forces, changes in pressure, gravity and other forces acting inside the fluid: an application of Newton's second law.

When dealing with fluid mechanics, two important aspects must be taken into account. The first is the nature and properties of the fluid; the second is that we are frequently concerned with the behaviour of a continuous stream of fluid, without beginning or end. A further problem is that it can be extremely difficult to specify either the precise movement of a stream of fluid or that of individual particles within it. It is, therefore, often necessary – for the purpose of theoretical analysis – to assume ideal, simplified conditions and patterns of flow. The results so obtained may then be modified by introducing appropriate coefficients and factors, determined experimentally, to provide a basis for the design of fluid systems. This approach has proven to be reasonably satisfactory. In so far as the theoretical analysis establishes the form of the relationship

[8] Claude Louis Marie Henri Navier (1785-1836) was a French engineer and physicist who specialized in mechanics. Navier formulated the general theory of elasticity in a mathematically usable form (1821), making it available to the field of construction with sufficient accuracy for the first time. In 1819 he succeeded in determining the *zero line* of mechanical stress, finally correcting Galileo Galilei's incorrect results, and in 1826 he established the elastic modulus as a property of materials independent of the second moment of area. Navier is therefore often considered to be the founder of modern structural analysis. His major contribution however remains the Navier-Stokes equations (1822), central to fluid mechanics.

[9] Sir George Gabriel Stokes, 1st Baronet (1819–1903) was an Irish mathematician and physicist, who made important contributions to fluid dynamics (including the Navier-Stokes equations), optics, and mathematical physics (including Stokes' theorem). He was secretary, then president of the Royal Society.

between the variables; the experimental investigation corrects for the factors omitted from the theoretical model and establishes a quantitative relationship (Grinstein 2006).

1.5 Biomedical applications

Not only has the study of fluids been of considerable practical importance since antiquity, but it has also had an important role in the development of modern science and technology (Cheng 1997, Johnson 1998). The development of the relation between the pressure, area and average fluid velocity by Daniel Bernoulli[10] (Bernoulli 1738) launched a period where scientists of the day described such diverse topics as combustion (phlogistic theory) and electricity in terms of the motion of a featureless, homogeneous fluid (Wolf 1939). Beginning with the seminal work of Jean Louis Marie Poiseuille[11] in the 1840s, the study of fluid dynamics has been important to the evolution of scientific thought and its application to technology. Poiseuille's classic paper on flow in capillaries gave rise to modern fluid dynamics (Herschel 1940).

Nowadays, fluid flow continues to be intensively studied. Chaotic and turbulent motions are among the more aggressively studied topics in the physical sciences (Stanley and Ostrowsky 1988, Ott *et al.* 1990, Bau and Wang 1991, Mathieu and Scott 2000, Sugii *et al.* 2005, Bonesi *et al.* 2007a, Bonesi *et al.* 2007b). In the macroscopic world, the continuum model for fluids is both valid and powerful and can be applied to the study of a wide variety of situations. However, it must be recognized that fundamental differences currently remain between the approaches available to determine the detailed

[10] Daniel Bernoulli (1700–1782) was a Dutch-born mathematician who spent much of his life in Basel, Switzerland. He worked with Leonhard Euler on the equations bearing their names. Bernoulli's principle is of critical use in aerodynamics. It is applicable to steady, inviscid, incompressible flow, along a streamline.

[11] Jean Louis Marie Poiseuille (1797–1869) was a French physician and physiologist. He was interested in the flow of human blood in narrow tubes. In 1838 he experimentally derived and in 1840 and 1846 formulated and published Poiseuille's law (or Hagen-Poiseuille law, named also after Gotthilf Heinrich Ludwig Hagen [1797-1884]). This concerns the voluminal laminar stationary flow of an incompressible uniform viscous liquid (so-called Newtonian fluid) through a cylindrical tube with constant circular cross-section. It can be successfully applied to blood flow in capillaries and veins, to air flow in lung alveoli, for the flow through a drinking straw or through a hypodermic needle.

distribution of flow properties in laminar and turbulent flows. That the Navier-Stokes equations provide a complete mathematical description of laminar flows (Douglas *et al.* 2001) is now so well established and so much taken for granted that many research workers no longer deem it necessary to compare their solutions of these equations with experiment. Solutions of the Navier-Stokes equations have come to be accepted as constituting a primary standard for data on laminar flow. For turbulent flows the situation is quite different. Here, although the Navier-Stokes equations describe the instantaneous motion, solutions of these equations for the time-averaged flow are not available and in this context the results of careful experimentation provide the primary standard for data on pressure and velocity distributions.

Some areas related with the presented work which require experimental flow measurements are reviewed below.

1.5.1 Blood flow characterization

Research in blood flow has a direct impact in improving the understanding and management of human health, including the need of information on volume blood flow or blood flow dynamics. Volume blood flow is a related measure of oxygen and nutrient concentrations in blood. Such concentration measurements are an indication of general cell health. Research on blood flow dynamics is important for studying circulatory diseases (Reger *et al.* 2007), for assistance during and for monitoring post surgical intervention, to study cerebral blood flow (Mishra 2002), to analyze volume blood flow and oxygenation in brain (Ndubuizu and LaManna 2007), to monitor retinal blood flow (Zarfati *et al.* 2000), and many other applications.

Blood is a non-Newtonian fluid and its motion is generally pulsed, when considered in live biological systems (Lowe 1988). Furthermore, blood is generally flowing in elastic ducts, whose shape may change dynamically. The Navier-Stokes equations are difficult to apply in this case, and therefore, practical clinical measurements are highly requested to validate theoretical modeling (Perktold and Rappitsch 1995, Cebral *et al.* 2002).

Scanning Laser Doppler Flowmetry (LDF) has been used to study blood flow in patients with normal-pressure glaucoma (Jonas *et al.* 2003). It has been proposed that glaucoma patients show a reduction in flow in the neuroretinal rim, the reduction being greater in high velocity regions than those with low velocity. The flow measurements decrease with increasing damage to the optic nerve. However, a clear relationship between stage of glaucoma and flow measurements was not found.

Retinal blood flow has also been studied in patients with diabetic retinopathy (Cuypers *et al.* 2000). They reported an association between the level of retinopathy and blood flow in the perifoveal and nasal areas. They noted an increase in blood flow, compared to controls, in the papillomacular region in diabetic patients without retinopathy suggesting that it might indicate the symptoms of early phases of diabetic retinopathy in the absence of visible changes in the retina. However, there is a large variability in the flow measurements and further work is needed to confirm the value of this technique.

LDF and reflectance spectrophotometry has been applied to study changes in skin blood flow and hemoglobin content of patients affected by port wine stains (Lanigan and Cotterill 1990). A port wine stain, or *naevus flammeus*, is a vascular birthmark consisting of superficial and deep dilated capillaries in the skin which produces reddish to purplish discoloration of the skin. These marks are present at birth and persist throughout life. Port wine stains that involve the upper and lower eyelids (trigeminal distribution) may be associated with the development of glaucoma (Salim *et al.* 2003). The most efficient treatment is done by lasers, because this is the sole method of destroying the cutaneous capillaries without significant damage the overlying skin. In this case it is important to monitor the changes in blood flow in response to the laser treatments *in situ*, to assist in assessing the efficacy of the laser therapy (Nelson *et al.* 2001).

Another important field in medicine in which blood flow measurements represent a fundamental diagnostic tool is cardiology, whose major aspect has been detailed discussed previously.

1.5.2 Tissue engineering

The "modern" age of organ and tissue transplantation is now many decades old[12]. As in almost every field of biomedical research, research in organ transplantation has been facilitated by the use of cell and tissue culture techniques. The first tissue culture was performed at Johns Hopkins in 1907, when Ross Harrison demonstrated that frog neural tissue could be maintained in a dish outside the organism. Methods for collection, purification, storage, characterization and use of donor blood have improved continuously over the last century, particularly after the discovery of blood typing by Karl Landsteiner[13]. Genetically engineered cells were first introduced into patients in the late 1980s.

The past decade has brought tremendous progress in transplantation, primarily because of improved surgical techniques and immunosuppressive agents. Unfortunately, all transplantation procedures suffer from a common problem: the demand for viable tissues or organs from donors far exceeds the supply. This problem will come more pronounced with time, as population growth and better treatments for other diseases produce more candidates for organ transplantation or tissue repair. The ethical dilemmas surrounding the availability of human organ transplantation were recognized early and are still frequently debated. Moral and legal problems will increase in the future as technology advances.

One possible solution for many of the tissue and organ deficiencies is the development of better methods for tissue engineering. In tissue engineering, organ or tissue substitutes are constructed in the laboratory for subsequent introduction into patients. Innovative efforts are currently being directed towards cell-based repair approaches,

[12] The idea of replacing organs or tissues is as old as human imagination. In Egypt, it was commonly believed that this exchange could occur by supernatural forces, even between species, as in the Sphinx. Greek mythology presented the feared and dangerous Chimera, a hybrid creature that inspired modern use of the term "chimera" for an organism containing cells from another animal.

[13] Karl Landsteiner (1868–1943), was an Austrian biologist and physician. He is noted for his development in 1901 of the modern system of classification of blood groups from his identification of the presence of agglutinins in the blood, and in 1930 he received the Nobel Prize in Physiology or Medicine. With Alexander S. Wiener, he identified the Rh factor in 1937. He was awarded a Lasker Award in 1946 posthumously.

using autologous cells expanded and seeded on solid cell carriers, or scaffolds (Boschetti *et al.* 2006). Optical diagnostic techniques are therefore an essential tool to evaluate the development process of engineered tissues and cellular responses to environmental stimuli (Langer and Vacanti 1993).

A significant amount of the data collected by cell biologists and tissue engineers relies on invasive imaging techniques, such as histology and Scanning Electron Microscopy (SEM), or, more recently, on non-invasive imaging techniques, such as OCT imaging applied in combination with Confocal Microscopy (CM) technique (Tan *et al.* 2004) to visualize dynamic structural and functional properties in engineered tissues. Tissue engineering makes use of complex 3D porous scaffolds for cell culture. In order to achieve functional tissue with the desired biomechanical properties, it is critical to stimulate mechanically the cells growing into the scaffolds. Bioreactors allowing culture medium perfusion may provide an effective strategy for cell growing by enhancing oxygen and nutrient delivery and providing flow-mediated mechanical stimuli (Freed and Vunjak-Novakovic, 2000). Flow perfusion culture permits the generation and study of a 3D, actively modeled, cell matrix structure and can therefore be a valuable tool for tissue engineering (Bancroft *et al.* 2002, Bagnaninchi *et al.* 2007)

1.5.3 Others

As it has been highlighted already, many are the areas in which fluid flow measurements are requested, and a full list of all the techniques and their applications is far beyond the purpose of this thesis. Nevertheless, it is worth to mention flow measurements related to micro-machining and micro-fluidic techniques and instrumentation, whose recent progress in research can be potentially applied to optical diagnostic measurements technique. The ability of miniaturizing flow measurement diagnostic devices can potentially lead to new ways of investigation, making possible the improvement of the application of important concepts for flow measurements in biology such as non- or minimally invasive and *in-vivo*. *Vice-versa*, the application of

optical diagnostic techniques for flow investigations can aid the design and development of micro-fluidic devices.

Miniaturized instrumentation and reactors have attracted great interest in the last decade. The first reported use of a microchip was in 1979, when a gas chromatograph air analyzer was fabricated on a silicon wafer. It was not until several years later, when flow injection analysis was performed on a chip, the microchips gained attention. Over the last decade, research in integrated micro-fluidic devices (which are typically referred to as lab-on-a-chip devices or Micro Total Analysis Systems (μTAS) has expanded to include sample preparation, fluid handling, microreactors, separation systems, cell handling and cell culturing. The incorporation of these techniques has led to micro-fluidic devices that have been used to perform capillary electrophoresis-based separations, magnetic microparticle-based separations, immunoassays, DNA analysis and clinical diagnostics, along with the design of highly efficient micro-reactors. They have been applied in medical analysis, environmental monitoring, biochemical analysis and microchemistry.

Chapter 2

Principles of time-domain low coherence imaging: Theory of Optical Coherence Tomography and Doppler Optical Coherence Tomography

2.1 Introduction

The rapid growth in laser and photonic technology has resulted in new tools being proposed and developed for use in the medical and biological sciences. Specifically, a discipline known as biomedical optics has emerged, which is providing a broad variety of optical techniques and instruments for diagnostic, therapeutic and basic science applications. New laser sources, detectors and measurement techniques are yielding powerful new methods for the study of diseases on all scales, from single molecules to specific tissues and whole organs. For example, novel laser microscopes permit spectroscopic and force measurements to be performed on single protein molecules (Tuchin 2004, Tuchin 2000); new optical devices provide information on molecular dynamics and structure to perform 'optical biopsy' non-invasively and almost instantaneously; optical coherence tomography and diffuse optical tomography allow visualization of specific tissue and organs (Tuchin 2004, Tuchin 2000).

In this exciting developmental panorama of biomedical optics technologies, low-coherence imaging technique plays an important role in achieving tomographic measurements of biological tissues with resolution approaching the micron scale.

The origins of the technique lie in white-light interferometry, whose use has a long history. Already in 1665, Robert Hooke[14] noted that the colours seen in white-light interference patterns are a sensitive measure of thickness between reflections surfaces (Hooke 1665). In 1893, Albert Michelson used white light to estimate the size of a series of step-shaped etalons as part of the procedure leading to the first comparison of the wavelength of light with the International Prototype Meter (Michelson 1893). Many of the traditional optical instruments for calibrating gauge blocks employing white light or multiple-colour sources, as well as special microscopes suitable for white-light interferometry, have been in use for a number of years (Barnes and Puttock 1953).

[14] Robert Hooke (1635–1703) was an English polymath who played an important role in the scientific revolution, through both experimental and theoretical work. In 1665 he published a book entitled *Micrographia* which contained a number of microscopic and telescopic observations, and some original observations in biology. Hooke coined the biological term *cell*, so called because his observations of plant cells reminded him of monks' cells which were called *cellula*. He is often credited with the discovery of the cell, although his microscope was very basic. Hooke's design was utilized by the Dutchman Anton van Leeuwenhoek, described as the father of microbiology.

White-light interference microscopes have been widely used for measuring film thickness and monitoring surfaces with discontinuities several wavelengths deep.

Although the basic principles of white-light and multiple-colour interferometry are fundamental concepts of optics, the practical implementation of these principles in automated instruments is a relatively recent development, which led to the implementation of the so-called fibre-based Optical Coherence Domain Reflectometry (OCDR) technology (Flournoy *et al.* 1972, Youngquist *et al.* 1987). Adolf F. Fercher and co-workers (Fercher *et al.* 1988) and Christoph K. Hitzenberger (Hitzenberger 1992) have extended broadband interferometry to diagnostic measurement of the eye. The publication in *Nature* of the paper by James G. Fujimoto and co-workers (Huang *et al.* 1991), has given a great impulse to the application of low-coherence fibre-based interferometry for imaging biological tissues (turbid media), coin for it the term *optical coherence tomography*. The presented technique was shown capable of imaging biological tissues with an axial resolution of about 30 μm. Since then, OCT has achieved sub-micrometre resolution in 2001 (Drexler *et al.* 2001) due to introduction of wide bandwidth light sources (sources emitting wavelengths over a 100 *nm* bandwidth range). At present, OCT has found its place as a widely accepted imaging technique, especially in ophthalmology (Drexler *et al.* 2003, Schuman *et al.* 2004, Ergun *et al.* 2005, Wollstein *et al.* 2005) and other biomedical applications (Bouma and Tearney 2002, Brezinsky 2006, Regar *et al.* 2007).

2.2 Principles of Time-Domain OCT

Optical Coherence Tomography (OCT) (Fercher 1996, Schmitt 1999) is a relatively recently developed non-invasive optical imaging modality based on low-coherence interferometry (Masters 1999), or white light interferometry, first described by Sir Isaac Newton[15]. OCT performs high-resolution, cross-sectional tomographic imaging of the

[15] Sir Isaac Newton (1643–1727) was an English physicist, mathematician, astronomer, natural philosopher, and alchemist. His treatise *Philosophiae Naturalis Principia Mathematica*, published in 1687, described universal gravitation and the three laws of motion, laying the groundwork for classical mechanics, which dominated the scientific view of the physical universe for the next three centuries and is the basis for modern engineering. He showed that the motion of objects on Earth and of celestial bodies

internal microstructure in materials and biological samples by measuring time-of-flight of backscattered or backreflected light[16] at varying axial (longitudinal) distances. In principle, the technique is similar to ultrasound B-mode[17] imaging, with the substantial difference that the measuring agent utilized in the system is light instead of sound waves. Because the sounding radiation in OCT propagates at very high speed, this implies that distance measurements using light requires ultrafast time resolution. The velocity of sound in water is approximately 1500 $m{\cdot}s^{-1}$, whereas the velocity of light in vacuum, c, is exactly[18] 299.792.458 $m{\cdot}s^{-1}$. Estimation of distance or spatial information may be determined from the time delay of the reflected echoes according to the formula $\Delta T = z{\cdot}u^{-1}$, where ΔT is the echo delay, z is the distance the echo travels and u is the velocity of the measuring agent (sound or light). Observing that the typical value of spatial resolution for ultrasound is ~100 μm, the resolved time resolution is of the order of 100 ns, a value well within the limits of electronic detection. Different is the case of the light propagation. The typical value of spatial resolution in OCT systems is 10 μm,

---

are governed by the same set of natural laws by demonstrating the consistency between Kepler's laws of planetary motion and his theory of gravitation, thus removing the last doubts about heliocentrism and advancing the scientific revolution.

[16] Properly, the term *light* describes electromagnetic radiation with a wavelength that is visible to the eye. In this context, as is commonly used in the technical or scientific language, the word will be used in its more broad meaning, intending electromagnetic radiation of all wavelengths.

[17] Four different modes of ultrasound are used in medical imaging. These are:

- *A-mode*: A-mode is the simplest type of ultrasound. A single transducer scans a line through the body with the echoes plotted on screen as a function of depth. Therapeutic ultrasound aimed at a specific tumour or calculus is also A-mode, to allow for pinpoint accurate focus of the destructive wave energy.
- *B-mode*: In B-mode ultrasound, a linear array of transducers simultaneously scans a plane through the body that can be viewed as a two-dimensional image on screen.
- *M-mode*: M stands for motion. In M-mode a rapid sequence of B-mode scans whose images follow each other in sequence on screen enables doctors to see and measure range of motion, as the organ boundaries that produce reflections move relative to the probe.
- *Doppler mode*: This mode makes use of the Doppler effect.

[18] From CODATA Speed of light in vacuum (*http://physics.nist.gov/cgi-bin/cuu/Value?c*) 2006 CODATA recommended values. National Institute of Standards and Technology. Retrieved on 3rd September 2007.

The speed of light in vacuum is an important physical constant denoted by the letter *c* for *constant* or the Latin word *celentas*, meaning "swiftness". It is the speed of all electromagnetic radiation, including visible light, in a vacuum. More precisely, it is the speed of anything with zero rest mass. The speed of light, when it passes through a transparent or translucent material medium, like glass, air or biological tissues, is slower than the speed in a vacuum. The ratio of *c* to the observed phase velocity is called the *refractive index* of the medium and indicated with the symbol *n*.

implying a required time resolution of the order of 10 *fs*! At present, no electronic devices are fast enough to accomplish such a fast detection. Therefore, the measurement of the time-of-flight in OCT is achieved via optical-based interferometric techniques instead of employing electronic-based devices, as the case of ultrasound imaging. OCT measuring technique relies on interference between a split and later re-combined broadband optical field. When two beams of light are combined, their fields rather than their intensities add and produce interference (Fercher 1996, Born and Wolf 1999). The typical embodiment of the interferometer in OCT is based on the Michelson configuration although other implementations are possible, such as the Mach-Zender interferometer (Casaubieilh *et al.* 2005, Fluerau *et al.* 2007).

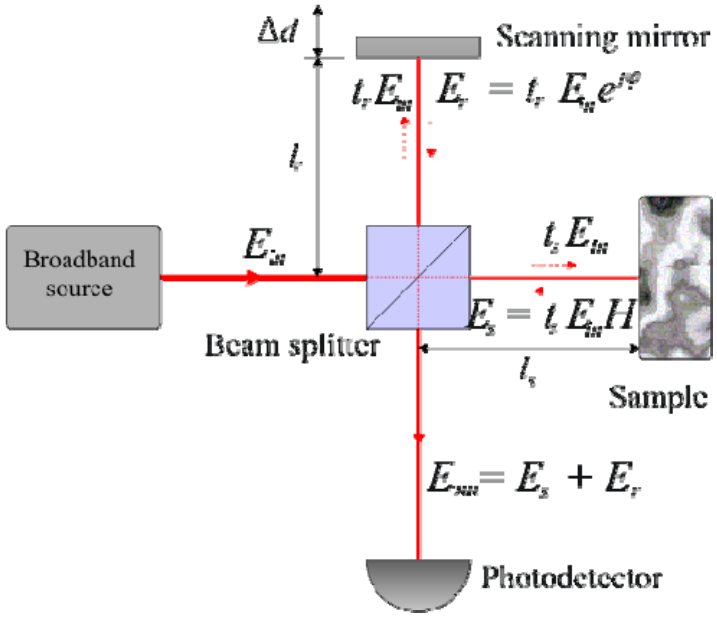

Figure 2.1 – *Schematic representation of a time-domain OCT system based on Michelson's interferometer with a scanning reference delay line.* l_r *and* l_s *represent the geometrical path length in the reference and sample arm respectively;* Δd *is the moving range of the scanning reference mirror;* E_{in} *and* E_{out} *represent the optical field in input and output of the interferometer respectively;* E_r *represents the optical field reflected off the scanning mirror and redirected into the beam splitter;* E_s *represents the optical field backscattered from the sample at different depth redirected into the beam splitter;* t_r *and* t_s *are the transmission coefficient of the beam splitter, typically* $t_r = t_s = 0.5$*;* H *is the sample response function and describes its internal structure.*

Figure 2.1 schematically illustrates a common OCT embodiment based on Michelson's interferometer with a scanning reference delay arm, which represent a typical implementation for the so called *Time-Domain OCT* (TD-OCT) configuration.

The incident optical radiation can be described as a plane wave and conveniently represented by the well known expression

$$E_{in}(t) = E_0 e^{-jkz}, \tag{2.1}$$

where E represents the electric field of the EM radiation, $k = 2\pi/\lambda$, λ is the wavelength and z the spatial coordinate. With reference to Figure 2.1, the subscript *in* represents quantities associated to the input arm of the interferometer, typically the input probing radiation coupled with the output of the light source; the subscripts *r* and *s* describe quantities associated to the reference and sample arm of the interferometer respectively; the subscript *out* describes quantities associated to the output arm of the interferometer, typically interfaced with photodetection devices. The input light is directed onto a beamsplitter that splits the incoming radiation into a reference beam directed towards a scanning mirror (SM) and a measurement or signal beam, also referred to sounding or probing radiation, directed towards the sample.

The reference beam E_r is then reflected from SM whereas the signal beam E_s is reflected and/or backscattered from multiple layers within the sample that is to be imaged. The mirror ideally is a perfect reflector and introduces a phase shift of 180° in the incident radiation. The interaction of the probing radiation with the sample in the sample arm can be expressed via the sample response function H, which describes the overall reflection from the structure of the sample. The two beams then recombine and interfere at the beamsplitter and the resultant beam is then directed onto an optical detector (PD). The output of the interferometer is the sum of the electromagnetic fields from the reference beam and the signal beam. PD measures the intensity of the output optical beam, which is proportional to the square of the electromagnetic field E_{out}.

$$I(\omega, \Delta z) = \left\langle \left| E_{out} \right|^2 \right\rangle = \left\langle E_{out}(\omega, t, \Delta l) E_{out}^{*}(\omega, t, \Delta l) \right\rangle \tag{2.2}$$

where ω is the angular frequency; t is the time and $\Delta l = l_r - l_s$ is the pathlength mismatch between the reference and sample arm of the interferometer respectively. Here the angled brackets denote a time-average operation. Substituting $E_{out} = E_r + E_s$ in Equation 2.2 it gives

$$I(\omega,\Delta z)=\left\langle E_s E_s^*\right\rangle+\left\langle E_r E_r^*\right\rangle+2\Re\left(\left\langle E_s E_r^*\right\rangle\right). \tag{2.3}$$

The first two terms on the right side of Equation 2.3 represent the DC component of the detected signal and can be identified as self-reference interference. The last term carries the wanted information and is expressed by the real part of the complex cross-correlation interference.

Expressing the reference and sample fields as (Bouma and Tearney 2002, Tomlins 2007)

$$E_r(\omega)=t_r t_s E_{in} e^{-j\varphi(\omega)}=A_r(\omega)e^{-j2(kl_r-\omega t)} \tag{2.4a}$$

and

$$E_s(\omega)=t_r t_s E_{in} H=A_s(\omega)e^{-j2(kl_s-\omega t)} \tag{2.4b}$$

respectively, where E_{in} and E_{out} are the optical field in input and output of the interferometer respectively; E_r represents the optical field reflected off the scanning mirror and redirected into the beam splitter; E_s represents the optical field backscattered from the sample at different depth redirected into the beam splitter; t_r and t_s are the transmission coefficient of the beam splitter, typically $t_r = t_s = 0.5$; H is the sample response function and describes its internal structure; l_r and l_s are the distances covered by the probing radiation in the reference and sample arm respectively. With reference to a broadband light source the photocurrent generated by PD is proportional to the sum of the interference due to each monochromatic plane wave component, according to

$$i\propto\Re\left[\int_{-\infty}^{+\infty}E_s(\omega)E_r^*(\omega)\frac{d\omega}{2\pi}\right]=\Re\left[\int_{-\infty}^{+\infty}S(\omega)e^{-j\Delta\phi(\omega)}\frac{d\omega}{2\pi}\right], \tag{2.5}$$

where

$$S(\omega)\doteq A_s(\omega)A_r^*(\omega) \tag{2.6}$$

and

$$\Delta\phi(\omega) \doteq 2k(l_s - l_r) \doteq 2k\Delta l \,. \tag{2.7}$$

If the sample and reference arm fields have the same spectral component as the light source, the Wiener-Khinchine theorem shows that $S(\omega)$ in Equation 2.6 is essentially equivalent to the power spectrum of the light source. For a source with Gaussian normalized[19] power spectral density given by

$$S(\omega - \omega_0) = \sqrt{\frac{2\pi}{\sigma_\omega^2}} \cdot e^{-\frac{(\omega-\omega_0)^2}{2\sigma_\omega^2}} \tag{2.8}$$

where ω_0 is the central frequency and σ_ω^2 is the standard deviation power spectral bandwidth, Equation 2.5 becomes

$$i \propto \Re\left\{\exp\left[-\frac{\sigma_\omega^2}{2}\Delta\tau_g^2\right] \cdot \exp\left[-j\omega_0\Delta\tau_p\right]\right\} = e^{-\frac{\sigma_\omega^2}{2}\Delta\tau_g^2} \cdot \cos\left(\omega_0\Delta\tau_p\right) \tag{2.9}$$

,

where

$$\Delta\tau_p = \frac{2\Delta l}{u_p} \tag{2.10a}$$

and

$$\Delta\tau_g = \frac{2\Delta l}{u_g} \tag{2.10b}$$

represent the phase delay mismatch and group delay mismatch respectively; u_p correspond to the centre frequency phase velocity and u_g is the group velocity. Equation 2.9 contains two oscillatory terms. The first oscillatory term is a rapid oscillatory term or the phase modulation. The second oscillatory term is much slower, is Gaussian in shape and is the envelope of the autocorrelation function. This latter term primarily carries ranging information whilst the former sense the overall velocities of moving

[19] Normalized to unit power

$$\int_{-\infty}^{+\infty} S(\omega)\frac{d\omega}{2\pi} = 1$$

constituents and/or particles via Doppler effect acting on ω. Figure 2.2 shows the shape of a typical interference signal generated by a TD-OCT system with implemented spectral broadband light source. The model of the interferometric pattern is described by Equation 2.9; with reference to Figure 2.2, the black curve represents the phase modulation and carries velocities information of the moving constituents of the system (scan device and moving parts in the sample), whilst the red curve represents the envelope of the autocorrelation function and carries structural information of the sample (morphology).

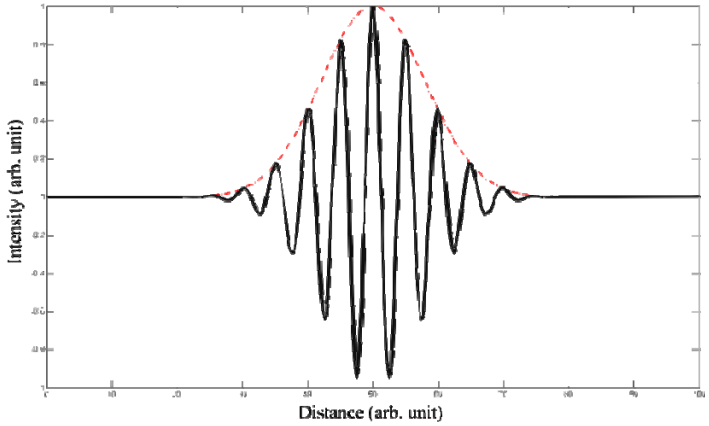

Figure 2.2 – *Typical shape of the cross-correlation component of the interferometric signal, as detected on the photodiodes and expressed by Equation 2.9 (numerical simulation). The red curve represents the envelope of the cross-correlation function, Gaussian in shape if the light source has a Gaussian spectrum. This curve primarily carries the ranging (structural) information of the sample. The second term in Equation 2.9 represents the phase of the cross-correlation signal and appears as high frequency oscillations. For example, variations in the phase term are used in Doppler assessments (see Figure 2.6).*

Due to the broadband nature of the probing radiation, interference between the optical fields is observed only when the reference and sample arm optical path lengths (OPL) are matched to within the coherence length, Δz, of the light source. In this meaning, the use of a broadband light source makes it possible to compare optical path lengths the light travels in the reference and sample arms of the interferometer within a resolution defined by Δz. This latter quantity is the spatial width of the field autocorrelation produced by the interferometer and its envelope is equivalent to the Fourier transform of the light source power spectrum (Bouma and Tearney 2002). For source with Gaussian power spectral distribution, Δz is defined as[20]

[20] Detailed derivation of Equation 2.11 can be found in (Brezinsky 2006) pp.106-112.

$$\Delta z = \frac{2\ln 2}{\pi} \cdot \frac{\lambda_0^2}{n\Delta\lambda} \tag{2.11}$$

where λ_0 represent the light source central wavelength; $\Delta\lambda$ is the Full Width Half Maximum (FWHM) of the light source power spectrum, n is the refractive index of the media and Δz is the FWHM of the autocorrelation function and represents the axial resolution for OCT systems. Equation 2.11 expresses the axial resolution of an OCT system as in function of the spectral characteristics of the light source (via λ_0 and $\Delta\lambda$) and the optical properties of the media (via n).

The transverse resolution is the same as for conventional optical microscopy and is determined by the focusing properties of an optical beam. For a Gaussian beam, the FWHM lateral resolution, Δx, is (Sampson and Hillman 2004)

$$\Delta x = \frac{2\sqrt{\ln 2}}{\pi} \frac{\lambda_0}{\mathrm{NA}} \tag{2.12}$$

where NA[21] is the numerical aperture of the focusing lens. Important properties of the Gaussian beam are its minimal radius (beam waist), Rayleigh range or confocal

[21] In optics, the numerical aperture (NA) of an optical system is a dimensionless number that characterizes the range of angles over which the system can accept or emit light. The exact definition of the term varies slightly between different areas of optics.
In *microscopy*, the numerical aperture of an optical system such as an objective lens is defined by NA = $n \cdot \sin\theta$, where n is the index of refraction of the medium in which the lens is working and θ is the half-angle of the maximum cone of light that can enter or exit the lens. In general, this is the angle of the real marginal ray in the system. The angular aperture of the lens is approximately twice this value (within the paraxial approximation). The NA is generally measured with respect to a particular object or image point and will vary as that point is moved. In microscopy, NA is important because it indicates the resolving power of a lens. The size of the finest detail that can be resolved is proportional to λ/NA, where λ is the wavelength of the light. A lens with a larger numerical aperture will be able to visualize finer details than a lens with a smaller numerical aperture. Lenses with larger numerical apertures also collect more light and will generally provide a brighter image.
In *laser physics*, the numerical aperture is defined slightly differently. Laser beams spread out as they propagate, but slowly. Far away from the narrowest part of the beam, the spread is roughly linear with distance – the laser beam forms a cone of light in the far field. The same relation is given for the NA = $n \cdot \sin\theta$, but θ is defined differently. Laser beams typically do not have sharp edges like the cone of light that passes through the aperture of a lens does. Instead, the irradiance falls off gradually away from the centre of the beam. It is very common for the beam to have a Gaussian profile. Laser physicists typically choose to make θ the *divergence* of the beam: the far-field angle between the propagation direction and the distance from the beam axis for which the irradiance drops to $1/e^2$ times the wavefront total irradiance. The NA of a Gaussian laser beam is then related to its minimum spot size by

$$\mathrm{NA} \cong \frac{2\lambda_0}{n\pi D}$$

parameter, intensity profile, power and radius of curvature. The Gaussian beam has a minimal radius at the beam waist, W_0. The beam waist is given by[22]

$$W_0^2 = \frac{\lambda_0 z_R}{n\pi} \tag{2.13}$$

where z_R is the Rayleigh range and n is the refractive index of the medium where the beam propagates. Two times z_R is known as the confocal parameter, b, or depth of focus and define the zone over which the beam is relatively collimated.

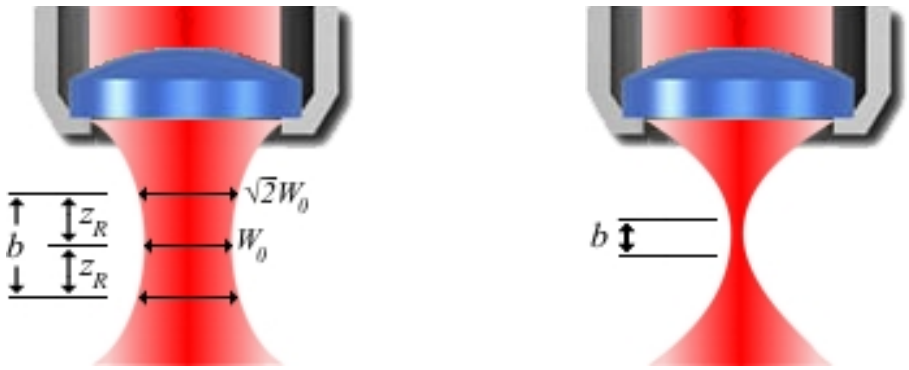

(a) (b)

Figure 2.3 – *(a) Low and (b) high numerical aperture focusing limits of OCT. Most OCT imaging is performed with low NA focusing, where the confocal parameter,* b*, is much longer than the coherence length. There is a trade-off between transverse resolution and depth of field. The high NA focusing limit achieves excellent transverse resolution with reduced depth of field. Low coherence detection provides more effective rejection of scattered light than confocal detection.* W_0 *represents the spot size, while* $2z_R$ *represent the Rayleigh range.*

A time domain interference pattern can be obtained by translating the reference mirror to change the reference path length and match multiple optical paths due to layer reflections within the sample. A two- or three-dimensional image is obtained by making multiple depths scans. These scans are performed whilst laterally scanning the beam in either one or two orthogonal directions. Typically, a 2D cross-sectional image may

---

where λ_0 is the vacuum wavelength of the light, and D is the diameter of the beam at its narrowest spot, measured between the $1/e^2$ irradiance points (full width at e^{-2} maximum). Note that this means that a laser beam that is focused to a small spot will spread out quickly as it moves away from the focus, while a large-diameter laser beam can stay roughly the same size over a very long distance.

[22] The equation holds for monochromatic waves. OCT systems make use of broadband sources. Since the focal length of lenses is wavelength dependent, chromatic aberration must be taken in account. For high-resolution OCT, appropriately designed achromatic lenses are indicated.

comprise approximately 500 depth scans covering a width of 5 *mm* (Tomlins and Wang 2005).

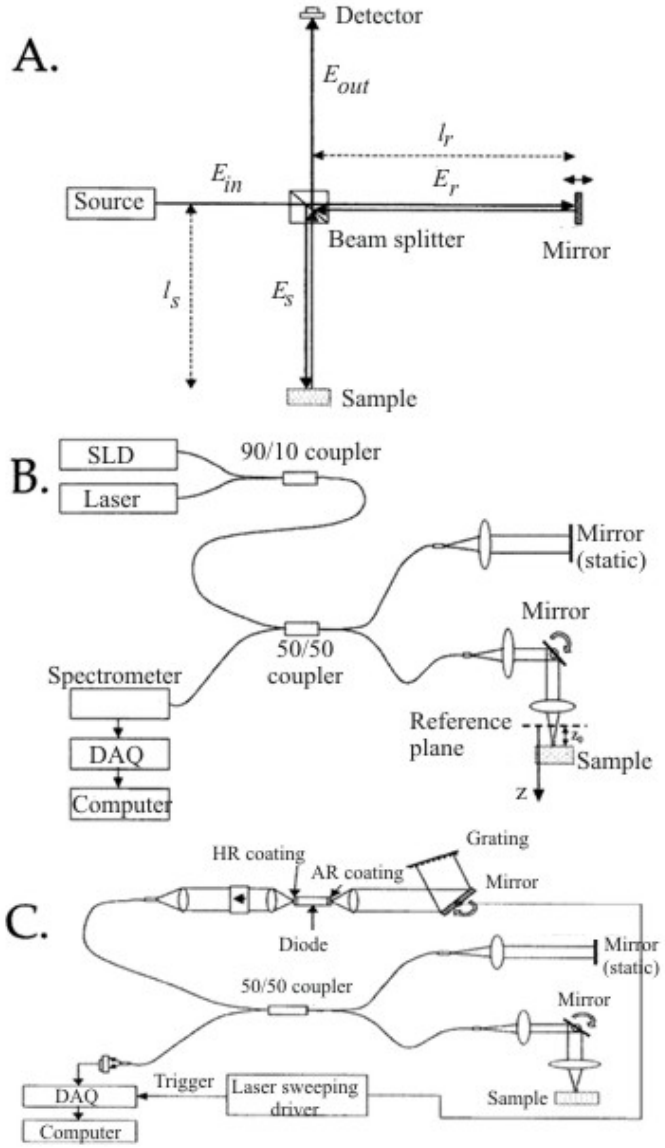

Figure 2.4 – *Low-coherence detection technique based on broadband light source and fibre-based Michelson interferometer. (a) Time-domain OCT. The embodiment includes a Rapid Scan Optical Delay line (RSDL), grating-based in the reference arm. (b) Fourier-domain OCT. There are no moving parts in the interferometer. The embodiment includes a spectrometer in the output arm of the interferometer. (c) Swept source OCT. There are no moving parts in the interferometer. The embodiment includes a swept laser source (from Brezinsky 2006).*

In scattering tissue and other turbid media, the depth scan is limited primarily by optical scattering, and hence maximum reported imaging depths are between 1 and 3 *mm*

(Brezinski and Fujimoto 1999) for a variety of tissues at wavelengths between 800 and 1300 *nm*.

In addition to the more commonly used TD-OCT, applying the same core interferometric technique in combination with different detection methods in the output arm of the interferometer and/or different types of light sources, other types of embodiments can be realized, namely Fourier-domain OCT (FD-OCT) and swept source OCT (SS-OCT) and schematically illustrated in Figure 2.4. A review of these techniques is discussed in (Tomlins and Wang 2005).

2.3 Applications of OCT in biomedicine

One of the major advantages of OCT is its non-invasive or minimally invasive nature of the measurement due to the use of electromagnetic radiation (light) as a probing agent. Understanding how light interacts with the sample gave rise to different modalities on how to develop and operate an OCT system and how to access the wanted information from the sample under test. In medical imaging, often the sample is represented by a turbid media such as a biological tissue or a (micro)fluidic system. Turbid media can be characterized by their optical properties, which directly influence the nature and quality of OCT imaging.

Under this perspective, two- and three-dimensional information of the structural composition of the sample (morphology) on the micrometric scale can be obtained illuminating the sample and measuring the intensity of the light backscattered at different depth position of the sample (Huang *et al.* 1991, Welzel 2001). This imaging modality can be classified as *conventional* OCT. Furthermore, taking into account the polarized nature of the light, added structural information can be extracted from samples that exhibit birefringence, such as tendons (Bagnaninchi *et al.* 2006, Ugryumova *et al.* 2005) or collagen fibres (Brezinsky and Fujimoto 2002, Pierce *et al.* 2004, Matcher *et al.* 2004). This imaging modality is named Polarization-Sensitive Optical Coherence Tomography (PS-OCT). Ultimately, taking into account the Doppler effect occurring when the probing radiation interacts with a moving particle, it is possible to map mono

or multi-dimensional velocity distribution of moving particles inside the sample (Bonesi *et al.* 2007a). This imaging modality is known as Doppler Optical Coherence Tomography (DOCT) and will be detailed described in the following paragraphs. These three imaging modalities can be obtained from any TD-OCT, FD-OCT or SS-OCT system implementation (Choma *et al.* 2003, Leitgeb *et al.* 2003, Yasuno *et al.* 2004, Wojtkowski *et al.* 2004, Zhang and Chen 2005).

The application of these OCT techniques benefit medical imaging in many different areas, *e.g.* ophthalmology, tissue engineering or cardiology; the list is in constant expansion as new ideas and technologies are brought on the scene. Exhaustive review of the major applications to date can be found in (Bouma and Tearney 2002, Fercher *et al.* 2003, Sampson 2004, Tomlins and Wang 2005, Brezinsky 2006, Regar *et al.* 2007).

2.4 Principles of DOCT

DOCT is a functional extension of OCT capable of simultaneously visualizing high-resolution, cross-sectional depth-resolved structures and associated flow velocity distribution profiles of moving particles in turbid media. The flow velocity measurement principle relies on the Doppler effect exhibited by electromagnetic (EM) wave phenomena: the apparent change in frequency due to the relative motion between an observer and a source. If the source is approaching the observer, the apparent frequency of the wave increases; if the source is moving away from the observer, the apparent frequency of the wave decreases.

For EM waves propagating in vacuum, consistently with the Lorentz transformations[23], this relationship is expressed by

$$f_D = \frac{\sqrt{1-\frac{u^2}{c^2}}}{1 \mp \frac{u}{c}} f_0 = \frac{\sqrt{c^2-u^2}}{c \mp u} f_0 \qquad (2.14)$$

[23] In physics, the Lorentz transformation converts between two different observers' measurements of space and time, where one observer is in constant motion with respect to the other.

where c is the speed of light in vacuum; u is the relative velocity of the moving particle, evaluated along the propagation direction of the light and considered positive when the particle is approaching the observer; f_0 is the frequency of the EM radiation incident on the particle and f_D is the observed frequency of the EM radiation reflected by the particle – namely the Doppler frequency. The sign '–' in the denominator indicates that the particle is approaching the observer, whilst '+' indicates that the particle is receding from the observer. For EM wave propagating in a media with refractive index n, Equation 2.14 becomes

$$f_D = \frac{\sqrt{1-\frac{u^2}{v^2}}}{1 \mp \frac{u}{v}} f_0 = \frac{\sqrt{v^2-u^2}}{v \mp u} f_0 \tag{2.15}$$

where $v = nc$. is the speed of light in the media. Knowing from Einstein's theory of relativity that for the speed of light it holds $c = \lambda f =$ const., Equation 2.14 (and similarly Equation 2.15) can be formulated in terms of wavelength λ of the EM radiation as

$$\lambda_D = \frac{c \mp u}{\sqrt{c^2-u^2}} \lambda_0 \tag{2.16}$$

where λ_0 is the wavelength of the incident radiation and λ_D is the wavelength of the radiation observed after the interaction with the moving particle. All quantities of Equations 2.14, 2.15 and 2.16 are measured in the observer's frame. Figure 2.5 graphically illustrates these concepts.

With reference to a time-domain DOCT system, in addition to the structural information, to retrieve data regarding velocity of flowing particles within the sample, estimation of the Doppler shift frequency, $f_D = \omega_D/2\pi$, superimposed at the probing radiation and stored on the acquired interferometric signal must be computed.

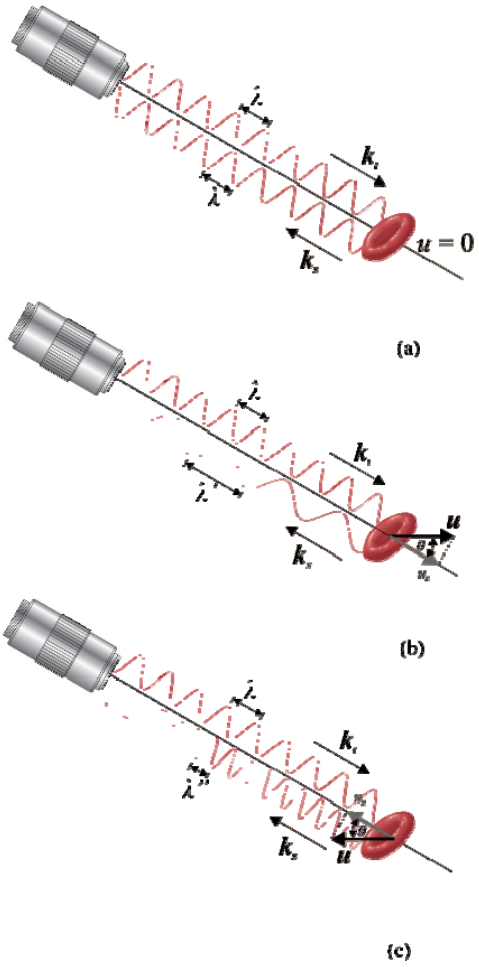

Figure 2.5 – *Schematic representation of the Doppler effect for EM waves. It manifests as an apparent change in frequency of the sounding radiation when interacting with a moving particle.* $\mathbf{k}_i$ *and* $\mathbf{k}_s$ *are the wave vectors of the radiation incident to and reflected from the moving particle respectively;* λ *is the wavelength;* **u** *is the particle vector velocity;* u_z *is the projection of* **u** *along the propagation direction of the probing radiation;* θ *is the angle between* **u** *and the propagation direction of the radiation. (a) If the particle is still relatively to the observer (radiation), no apparent change in frequency is observed. (b) If the particle is in relative motion relatively to the observer, an apparent change in frequency is observed; the frequency decrease (higher wavelength,* λ'*) if the particle is receding from the observer (c) or increase (lower wavelength,* λ''*) if the particle approach the observer.*

Each pixel associated to a spatial point within the sample composing a DOCT image is generated by heterodyne detection of the two waves

$$E_r = E_1 \cos\left(kz + \omega_0 t + \varphi_1\right) \tag{2.17}$$

$$E_s = E_2 \cos\left(kz + (\omega_0 + \omega_D)t + \varphi_2\right) \tag{2.18}$$

travelling in the reference arm and the sample arm of the interferometer respectively (Bouma and Tearney 2002, Fercher *et al.* 2003, Brezinski 2006). Here $\omega_0 = 2\pi \cdot f_0 = 2\pi \cdot u_m/\lambda_0$ is the carrier frequency due to the scan movement; $k \cdot z = 2\pi \cdot ct/\lambda_0$ is the phase of the electric field; u_m is the velocity of the moving element in the scan system, generally linearly time-dependent; c is the speed of the light in the medium; λ_0 is the light source central wavelength; z is the scanning distance; t is the time; φ_i (i = 1, 2) represent the phase of the wave evaluated at $t = 0$, $z = 0$; $\omega_D = 2\pi \cdot f_D = 2\pi \cdot u_z/\lambda_0$ is the Doppler frequency shift evaluated at each depth point in the sample and u_z is the resolved velocity component parallel to the beam propagation direction.

Both waves are mixed on the detector and, after eliminating DC components and filtering low-frequency components from the heterodyne detected signal, the observed electronic signal can be described by:

$$I_d(t) = I_0(t)\cos\left[\omega_D t + \Delta\varphi(t)\right] \tag{2.19}$$

where $\Delta\varphi(t) = \varphi_1 - \varphi_2$ and $I_0(t)$ is the amplitude modulation of the interferometric signal due to sample heterogeneities and carries the structural information (morphology) of the sample. The Doppler shift evaluated at every in-depth position is expressed by the difference (ω_0 - ω_D), and includes velocities variations arising both from the reference arm (ω_0) and sample arm (ω_D).

Assuming u_m = const., *i.e.* constant velocity of the scanning element in the reference arm, the term ω_0 in Equation 2.19 can be neglected. Hence, only the Doppler shift variations due to the motion of the flow in the sample arm are considered. The Doppler shift can be evaluated by (Gill 1965, Gjurchinovski 2004)

$$\omega_D = \left(\boldsymbol{k}_s - \boldsymbol{k}_i\right) \cdot \boldsymbol{u}_D \tag{2.20}$$

where $\boldsymbol{k}_s$ and $\boldsymbol{k}_i$ are the wave vectors of the backscattered and incident light respectively and $\boldsymbol{u}_D$ is the velocity vector of the moving constituents. With knowledge of the angle θ between ($\boldsymbol{k}_s$ - $\boldsymbol{k}_i$) and $\boldsymbol{u}_D$, measurement of ω_D allows the point flow velocity to be determined. To detect the non-zero Doppler shift, the difference ($\boldsymbol{k}_s$ - $\boldsymbol{k}_i$) must have a nonvanishing component along a direction parallel to the velocity vector $\boldsymbol{u}_D$, this latter

evaluated at the backscattering centre. Assuming $\boldsymbol{k}_s = -\boldsymbol{k}_i$ (single backscattering event coupled back into the fibre), the estimation of the flow velocity can be expressed via the Doppler formula (Bouma and Tearney 2002, Fercher *et al.* 2003, Brezinski 2006)

$$\left|\boldsymbol{u}_D\right|_z = \frac{f_D \lambda_0}{2 \cdot n \cdot \cos\theta}, \tag{2.21}$$

where n is the refractive index of the sample, f_D is the centroid of the Doppler spectrum and the subscript z denotes the fact that only the flow velocity component evaluated along the beam direction is detected.

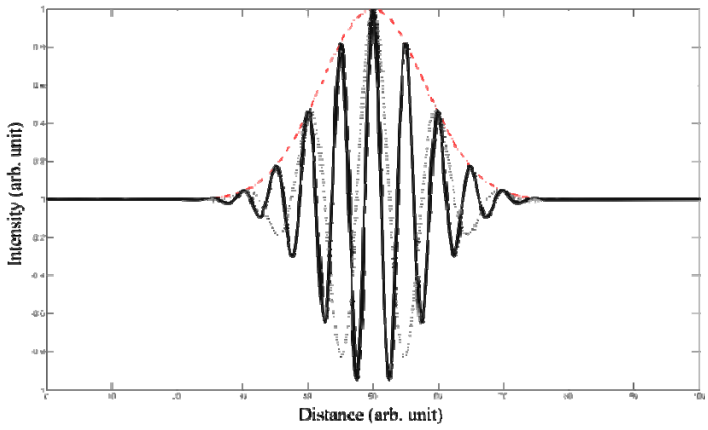

Figure 2.6 – *Effect of the interaction of the probing radiation with a moving particle on the cross-correlation interferometric signal. The red curve represents the envelope of the cross-correlation signal and doesn't change. The black curve represents the phase of the cross-correlation signal and is sensitive to changes in frequency due to the Doppler effect; the dotted curve represents a change in the phase of the signal due to the Doppler interaction between the probing radiation and a moving particle in the sample (see Equations 2.9 and 2.19).*

If $f_D = \omega_D/2\pi \neq 0$, *i.e.* presence of moving scattering particles with velocity $\pm u_{D,z} \neq 0$, the Doppler frequency shift will be to the left or to the right of the modulation frequency $f_0 = \omega_0/2\pi$ introduced by the scanning device, depending on the sign of $u_{D,z}$. The difference between f_D and f_0 is proportional to the magnitude of the flow velocity component evaluated along the beam direction. The quantity $(\omega_0 - \omega_D)$ in Equation 2.19, or, more particularly, ω_D, can then be numerically estimated following different strategies, including Fourier analysis applied on each A-scan separately and detection of phase changes between consecutive A-scans. The adoption of a particular strategy give rise to classifications of DOCT technique in sub-classes, the most relevant of which are briefly analyzed in the following paragraphs.

2.4.1 Concepts of DOCT imaging

The most straightforward method to detect the Doppler frequency shift is spectral analysis using the Fourier transformation. The method is based on calculations of the *Short-Term Fast Fourier Transform* (ST-FFT) algorithm on each acquired A-scan, generating a *spectrogram* as outcome. (Chen *et al.* 1997a, Chen *et al.* 1997b, Brezinski 2007). Details on theoretical and practical aspects of the ST-FFT algorithm can widely be found in literature (see for example Meyer 1995). In its more general conception, the spectrogram is the result of calculating the frequency spectrum of windowed frames of a compound signal. It is a three-dimensional plot of the energy of the frequency content of a signal as it changes over time. With reference to a single A-scan, the implementation of ST-FFT for DOCT generates a 2D plot in the time-frequency domain (abscissa and ordinate axis) with colour-coded spectrum amplitude. The graph represents the instantaneous frequency content of the signal, which is then converted into instantaneous velocity information at every depth inside the sample.

For a time-domain OCT system, the knowledge of the time-dependent law that defines the position of the scan element in time allows to convert the time scale of the spectrogram into distances, which represent the axial position (depth) of the measured element (voxel) inside the sample. The velocity information is obtained converting the instantaneous frequency Doppler shift using Equation 2.21.

The chosen parameters of the ST-FFT computation define the resolution of the time-frequency scales, influencing velocity sensitivity and spatial resolution in DOCT. The definition of the window size is critical to the ST-FFT result and the performance of the velocity estimation. Figure 2.7 schematically illustrate this imaging technique.

The relationship between frequency resolution δf and time resolution δt follows Heisenberg uncertainty

$$\delta f \delta t \geq \frac{1}{4\pi} \tag{2.22}$$

Higher time resolution, *i.e.* higher spatial resolution, is obtained with narrow Fourier transform window but will result in lower frequency resolution, *i.e.* poor velocity resolution.

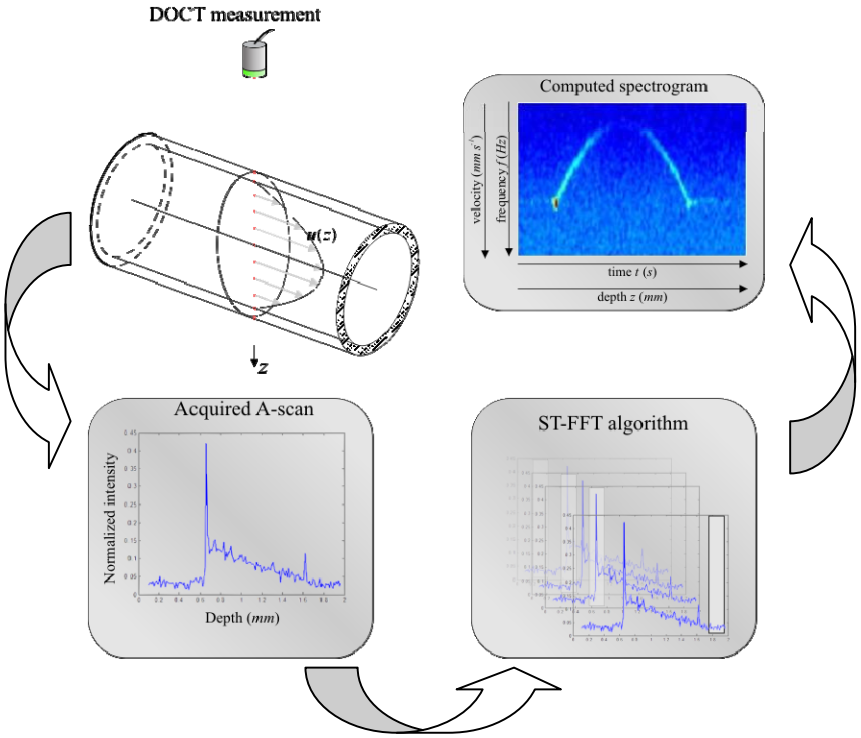

Figure 2.7 – *Schematic representation of DOCT flow velocity data analysis. The flow is detected with DOCT technique (top left). For each transverse position in on the sample, an A-scan is generated and acquired (bottom left). The digitized signal is processed via ST-FFT algorithm (bottom right), whose output is a spectrogram (top right). Analysis of the computed spectrogram set will furnish cross-sectional velocity mapping of moving particles in the sample.*

The major limitation of this technique applied to DOCT imaging is that this method depends on the FFT window time, which limits axial scanning speed and spatial resolution, as described in the following paragraph. For example, this can represent a serious limitation when measuring slow-moving blood flow in small vessels, which requires high velocity sensitivity at spatial high-resolution.

2.4.2 Sensitivity and resolution

The digital detection of the Doppler shift is obtained computing the spectrogram via ST-FFT algorithm on each acquired A-scan. Since the detection of the Doppler shift

requires sampling of the interference fringe intensity over at least two samples per oscillation cycle, the minimum detectable Doppler frequency shift, $\Delta f_{\mathrm{D}}^{\min}$, varies inversely with the FFT time-window size, N, and the sampling interval, T_{s},

$$\Delta f_{\mathrm{D}}^{\min} = \frac{1}{N \cdot T_{\mathrm{s}}}, \tag{2.22}$$

where $N \cdot T_{\mathrm{s}}$ defines the window time interval. This introduces a trade-off between velocity sensitivity and scanning speed as well as spatial resolution (Kulkarni *et al.* 1998, Zhao *et al.* 2000a, Zhao *et al.* 200b). The sampling frequency $f_{\mathrm{s}} = 1/T_{\mathrm{s}}$ and the ST-FFT parameter N determine the velocity resolution, defined as the minimum resolvable velocity, $u_{\mathrm{D}}^{\min}$, which is directly proportional to the minimum detectable Doppler shift as expressed in Equation 2.22 (Bouma and Tearney 2000). Substituting Equation 2.22 in Equation 2.21 gives

$$u_{\mathrm{D}}^{\min} = \frac{\lambda_0}{2n\cos\theta} \frac{1}{N \cdot T_{\mathrm{s}}}. \tag{2.23}$$

Larger values of $N \cdot T_{\mathrm{s}}$ will increase the velocity sensitivity. However, the depth spatial resolution δz, is proportional to the ST-FFT time-window as follow:

$$\delta z = u_{\mathrm{m}} N T_s. \tag{2.24}$$

where u_{m} is the velocity of the moving elements in the scanning device of the reference arm. Equations 2.23 and 2.24 define the velocity resolution and the spatial resolution of a DOCT system respectively. These two quantities are coupled via the ST-FFT time-window term $N \cdot T_s$; increasing this value will give a better velocity sensitivity at the cost of sacrificing the spatial resolution. A reduction of u_{m} could improve δz, but implementing high-speed scan velocity must be taken in account in order to minimize motion related artifacts. High spatial resolution is obtained at the cost of sacrificing high velocity sensitivity. Furthermore, the precision of the estimated Doppler shift is also limited by the Doppler signal bandwidth, which is proportional to the optical source spectral width (Kulkarni *et al.* 1998), which will result in a practical velocity resolution worse than the one estimated with Equation 2.23. For example, if a DOCT image

consisting of 100×100 pixels is acquired with a frame rate of 1 *Hz*, the acquisition time of each pixel is 0.1 *ms*, corresponding to a minimum resolvable Doppler shift of 10 *kHz*. This results in a velocity sensitivity of 25 $mm \cdot s^{-1}$ for a light source with central wavelength of 1300 *nm* at an angle of 80° to the direction of the flow (Moger 2003).

2.5 Other implementations of DOCT imaging

2.5.1 Phase-resolved DOCT

Phase-resolved Doppler optical coherence tomography decouples the velocity sensitivity from the spatial resolution while maintaining a high image acquisition rate (Zhao *et al.* 2000a, Zhao *et al.* 2000b, Zhao *et al.* 2002, Moger *et al.* 2002, Pedersen *et al.* 2003). Phase-resolved DOCT uses phase changes measured between sequential axial scans to reconstruct the velocity image from continuation of the analytic signal. The time interval between sequential axial scans is much greater than the acquisition time of an individual pixel, hence reducing the minimum detectable Doppler frequency by several orders of magnitude.

Doppler shifts from moving particles induce phase changes in the interferometric signal. By comparing the phase change at the same pixel between sequential axial scans velocity information can be obtained with high sensitivity while maintaining high spatial resolution. The total B-scan (see note 13) signal in DOCT is a time-sequential cascade of nonstationery signal slices in terms of A-scans, whereas the adjacent A-scans have a fixed phase shift

$$\Delta\phi = 4\pi k u_{\mathrm{D}} n T_A \cos\theta \,. \tag{2.25}$$

where T_A is the time period between two consecutive A-scans. Keeping T_A constant, the Doppler velocity can be retrieved by measuring the phase variation between adjacent A-scans

$$u_{\mathrm{D}} = \frac{\Delta\phi}{4\pi k n T_A \cos\theta} \,. \tag{2.26}$$

The velocity resolution will be

$$u_{\mathrm{D}}^{\min} = \frac{\lambda_0}{2n\cos\theta} \cdot \frac{1}{T_A} . \tag{2.27}$$

A comparison of Equation 2.27 with Equation 2.23 will show that phase-resolved DOCT have a better velocity resolution than DOCT based on ST-FFT algorithm, because generally holds that $T_A >> N \cdot T_s$, while maintains high spatial resolution.

The Doppler shift is retrieved computing the analytical signal associated to the acquired A-scans. At each A-scan, $i(t)$, can be associated its analytical signal, $i_a(t)$, via Hilbert transform as follow:

$$i_a(t) = i(t) + j \cdot \hat{i}(t) = i(t) + \frac{j}{\pi} P \int_{-\infty}^{+\infty} \frac{i(t)}{\tau - t} dt = A(t) e^{j\phi(t)} \tag{2.28}$$

where $\hat{i}(t)$ represents the Hilbert transform of $i(t)$, P denotes the Cauchy principle value, $A(t)$ express the module and $\phi(t)$ the phase of the analytical signal, which also expresses the phase shift between consecutive A-scans. From the calculated analytical signal, the Doppler shift is determined from the average phase shift between several A-scans as follows

$$f_{\mathrm{D}} = \frac{1}{2\pi T_A} \tan^{-1}\left[\frac{\Im\left(\sum_{i=1}^{m} i_{a,i} \cdot i_{a,i+1}^{*} \right)}{\Re\left(\sum_{i=1}^{m} i_{a,i} \cdot i_{a,i+1}^{*} \right)} \right] \tag{2.28}$$

where m is the number of axial scans that are averaged, $\Im$ and $\Re$ represent the imaginary and real part of the computed value respectively.

2.5.2 Doppler Amplitude OCT

The contrast of an OCT image is derived from the amplitude of interferometric signal demodulated at the reference frequency f_0. If the sample contains moving scatters, *i.e.*

RBC, then the carrier of the interferometric signal is Doppler shifted by frequency, f_D. Therefore, areas of the sample containing flowing particles, such as blood vessels, appear empty or very low in intensity because the backscattered signal from the moving particles has been Doppler shifted away from the demodulation frequency f_0. This means that information on the density of flowing scattterers in a vessel is lost. Doppler optical coherence tomography uses the frequency shift in the interferogram carrier frequency as a source of image contrast to generate a map of flow velocity, often using colour to indicate flow direction (Yazdanfar *et al.* 1997).

Doppler Amplitude OCT is a functional extension of DOCT in which the image contrast is derived from the amplitude of the interferogram at the Doppler shifted reference frequency ($f_0 + f_D$) (Moger *et al.* 2003). This source of contrast is sensitive to the density of scatterers rather than their velocity, hence giving a useful additional parameter for characterizing the distribution of particles flowing within a conduit. The digitized interferometric signal is analyzed in software to find the peak in the interferogram, corresponding to the Doppler shifted reference frequency; the squared amplitude of this peak is used as the image contrast (Moger 2003).

2.6 Summary

The significant improvements in optical and electronic technologies of the past decades yielded to a broad panorama of applications in biomedicine based on optical methods. *Optical coherence tomography*, a high-resolution, non-invasive optical technique based on interferometry achieved micrometric and, more recently, sub-micrometric resolution for the investigation of structures in turbid media such as biological tissues. Taking into account the nature and the interaction mechanisms of the utilized probing radiation with the biological tissue under test, functional extension of OCT technology can be derived. Investigation of birefringent biological tissues with broadband polarized light gave rise to the definition of *polarization-sensitive OCT*, a technique capable to detect the optical axis of the birefringent tissue or infer farther structural information not accessible with conventional OCT. Taking into account the Doppler effect experienced by the probing

radiation when interacting with moving constituents inside the sample, make it possible mapping velocity distribution of particles inside the sample. This OCT modality is known as *Doppler OCT*. DOCT is a very promising functional extension of OCT that can effectively support flow dynamic investigations. The implementation of the algorithms for computational determination of the Doppler shift can benefit for the long experience derived from Doppler radar, a mature technology with decades of developed experience. DOCT detection has also improved with the implementation of phase-resolved DOCT and Doppler amplitude OCT techniques. Both approaches take advantage of the Fourier domain OCT technique, which offers better dynamic range and maintain high spatial resolution and high sensitivity in velocity detection simultaneously. Doppler OCT find useful applications in all these situations involving complex flow dynamic investigations which are difficult to describe with mathematical models or not conveniently accessible with other imaging techniques.

Chapter 3

Elements and Principles of Fluid Mechanics

3.1 Introduction

From the Oxford Advanced Learner's Dictionary:

> **fluid** (*noun* [C, U][24]) a liquid; a substance than can flow.
>
> **liquid** (*noun* [C, U]) a substance that flows freely and is not a solid or a gas, for example water or oil.

From the above definitions, it follows that the constituent particles of a fluid may continuously change their positions relative to one another. A fluid is a substance that continually deforms (*flows*) under an applied shear stress regardless of the magnitude of the applied stress. This means that, if the fluid is at rest, no shear force can exist in it. Fluids flow under the action of applied forces, deforming continuously for as long as the force is applied. A fluid is unable to retain any unsupported shape; it flows under its own weight and takes the shape of any solid body with which it comes into contact.

An absolutely complete analysis of the behaviour of a fluid would have to account the molecular nature of the substance. Although the properties of a fluid arise from its molecular structure, in most applications interest centres on the average conditions of the describing parameters such as velocity, pressure, temperature, density and so on. The number of molecules involved is immense, and the separation between them is normally negligible by comparison with the distance involved in the practical situation being studied. Under these conditions, it is usual to consider a fluid as a *continuum* – a hypothetical continuous substance – and the conditions at a point as the average of a very large number of molecules surrounding that point within a distance which is large compared with the mean intermolecular distance (although very small in absolute terms). Quantities such as velocity and pressure can then be considered to be constant at any point and changes due to molecular motion may be ignored. Point to point variations in such quantities can also be assumed to take place smoothly, considering their changes a continuous function of space and time.

[24] C – countable noun; U – uncountable noun.

The mechanics of fluids is the study in which the fundamental principles of general mechanics are applied to liquids and gases. These principles are those of the conservation of matter, the conservation of energy and Newton's laws of motion. To the study of compressible fluids some of the laws of thermodynamics are also applied. By the use of these principles it is possible not only to explain and bring into relation observed phenomena but also to predict, at least approximately, the behavior of fluids under a set of specified conditions. It is not always easy to decide whether a particular simplifying assumption is justifiable, and ultimately experimental verification of theoretical results is always required. Conversely, experimental results themselves sometimes suggest assumptions that may profitably be made in further theoretical work.

3.2 Mechanical properties of fluids

Some of the basic concepts of fluid properties, and, later in this chapter, of fluid flow, which will be encountered in the rest of the thesis are now briefly reviewed and discussed. More wide and detailed explanations and discussions on properties and motion of fluids can be found in the references and suggested bibliography included at the end of this chapter.

3.2.1 Shear stress in a moving fluid

Fluid deformation is caused by shearing forces, which act tangentially to the surface to which they are applied and cause the material to occupy new space. Although there can be no shear stress in a fluid at rest, shear stresses are developed when the fluid is in motion. If the particles of the fluid move relative to each other so that they have different velocities, the original shape of the fluid to become distorted. If, on the other hand, the velocity of the fluid is the same at every point, no shear stresses will be produced, since the fluid particles are at rest relative to each other. Flow in contact with solid boundary, adheres to it and will, therefore, have the same velocity as the boundary.

Considering successive layers parallel to the boundary, the velocity of the fluid will vary from layer to layer as the distance from the boundary increases.

The shear stress τ acting on an element in a fluid is defined as the ratio of the force F acting over a unit area A; the deformation, measured by the angle Φ and called shear strain, will be proportional to the shear stress. In a fluid, the shear strain will continue to increase with time and the fluid will flow. It is found experimentally that, in a true fluid, the rate of shear strain is directly proportional to the shear stress.

If, in the time t a particle at a distance y from the boundary moves through a distance x, then,

$$\text{Shear strain} = \Phi = \frac{x}{y}$$

$$\text{Rate of shear strain} = \frac{x}{yt} = \frac{x/t}{y} = \frac{u}{y}$$

where u is the velocity of the particle. Expressing the ratio u/y in differential form, the shear stress is

$$\tau = \eta \frac{du}{dy} \tag{3.1}$$

where the constant of proportionality η is known as dynamic viscosity (or simply viscosity) of the fluid. Equation 3.1 is Newton's law of viscosity. The value of η depends upon the fluid under consideration. In the *Système International d'unités* (SI), the viscosity[25] η is expressed in $Pa{\cdot}s$,

[25] Data for viscosity are still commonly found in terms of units from the c.g.s. system where the *dyne* was the unit of force, the centimetre (*cm*) the unit of length and the second the unit of time interval. Thus the resulting unit of viscosity was $s{\cdot}dyne/cm^2$. This was termed the *poise* (abbreviated *P*) in honour of J. L. M. Poiseuille (1799-1869).

3.2.2 Newtonian and non-Newtonian fluids

Even among substances commonly accepted as fluids, there is a wide variation in behaviour under stress. Fluids obeying Newton's law of viscosity (Equation 3.1) and for which η has a constant value are known as Newtonian fluids. Most common fluids falls into this category, for which shear stress is linearly related to velocity gradient. Fluids which do not obey Newton's law of viscosity are known as non-Newtonian and fall into one of the following groups:

- *Plastic*, for which the shear stress must reach a certain minimum value before flow commences.
- *Pseudo-plastic*, for which dynamic viscosity decreases as the rate of shear increases (*e.g.* colloidal solutions, clay, milk, cement).
- *Dilatant substances*, in which dynamic viscosity increases as the rate of shear increases (*e.g.* quicksand)
- *Thixotropic substances*, for which the dynamic viscosity decreases with the time for which shearing forces are applied (*e.g.* thixotropic jelly paints).
- *Rheopectic materials*, for which the dynamic viscosity increases with the time for which shearing forces are applied.
- *Viscoelastic materials*, which behave in a manner similar to Newtonian fluids under time-invariant conditions but, if the shear stress changes suddenly, behave as if plastic (*e.g.* blood).

The above is a classification of actual fluids. In analyzing some of the problems arising in fluid mechanics we shall have cause to consider the behaviour of an ideal fluid, which is assumed to have no viscosity. Theoretical solutions obtained for such a fluid often give valuable insight into the problems involved, and can, where necessary, be related to real conditions by experimental investigation.

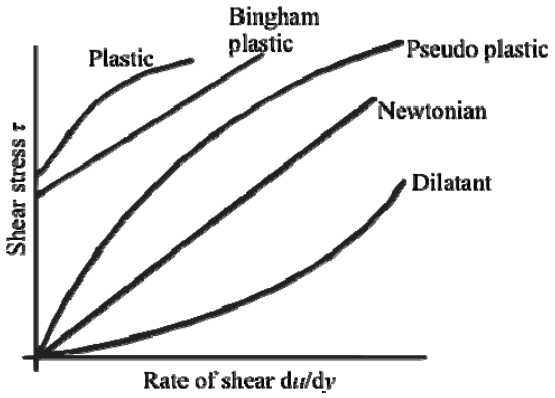

Figure 3.1 – *Variation of shear stress with velocity gradient (from* www.cartage.org.lb*).*

3.2.3 Density

The density of a substance is that quantity of matter contained in unit volume of the substance. It can be expressed in mass density ρ, specific weight w or relative density σ.

- *Mass density* is defined as the mass of the substance per unit volume. The mass density at a point is determined by considering the mass δm of a very small volume δV surrounding the point. δV cannot be made smaller than x^3, where x is a linear dimension which is large compared to the mean distance between molecules.
- *Specific weight* is defined as the weight per unit volume. Since weight is dependent on gravitational attraction, the specific weight will vary from point to point, according to the local value of gravitational acceleration[26] $\boldsymbol{g}$. The relation between w and ρ is derived from Newton's second law, $w = \rho \cdot \boldsymbol{g}$.
- *Relative density* (or specific gravity) is defined as the ratio of the mass density of a substance to some standard mass density. For liquids, the standard mass density chosen is the maximum density of water (which occurs at $4°C$ at atmospheric pressure).

[26] The bold italic notation indicates a vector quantity. The same symbol in italic only indicates its magnitude.

3.2.4 Viscosity

Although all real fluids resist any force tending to cause one layer to move over another, the resistance is offered only while the movement is taking place. Thus, when the external force is removed, the flow subsides because of the resisting forces, but when the flow stops, the particles of fluid stay in the positions they have reached and have no tendency to revert to their original positions. This resistance to the movement of one layer of fluid over an adjoining one is ascribe to the *viscosity* of the fluid. It is a matter of common experience that, under particular conditions, one fluid offer greater resistance to flow than another. Viscosity is a property of the fluid and a scalar quantity.

From Equation 3.1, the coefficient of dynamic viscosity η can be defined as the shear force per unit area (or shear stress τ) required to drag one layer of fluid with unit velocity past another layer a unit distance away from it in the fluid.

In many problems involving viscosity, it is of interest to know the magnitude of the viscous forces compared with the magnitude of the inertia forces, that is forces causing acceleration of particle of the fluid. Since the viscous forces are proportional to the viscosity η and the inertia forces to the density ρ, the ratio η/ρ is frequently involved and regarded almost as a property of the fluid. The ratio of viscosity to density is known as *kinematic viscosity* and denoted by the symbol υ.

One possible cause of viscosity considers the forces of attraction between molecules (Brush 1962, Massey 1990). In a liquid there are substantial attractive, cohesive forces between the molecules and shear stress due to molecular interchange between adjacent layers. Both molecular interchange and cohesion contribute to viscous shear stress in liquids. Temperature and pressure are the most relevant parameters that affect viscosity in a liquid.

3.3 Concepts of fluid flow

The flow of a real fluid is usually extremely complex and, as a result, complete solutions of problems can seldom be obtained without recourse to experiment.

Mathematical analysis of problems of fluid flow is generally possible only if certain simplifying assumptions are made. Very often the fluid is regarded as ideal without viscosity. In analyzing fluid flow, the concept of a *streamline* is also applied, which represents an imaginary curve in the fluid across which, at a given instant, there is no flow. Thus, the velocity of every particle of fluid along the streamline is tangential to it at that moment and relatively steady. If a series of streamlines are drawn through every point on the perimeter of a small area of the stream cross-section, they will form a *streamtube*, a useful concept that allows elements of the fluid to be isolated for analysis.

In general the parameters which describe the behaviour and state of a fluid are not constant in a particular set of circumstances. They may vary from one point to another or from one instant of time to another or they may vary with both position and time. Flow is described as *uniform* if the velocity at a given instant is the same in magnitude and direction at every point in the fluid. If at the given instant the velocity changes from point to point, the flow is described as *non-uniform*. A *steady* flow is defined as that in which the various parameters at any point may vary from point to point but do not change with time. Flow in which changes with time do occur is termed *unsteady* or *non-steady*. There are, therefore, four possible types of flow:

- *Steady uniform flow*; *e.g.* flow of a liquid through a pipe of uniform bore running completely full at constant velocity.
- *Steady non-uniform flow*; *e.g.* flow of a liquid at a constant rate through a tapering pipe running completely full.
- *Unsteady uniform flow*; *e.g.* accelerating flow of a liquid through a pipe of uniform bore running full.
- *Unsteady non-uniform flow*; *e.g.* a wave travelling along a channel.

All fluids are *compressible*, so that their density will change with pressure. A fluid is termed compressible if the pressure variations in the flow field are large enough to effect substantial changes in the density of the fluid. Flows of liquids with pressure variations much smaller than those required to cause phase change (cavitation) are termed *incompressible*. For liquids, whether the incompressible assumption is valid depends on the fluid properties and the flow conditions.

In general, fluid flow is *three-dimensional* (3D), in the sense that the flow parameters vary in all three coordinate directions. Considerable simplification in analysis may be often be achieved by selecting the coordinate directions so that appreciable variation of the parameters occurs in only two directions, or even in only one. Flow is described as *one-dimensional* (1D) if the parameters describing the flow at a given instant may be expressed as functions of time and one space coordinate only. This single space coordinate is usually the distance measured along the central streamline of the flow, even though this may be a curve in space, and the value of the parameters will represent the average values across a section normal to the streamline. In *two-dimensional* (2D) flow the parameters are functions of time and two rectangular space coordinates only (say x and y). There is no variation in the third coordinate (say z) and therefore the same streamline pattern could at any instant be found in all planes in the fluid perpendicular to z. A special case of 2D flow occurs when the cross-section of the flow is circular and the flow parameters vary symmetrically about the axis.

Any element of fluid will obey the normal laws of mechanics and its behaviour can be predicted from Newton's laws. In a body of flowing fluid, in general the velocity is a function of both time and position. As the particle moves from one location to another, say from A to B, the total change of velocity δu through a distance δs in time δt is due to the difference of velocity between the two locations at a given instant plus the change of velocity at B occurring in time δt. In symbols:

$$\delta u = \frac{\partial u}{\partial s}\delta s + \frac{\partial u}{\partial t}\delta t \tag{3.2}$$

where $\partial u/\partial s$ is the rate of change of velocity with position at a given time and $\partial u/\partial t$ is the rate of change of velocity with time at a given point. The forces acting on a particle are related to the resultant acceleration $\delta u/\delta t$ of the particle (Newton's second law). The acceleration a is expressed by the substantive derivative, D/Dt, to denote that a is obtained by following the motion of a single particle. In symbols:

$$a = \frac{Du}{Dt} = u\frac{\partial u}{\partial s} + \frac{\partial u}{\partial t} \tag{3.3}$$

The first term on the right side of Equation 3.3 represents the convective acceleration due to the movement of the particle from one point to another point at which the velocity at the given instant is different; the second term represents the local or temporal acceleration due to the change of velocity at every point with time. In addition, when a particle moves in a curved path, it changes direction and so has an acceleration a_n towards the centre of curvature of the path, *i.e.* perpendicular to the direction of motion, whether or not the magnitude of the velocity u is changing. In symbols:

$$a_n = \frac{u^2}{r_s} + \frac{\partial u_n}{\partial t} \tag{3.4}$$

where r_s is the radius of curvature, u^2/r_s is the convective term and $\partial u_n/\partial t$ is the temporal term which appears if u has a component towards the instantaneous centre of curvature.

3.3.1 Continuity equation

Except in nuclear processes, matter is neither created nor destroyed. This principle of Conservation of Mass is applied to fluid flow and is expressed by the *equation of continuity*. It states that at any fixed region in the flow, the mass of fluid entering in it per unit time equals the mass of fluid leaving per unit time plus any variation of mass of fluid in the control volume per unit time. For steady flow through a streamtube, the equation of continuity became

$$\rho_1 \delta A_1 u_1 = \rho_2 \delta A_2 u_2 = \ldots = \text{constant} \tag{3.5}$$

where the ρ_1 and ρ_2 are the densities evaluated to the cross-sectional areas δA_1 and δA_2 respectively and u_1 and u_2 are the velocities measured at right angles to the cross-sectional areas. For flow of a real fluid through a pipe, the velocity will vary from wall to wall. However, using the mean velocity $\bar{u}$, the equation of continuity for steady flow can be written as

$$\rho_1 A_1 \overline{u}_1 = \rho_2 A_2 \overline{u}_2 = \dot{m} \tag{3.6}$$

where A_1 and A_2 are the total cross-sectional areas and $\dot{m}$ is the mass rate of flow. If the flow is considered incompressible, so that $\rho_1 = \rho_2$, Equation 3.6 reduces to

$$A_1 \overline{u}_1 = A_2 \overline{u}_2 = Q \tag{3.7}$$

where Q is the volume flow rate. The equation of continuity is one of the major tools of fluid mechanics, providing a means of calculating velocities at different point in a system. The equation can also be applied to determine relation between the flows into and out of a junction.

3.3.2 Momentum equation

In mechanics, the momentum of a particle is defined as the product of its mass m and its velocity $\boldsymbol{u}$. In symbols:

$$\boldsymbol{p} = m\boldsymbol{u} .$$

Particles of a fluid stream will possess momentum and, whenever the velocity of the stream is changed in magnitude or direction, there will be a corresponding change in momentum. From Newton's second law, the net force acting on a body in any fixed direction is equal to the rate of increase of momentum of the body in that direction. The relation between force and momentum is

$$F = \dot{m}\left(u_2 - u_1\right) \tag{3.8}$$

where $\dot{m}$ is derived from Equation 3.6. Equation 3.8 expresses the resultant force action on a fluid element in the direction of motion and represents very useful tools to evaluate the force exerted by the fluid on a solid body, such as forces exerted on pipe bends or bifurcations. It must be noticed that Equation 3.8 is based on the assumption that the velocity is constant across any given cross-section. This assumption is not applicable when considering real fluid flow past solid boundary, due to the shear stress and

consequent non-uniform cross-sectional velocity distribution. In this case, the momentum of the whole flow can be evaluated by summing the momentum per unit time through each basic element in which the considered cross-section can be thought. For known geometries, such as turbulent flow through a pipe, it is possible to evaluate a correction factor which takes into account the shape of the cross-section and the velocity distribution.

3.3.3 Laminar and turbulent flow

Observation shows that two entirely different types of fluid flow exist. Although the work of Gotthilf Hagen[27] (Hagen 1839, Tighe and Matthias 2007) in about 1840 served to emphasize certain consequences between this difference, it was not until the experiments of Osborne Reynolds[28] in the early 1880s that the essential nature of the two types of flow was clearly demonstrated (Reynolds 1883). Although Reynolds used water in his original tests, subsequent experiments have shown beyond any doubt that the phenomenon is exhibited by all fluids. Moreover, the two types of flow are to be found whatever the shape of the solid boundaries (Massey 1990).

At low flow velocity, it was found that the particles moved in parallel lines, moving in an orderly manner and retaining the same relative positions in successive cross-sections. This type of flow is known as *laminar*, *viscous* or *streamline*. At increased velocity, a point is eventually reached at which the particles no longer moved in an orderly manner but occupied different relative positions in successive cross-sections. This type of flow is known as *turbulent* and is characterized by continuous small fluctuations in the magnitude and direction of the velocity of the fluid particles, which are accompanied by corresponding small fluctuations of pressure.

[27] Gotthilf Heinrich Ludwig Hagen (1797-1884) was a German physicist and hydraulic engineer. Independently of Jean Louis Marie Poiseuille (1797-1869), Hagen in 1839 carried out the first carefully documented friction experiments in low-speed tube laminar flow, from which the Hagen-Poiseuille law arose.

[28] Osborne Reynolds (1842-1912) was a British fluid dynamics engineer. Reynolds famously studied the conditions in which the flow of fluid in pipes transitioned from laminar to turbulent. From these experiments came the dimensionless Reynolds number *Re* for dynamic similarity – the ratio of inertial forces to viscous forces.

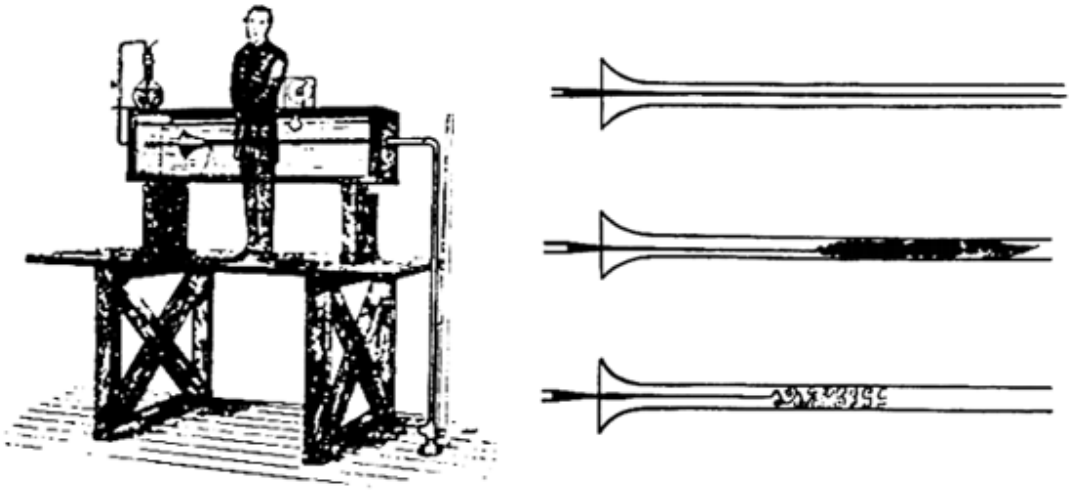

Figure 3.2 – *(a) Reynolds's experimental apparatus for investigating the transition from laminar to turbulence in pipe flow (from Boundary Layer Analysis figure 6-1 p177, the classic pipe flow experiments of Reynolds). (b) Reynolds's sketches of flow observations. From top to bottom: low speed (low* Re*), laminar flow; higher speed (higher* Re*), turbulent flow; spark illumination.*

When the motion of a fluid particle in a stream is disturbed, its inertia will tend to carry it on in the new direction, but the viscous forces due to the surrounding fluid will tend to make it conform to the motion of the rest of the stream.

The criterion which determines whether flow will be viscous or turbulent is the ratio of the inertial force to the viscous force acting on the particle, which is expressed by the quantity

$$\frac{Inertial\ force}{Viscous\ force} \propto \frac{\rho u l}{\eta} = Re \tag{3.9}$$

where l is a characteristic length in the system under consideration, *e.g.* the diameter of a pipe. The ratio $\rho ul/\eta$ is known as the *Reynolds number,* indicated by the symbol *Re*. The Reynolds number expresses a ratio of forces, and therefore is a pure number. It has been experimentally proved that values of *Re* below 2000 will normally indicate a laminar (viscous) flow. In pipes, values of *Re* above 2000 will not necessarily indicate turbulent flow, but flow conditions are instable and any disturbance will cause reversion to normal turbulent flow.

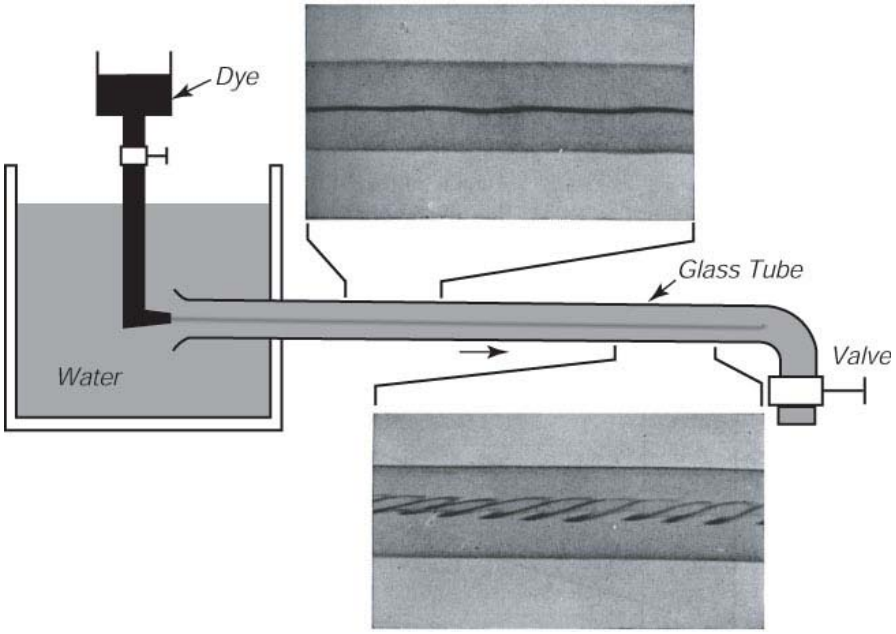

Figure 3.3 – *Schematic representation of Reynolds apparatus for investigating the transition from laminar to turbulence in pipe flow, with photographs of near-laminar flow (top) and turbulent flow (bottom) in a clear pipe much like the one used by Reynolds (from Binder 1953).*

Turbulent motion is essentially irregular motion on a small scale. The movement of individual particle have no definite frequency, or is there any ordered pattern as may be observed in large scale eddies making turbulent flow very complex. Whereas laminar flow may be studied mathematically without the need for additional information obtainable only from experiments, a rigid mathematical analysis of turbulent flow is impossible because the erratic motion of one particle in the flow is not exactly repeated by any other particle. Therefore, calculations relating to turbulent flow are forced to use experimentally determined figures.

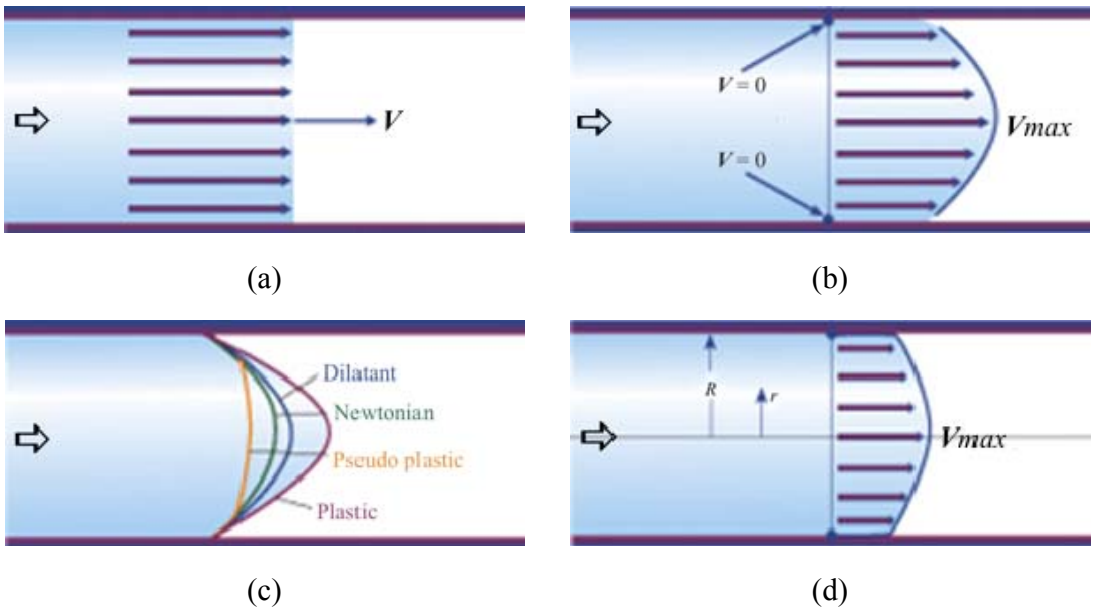

Figure 3.4 – *Examples of flow velocity profiles in pipe. (a) Ideal flow; viscosity is zero. (b) Laminar flow velocity profile for Newtonian fluid; the velocity is zero at the pipe wall and increases parabolically from the wall towards the centre of the pipe, reaching its maximum at the centre. (c) Comparison of steady, laminar velocity profiles between non-Newtonian fluids (dilatants, pseudo plastic and plastic) and Newtonian fluids. (d) Turbulent flow velocity profile for a Newtonian fluid; the velocity is zero at the pipe wall, but the frontline velocity is straighter and squared up when compared to similar flow velocity profile in laminar regime. The black arrow at the left of each image indicates the direction of the flow stream.*

3.4 Examples of fluid flow in ducts

3.4.1 Flow in circular pipes

The analysis of steady, uniform, laminar flow in a circular cross-section pipe is based on the application of the momentum equation to an element of flow within the conduit; the application of the shear stress-velocity gradient relationship (Equation 3.1) and the knowledge of the flow condition at the pipe wall, which allows the constants of integration to be evaluated (no-slip condition). In these hypotheses, the flow can be treated as two-dimensional and the cross-sectional velocity distribution is

$$u = -\frac{\left(R^2 - r^2\right)}{4\eta}\frac{d}{dx}\left(p + \rho \mathbf{g} h\right) \tag{3.10}$$

where R is the radius of the pipe, r is the internal radius, p is the static pressure and h is the elevation of the pipe above some horizontal datum. Equation 3.10 describes the variation of local fluid velocity u across the pipe and from the form of the equation, this velocity profile may be seen to be parabolic. The negative sign is due to the fact that the pressure gradient will be negative in the flow direction. The term ($p+\rho \mathbf{g} h$) is the flow piezometric pressure and is independent of r. The volume flow rate Q may be calculated by integration across the cross-section, leading to the expression

$$Q = -\frac{\pi}{8\eta}\frac{d}{dx}\left(p + \rho \mathbf{g} h\right) R^4 \tag{3.11}$$

Or, in terms of a pressure drop Δp over a length l of pipe of diameter d,

$$Q = \frac{\Delta p \pi d^2}{128 \eta l} \tag{3.12}$$

To compute the Reynolds number for real flow in a circular pipe, the representative velocity in Equation 3.9 is the mean velocity in the axial direction. The mean flow velocity is given by Q/A, where A is the pipe cross-sectional area $\pi d^2/4$. Hence,

$$\overline{u} = -\frac{\pi}{8\eta}\frac{d}{dx}\left(p + \rho \mathbf{g} h\right) R^2 = \frac{1}{2} u_{\max} \tag{3.13}$$

Moreover, Equation 3.12 may be rearranged for the pressure loss giving the well-known Hagen-Poiseuille equation:

$$\Delta p = 128 \frac{\eta l Q}{\pi d^4} \tag{3.14}$$

For steady, incompressible and uniform turbulent flow, the mathematical prediction of the cross-sectional velocity distribution is much more difficult.

For values of Reynolds number greater than the critical value, the pressure drop per unit length for a particular velocity is greater for turbulent flow than for laminar. The drop in pressure, as the fluid flows along, represents a loss of mechanical energy. Contrarily at laminar flows, where mechanic energy is required only to overcome the viscous stress

between layers, in turbulent flow there is a continuous interchange of fluid between different parts of the flow and innumerable small variations of velocity both in magnitude and direction. Figure 3.5 shows the transaction between laminar and turbulent regime, described by increasing values of *Re*.

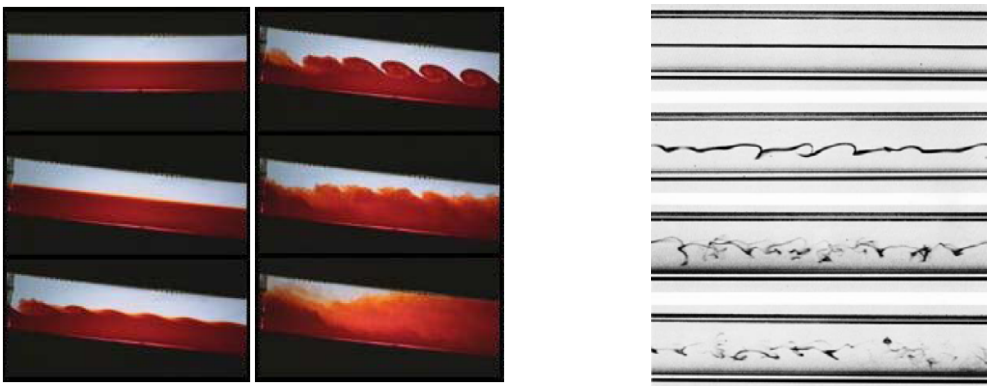

(a) (b)

Figure 3.5 – *Examples of transitions from laminar to turbulent flow. (a) Two-phase liquid in cylindrical duct. The flow velocity is increased by tilting the water tank; the images, in sequence from top to bottom and from left to right, refer to progressively increasing velocities. (b) Die filament injected in a water flow at increased flow velocities (from top to bottom). The flow stream moves from left to right in both cases.*

Dissipation of energy consequently occurs at greater rate. Calculation of losses in turbulent pipe flow is dependent on the use of empirical results (Darcy 1856, Blasius 1913, Nikuradse 1930) and the most common reference source is the Moody chart, which is a logarithmic plot of the friction factor *f versus Re* for a range of values of the ratio k/d, where k is a measure of the size of the wall roughness and d is the pipe diameter.

3.4.2 Blood flow

Blood is a highly specialized circulating tissue consisting of several types of cells suspended in a fluid medium known as plasma. Blood represents about the 7% of the human body weight (Alberts *et al.* 2002), with an average density of approximately 1060 $kg \cdot m^{-3}$ (Elert 2004). The average human adult has a blood volume of roughly 5 litres, composed of plasma and several kinds of cells (occasionally called *corpuscles*);

these formed elements of the blood are *erythrocytes* (red blood cells), *leukocytes* (white blood cells), and *thrombocytes* (platelets). The cells constitute about 45% of whole blood by volume.

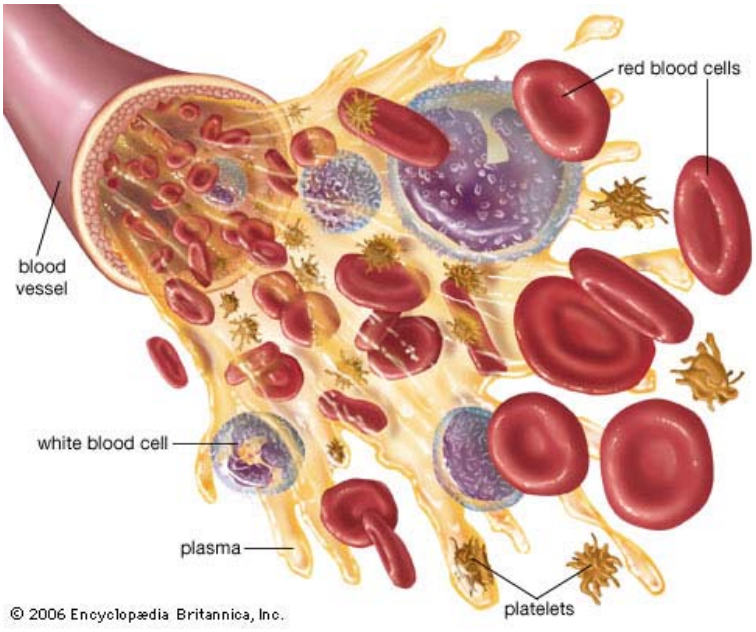

Figure 3.6 – *Blood flow in vessel. From "*red blood cell: blood*" Online article Encyclopædia Britannica Online. (Retrieved on 9th July 2007 from http://www.britannica.com/eb/art-88528).*

Each litre of blood contains (Alberts *et al.* 2002):

- 5×10^{12} erythrocytes (45.0% of blood volume) – in mammals, mature red blood cells lack a nucleus and organelles. They contain the blood's haemoglobin and distribute oxygen. The red blood cells (together with endothelial vessel cells and some other cells) are also marked by glycoproteins that define the different blood types. The proportion of blood occupied by red blood cells is referred to as the hematocrit. The combined surface area of all the red cells in the human body would be roughly 2,000 times as great as the body's exterior surface (Tallitsch *et al.* 2005).

- 9×10^{9} leukocytes (1.0% of blood volume) – white blood cells are part of the immune system; they destroy and remove old or aberrant cells and cellular debris, as well as attack infectious agents (pathogens) and foreign substances.

- 3×10^{11} thrombocytes (<1.0% of blood volume) – platelets are responsible for blood clotting (coagulation). They change fibrinogen into fibrin. This fibrin creates a mesh onto which red blood cells collect and clot. This clot stops more blood from leaving the body and also helps to prevent bacteria from entering the body.

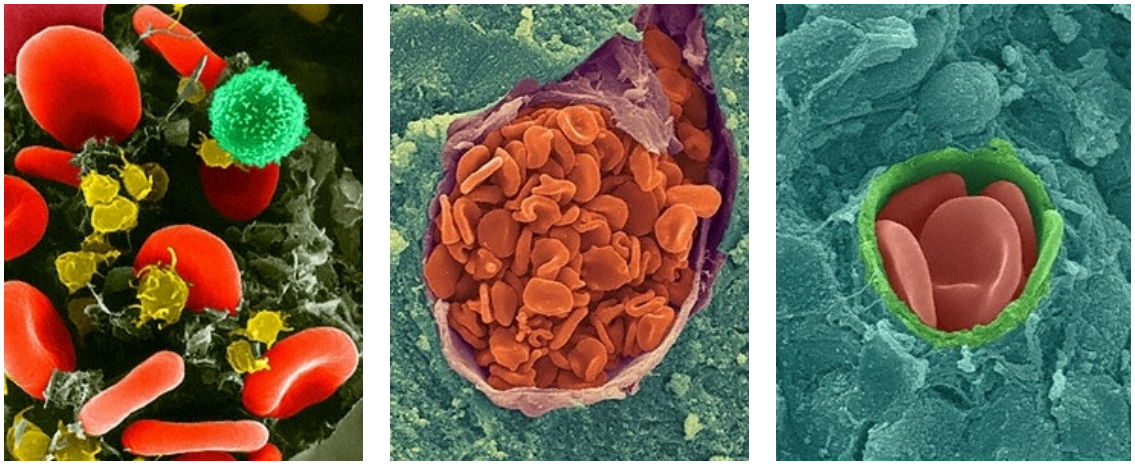

(a) (b) (c)

Figure 3.7 – *Scanning Electron Microscopy (SEM) images of human blood constituents. (a) RBCs (red), WBCs (T lymphocytes, light green) and platelets (yellow); magnification ×1300. (b) Artery (blood vessel) in the human cerebellum containing red blood cells; magnification ×1000. (c) Human RBCs in a cerebellum capillary; magnification ×1300. Images from Dennis Kunkel Microscopy, Inc. 2004.*

The other 55% (making up a total of 2.7-3.0 litres in an average human) is blood plasma, a fluid that is the blood's liquid medium, appearing golden-yellow in colour. Blood plasma is essentially an aqueous solution containing 92% water, 8% blood plasma proteins and trace amounts of other materials. Some components are:

- Serum albumin
- Blood clotting factors (to facilitate coagulation)
- Immunoglobulins (antibodies)
- Hormones
- Carbon dioxide
- Various other proteins

- Various electrolytes (mainly sodium and chloride)

Together, plasma and cells form a *non-Newtonian fluid* whose flow properties are uniquely adapted to the architecture of the blood vessels. The term *serum* refers to plasma from which the clotting proteins have been removed. Most of the protein remaining is albumin and immunoglobulins.

Blood flow is the flow of blood in the cardiovascular system. The discovery that blood flows is attributed to William Harvey[29]. The blood is circulated around the lungs and body by the pumping action of the heart. Additional return pressure may be generated by gravity and the actions of skeletal muscles. As the heart beats, it pumps blood through a system of blood vessels called the circulatory system or cardiovascular system.

The blood that these vessels carry is essential for the body to function. Blood carries oxygen and nutrients such as glucose, amino acids and fatty acids (dissolved in the blood or bound to plasma proteins) to the body's tissues; assists in the removal of carbon dioxide and waste products such as urea and lactic acid and promotes the overall health of the body's tissues. Other important functions associated to blood flow circulation are immunological functions, including circulation of white blood cells (WBCs) and detection of foreign material by antibodies; coagulation, which is one part of the body self-repair mechanism; messenger functions, including the transport of hormones and the signalling of tissue damage; regulation of body pH and hydraulic functions.

There are three main types of vessels composing the cardiovascular system:

- *arteries* – carry oxygen-rich blood away from the heart to the body's tissues;
- *veins* – take oxygen-poor blood back to the heart;

[29] William Harvey (1578–1657) was an English medical doctor, who is credited with being the first to correctly describe, in exact detail, the properties of blood being pumped around the body by the heart. This developed the ideas of René Descartes who in his *Description of the Human Body* said that the arteries and veins were pipes which carried nourishment around the body. Although Spanish physician Michael Servetus discovered circulation a quarter century before Harvey was born, all but three copies of his manuscript *Christianismi Restitutio* were destroyed and as a result, the secrets of circulation were lost until Harvey rediscovered them nearly a century later.

- *capillaries* – small blood vessels that connect arteries and veins.

Blood enters the heart through two large veins, the inferior and superior vena cava, emptying into the right atrium. Blood flows from the right atrium into the right ventricle through the tricuspid valve. Blood then leaves the right ventricle and the heart through the pulmonic valve into the pulmonary artery and to the lungs. Oxygenated blood returns from the lungs to the heart via the pulmonary vein into the left atrium. From the left atrium, blood flows to the left ventricle through the mitral valve. From the left ventricle blood leaves the heart through the aortic valve into the aorta and to the body.

The heart muscle needs its own supply of oxygen and nutrients to pump properly. Although its chambers are full of blood, the heart receives no nourishment from this blood. The heart receives its own supply of blood through a network of arteries known as the coronary arteries. The coronary arteries wrap around the surface of the heart (see Figure 3.8). The two main coronary arteries, the right coronary artery and the left coronary artery, branch off from the aorta.

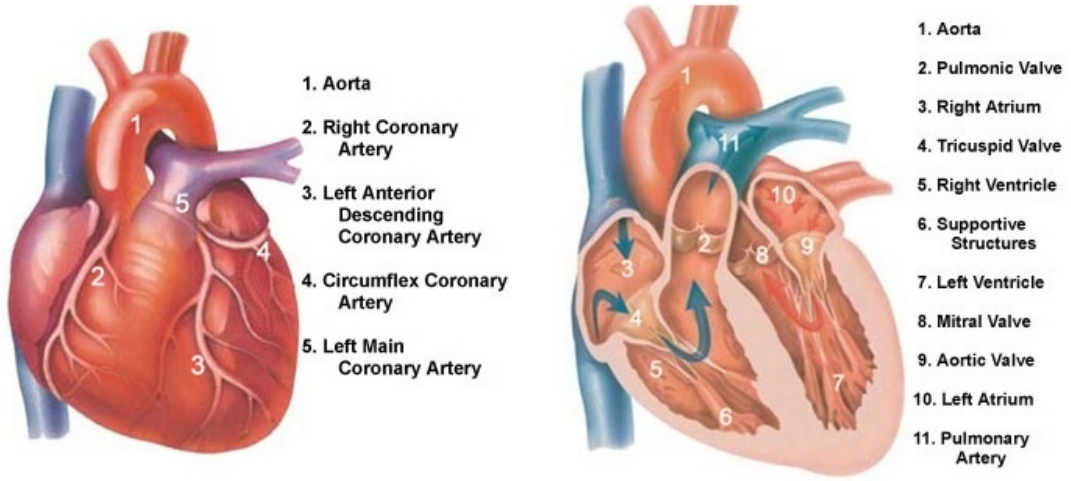

(a) (b)

Figure 3.8 – *Anatomy of human heart. (a) External view. (b) Sectional view; the arrows represent the stream direction of blood flow inside the heart.*

The heart also includes a system of arteries that branch off of the main coronary arteries that assist in supplying the heart with the needed oxygen and nutrients. The right coronary artery supplies the right atrium and right ventricle. It branches into the

posterior descending artery. The left coronary artery branches into the circumflex artery and the left anterior descending artery. The left coronary artery supplies the left atrium and the left ventricle. Collateral circulation is a network of tiny blood vessels that usually remain inactive.

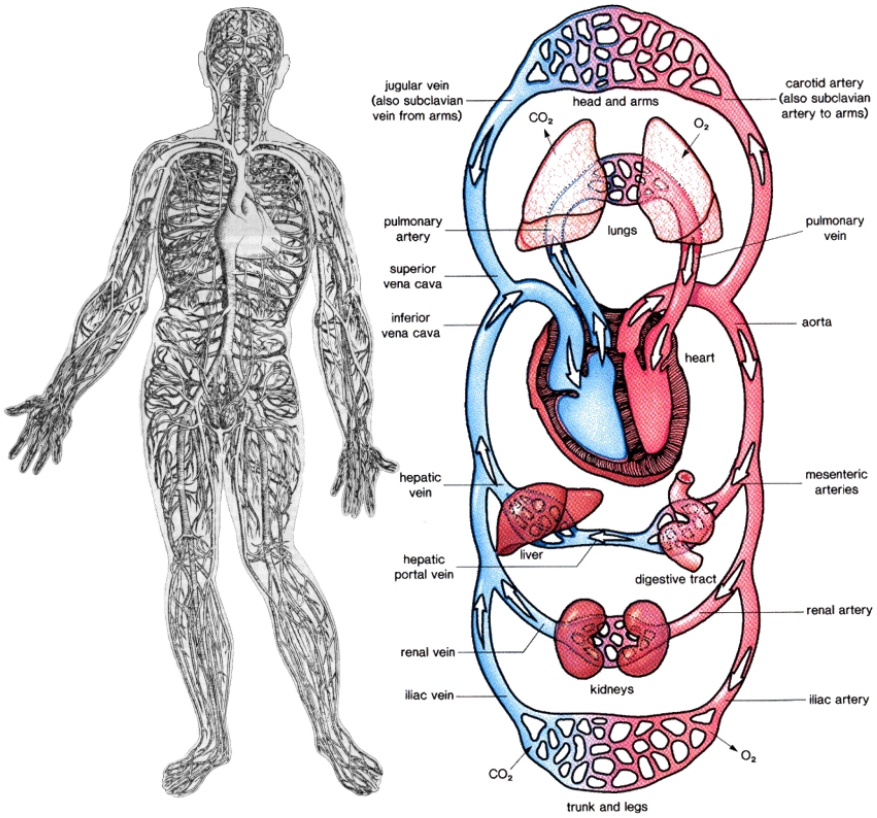

(a) (b)

Figure 3.9 – *(a) Vesalius, The vein man (1554); Vesalius[30] published the first illustrated atlas of anatomy. He is a very important figure in the history of science because he was one of the first to assert that it was important to 'look at nature' rather than to appeal solely to the classical writers such as Aristotle and Galen. (b) Schematic representation of human cardiovascular system. The arrows indicate the direction of the blood stream. Red vessels (right side) represent blood carrying blood; blue vessels (left side) represent blood with no oxygen.*

[30] Andreas Vesalius (1514–1564) was an anatomist, physician, and author of one of the most influential books on human anatomy, *De humani corporis fabrica*. Vesalius is often referred to as the founder of modern human anatomy. Vesalius' name is also referred to as Andreas Vesal or Andreas van Wesel, depending on the source.

When coronary arteries narrow to the point that blood flow to the heart is limited, collateral vessels become enlarged and active. This process allows for blood flow around the blocked artery to the heart muscle. Problems with blood composition or circulation can lead to downstream tissue dysfunction. The term *ischaemia* refers to tissue which is inadequately perfused with blood.

Mathematically, blood flow is described by Darcy's[31] law (which can be viewed as the fluid equivalent of Ohm's law) and approximately by Hagen-Poiseuille's law, as it is accurate only for Newtonian fluids, while blood flow is non-Newtonian and its flow can be described as laminar only in smaller vessels, elsewhere it is turbulent. Equation 3.15 below is Darcy's law, Equation 3.16 is the Hagen-Poiseuille law:

$$Q = \frac{-\kappa A}{\mu} \cdot \frac{\Delta P}{l} = \frac{\Delta P}{R} \tag{3.15}$$

$$R = \frac{8}{\pi} \cdot \frac{\upsilon l}{r^4} \tag{3.16}$$

where Q is the volume blood flow per time (units of volume per time, *e.g.* $m^3 \cdot s^{-1}$); κ is the permeability of the medium (units of area, *e.g.* m^2); A is the cross-sectional area; η is the dynamic viscosity; ΔP is the pressure drop; l is the length of the tube along which the pressure drop is taking place; R is the resistance; υ is the fluid kinematic viscosity and r is the radius of the tube. The negative sign in Equation 3.15 is needed because fluids flow from high pressure to low pressure. In Equation 3.16 it is important to note that resistance to flow changes dramatically with respect to the radius of the tube. This is important in angioplasty, as it enables the increase of blood flow with balloon catheter to the deprived organ significantly with only a small increase in radius of a vessel.

[31] Henry Philibert Gaspard Darcy (1803–1858), was a French scientist who made several important contributions to hydraulics. He modified the Prony equation for calculating head loss due to friction, which after further modification by Julius Weisbach would become the well-known Darcy-Weisbach equation still in use today. In 1855 and 1856 he conducted column experiments that established what has become known as Darcy's law; initially developed to describe flow through sands, it has since been generalized to a variety of situations and is in widespread use today. The unit of fluid permeability, *darcy*, is named in honour of his work.

Blood flow dynamics and velocity profile characterization inside the human circulatory system has been of interest since antiquity. Most of the conjectures and beliefs regarding the nature of the cardiovascular system made by ancient Egyptians, Greeks and Islamic physicians and philosophers were based on the application of *a priori* concepts to a modest base of anatomical knowledge. Dissection, particularly of human subjects, was uncommon for a variety of social and religious reasons. It was only in the 13th century that dissection became more widely practiced in the education of doctors and as a form of public display (Carlino 1999). However the purpose of these dissections was mainly to compliment the reading of standard anatomical text rather than to effect radical discoveries and understand anew the physiology of the body system. It was with the pioneering studies of Leonardo da Vinci[32] on the cardiovascular system that an attempt to image the blood flow dynamics was made (Kemp 1972, Keele and Pedretti 1979, Kemp 1989).

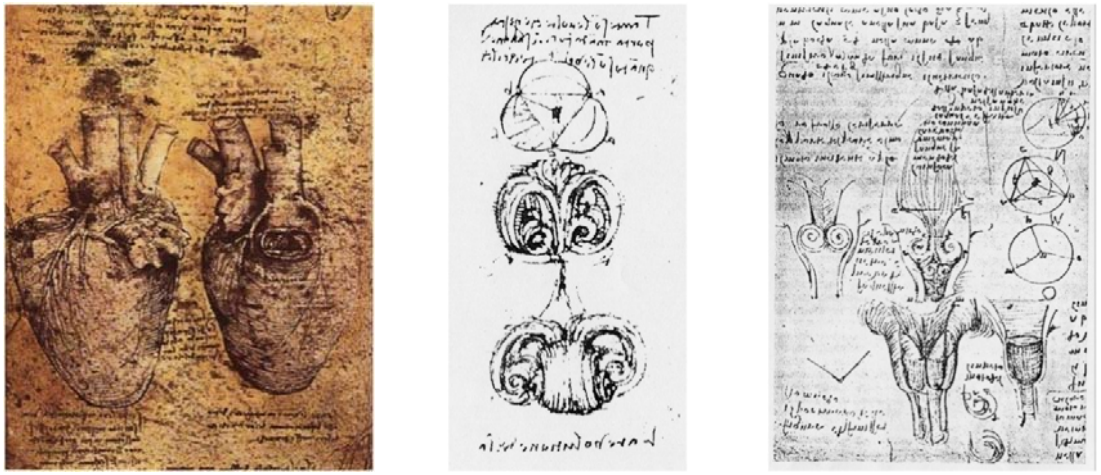

(a) (b) (c)

Figure 3.10 – *Leonardo da Vinci anatomy sketches. (a) The heart and its vessels (Bibilioteca Ambrosiana, Milan). (b, c) Vortex flow (very similar to a smoke ring) in the sinuses of Valsalva.*

At present, modern imaging techniques, such as MRI, PIV, near-infrared (NIR) diffuse optical tomography (ODT) or DOCT, are applied to visualize and characterize blood

[32] Leonardo di ser Piero da Vinci (1452–1519) was an Italian polymath: scientist, mathematician, engineer, inventor, anatomist, painter, sculptor, architect, musician and writer. Leonardo has often been described as the archetype of the "Renaissance man", a man whose seemingly infinite curiosity was equalled only by his powers of invention. He is widely considered to be one of the greatest painters of all time and perhaps the most diversely talented person ever to have lived.

flow dynamics *in vitro* and *in vivo* (Chen *et al.* 1997, Hong and Fox 1997, Zhao *et al.* 2000, Kilner *et al.* 2000, Zhao *et al.* 2001, Moger *et al.* 2004, Sugii *et al.* 2005, Piao and Pogue 2007). Experimental measurements are supported by theoretical modeling to evaluate flow parameters, such as wall shear stress. Experimental data can be integrated as boundary conditions to solve the Navier-Stokes equations using Computational Fluid Dynamics (CFD) to predict blood flow dynamics in complex geometry vessels (Long *et al.* 2000, Steinman *et al.* 2002, Marshall *et al.* 2004).

3.5 Modeling and numerical computation of fluid flow

The starting point for any systematic and rational mathematical analysis, which seeks to take account of the three-dimensional, viscous nature of fluid motion, is the system of equations known as the Navier-Stokes equations. The equations describe the motion of fluids and establish that changes in momentum in infinitesimal volumes of fluids are the sum of dissipative viscous forces, changes in pressure, gravity and other forces acting inside the fluid: an application of Newton's second law. They are one of the most useful sets of equations because they describe the physics of a large number of phenomena of academic and economic interest. They may be used to model weather, ocean currents, water flow in a pipe, flow around an airfoil (wing) and motion of stars inside a galaxy. As such, these equations, in both full and simplified forms, are used in the design of aircraft and cars, the study of blood flow, the design of power stations, the analysis of the effects of pollution, etc. Coupled with Maxwell's equations they can be used to model and study magnetohydrodynamics.

The Navier-Stokes equations are differential equations which, unlike algebraic equations, do not explicitly establish a relation among the variables of interest (*e.g.* velocity and pressure), rather they establish relations among the rates of change. For example, the Navier-Stokes equations for simple case of an ideal fluid (inviscid) can state that acceleration (the rate of change of velocity) is proportional to the gradient (a type of multivariate derivative) of pressure (see Equation 3.1).

Contrary to what is normally seen in classical mechanics, the Navier-Stokes equations dictate not position but rather velocity. A solution of the Navier-Stokes equations is called a velocity field or flow field, which is a description of the velocity of the fluid at a given point in space and time. Once the velocity field is solved for, other quantities of interest (such as flow rate, drag force, or the path a particle of fluid will take) may be found. The most general form of the Navier-Stokes equation is:

$$\rho \frac{D\mathbf{u}}{Dt} = -\nabla p + \nabla \cdot \mathbb{F} + \mathbf{f} \tag{3.15}$$

where the left-side term express the change in momentum and the right-term express a summation of body forces. The operator D/Dt is the substantive derivative[33]; ∇p is a pressure gradient and arises from normal stresses that turn up in any flow; the term $\nabla \cdot \mathbb{F}$ represents the shear forces in the fluid, normally due to viscous effects and the term **f** represents other forces, such as gravity. It has to be noted that the Navier-Stokes equations hold for the description of *instantaneous* motion in both laminar and turbulent flows. Nevertheless, while in laminar flow the shear stress is proportional to viscosity and the rate of shear strain, turbulent stresses are complex and no wholly satisfactory model exist to be used in developing analogous forms of the Navier-Stokes.

At the interface between a fluid and a surface in relative motion, a condition known as "no slip" dictates an equivalence between fluid and surface velocities. Away from the surface the fluid velocity rapidly increases; the zone in which this occurs is known as the *boundary layer* and its definition is fundamental to all calculations of surface drag and viscous forces. The introduction of an eddy[34] viscosity, ε, which includes the turbulence effects and is based on various turbulence models (Prandtl 1904,

[33] The *substantive derivative* is known also as the *material time* or *Eulerian*. For the rectangular Cartesian coordinate system with coordinates x, y and z, D/Dt is:

$$\frac{D}{Dt} = \frac{\partial}{\partial t} + u_x \frac{\partial}{\partial x} + u_y \frac{\partial}{\partial y} + u_z \frac{\partial}{\partial z},$$

where u_x, u_y and u_z are the components of the velocity vector evaluated along the corresponding axis.

[34] In fluid dynamics, an *eddy ford* is the swirling of a fluid and the reverse current created when the fluid flows past an obstacle. The moving fluid creates a space devoid of downstream-flowing water on the downstream side of the object. Fluid behind the obstacle flows into the void creating a swirl of fluid on each edge of the obstacle, followed by a short reverse flow of fluid behind the obstacle flowing upstream, toward the back of the obstacle.

Kolmogorov 1941, Schlichting 1979), allows the Navier-Stokes equations to become central tools for developing models of complex flow, particularly to the developing field of CFD. The development of computing capacity over the past two decades has been exponential and has made possible the implementation of numerical methods to solve fluid dynamics problems based on the Navier-Stokes equations. The application of numerical methods is still a discipline in developmental stage and care must be taken when applied to simulation predictions of turbulent flow, since its description has not been wholly solved yet. The literature on CFD is now extensive and further details can be found in the references at the end of this chapter (see Smith 1985, Abbott and Blasco 1989, Zeinkiewicz and Taylor 1991, Anderson 1995, Versteeg and Malalasekera 1995 for details).

To support CFD predictions, it is essential to validate the model. Validation normally includes a mathematical/numerical verification and a physical validation through comparing predicted results with experimental data. Due to the non-invasive or minimally invasive nature of the measurement, optical diagnostic techniques can be applied with profit for CFD model validations.

3.6 Summary

Basic concepts of fluid flow were introduced. A description of the fundamental parameters that describe fluids and motion of fluids is reported, with particular attention to the concept of continuity and momentum equation. The distinction between laminar and turbulent flow is introduced and discussed, followed by examples of fluid flow in ducts.

The optical and mechanical properties and complex flow dynamics of Newtonian and non-Newtonian fluids, such as blood, can be modeled applying very complex mathematical models. Computational analysis is performed by very powerful supercomputer, *e.g.* implementation of coronary blood flow models with the CRAY C90, and normally requires a very long time (up to days) to fully simulate the dynamic of the blood flow during a heartbeat (0.75 *s*). DOCT is a very promising technique,

ideally suited to access cross-sectional flow velocity distributions of Newtonian and non-Newtonian fluids in quasi real-time. A basic knowledge of the major concepts of fluid properties and fluid dynamics is essential for a correct interpretation and analysis of flow dynamic measurements.

Chapter 4

Development of the DOCT Experimental System

4.1 Introduction

The developed Doppler OCT system was built based on the fibre-optic Michelson's configuration, as described in Chapter 2, with implemented balanced photodetection. A schematic of the system is shown in Figure 4.1.

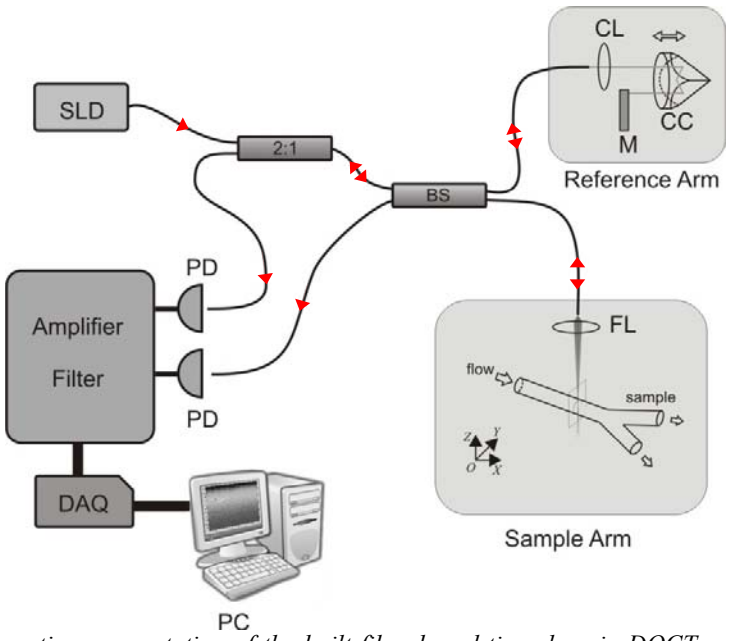

Figure 4.1 – *Schematic representation of the built fibre-based time-domain DOCT system. SLD – light source; 2:1 – fibre coupler; BS – 50/50 beam splitter; CL – collimating lens; CC – corner cube; M – retroreflecting mirror; FL – focusing lens; PD – photodetector; DAQ – data acquisition card; PC – personal computer. The red arrows indicate the direction of propagation of the light in the system.*

The light emitted from the broadband light source, a superluminescent diode (SLD), is sent to the fibre coupler 2:1, from where it travels to the 50/50 beam splitter (BS). Here, the split light is sent to the reference arm through collimating optics (CL) and to the sample arm through focusing optics (FL); the focal plane of the lens in the sample arm is set about in the midpoint of the scan range. The scan delay line in the reference arm is based on a linear coil motor translation stage, operated at 3.85 *Hz*. The back reflected and/or backscattered portion of the light returning from the two arms of the interferometer is sent back to the BS to generate the interferometric signal. Afterwards, this signal exits the interferometer and is square mixed at the balanced photodetectors (PD) and converted into an equivalent electric signal. The implementation of balanced

photodetection reduces considerably the excess of noise introduced by the light source. After the optic-to-electric transduction, the signal is amplified and filtered by a broadband band-pass filter centred at f_{PB} = 150 *kHz* and bandwidth of 200 *kHz*, allowing a flow velocity detection in the range of ±65 $mm \cdot s^{-1}$. Once properly conditioned, the signal is fed to a 12-*bit* analog-to-digital (A/D) converter connected to the personal computer (PC). The sampling frequency of the A/D is f_s = 1 *MHz*. A *Pentium™ II*, 700 *MHz* computer is employed for the digital processing of the signal and remote control of the system (the latter not depicted in the figure).

The described system was developed particularly for mapping non-laminar flow regimes arising in complex geometry phantoms, otherwise difficult to obtain with theoretical predictions or mathematical modeling. The system also enabled quantitative analysis of the influence of the vessel geometry on the dynamic of the flow. Therefore, the design criteria for evaluation and realization of the system aimed to construct a robust and reliable DOCT device, capable of detecting a sufficiently wide range of velocities (1-65 $mm \cdot s^{-1}$) at high spatial resolution (~14 μm in air). In general terms, the system must be able to resolve structures within the sample with sufficient detail over a useful depth while maintaining a good sensitivity and range of Doppler flow detection. These fundamental requirements were accomplished and useful, reliable, repeatable and accurate measurement of morphology and flow dynamics in complex geometry vessels were obtained. A summary of the experimental work is presented in Chapter 5.

4.2 Low coherence broadband light source

A SLD with central wavelength λ_0 = 1298 *nm*, 3*dB* bandwidth, or FWHM, $\Delta\lambda$ = 52 *nm* and output power W_{out} = 0.5 *mW* (Superlum, RU), was employed in the system as broadband light source. According to manufacturer's specifications, the spectrum of the source fit with good approximation a Gaussian shape (see Figure 4.2), giving an axial resolution in air of about 14 μm, as derived from Equation 2.11. The SLD was pigtailed by the manufacturer, *i.e.* the emitted light was directly coupled into optic fibre within

the SLD packaging, with an optic fibre suitable for 1300 *nm* wavelength single mode propagation.

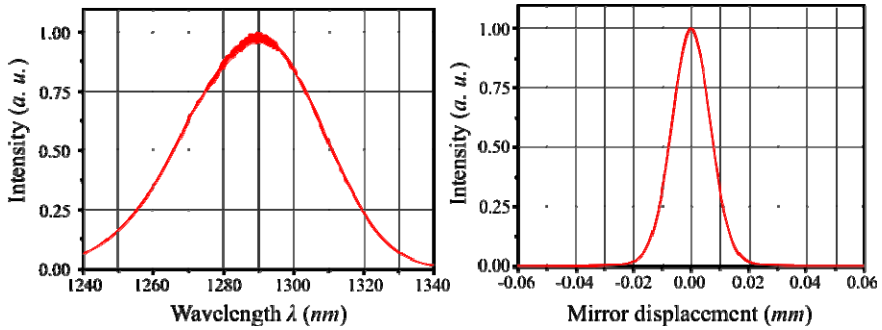

Figure 4.2 – *SLD intensity emission spectrum as quoted from manufacturer data (Superlum, RU); central wavelength* $\lambda_0 = 1298$ nm*; FTWH* $\Delta\lambda = 52$ nm*; output power* Wout *= 0.5* mW *(left). Coherence function with FWHM of ~14* µm *this quantity is assumed as system axial resolution (right).*

The output fibre was connected to the 2:1 coupler, which directed the light towards the input arm of the interferometer.

Parameter	Value	Unit
Single mode output power	0.5	*mW*
Central wavelength	1298	*nm*
3 dB (FWHM) spectrum width	52	*nm*
Output isolation	Built-in optical isolator (-30 dB)	
Fiber	SM, corning SMF-28	
Long-term stability	±0.5%	*%*

Table 4.1 – *Broadband light source specifications as quoted from the manufacturer (Superlum, RU).*

The choice of the spectral properties of the SLD, particularly its spectral range, was derived from considerations on the optical properties of the liquids (turbid media) to be used in the experiments and the nature of their interaction with the probing light. From the system perspective, the illuminated liquid must be capable of returning a good backscattered signal into the interferometer, detected through all the lumen of the vessel under test. In the infrared (IR) region, the absorption of the light in biological turbid media increases with longer wavelengths due to tissue water content (Hale and Querry 1973). Scaling the pure water absorption by 75% mimics a typical tissue with 75% water content. In the near-infrared (NIR) region, the so called diagnostic and therapeutic

window, absorption is minimal, but scattering is higher and limits the effective probing depth.

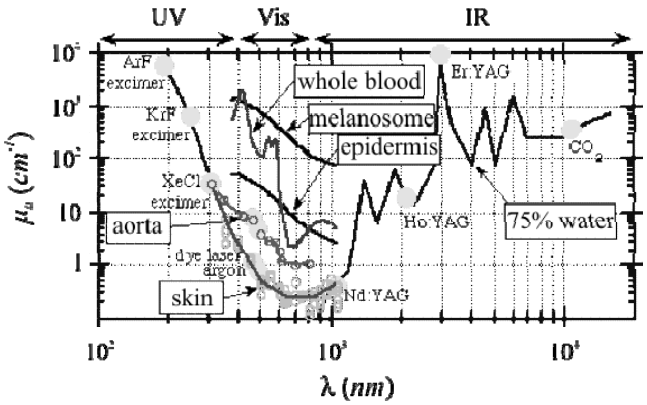

Figure 4.3 – *Variation of the absorption coefficient* μ_a *in function of the wavelength* λ *in the NIR region for several turbid media typically involved in OCT and DOCT measurements. Both axes are expressed in logarithmic units. (From S. L. Jaques and S. A. Prahl 1998 ECE532 Biomedical Optics; figure retrieved online on 5th November 2007 at http://omlc.ogi.edu/classroom/ece532/class3/muaspectra.html).*

Over the past recent years, intralipid has become popular in the optic community as imaging media for flow dynamic studies due to its optical properties similar to those of biological tissues.

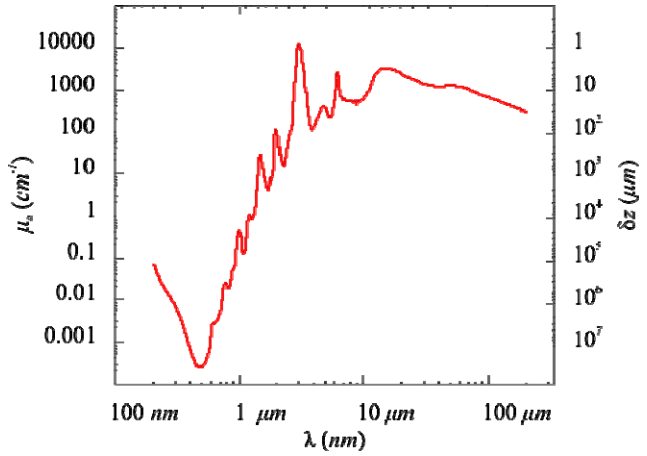

Figure 4.4 – *Variation of the absorption coefficient* μ_a *of water in function of the wavelength* λ *in the region 200-2000* nm*. The scale on the right represents the depth of penetration (from Hale and Querry 1973). The scales in the graph are expressed in logarithmic units.*

Used as diluted solution in RO water[35] at very low concentration, typically 1% in volume, it permits the application of the DOCT technique for mapping of flow

[35] The acronym "RO" stays for **Reverse Osmosis**, and describes a separation process that uses pressure to force a solution through a membrane that retains the solute on one side and allows the pure solvent to pass

dynamics in a wide range of artificial vessel sizes, from hundreds of microns to few millimetres. The obtained solution offers the desired backscattering property for DOCT signal detection, while the overall absorption is mainly ruled by the absorption of water. Figure 4.4 illustrates the dependence of the absorption coefficient of water, μ_a, at $20°C$ and penetration depth, δz, in function of the wavelength λ.

Under the light of these observations, the broadband light source of central wavelength around 1.3 μm was chosen to obtain flow velocity cross-sectional mapping through the whole lumen of the built artificial vessels. This choice reflects a good compromise between depth of penetration and scattering properties of IR light propagating in turbid media such as stock intralipid or haemoglobin solutions.

4.3 Core of the system

The Michelson's interferometer consisted in a 2×2 fibre coupler, also referred as *beam splitter* in the text, with a splitting ratio of 50/50. The distal ends of the input and output terminals of the coupler are terminated with APC-ST connectors for easy interfacing with the other optics of the system. The angled connectors are used to reduce internal back reflections, which could be seen as artifacts in the images, *e.g.* unwanted interferometric peaks not arising from the sample. The use of angled connectors also reduces the amount of light redirected into the light source and limits photodetector saturation. The distal ends of the fibres composing part of the reference and sample arm paths terminate with bare fibre and are coupled to the delay line and the sample with dedicated optic mounting respectively. Details on these constructions are given in the following paragraphs. The input terminal of the beam splitter is APC-ST coupled with the I/O terminal of a 2:1 fibre-based coupler. The role of the 2:1 optic coupler is to

---

to the other side. More formally, it is the process of forcing a solvent from a region of high solute concentration through a membrane to a region of low solute concentration by applying a pressure in excess of the osmotic pressure. This is the reverse of the normal osmosis process, which is the natural movement of solvent from an area of low solute concentration, through a membrane, to an area of high solute concentration when no external pressure is applied. The membrane here is semi-permeable, meaning it allows the passage of solvent but not of solute.
This process is best known for its use in desalination (removing the salt from sea water to get fresh water), but it has also been used to purify fresh water for medical, industrial and domestic applications since the early 1970s.

direct the light it receives in input from the light source into the input terminal of beam splitter and to divert part of the recollected light from the interferometer towards one of the two detectors used in the implemented balanced photodetection configuration. The distal ends of the 2:1 coupler are also terminated with APC-ST fibre-optic connectors.

4.3.1 Reference arm delay line

For a time-domain DOCT system, the heterodyne scanning on the sample is obtained by varying the optical path length in the reference arm. In the presented system, this is achieved by shifting a corner cube (Edmund Optics) mounted on a linear translation stage remotely controlled by the PC. Detailed illustration of the reference arm components and configuration is reported in Figure 4.5.

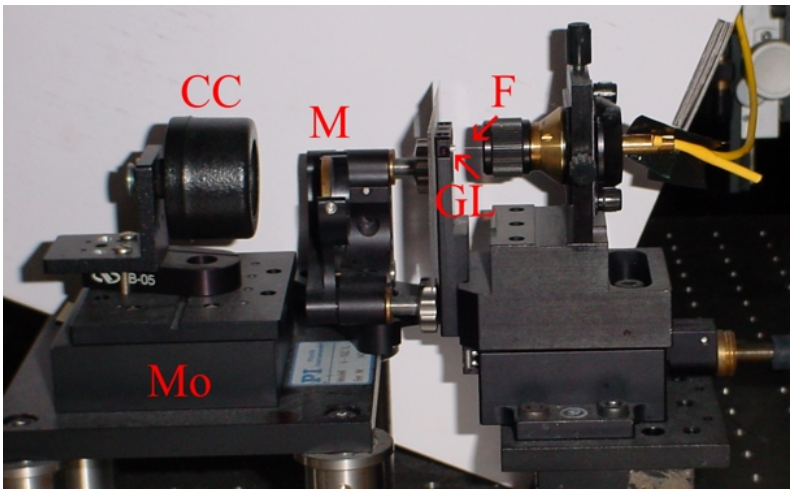

Figure 4.5 – *Reference arm components implemented in the DOCT system. F – distal end of the beamsplitter reference arm; GL – collimating grin lens; CC – retroreflecting corner cube mounted on linear translation stage; Mo – linear translation stage; M – reflecting mirror. The motor (Mo) is connected to its driver and governed by a sawtooth signal generated by an external function generator.*

The translation stage consists of a *QuickScan Voice-Coil Scanning System mod. V-102*, purchased from Physik Instrumente (PI), GmbH. The motor generates high-precision, repeatable uni-axial linear translation and performs faster than conventional leadscrew drivers. Table 4.2 reports the motor technical data as quoted by the manufacturer.

On top of the moving part of the motor are mounted the optic components holding the corner cube. The light arriving from the beam splitter through the reference arm and exiting the optic fibre is collimated via a grin lens and launched towards the reflecting mirror, passing through the corner cube. The mirror reflects back the quasi totality of the incident light (normal incidence) via the same incoming path and is then re-coupled onto the fibre.

Model	V-102
Positioning range	5 *mm*
Min. incremental motion	0.1 μm (noise ≤50 *nm* p-p)
Repeatability	0.2 μm
Velocity	Up to 150 $mm \cdot s^{-1}$
Displacement sensor	LVDT (Linear Variable Differential Transformer)
Controller	Digital PID controller 32-*bit* processor
Waveforms	Sine, triangle, saw tooth, step; internally generated, amplitude and frequency programmable
Interfaces	Digital: IEEE 488, RE-232 analog: commanded position: 0 to +5 *V*, internally 12-*bit* A/D converter, 3.33 *KHz* actual position output: -10 to 10 *V*, 12-*bit* D/A converter, 10 *KHz* sample rate.
MTBF	> 20000 hours
External control mode conversion ratio	1.2 *mm/V*

Table 4.2 – *Translation stage* QuickScan Voice-Coil Scanning System mod. V-102 *technical data as quoted by the manifacturer.*

With reference to Figure 4.5, a linear translation of the corner cube, moved parallel along the axis defined by the propagation direction of the collimated beam exiting the grin lens, will introduce a change in the optical distance between the surface of the grin lens facing the corner cube and the corner cube surface and between the reflecting mirror and the corner cube surface. Keeping constant all the other lengths composing the optical path in the reference arm and varying in a controlled manner the position of the corner cube, *i.e.* the instantaneous position of the scan motor, will introduce that

changes in the *optical* path length[36] (OPL) of the reference arm that enables performing the heterodyne scan of the sample.

In practice, the position of the scan motor is controlled by an external function generator interfaced with the motor driver. The control signal is a sawtooth and is expressed by voltage variations in time (see Figure 4.6 top). Its instantaneous amplitude is linearly proportional to the instantaneous motor position $p(t)$ via a constant factor as quoted by the manufacturer. $V_{p\text{-}p}$ is the peak-to-peak voltage and defines the total depth scan range. The time derivative of $p(t)$ describes the instantaneous velocity of the motor, $u_m(t)$ (see Figure 4.6 bottom). Knowledge of this latter quantity is important because it directly defines the modulation frequency, $\omega_0 = 2\pi f_0$, of the interferometric signal as expressed by Equation 2.9 or Equation 2.19.

For accurate DOCT measurements using ST-FFT Doppler shift detection, an *a priori* knowledge of ω_0 is important because the implemented ST-FFT algorithm compute the *overall* "instantaneous" frequency content of the acquired signal $I_d(t)$ and is not capable to separate the contributions from ω_0 and ω_D (see Equation 2.19). If ω_0 is known, then it can be subtracted from the computed quantity ω_0 - ω_D to isolate the Doppler shift associated to the moving constituents in the sample. In general terms, the modulation frequency can be expressed in function of the motor velocity similarly to Equation 2.19, where the wanted quantity is now f_0.

$$f_0(t) = 2\frac{u_m(t)}{\lambda_0} \tag{4.1}$$

where λ_0 is the central wavelength of the probing radiation.

Therefore, to estimate f_0, the time-law that expresses the motor velocity $u_m(t)$ must be known. Ideally, $u_m(t)$ can be estimated from the motor driving signal as follow:

[36] In optics, **optical path length** (OPL) is the product of the geometric length of the path light follows through the system, and the index of refraction of the medium through which it propagates. A difference in optical path length between two paths is often called the **optical path difference** (OPD). Optical path length is important because it determines the phase of the light and governs interference and diffraction of light as it propagates.

frequency into velocity scale in the spectrogram. In practice things differ consistently from the ideal situation, because the actual driving signal which arrives on the motor, $p'(t)$, is affected by non-linear distortion. By consequence, the motor velocity will be affected by non-linear distortion and so will be f_0.

This fact was to be expected, since it is not possible to impose sudden change in velocity when reversing the motor direction.

Description	Symbol	Value	SI Unit
Peak-to-peak voltage	$V_{p\text{-}p}$	5.0	*V*
Offset	V_{os}	2.5	*V*
Period	T_m	~259	*ms*

Table 4.3 – *Values of the parameter of the scan motor driving signal, as selected on the function generator.* $f_m = 1/T_m = 3.85$ Hz.

Using the motor in "external control mode" configuration – *i.e.* driving the motor via an external function generator, as is the case – the nominal input voltage range on the motor driver is 0 to +5 *V* and is taken as ideal target position. The input signal is digitized and properly conditioned by the motor driver. Due to the limitation of the 12-*bit* A/D converter, the smallest position increment is ~1.4 μm, which is still one order of magnitude smaller than the system axial resolution, ~14 μm in air. Figure 4.7 shows a comparison of the driving signal measured at the output of the function generator (black curve) and from the "position monitor" pin of the motor driver (red curve).

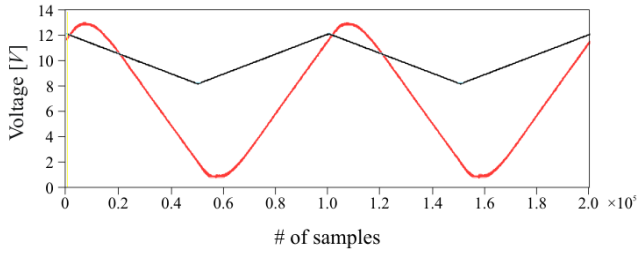

Figure 4.7 – *Comparison of the driving signal measured at the output of the function generator (*p(t)*, black curve) with the "position monitor" output of the motor driver (*p'(t)*, red curve). Ideally, the two curves differ only for a multiplicative factor. Due to the signal conditioning and to avoid abrupt variations of the position and velocity, the motor driver introduce distortion and time-delay on the input signal received from the function generator.*

If not corrected, this distortion will appear in the DOCT images and misinterpreted as variations in velocities originated from the sample constituents, while it is due to velocity variations of the scan element in the reference arm. Since the real position is monitored by the motor driver and its signal is available as an output, one possible approach to correct the distortion is to acquire $p'(t)$, compute its time-derivative and estimate f_0 with Equation 4.1, where $u_m(t) = \partial p'/\partial t$.

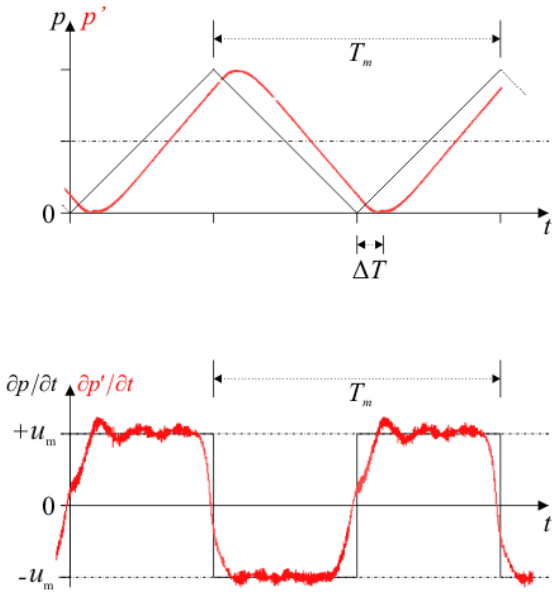

Figure 4.8 – *Comparison of ideal (black curves) and real (red curves) motor driving signals. Instantaneous motor position (top) and its computed derivative (bottom), which expresses the instantaneous velocity of the scan element in the delay line of the reference arm. The non-linear distortions introduced by the motor driver (top, red curve) impose a non-linear velocity variation of the scan element which is seen as unwanted velocity variation while computing DOCT data.*

A more convenient approach is to determine f_0 experimentally. This can be done inserting a static sample in the sample arm (sample with no moving constituents) and recording the associated spectrogram all along the scan range. The sample can be, for example, intralipid solution kept still, which will enable the detection of the wanted signal with a good SNR. In this case, the Doppler frequency shifts detected with the ST-FFT algorithm will be associated with the only moving part in the system: the scan element. In terms of Equation 2.19, it means that $\omega_0 = \omega_0(t)$ and $\omega_D = 0$. If its velocity will be constant, f_0 will be constant and a constant line will be imaged in the spectrograms. That line will appear horizontal if time is plotted in the abscissa and

frequency in the ordinate. The measured value of f_0 will also define the zero in the velocity scale. Otherwise, for non-constant velocity of the scan element in the reference arm, as is the case in practice, the computed spectrogram will return a curve whose deviations from a frequency reference value will be proportional to its instant velocity. The selected reference value expresses the averaged value of the motor velocity during the sampling time window. Figure 4.8 illustrate how non-linear distortion superimposed at the position signal $p(t)$ affects the velocity of the scan element and, by consequence the modulation frequency.

Assuming that the introduced distortion is repeatable at each cycle, the first approach to correct the distortion has the advantage that it needs to be done only once. Acquiring the position monitor signal over several periods make possible to compute the real (averaged) instant velocity for each position of the full scan range. But because the data are acquired only during a portion of the full scan range during the normal DOCT procedure, it requires the introduction of a procedure that selects the proper data window from the computed $u'_{\mathrm{m}}(t)$ coincident with the data window of the acquired signal. This synchronization is lost every time the distance between the sample and the probing lens in the sample arm is changed and is difficult to retrieve with sufficient precision and accuracy. The adoption of the second approach is preferable because avoids the need of precise overlap of the sampled interval with the correspondent interval in the data set of $u'_{\mathrm{m}}(t)$ and can also be seen as a calibration before acquiring the data. In any case, in order to avoid distortion and to isolate the Doppler contribution arriving only from the moving constituents of the sample, ω_0 must be determined experimentally and then subtracted from the computed difference ω_0 - ω_{D}.

4.4 Beam delivery

Sample arm optics and sample lateral scan

Figure 4.9 schematically shows the details of the sample arm construction and parts. The probing beam exiting from the distal tip of the optic fibre representing the sample arm of the interferometer is directed toward the sample through a focusing lens (FL)

mounted vertically. The lens consists of a ×10 microscopic objective, characterized by focal distance of about 60 *mm* and NA of 0.25, connected to a motorized translational stage to perform the lateral scan on the sample. The optical fibre facing FL is mounted on a XY manual translational stage, integral with the motorized stage and the FL, for precise and efficient coupling of the probing beam into the lens. The motorized translational stage is controlled directly by the personal computer and consists of a stepper motor model *x.act Linear Stage LT 100 ST* (Linos Photonics Ltd., UK) and a 10-*bit* resolution stepper motor driver card *M40.PCI* plugged into the PC. The features of the motor, as quoted from the manufacturer, are reported in Table 4.4. The sample under test is positioned under the probing beam, on separate mounting. The mountings that hold the sample consist of a goniometric stage attached to a kinematic positioning stage integral to a linear translator mounted vertically and operated manually.

Linear stages x.act LT with stepping motor	x.act LT 100 ST
Travel	100 *mm*
Starightness/flatness	15 μm
Resolution	1 μm
Reproducibility	1 μm
Load capacity	300 *N*
Maximum velocity	40 $mm \cdot s^{-1}$

Table 4.4 – *Lateral scan translational stage technical data as quoted by the manufacturer.*

The goniometric and kinematic stages are needed to precisely position of the sample in respect to the direction of the probing beam. The vertical translator permits to select and adjust the relative axial position of the sample within the range of the probing region as defined by the optical path length and scan range in the reference arm. To enable flow dynamic measurements, the sample is interconnected with an open-loop hydrodynamic system composed by a syringe pump model *Harward 975*, interconnection flexible pipes and a dedicated sink to recollect the liquid dripping out from the outlet arm(s) of the sample. The use of the syringe pump granted constant input volume flow rate, important to create steady flow regimes. This need was dictated by the relatively high data acquisition time of flow measurements. As exposed in Chapter 2.4, particularly in 2.4.2, in a time-domain DOCT system with implemented ST-FFT algorithm, the

velocity resolution and the spatial resolution are coupled and it is not possible to improve one without degrading the other. To maintain an axial spatial resolution quantitatively close to the theoretical value offered by the used light source (~14 μm), the scan speed was set to a low value by selecting the frequency of the scan motor driving signal to 3.85 *Hz*, *i.e.* completing a single A-scan every ~259 *ms*.

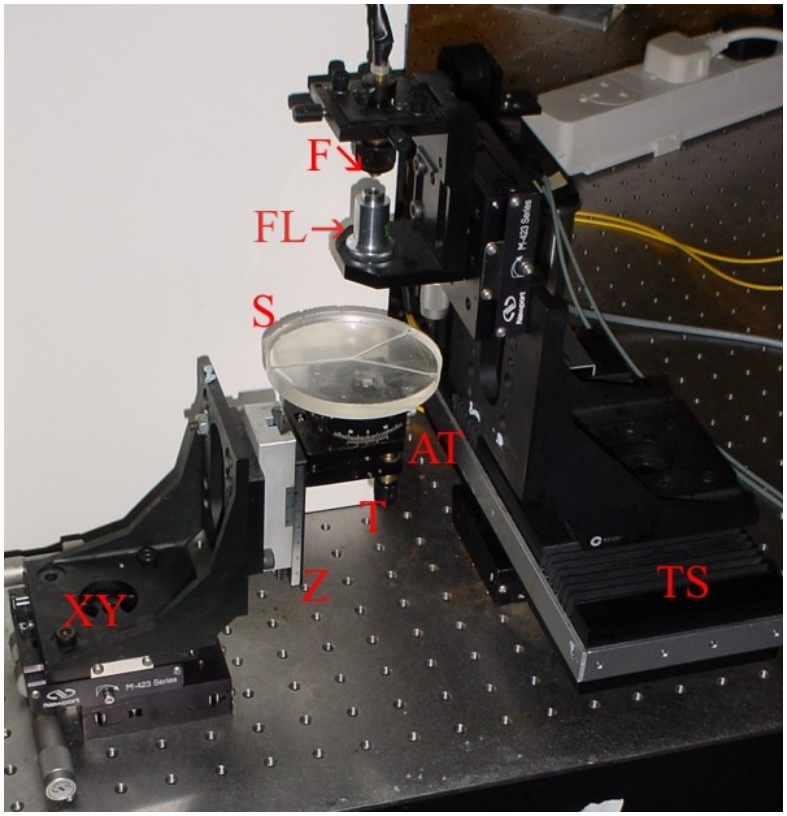

Figure 4.9 – *Sample arm components configuration implemented in the DOCT system. XY – xy manual translational stage; Z – z manual translational stage; S – sample; AT – angular tilter; T – tilter; FL – microscope objective (focusing lens); F – distal end of the sample arm of the interferometer; TS – linear translational stage. The linear translational stage is controlled by its driver, interfaced with the PC.*

Furthermore, to improve the SNR, each imaged position on the sample was obtained averaging 20 acquired A-scan. Therefore, the total time required to image a single position on the sample was about 5 *s*. This data acquisition time increases significantly when collecting data to generate a two-dimensional DOCT image. A 2D cross-sectional DOCT image is composed by a cascade of averaged A-scan acquired at each selected position on the sample, normally equally spaced and linearly translated from the previous by a selected quantity, this latter referred as “lateral step” in the text.

Therefore, the total time required to collect 2D data is given by the product of the scan period times the number of repetitions on the same position (average) times the number of positions composing the tomography. Typically, a flow velocity mapping image of a vessel with circular cross-section of 1 *mm* in diameter imaged with a lateral step, *i.e.* shift between two adjacent positions, of 20 μm requires a minimum of 50 points to cover the entire lumen of the vessel. Each point represents the average value of 20 A-scan, leading to a total data acquisition time of ~259 *s*. To keep the whole flow measurement consistent, it is very important that during this time the flow must remain steady. The liquid flowing through the samples used in the experiments was set in motion by the use of the syringe pump, which granted constant input volume flow rates into the sample. By selecting the proper range of input volume flow rates in relation with the geometry of the vessel, it was possible to obtain steady flow inside the sample, in both laminar and turbulent regimes.

To contain the degradation of the Doppler signal due to multiple scattering, the sample was positioned at an axial position such as the focus of FL was located at about the midpoint of the flowing channel. This distance corresponded also at the midpoint of the data collection window.

Finally, to obtain a 2D cross-sectional velocity mapping, the relative position of the sample in respect to the probing beam was varied in a controlled manner. This was achieved by shifting the probing beam parallel to itself while maintaining fixed the spatial position of the sample, the movement being generated by the *Linos* stepper motor. The sample was kept fixed in order to avoid any external disturbance in the flow.

4.5 Signal treatment and data analysis

After the recombination in the beam splitter, the light is directed to the photodiodes for subsequent optical-to-electrical transduction according to the balanced photodetection scheme and signal conditioning. Figure 4.10 schematically illustrates the custom-made circuitry for the optical-to-electrical transduction and subsequent signal filtering and amplification. The circuitry was embedded in a box, whose inputs are the two optical

output signals from the interferometer and the output is the conditioned (filtered and amplified) electronic signal to be sent to the data acquisition card (DAQ). The box also included two monitor terminals located after the optic-to-electronic conversion for monitoring the DC levels of the input signals for correct balance detection.

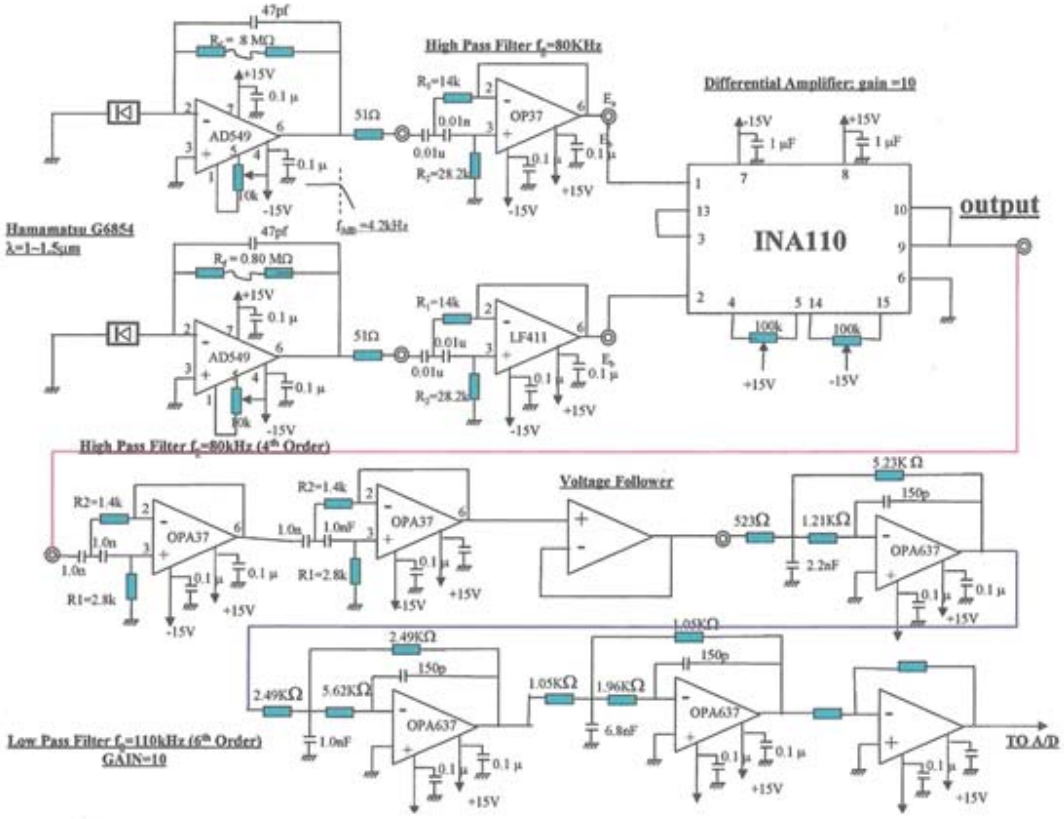

Figure 4.10 – *Schematics of the electronic circuitry for the optic-to-electronic transduction and signal conditioning.*

The pass-band electronic filter was realized using operational amplifiers devices (Sallen-Key implementation) and obtained as a cascade of a low-pass filter followed by a high-pass filter. The filter was designed to operate in two modalities:

- narrow band modality: with a bandwidth of 5 *kHz*, centred at 150 *kHz*, for structural imaging only (no flow detection);

- broad band modality: with a bandwidth of 200 *kHz*, centred at 150 *kHz*, for both structural and flow imaging.

To obtain a Doppler flow velocity detection, after the optic-to-electric transduction, the signal was amplified and filtered by the broadband band-pass filter centered at $f_{0,PB}$ = 150 *kHz* and bandwidth of 200 *kHz*, allowing flow velocity detection in the range ±65 $mm \cdot s^{-1}$. Then the signal was fed to a 12-*bit* analog-to-digital (A/D) converter connected (*National Instrument*, DAQ6111) to the personal computer (PC). The sampling frequency of the A/D is f_s = 1 *MHz*. A *Pentium™ II*, 700 *MHz* computer was employed for the digital processing of the data and remote control of the scan systems (the latter not depicted in Figure 4.1).

The DAQ sampling frequency and the parameters defining the driving signal fed to the scan motor in the reference arm, as described in paragraph 4.3.1, were kept constant for all the of set of measurements performed with the DOCT system. The time required by the scan motor to translate from one extreme of the scan range to the other – total shift of 5 *mm* - was $T_m/2$ = 130 *ms*. (see Table 4.2 and Table 4.3); imposing f_s = 1 *MHz*, implies that a digital sample is acquired every 0.001 *ms*, for a total of 130000 samples during the 5 *mm* translation or a digital sample each 0.035 μm. Because the real data acquisition was affected by non-linear distortion (see paragraph 4.3.1), the acquisition duty cycle was reduced to a portion of the motor translation range and not to its full extension. Typically, the window data was composed by 50000 or 40000 digital samples, which corresponded to a motor translation of about 1.92 *mm* or 1.54 *mm*, sufficient to cover the (optical) distances composing the lumen of the built artificial vessels used in the experiments. The width of the sampled data window and the number of offset points, defined with respect the starting point of each period of the sawtooth driving signal, were selectable via software. These parameters could be changed to best fit the width and position of the data acquisition window in respect to the position of the scan motor and the disposition of the sample and also to minimize the effects of the unavoidable non-linear velocity variations of the scanning element in the reference arm.

The software to perform the data acquisition, synchronize and control the scanning motors in the reference and sample arms and generate the DOCT data sets was written in *LabVIEW*™ ver. 6.1. From the main GUI interface, the values of the parameters that

defined the DOCT data acquisition modality were selectable, as illustrated in Figure 4.11.

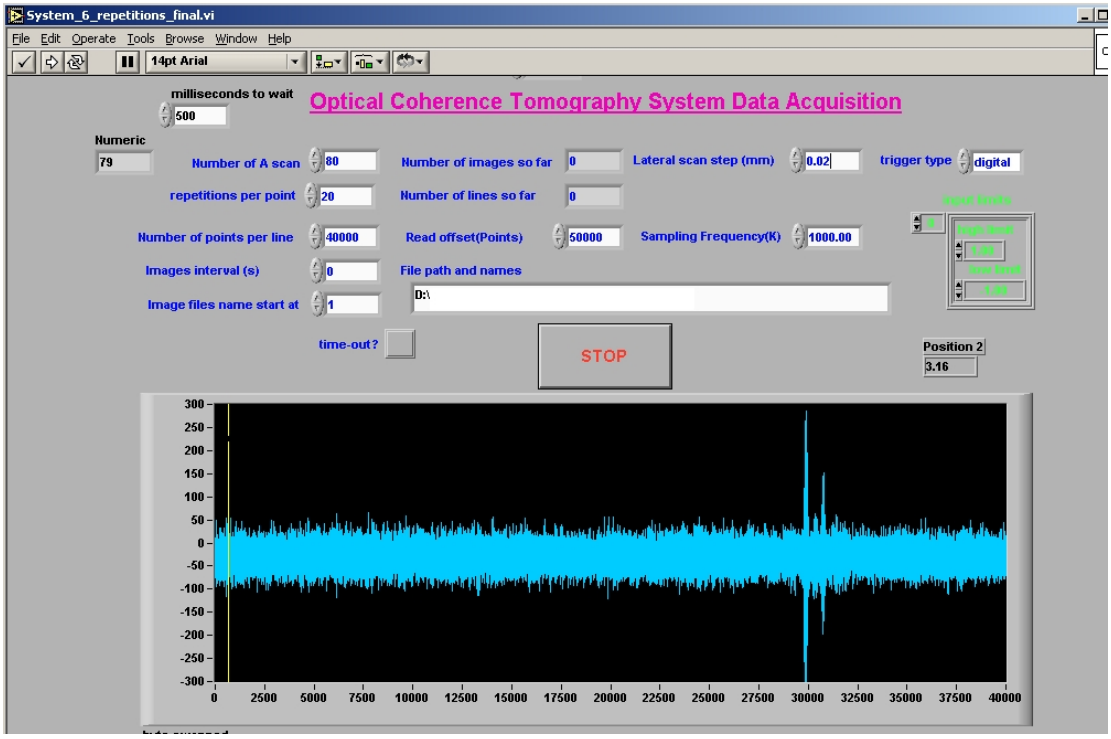

Figure 4.11 – *GUI of the LabVIEW script to perform DOCT data acquisition.*

As a result of the DOCT measurement, the *LabVIEW*™ script generated an output set of files, each containing, in binary format, the acquired A-scan values associated to each selected position on the sample. To convert the raw data into flow images, the file set was then computed using *Matlab*™. The developed Matlab scripts extracted the flow velocity information by implementing the ST-FFT algorithm as described in paragraph 2.4.1.

4.6 TD-DOCT with improved RSDL

To extend the studies of complex flow dynamic to *in vivo* samples, the original DOCT system described in previous paragraphs was further modified. The presented results were obtained in collaboration with Dr. Sergey Proskurin during his remain at Cranfield University in Silsoe. What follow is a description of the extended DOCT system with

implemented RSDL. A summary of the obtained results with this set-up are presented in paragraph 5.4.2. Figure 4.12 schematically demonstrates the extended experimental set-up composed of the Michelson interferometer with two 1×2 and one 2×2 fibre couplers (Proskurin *et al.* 2004a). Due to portability and convenience in delivery of radiation, modern OCT systems are typically based on the fibre-optic Michelson interferometer. OCT systems based on 830 *nm* light sources demonstrated imaging to depths of about 700 *μm* in skin (Welzel *et al.* 1997, Pan and Farkas 1998), with reduced scattering in the 1310 *nm* wavelength region enabling imaging to depths of about 1.2 *mm* (Welzel *et al.* 2001, Gladkova *et al.* 2000).

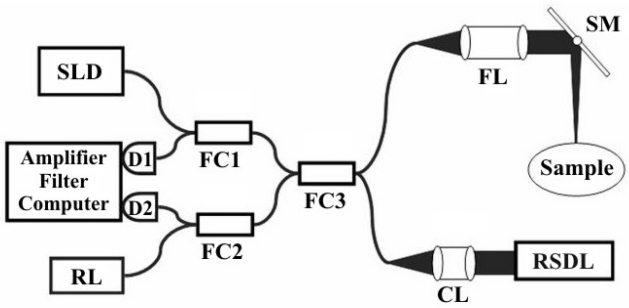

Figure 4.12 – *Schematic presentation of OCT experimental setup assembled on the basis of single mode fibre optic Michelson interferometer: SLD - super-luminescent diode; FC - fibre couplers; D1 and D2 – balanced photo-detectors; RL - pointing red light diode laser; FL – focusing lens; CL - collimating lens; SM – sample arm scanning mirror; RSDL - rapid scanning optical delay line. SLDs of two central wavelengths 1.3* μm *and 1.5* μm *were used in the experiments.*

Similar to confocal microscopy (Wilson 1990) the transverse resolution of OCT images is a function of numerical aperture of the optical elements used in the sample arm (SA) where the optical fibre acts as a narrow-width collimator. It should be recognized that with increased imaging depth, transverse resolution must be sacrificed to ensure that the optical radiation remains well focused over the entire imaging depth. The reduced imaging depth achievable with 830 *nm* sources permits the use of focusing optics with higher numerical apertures, with a correspondingly smaller size of the focusing spot, resulting in higher transverse resolution though over a reduced depth range. Systems based on 1300 *nm* light sources seem to be the most prominent for imaging of vessels in the deep layers of human skin. It should be pointed out that in OCT axial and transverse

resolutions degrade with increasing depth in scattering media such as skin, and with dependence on tissue optical properties and parameters of incident optical radiation.

Light sources with 1.3 μm (λ_0 = 1298 nm, $\Delta\lambda$ = 52 nm) and 1.5 μm (λ_0 = 1482 nm, $\Delta\lambda$ = 60 nm) were used in the system, which gave an axial (depth) resolution in air of 14 μm and 16 μm respectively. Sounding optical radiation delivered to sample by single mode optical fibre propagates through the system of lenses in the SA and focuses on the sample at about 5 cm from the scanning mirror (SM). As a result, the transverse resolution degrades to L_{tr} = 70 μm which is a low value as compared to other systems utilizing high numerical aperture focusing optics (Pierce *et al.* 2002, Zhao *et al.* 2000). Low numerical aperture of the SA optics is a compromise between the lateral resolution and the probing depth.

Despite the loss of the lateral resolution, this approach helps to achieve additional discrimination between backscattered/backreflected photons and multiply scattered photons. Transverse scanning on the sample is performed by a galvo-scanner instead of a linear scanning stage, which is essential for *in vivo* applications. It should be emphasized that the focusing properties of the sounding radiation in the SA can be easily modified by selecting FL with appropriate focal length. Optics with short focal distance can significantly increase the transverse resolution, but does not allow the transcutaneous skin layer structure to be visualized deeper than 0.8 mm. However, such imaging depth is quite suitable for imaging of nails and skin topical tissue structures, that is also beneficial for some dermatological studies (Tuchin 2004).

Figure 4.13 shows the modified implementation of the reference arm (RA) double pass rapid scan optical delay line (RSDL). Alignment of the Fourier-domain scanning grating distinguishes the current implementation from that described earlier (Kwong *et al.* 1993, Rollins *et al.* 1998). The incident, collimated broadband optical radiation (λ_0 = 1.3–1.5 μm) propagates to the edge of the diffraction grating (GR) positioned at the tuneable angle β = 7–8° (Smith *et al.* 2002, Tearney *et al.* 1997, Zvyagin *et al.* 2003), then it is diffracted there and spectrally dispersed. The lens L focuses the dispersed spectrum to a line on the SM. It must be noticed that the edge of the lens acts as a prism partly compensating light dispersion (Smith *et al.* 2002). The scanning mirror introduces a

linear phase ramp on the spectrum and redirects the light back through the lens, which re-focuses the radiation on the grating.

The spectral components of the light then recombine in a collimated beam and propagate towards the double-pass mirror M. The radiation emerging from the grating is collinear with the incident beam (Rollins *et al.* 1998). The double-pass mirror returns the light back through an identical path (see Figure 5.28), re-coupling the light into the interferometer via CL.

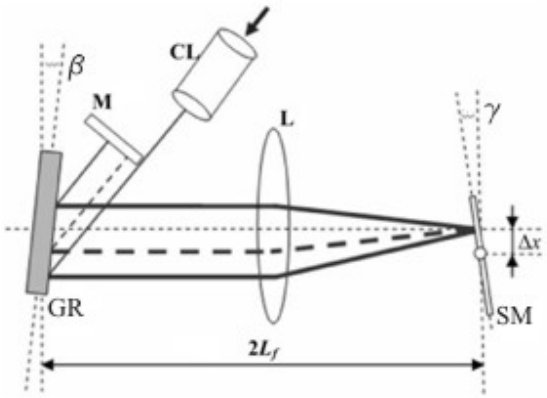

Figure 4.13 – *Schematic of the RSDL optical delay line (view from above). CL – collimating lens; M – double pass mirror; GR – diffraction grating; L – lens with the focal length L_f; SM – galvanometer scanning mirror; β and γ – tilting angles of the grating and the scanning mirror respectively; Δ*x *– lateral offset of the galvo pivoting point.*

Small distortions of the optical path-length are achieved along with the efficient re-coupling of the light to the fibre tip in this geometry. Smaller dimensions of the RSDL can also be achieved by the use of lenses L with shorter focal length. The use of such lenses for the efficient re-coupling of the broadband light is essential, since the divergence of a broadband light is greater than the divergence of a narrowband light. For example, the use of lens with 60 *mm* focal length results in the linear scanning depth up to 8 *mm*, L_f = 50 *mm* lens gives up to 5 *mm*, and up to 3 *mm* for L_f = 45 *mm* lens, according to group delay relationship (Rollins *et al.* 1998, Zvyagin *et al.* 2003). It is possible to configure the delay line in such a way that the propagation directions of the incident (from the collimator CL) and reflected (from the mirror M) radiations are in different geometrical planes. In this case the double pass mirror M can be moved toward

and underneath the line parallel to the propagation direction of the incident radiation, resulting in a smaller dimension of the RSDL.

The lowest envelope dispersion is achieved by adjusting the angle and position of the lens L, while keeping the position of the grating GR fixed (Tearney *et al.* 1997, Smith *et al.* 2002, Zvyagin *et al.* 2003). We utilized this technique to compensate for the dispersion in the RA during the scanning period and readily achieve theoretical axial resolution, L_{ax} = 0.44 $\lambda^2/\Delta\lambda \cdot n$ for the wavelength range 1.3–1.5 μm simultaneously, where n is the refractive index of the medium. Typical value of n for biological tissues is ~1.4 (Tuchin 2000). In addition, the described RSDL line allows increasing scanning depth without compromising the carrier frequency f_0 and stability (Zvyagin *et al.* 2003):

$$f_0 = 4\frac{\Delta x}{\lambda}\frac{\partial \gamma}{\partial t} \tag{4.3}$$

where γ describes the angular position of the scanning mirror SM, t is time and Δx is the scanning mirror offset.

Matching the intensities of the probing radiation from the reference arm and the radiation from the sample arm gives considerable, up to 34 *dB*, SNR improvement (Sorin and Baney 1992). In our case, the recombination of broadband light is more efficient; hence, the size of RSDL is small. Smaller size gives shorter light pathlength inside the RSDL. This is particularly important when using a broadband light source such as a SLD, which has essentially bigger divergence. The adopted balanced photodetection scheme reduces the detected phase noise (Rollins and Izatt 1999, Youngquist *et al.* 1987). In addition to that, it is possible to use a low-power, and consequently low-noise, SLD. The detected intensity on the photodetector is:

$$I = I_{in} + I_r + I_s + 2\sqrt{I_r I_s}\cos\left(2\pi\left(f_0 - f_{\mathrm{D}}\right)t\right) \tag{4.4}$$

where I_r and I_s are the radiation intensities in the reference and sample arms respectively and I_{in} is the incoherent component that appears as phase noise (Youngquist *et al.* 1987).

The measurements of velocity profiles with DOCT are based on the Doppler principle that states that the frequency of the light scattered from a moving particle experiences a Doppler shift f_D

$$f_D = \frac{1}{2\pi}(\mathbf{k}_s - \mathbf{k}_i)\cdot\mathbf{u} \tag{4.5}$$

Here $\mathbf{k}_i$ and $\mathbf{k}_s$ are the wave vectors of incident and scattered sounding radiation, respectively, and $\mathbf{u}$ is the velocity vector of the moving particle (see Figure 5.29). Assuming $\mathbf{k}_s$ parallel to $\mathbf{k}_i$ and domination of a single scattering event in the detected signal, Eq. (5.5) can be simplified to:

$$f_D = 2\frac{|\mathbf{u}|\cos\theta}{\lambda_0} \tag{4.6}$$

where θ is the angle between the propagation direction of the probing radiation and the flow velocity vector, *i.e.* angle between $\mathbf{k}_s$ - $\mathbf{k}_i$ and $\mathbf{u}$. The frequency of the resultant interferogram is either the sum or the difference of f_D and f_0, depending on the relative motion of the scatterers and the reference mirror, and therefore provides a local measure of $\mathbf{u}$.

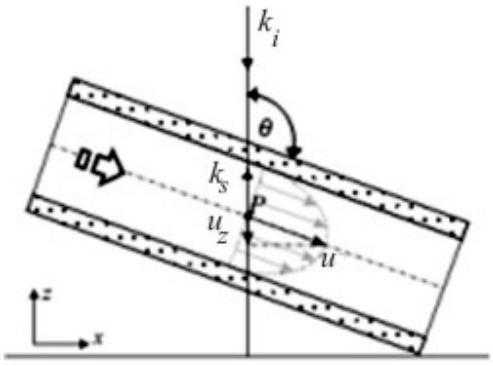

Figure 4.14 – *Schematic representation of flow profile measurement with Doppler OCT (Pierce et al. 2002, Zhao et al. 2000).* $\mathbf{k}_s$ *is the incidence direction,* $\mathbf{k}_i$ *is the direction of scattering. The incident sounding radiation is entering the sample and back-scattering at each point P along the scan. The recorded Doppler shift is proportional to* u_z*;* θ *is the angle between the scan direction and the velocity vector, assumed parallet to the sample's axis of symmetry.*

The envelope of the interferogram provides a local measure of the mean reflectivity at f_0. For a given θ, the velocity profile of particles at different spatial locations within the

sample is determined by computing f_D from the recorded interferometric signal via the Short-Term Fast Fourier Transform (ST-FFT) (Bouma and Tearney 2001). Figure 4.14 schematically illustrates how the flow velocity profiles are recorded along the scan. The introduction of a pivoting offset point Δx on the SM in the delay line (see Figure 4.13) corresponds to the width Δf of the spectrum in the Fourier transform of the auto-correlation function similar to the width of the bandpass filter (Rollins *et al.* 1998)

$$\Delta f = \frac{1.76}{L_{ax}}\left(\Delta x - \frac{L_f \lambda}{d}\right)\frac{\partial \gamma}{\partial t} \tag{4.7}$$

where d is the pitch of the grating. Special care must be taken while setting the scanning mirror offset, Δx (see Figure 4.13). Increasing Δx increases the carrier frequency ($f_0 >$ 100 *kHz*), while decreasing the offset results in a partial overlapping of the broadband spectrum in the Fourier plane. By adjusting Δx the carrier frequency f_0 can be kept within the range of 100 *kHz*. It simultaneously reduces low frequency noise $1/f$ and has the technological advantage of avoiding the application of high frequency electronics. At the same time, when the condition $f_0 \approx 100$ *kHz* holds, the broadband filter can be utilized, that increases the range of detectable frequencies and hence velocities. This is the important and crucial factor for simultaneous OCT (morphology) and Doppler OCT (velocity detection) signal processing.

In the performed experiments, a cross-sectional flow velocity profile distribution was composed of a set of adjacent A-scans, lying on a plane parallel to the scan direction and normal to the main flow stream. The time domain OCT signal is converted to the space domain, by converting the sampling time interval into the depth distance z along the sample. The broadband pass-band filter was centred at $f_0 = 150$ *kHz* with bandwidth of 200 *kHz*, giving a flow velocity detection range of ±65 $mm \cdot s^{-1}$. The lateral step between two subsequent A-scans composing a tomography was set equal to 20 μm. Each spectrogram was composed by 513×127 pixels and plotted in the time-frequency domain, with a time resolution of 0.312 *ms* and a frequency resolution of 974 *Hz*. These values lead to a pixel in-depth resolution of 21 μm and flow velocity 0.44 $mm \cdot s^{-1}$ respectively. Image processing has been digitally performed offline with the previously applied standard demodulation algorithm (Proskurin *et al.* 2003b, Proskurin *et al.*

2004a, Proskurin *et al.* 2004b). The algorithm utilized a ST-FFT with the sliding Hanning window. The data processing takes ~1-2 seconds using a 2.4 *GHz*, Pentium IV processor. Utilizing C++ language it is possible to design dedicated software and perform real time signal processing simultaneously with up to 1 *kHz* RA scanning frequency (Park *et al.* 2003). Using a RA scanning frequency of about 80–100 *Hz* it is obviously possible to perform such processing at one to two frames per second (100–150 lines per frame) that is sufficient for real-time imaging and visual feedback.

4.7 Phantoms design

As previously stated in Chapter 1, specific objective of this work includes analysis of flow dynamic in vessels with bifurcations or irregularities in their geometry such as aneurysms, anastomosis[37] or by-pass. To enable the study of flow dynamics in complex geometry vessels, a set of phantoms suitable to be used with the developed DOCT system and with desired shape and dimensions were needed. The material the artificial vessel should be made of must be such that it allows the detection of the Doppler shift from the flowing particles without the surrounding media housing the channel significantly degrading the signal, *e.g.* because of excess of absorption or scattering of the probing radiation. The phantom must also be simple to build, highly customizable in shape and possibly not expensive to make. The market offers a very wide selection of materials, such as glass or different types of plastics, and sizes, from capillary tubes with diameter below 100 μm, but these on-the-shelf phantoms are found mainly with cylindrical or tubular shape, insufficient for the purposes of the presented studies. We briefly investigated the possibility to have the sample custom manufactured, particularly from manufacturer operating in scientific and biomedical sectors, but the prototyping nature of the request made the building cost relatively too high. Therefore, we decided to develop the phantoms in-house. The goal was to obtain complex geometry vessel with circular or square cross-section in the range of 0.5-2 *mm* of diameter or side

[37] From the Greek word *anastomoun*, "to furnish with a mouth". In medicine, the term indicates the connection of separate parts of a branching system to form a network, as of leaf veins or blood vessels (From *The American Heritage Dictionaries*).

respectively. The choice of circular cross-section reflected the intention to built samples capable to enable the study of flow dynamic in complex geometry vessels which mimic the morphology of human blood vessel. Samples with square cross-section were designed for example to imitate possible geometries encountered in micro fluidic devices, in a similar or larger scale. Several techniques were investigated to determine the most convenient method to construct the samples. The main constrain on the choice of the material was dictated by its intrinsic optical properties in the IR region: simply, the selected material must have been transparent to EM radiation in the region 1250-1350 *nm*, which represents the wavelength bandwidth of the light source used in the experiments. One initial idea was to use *Perspex*[38] sheets, because they are easy to find, cheap, manufactured in different sizes and sufficiently match the desired optical properties. Phantoms with circular cross-section and with Y- or T-shape can be obtained from a block of *Perspex* by drilling intersecting channels in it, which may represent the inlet and outlet arms of the complex geometry vessel. Figure 4.15 illustrates an example of a design for a Y-shaped vessel.

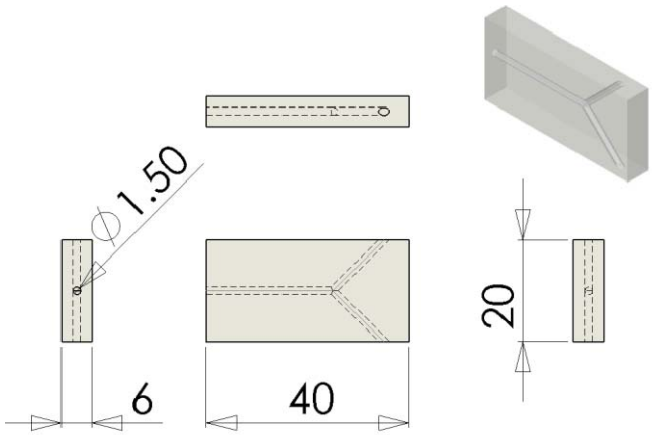

Figure 4.15 – *Design of a Y-shaped complex geometry vessel with circular cross-section. The phantom is obtained drilling intersecting channels in a block of Perspex. Dimensions are expressed in* mm.

After few trials, this approach was abandoned because of the difficulty to obtain accurate junctions and because the act of drilling produced channels with a not perfectly transparent and smooth internal walls. Furthermore, the *Perspex* is a rigid material and

[38] Also called *Plexiglas*, British *Perspex* is the trademark name of polymethyl methacrylate, a synthetic organic compound. It is a transparent thermoplastic acrylic resin generally used as a substitute for glass.

doesn't allow the creation of vessel which can also mimic the mechanic and elastic properties of a human blood vessel, in addition to its morphology.A successful solution, alternative to utilize *Perspex* sheets, was found in creating the complex geometry vessels as moulded cavities in a silicon rubber substrate. The used silicon, *Q Sil-215* (Ambersil Ltd, UK), is a 2 part (silicon and catalyst) clear liquid silicone, transparent to IR, which will cure at room or elevated temperature. Its typical optical and mechanical properties, as quoted from the manufacturer and referred to the final mixture, are shown in Table 4.5.

Colour	Clear, colourless
Work time	2 *h*
Hardness	40 *shore A*
Tensile strength	700 *psi*
Refractive index	1.406
Temperature range	-60 to 200 *°C*
Coefficient of thermal expansion	27.5×10^{-5} $°C^{-1}$

Table 4.5 – *Typical property values of the silicone rubber* Q Sil-215 *utilized in the preparation of the complex geometry vessels.*

The building technique consisted in creating a "negative" with the desired custom shape of the final vessel, fixing it in a container and then pouring the silicone mixture around it, *i.e.* immersing the negative in the liquid silicone. Once the mixture solidified the negative was removed, creating the complex geometry vessel as a moulded cavity in the silicone substrate. To remove the presence of air bubbles, the construct was kept under vacuum during its formation.

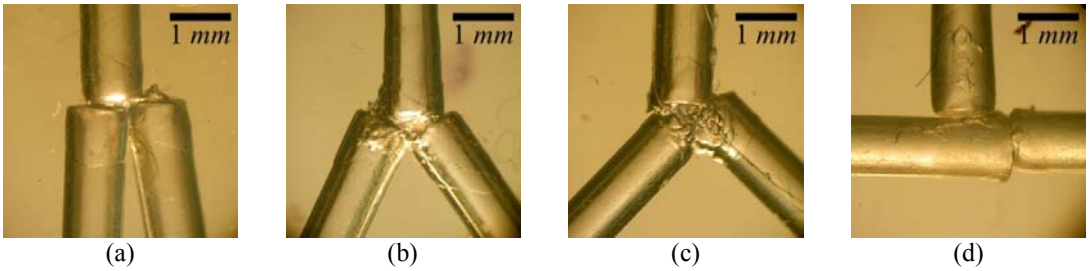

(a) (b) (c) (d)

Figure 4.16 –*Photos of Y- and T-shaped vessels created as moulded cavities in silicone substrate using joined metal rods as negative.*

Using this technique, a broad set of phantoms, with circular cross-section of different diameters and variable custom shapes were obtained. In the attempt to conveniently

create the negatives, several materials and techniques were investigated. Figure 4.16 shows some of the results of preliminary attempts to obtain Y-shaped junctions with different angles between outlet arms. In the illustrated example, the negative consisted in three metal rods of about 1 *mm* in diameter joined together with a thin film of cyanoacrylate. The metal rods created regular inlet and outlet channels but the geometry at the junction resulted very irregular and difficult to control during its formation. Nevertheless, the technique was promising and further efforts were spent to obtain better negatives. The idea was to employ a material easy to model with the desired precision and that can be removed from the silicone substrate without degrading its mechanical and optical properties or disrupting the channel geometry. Such material was individuated in *paraffin wax*[39], a waxy white or colourless, tasteless, odourless hydrocarbon mixture, generally used to make lubricants, sealing materials or candles. Paraffin wax is solid at room temperature (20°C) and melts between 47°C and 65°C; it is insoluble in water but soluble in ether, benzene and certain esters. Paraffin wax was used to make original models for creating the wanted negatives, even if it is relatively brittle at room temperature and usually cannot be cold-carved without excessive chipping and breaking. Soft, pliable waxes, such as *beeswax*, could be preferred for the making of the negatives, but since good results were already obtained from using paraffin wax, available in the lab, we didn't experimented other materials. Once created the phantoms with the above illustrated technique, the paraffin was removed from the silicone by melting it in a temperature-controlled oven. Excess of melting temperature can cause the paraffin to penetrate into the surrounding silicon with consequent degradation of the optical properties of the silicone around the created channel. Due to wax penetration, the silicon will lose its clear transparency, with increase of scattering of the probing radiation and possibly degradation of the quality of the DOCT signal. If this happens, the penetrated paraffin can still be removed from the silicone by immersing and washing the phantom in proper solvent, such as *n-hexane*. The drawback of this method is a possible degradation of the elastic properties of the silicon – it may become more stiff and subject to rupture – but the removal of the wax will restore its

[39] Chemically, *paraffin* is a mixture of high-molecular-weight alkanes, *i.e.* saturated hydrocarbons with the general formula C_nH_{2n+2}, where *n* is an integer between 22 and 27. The solid forms of paraffin, called *paraffin wax*, are from the heaviest molecules. Paraffin wax was identified by Carl Reichenbach in 1830.

transparency at IR wavelengths. Using paraffin wax, negatives with different shapes were created, including T-shaped junctions, Y-shaped junctions and vessels with aneurisms.

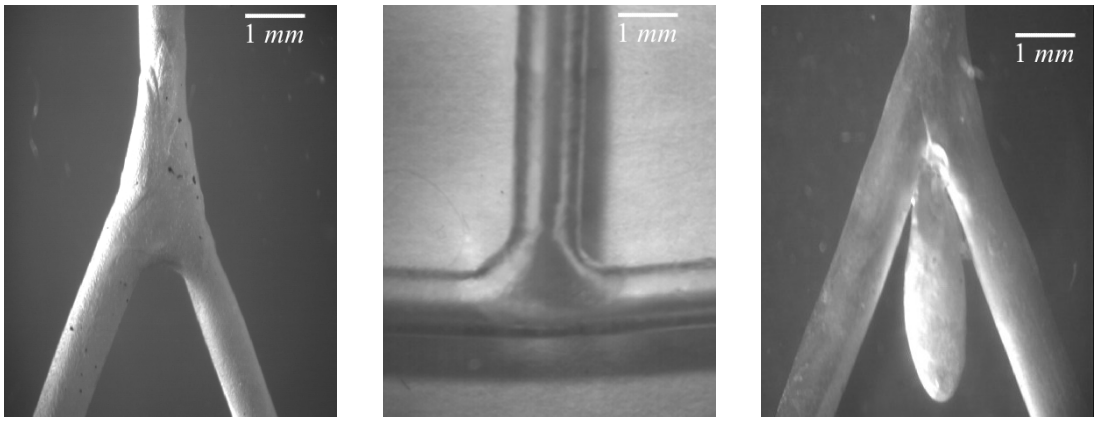

(a) (b) (c)

Figure 4.17 *–Photos of (a) Y- and (b) T-shaped vessels (c) and vessel with aneurysm with circular cross-section, created as moulded cavities in silicone substrate using paraffin wax as negative.*

Figure 4.17 illustrates some of the complex geometry samples obtained applying the described technique. In addition to the phantoms with circular cross-sections, a set of complex geometry phantoms with square cross-sections were built.

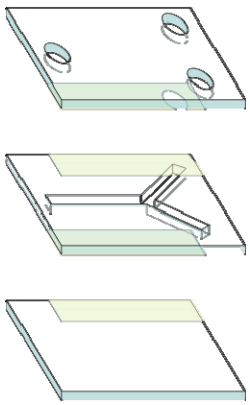

Figure 4.18 – *Schematic representation of the construction of the complex geometry phantoms with square cross-section used in the experiments. The figure illustrates an exploded view of the layers composing the phantoms. From top to bottom: top PVC layer with circular apertures for interconnection with syringe pump; bi-adhesive layer; middle PVC layer including the carved channel; bi-adhesive layer; bottom plain PVC layer.*

Due to the different cross-sectional geometry, a diverse construction technique was adopted, in respect from the above described method. In this case, the samples were created using a 1 *mm* thick sheet of PVC[40].

To construct the sample, three rectangular blocks of identical dimension of about 4×3×1 mm^3 were cut from the PVC sheet and overlapped one on top of the other. The three layers were joined together using a special hydrophobic bi-adhesive tape suitable for medical applications. Figure 4.18 schematically illustrates the construction technique. The bottom layer was kept plain and closes the bottom side of the complex geometry channel; the middle layer includes the flowing chamber of the complex geometry channel and the top layer closes the top side of the channel and includes apertures for convenient interfacing of the complex geometry channel with the syringe pump. The channel in the middle layer was carved from the PVC block using a CO_2 laser, which allowed high precision cuts through the thickness of the PVC. Similar procedure was applied to create the apertures in the top layer.

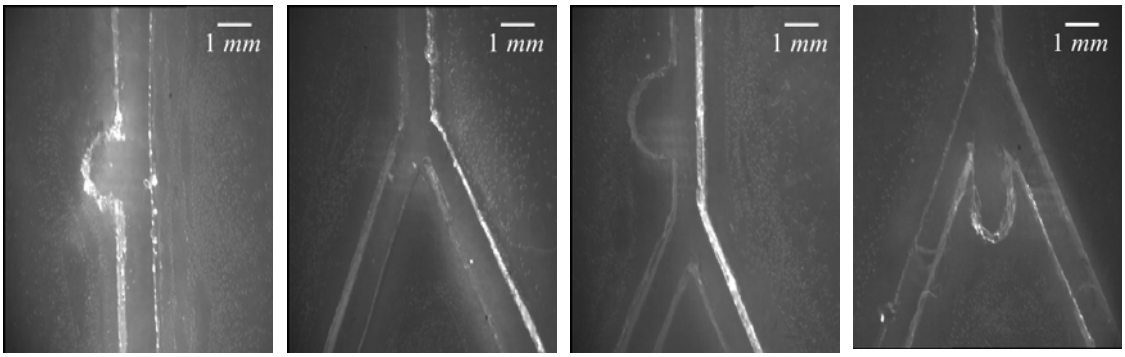

(a) (b) (c) (d)

Figure 4.19 – *Photos of complex geometry vessel with square cross-section of 1×1* mm^2 *obtained from PVC sheets. (a) Straight channel with lateral aneurism. (b) Vessel with bifurcation. (c) Vessel with bifurcation and lateral aneurism on the inlet arm. (d) Vessel with bifurcation and aneurism between outlet arms.*

The apertures consisted of circular holes of about 1 *mm* in diameter, coincident with the entrance point of the inlet arm and the exit(s) point(s) of the outlet arm(s) of the channel in the middle layer. Semi-rigid *Teflon* tubes of about 1 *mm* of internal diameter and 1 *cm* long were glued on top of these apertures for ease interconnection of the sample

[40] Abbreviation for polyvinyl chloride, a common thermoplastic resin used in a wide variety of manufactured products.

with the syringe pump. Figure 4.19 illustrates some of the samples obtained applying the described technique.The presented adopted solutions permitted the construction of a wide variety of complex geometry vessels with custom shapes to be used in the DOCT measurements. The building techniques were easy to perform and the samples were relatively cheap to make, allowing great versatility in the design of the experiments.

4.8 Summary

A Doppler optical coherence system has been developed for mapping of flow dynamics in complex geometry vessels. A description of its component and operational methods is reported. The original DOCT system was further improved with the implementation of the RSDL in the reference arm. The modified low power portable (~11×7×5 cm^3) RSDL in the reference arm of the scanning interferometer has been developed and used to obtain quantitative evaluation of flow dynamics in the vessel phantom and imaging of subcutaneous blood vessels *in vivo*. The RSDL was developed to be used in combination with SLD of 1.3 μm and 1.5 μm (and, ideally, with any wavelengths in between) and ~10-100 *kHz* carrier frequency range without the need of any modification or tuning of the RSDL itself. In addition, it enabled dispersion compensation without the need for added external optical components, improving the axial resolution while maintaining small dimensions. Application of the described RSDL enabled usage of carrier frequencies less than 100 *kHz*. This allows direct detection of the Doppler shift introduced by slow flow (~1–50 $mm{\cdot}s^{-1}$) in the sample arm via ST-FFT on each single A-scan rather than comparing the phase shift between two consecutive A-scans (Proskurin *et al.* 2004b).

The DOCT system makes use of one single probing beam for velocity detection. Extending the detection technique from single angle detection, where only one component of the velocity vector is detected – the one parallel to the probing radiation – to multiple angle detection makes it possible to reconstruct the complete velocity vector, from which a detailed computation of the shear stress can be performed. This data represent very useful information in biorheology. Particularly in cardiology, where the

knowledge of the shear stress acting on vessel's walls can help to determine the influence of those blood flow factors, such as shear stress, that could be involved in the genesis of atherosclerotic diseases.

To enable the flow dynamic investigation in complex geometry vessels, a set of custom developed phantoms were designed and built in the labs. The home-built complex geometry vessels are highly customizable in shape, inexpensive, easy to build and can more realistically mimic the shape of human blood flow vessels. These phantoms can be used in conjunction with DOCT methodology for a full cross-sectional velocity mapping of complex flow. Further development in the building technique may take in account mechanical and elastic properties of the vessels to imitate those of a real blood vessel. These features can enable study of blood flow dynamic in phantoms that best resemble human vessel without the need of excision and preservation of the biological sample.

Chapter 5

Results and discussion

5.1 Intralipid

Intralipid™ (Fresenius, Rauncourt, UK) is a brand name for an aqueous suspension of lipid droplets that is sterile and suitable for intravenous feeding of patients. In the biomedical optics community it is widely used as a scattering medium for phantoms that mimic turbid tissues. There are other brands such as *Nutralipid*™ (Pharmacia, Montreal, QC, CAN) or *Liposyn*™ (Abbott Laboratories, Chicago, IL, USA) which should be similar in composition. The product is commercially available as *Intralipid*™*10%* or *Intralipid*™*20%*, the *n*% indicates *n* grams of lipid per 100 *ml* of suspension. The constituent of *Intralipid*™*10%* in a 500 *ml* bottle, according to the manufacturer are summarized in Table 5.1.

Active ingredient	*g*	*mL*
Purified soya bean oil	50.00	53.94
Inactive ingredient		
Purified egg phospholipids	6.00	5.82
Glycerol anhydrous	11.00	8.30
Water for injections	431.94	431.94
TOTAL	498.94	500.00

Table 5.1 - *Constituent of* Intralipid™10% *in a 500* ml *bottle as quoted by the manufacturer (ex Pharmacia, Milton Keynes, UK, 2004).*

The content of the solid particles of intralipid is soya bean oil, egg yolk phospholipids and glycerol. The particles of soya bean oil determine the diffusion phenomenon in the water-based intralipid solution. The egg phospholipids and glycerol particles enable the particles of soya bean oil to be distributed in the distilled water in a homogeneous way. The glycerol anhydrous is soluble in water, dissolving into individual molecules and does not scatter the light (Drakaki *et al.* 2005). The difference in the refractive index of this water-glycerin solution from that of pure water has no measurable influence on the scattering parameters (van Staveren *et al.* 1991). The scattering particles in the solution

consist of soybean oil encapsulated within a monolayer membrane of lecithin (purified egg phospholipids) with a thickness of approximately 2.5-5 *nm* (van Staveren *et al.* 1991). The particles have spherical shape with diameter in the range from tens to hundred of *nm*. The optical properties of intralipid in the wavelength range of 400-1100 *nm* (from visible blue to near infrared region) have been studied by several groups (Driver *et al.* 1989, van Staveren *et al.* 1991, Flock *et al.* 1992) in the early 90s, as intralipid became interesting for optics and recently by Chen and co-workers in the wavelength range of 550-1630 *nm* (Chen *et al.* 2006).

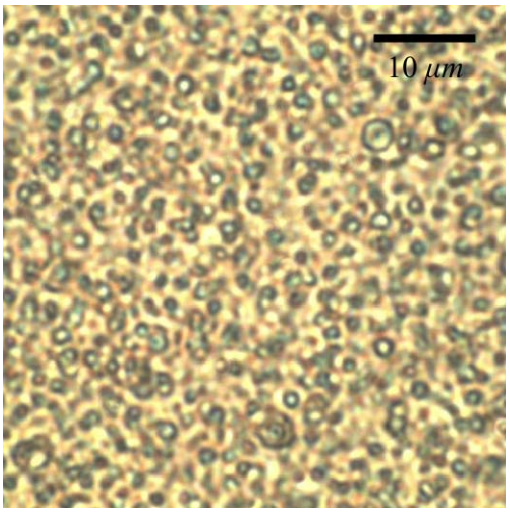

Figure 5.1 – *Particles of* Intralipid™10%. *The image is obtained from an optical microscope with a ×100 magnification. The size of the image is 50* μm × *50* μm.

H. J. van Staveren and co-workers analyzed size and distribution of the scattering particles determined by transmission electronic microscopy and derived the optical properties based on the Mie theory calculations for *Intralipid™10%*. The theoretical values were compared with the obtained experimental results of the optical properties investigated at 457.9 *nm*, 514.5 *nm*, 632.8 *nm* and 1064 *nm* wavelength, using concentration of *Intralipid™10%* less than 17~4% for the selected wavelength range. The detected particle diameter ranged from 25 *nm* (and below) up to 700 *nm*, with a mean value of 97±3 *nm*. S. T. Flock and co-workers investigated the optical properties of *Intralipid™10%* in the wavelength range from 460 to 690 *nm* and discussed the design of an optically tissue-equivalent phantom consisting of *Intralipid™10%* and black India ink.

A comparison of the results obtained by these two groups is reported in Figure 5.2.

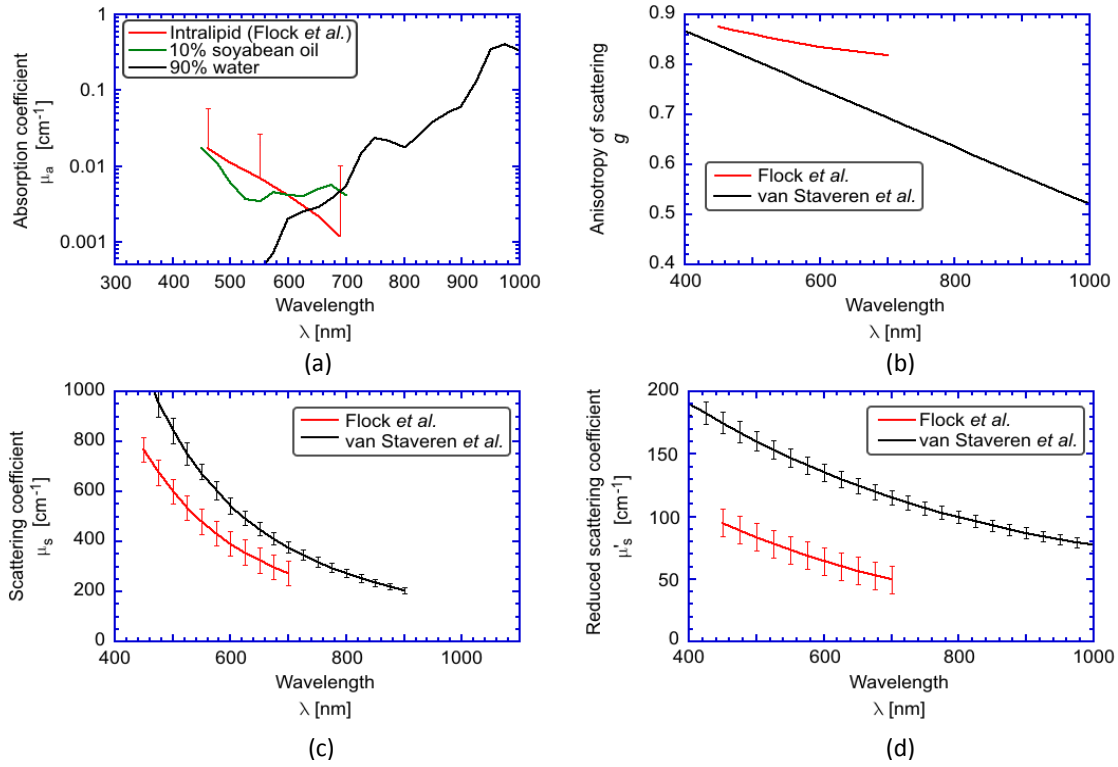

Figure 5.2 – *(a) Optical properties of water solution of* Intralipid™10% *at [10%] volume concentration. Absorption coefficient. The vertical bars represent the standard deviation; the results show that the approximate absorption of* Intralipid™10% *is probably well approximated by the combination of 10% soya bean oil and 90% water. (b) Anisotropy of scattering. The red curve represents the Flock model* g = $2.25\lambda^{-0.155}$*, whilst the black curve follows the Mie theory approximation (van Staveren* et al. *1991)* g = $1.1 - 0.58\times10^{-3}\lambda$.. *(c) Scattering coefficient. The red curve represent the Flock model* $\mu_s = 1.17\times10^{9}\lambda^{-2.33}$*. The black curve express the Mie theory approximation* $\mu_s = 2.54\times10^{9}\lambda^{-2.4}$*. (d) Reduced scattering coefficient* $\mu'_s = \mu_s(1\text{-}g)$*. For both expressions in (b) and (c),* λ *is expressed in* nm.

In particular, the group of van Staveren stated that the found dependence of the scattering coefficient μ_s and the anisotropy factor g on the wavelength λ can be expressed via the following equations:

$$\mu_s(\lambda) = 0.016\lambda^{-2.4} \qquad (\pm 6\%) \qquad (5.1)$$

$$g(\lambda) = 1.1 - 0.58\lambda \qquad (\pm 5\%) \qquad (5.2)$$

for $0.4 < \lambda < 1.1$, where λ is expressed in μm and μ_s is in mm^{-1}. They stated the equations are valid for a maximum concentration of ~4% at 1100 *nm* and ~17% at 400 *nm*; beyond this limits these equations may lead to incorrect results due to the fact that the

value of the refractive index of intralipid is unknown and the scattering events cannot be considered independent anymore.

What is emerging from the literature is that there is a sufficient bottle-to-bottle variation in the values of the optical properties of *Intralipid™10%*, or other brands, that the exact values of the optical properties should be verified individually at every use. Nevertheless, these approximate indication are sufficient for the purposes of Doppler OCT measures, whose aim in this meaning is to retrieve from the fluid an optical backscattered signal above the noise level in the region of the measurement.

The quality of the interferometric signal has been verified experimentally at different concentrations of water solutions of *Intralipid™10%* or *Intralipid™20%*, ranging from [0.0%] in volume (pure RO water) to [10%]. For each chosen value of concentration, averaged measurements from still (motionless) solution were acquired.

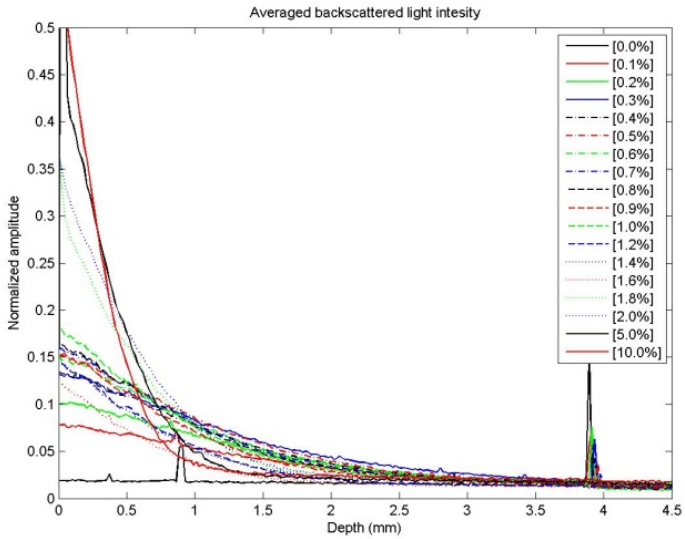

Figure 5.3 – *Measured backscattered light intensity of intralipid water solution at different volume concentrations. The total volume of the solution was kept constant while changing the respective quantities of the constituents. The concentration values refer to the absolute values of solute (intralipid) and solvent (water) in volume;* e.g. *100* ml *of solution at [1%] in volume is obtained diluting 10* ml *of* Intralipid™10% *in 90* ml *of RO water. The peak visible at about 1* mm *depth in the [0%] curve (pure solvent) is an artefact and doesn't represent a sample discontinuity.*

Figure 5.3 summarizes the acquired data. From the figure, it is possible to recognize the influence of the changes in the scattering coefficient as a function of concentration. Increasing the intralipid concentration in the water solution will increase the intensity of

the backscattered light collected back into the interferometer while reducing the depth of scan range inside the fluid due to a more intense scattering activity. From the curves reported in Figure 5.3 and taking in account a max depth of scan of 2 *mm*, we chosen a concentration of [1%] in volume as standard intralipid water solution to be used in the experiments. This choice was good enough to be used in combination with the developed complex geometry vessels, whose max diameter was less than 2 *mm*.

To estimate the (average) refractive index of the intralipid water solution, n_s, used in the experiments, a set of comparative OCT measurements were taken. Figure 5.4 shows DOCT measurements at a fixed selected position of a circular cross-sectional vessel. Figure 5.4a represents the empty channel (channel filled with air); while Figures 5.4b and 5.4c represent the same channel filled with RO water and [1%] of stock solution of intralipid respectively.

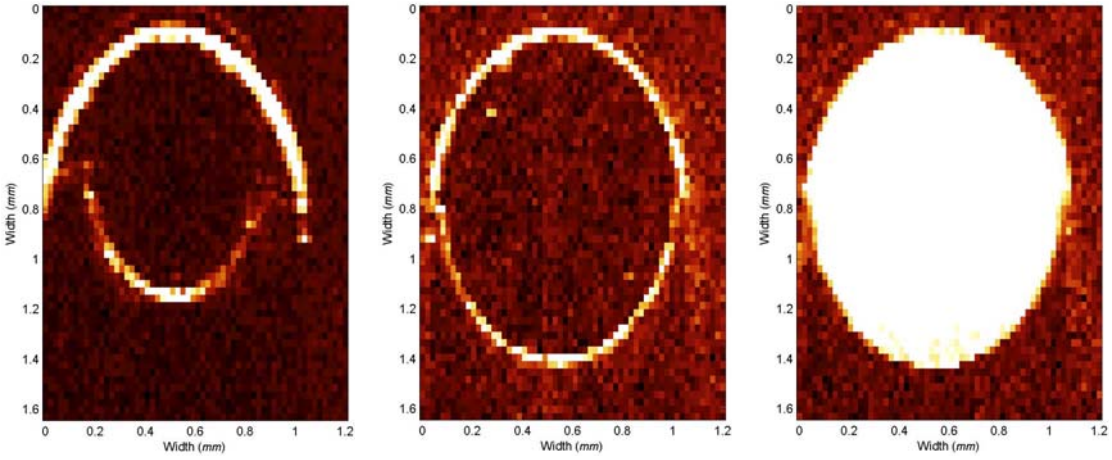

(a) (b) (c)

Figure 5.4 – *OCT measurements of media with different refractive index. (a) Cross-sectional image of a channel filled with air, (b) RO water and (c) stock solution of intralipid in RO water for a total concentration of 1% in volume. The white disk represents the backscattered light from the stock solution. Because OCT imaging measures optical path length rather than geometrical path length, the differences in the shape of the vessel in the images is due to differences in the refractive index of the medium encountered by the probing radiation.*

The vessel was created as a moulded cavity in a silicon substrate. The influence of the refractive index of the media in the OCT images is evident from the figures. The geometrical dimensions of the channel are the same for all the three measurements, while the optical properties of the fluid contained in the channel are different. A comparison of the channel cross-section in Figures 5.4b and 5.4c it allows to consider

the value of the refractive index of the 1% stock solution of intralipid close to the one of pure water (n_w = 1.3329). For a better insight, the estimation of n_s was also computed using the OCT system, observing that the axial position of an object in an OCT image is dependent upon the OPL. The thickness of the inner chamber of a rectangular couvette was measured filling it with three different media (see Figure 5.5). Similarly to the results presented in Figure 5.4, the inner chamber of the couvette was filled with air, RO water and 1% stock solution of intralipid, respectively. The probing radiation was set at normal incidence on the surface of the couvette and the measurements with the three media were performed at the same position on the sample; the couvette wasn't moved between the set of measurements. This was done to grant that the geometrical distance between the inner walls of the chamber was exactly the same for all the measurements. Data were acquired at room temperature and ambient pressure and the results are reported in Table 5.2.

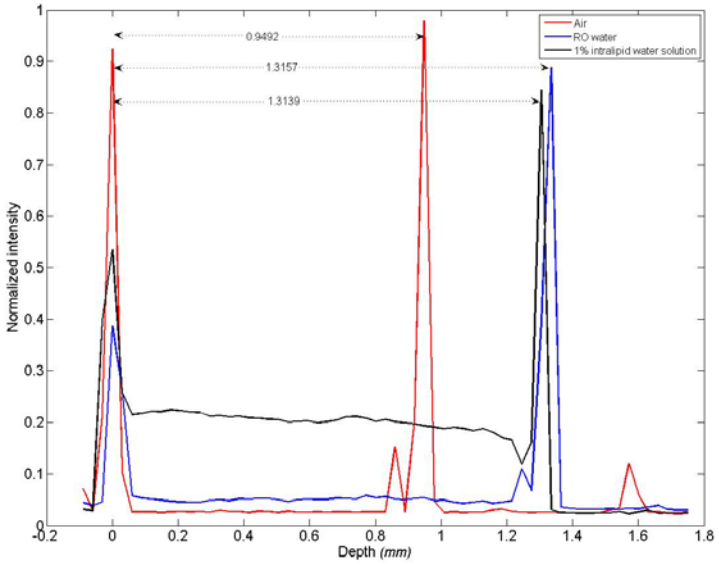

Figure 5.5 – *Estimation of the refractive index of RO water and 1% stock solution of intralipid in RO water, by comparing the optical distances the light travels within a same sample (couvette) filled with a reference media (air, red curve) or with the media under examination (RO water, blue curve or intralipid solution, black curve) respectively. The values of the refractive index of air is assumed equal to* n_a *= 1.00 and used as reference (see text for details). The peaks in the curves represent the optical positions of the discontinuity interfaces glass/media (left peak) and media/glass (right peak) of the internal chamber of the couvette.*

The values of the refractive index of RO water, n_w, and 1% intralipid water solution, n_s, were estimated as follow: known that the optical path is defined as the product of the

geometrical path times the refractive index of the media where the path is considered and observing that

$$\text{geometrical path length} = \frac{\text{optical path length}\big|_{\text{reference}}}{n_{\text{reference}}} = \frac{\text{optical path length}\big|_{\text{media}}}{n}$$

it follows

$$n_{\text{w}} = n_{\text{air}} \frac{\text{optical path length}\big|_{\text{water}}}{\text{optical path length}\big|_{\text{water}}}$$

and

$$n_{\text{s}} = n_{\text{air}} \frac{\text{optical path length}\big|_{\text{intralipid solution}}}{\text{optical path length}\big|_{\text{air}}}$$

The refractive index of air, n_{air}, was assumed to be equal to 1.00 and its value used as reference. The optical path lengths were estimated from the acquired A-scans, evaluating the distance of the high backscattered peaks from the OCT images, representing the thickness of the inner chamber of the couvette. These peaks were associated to the glass/media and media/glass discontinuities, where the media was air, RO water and 1% intralipid solution respectively. From the acquired data, the computed values for n_{w} and n_{s} differ slightly from the ones reported in literature.

	Optical distance	Standard deviation	Refractive index
Air	0.9492	0.0012	1.0000 (ref.)
RO water	1.3157	0.0027	1.3861
1% intralipid water solution[41]	1.3139	0.0018	1.3842

Table 5.2 – *Estimation of the refractive index of RO water and 1% stock solution of intralipid. The refractive index of air is assumed equal to 1.0000 and taken as a reference; the refractive index of RO water and intralipid water solution are calculated as a ratio of optical distances as estimated via OCT measurement (see text for details).*

[41] Estimated at $\lambda_0 = 1298\ nm$.

The typical value of the refractive index of water at ambient temperature and pressure is $\underline{n}_w = 1.3329$. More difficult is a precise estimation of n_s, since exist a great variability in the bottle-to-bottle composition of the commercially available intralipid. Boppart and co-workers, using an OCT system with a broadband light source of 1310 *nm*, have estimated for *Intralipid™10%* a value of $n_s = 1.351 \pm 0.009$ (Zysk *et al.* 2007). These discrepancies arise from the fact that the OCT system wasn't optimized for this kind of measurement and no error compensation has been taken into account while processing the data. Therefore, the presented results must be considered only quantitatively, and its analysis allows considering the value of the refractive index of 1% intralipid water solution close to the one of RO water at room temperature and pressure. A detailed description of refractive index measurements using OCT technique can be found in Tomlins's dissertation (Tomlins 2007). To summarize, the optical properties of intralipid can be described by

- absorption coefficient, μ_a, expressed in cm^{-1};
- reduced scattering coefficient, μ_s', expressed in cm^{-1};
- scattering coefficient, μ_s, expressed in cm^{-1};
- anisotropy of scattering, g, adimensional;
- refractive index, n_s, adimensional.

Figure 5.6 shows the variation of μ_a, μ_s and g in function of λ (Chen *et al.* 2006) in the wavelength range of 550-1630 *nm.* From the graph, the values of the optical parameters of intralipid can be estimated for $\lambda = 1298$ *nm*, which is the value of the central wavelength of the light source used in our experiments.

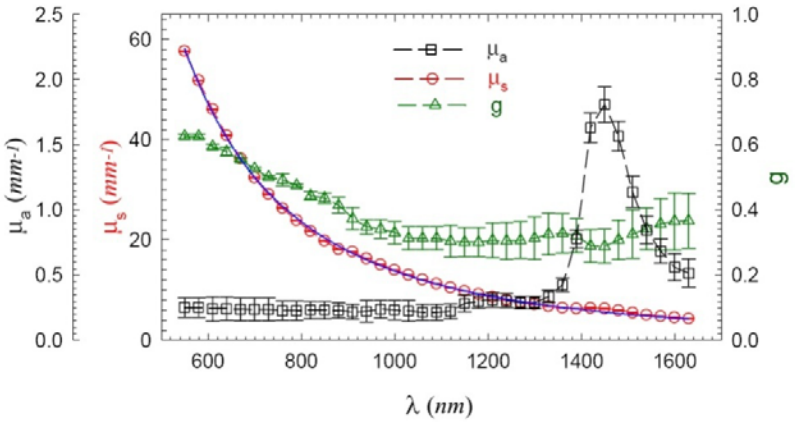

Figure 5.6 – *The wavelength dependence of the optical parameters of Intralipid™20%. The symbols and error bars are the means and standard deviations. The dashed lines are visual guides and the blue solid line is a power law fitting of* $\mu_a = C\,\lambda^{-2.407}$*, where* C *is a constant (from Chen* et al. *2006).*

Figure 5.7 reports the variation of μ_a of stock solution of *Intralipid™20%* in RO water, obtaining a final concentration of [1%] in volume, as measured in the lab, which is in good agreement with the data presented by Chen and co-workers.

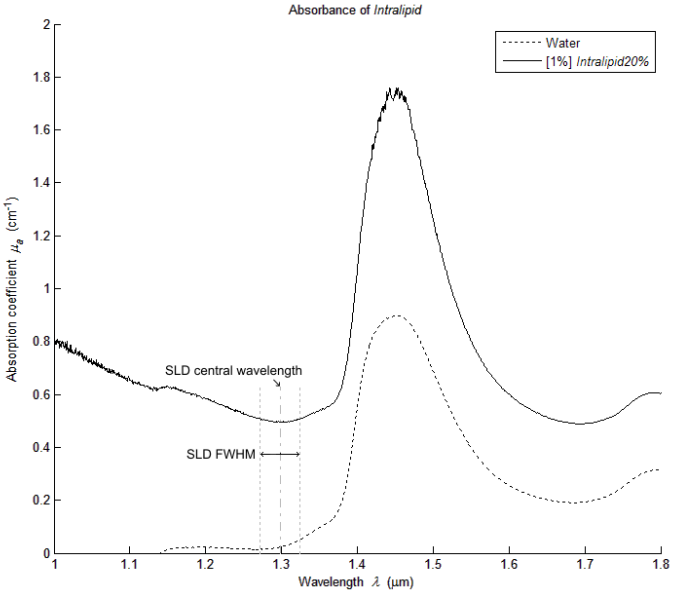

Figure 5.7 - *Measurement of the absorption coefficient* μ_a *of stock solution of intralipid at [1%] in volume.*

5.3 Haemoglobin and RBC

Knowledge about the optical properties – absorption, scattering and anisotropy of scattering – of human blood plays an important role for many diagnostic and therapeutic applications in laser medicine and medical diagnostic. Their determination strongly depends on physiological and biochemical parameters, including blood flow conditions and wall shear rate. Applied to DOCT measurements, the knowledge of the optical parameters is important to determine the light distribution in blood perfused tissues or phantoms, since this directly influence the quality of the acquired images. The optical properties of blood in motion can differ from still blood, due, for example, to a variable oxygen content or cell axial migration, influencing absorption or scattering.

Normal human whole blood consists of about 55% in volume of plasma (90% water and 10% proteins) and 45% in volume (haematocrit) of cells – 99% RBC "erythrocytes" and 1% leukocytes and thrombocytes. The RBC has a mean volume of 90 μm^3 and contains 30 pg of haemoglobin that allows oxygen transport. The cell concentration in blood under physiological conditions is approximately $5\times10^{12}\ L^{-1}$.

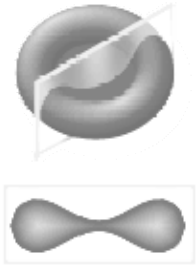

Figure 5.8 – *Typical shape of a normal red blood cell "erythrocyte".*

The haemoglobin concentration ranges from 134 to 173 gL^{-1} for whole blood and from 299 to 357 gL^{-1} for RBCs. Flow induced shear stress can influence phenomena such as sedimentation, reversible agglomeration, axial migration or cell deformation and orientation. The flow parameters depend on the blood viscosity and they are influenced by the fact that blood is a non-Newtonian fluid.

With reference to the NIR region of the spectra, what is emerging from literature is an agreement on values of absorption coefficient, μ_a, estimated about 0.75 mm^{-1} and anisotropy factor, g, estimated about 0.99. The reported results for the scattering

coefficient show variations in the range 50-300 mm^{-1} due also to the fact that there is no access to analytical models which can grant sufficient precision. Roggan and co-workers found that μ_s showed a maximum around 500 *nm* and decreased with wavelength at a rate of approximately $\lambda^{-1.7}$ in the wavelength region 400-2500 *nm* and that axial migration was the predominant factor influencing the optical properties with respect to the flow parameters (Roggan *et al.* 1998).

To further extend the characterization of flow dynamics in complex geometry vessel, a preliminary study using bovine haemoglobin (Sigma Aldrich), a non-Newtonian fluid, diluted in Phosphate Buffered Saline (PBS) solution at different concentrations was used in the experiments. Figure 5.9 shows stock solution of bovine haemoglobin diluted at 20% in weight in PBS solution. To obtain a high backscattering signal from the haemoglobin solution, comparable with the one obtained from stock solution of intralipid, a high concentration haemoglobin crystals was needed to prepare the solution. Stock solutions with high haemoglobin content were characterized by a very high viscosity and a prone tendency to coagulate at room temperature, which made the DOCT measurements impossible to perform.

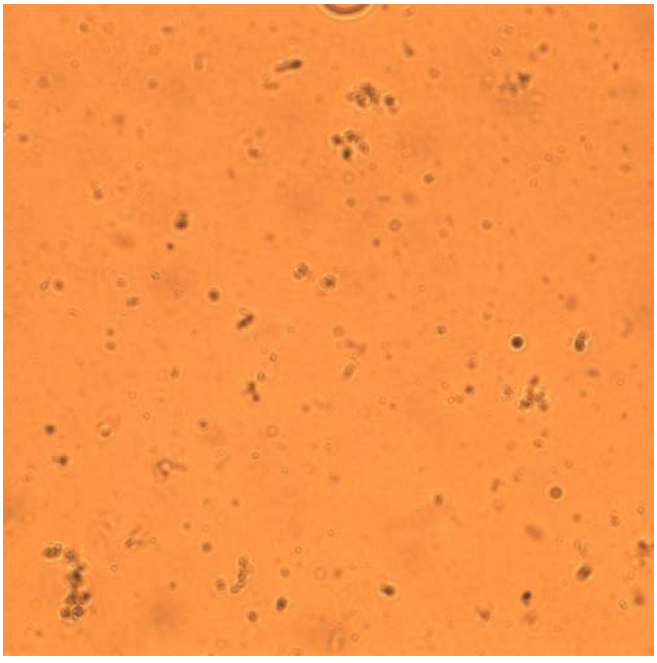

Figure 5.9 – *Particles of bovine haemoglobin diluted in RO water at 20%. The image is obtained from an optical microscope with a ×40 magnification.*

To obtain stock solution of haemoglobin with adequate viscosity for DOCT measurements, a small dosage of haemoglobin crystals were applied during the solution preparation. A comparison of Figure 5.9 with Figure 5.1 shows that haemoglobin solution presented a lower concentration of particles when compared with the stock solution of intralipid at similar viscous properties. Figure 5.10 reports the recorded backscattered signal from haemoglobin solutions at different concentrations. The curves are associated to haemoglobin stock solutions which presented viscous-mechanic properties suitable to use the solutions in the flow dynamic experiments. Those properties were determined empirically. Due to low concentration of particles, the intensity of the backscattered signal is just above the noise level, making the flow velocity detection difficult to detect with the developed DOCT system. Nevertheless, cross-sectional velocity profiles were acquired from the developed phantoms in combination with the above mentioned prepared haemoglobin stock solutions. The acquired results are partially reported and discussed in paragraph 5.4.1.

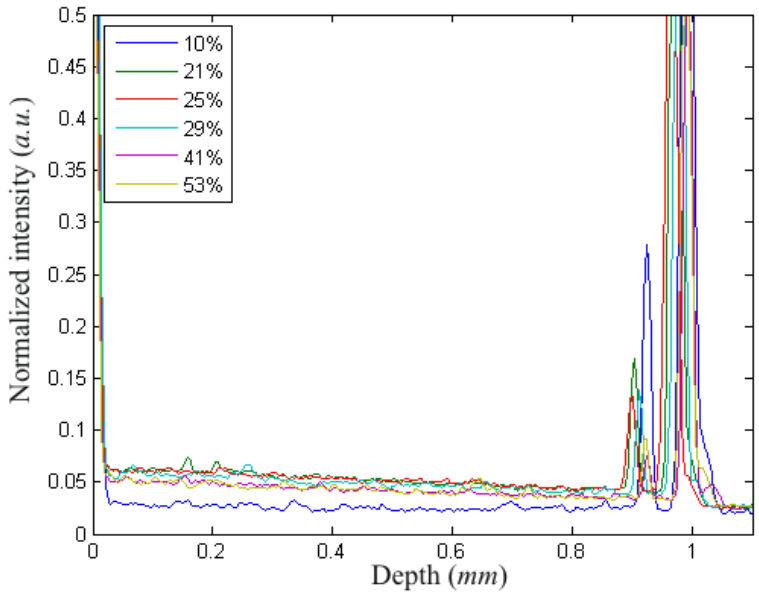

Figure 5.10 – *Backscattered intensity recorded from bovine haemoglobin diluted in PBS at different concentrations in weight. The backscattering signal from stock solution was measured using a couvette of 0.98* mm *thick. Due to low concentration of particles in the stock solution, a weak backscattered intensity is recorded.*

5.4 Flow in complex geometry vessels

To validate the system we performed a number of experiments for a range of phantom vessels to get better insight into flow dynamics and formation at the junction site of the side branches of the vessel. The selected results are presented in the following section. Additional i*n vivo* results, obtained after implementing a rapid scan delay line (RSDL) in the DOCT system, of superficial human skin blood vessels imaging are presented in section 5.4.2.

5.4.1. Phantom studies

The phantom vessel used in the experiment was obtained as moulded cavity in a transparent silicon substrate, with circular cross-sections of 1 *mm* in diameter and 50° between the side branches. *Intralipid™10%* (Sigma-Aldrich) was diluted in distilled water to obtain an overall stock intralipid solution at a concentration of 1% in volume. The optical properties of the solution were estimated from (Chen *et al.* 2006).

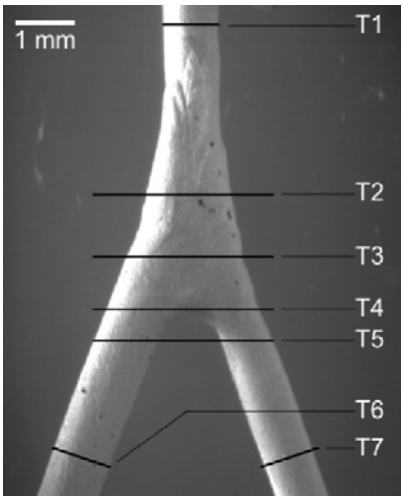

Figure 5.11 – *Y-shaped phantom vessel used in the experiment. The inlet and outlet arms have a circular cross-section of ~1* mm *in diameter. Labels T1–T7 indicate the positions where the images were taken.*

Due to the low concentration of intralipid, the refractive index of the final solution was assumed similar to the one of water, n_w, at ambient temperature ($n_w \approx 1.33$). The liquid was set in motion by a syringe pump (*Harward, mod.975*), which allowed constant input volume flow rate under laminar regime. The selected input volume flow rate in the

presented experiments was set to 3.7 $cc \cdot min^{-1}$, giving a nominal average flow velocity of about 78.5 $mm \cdot s^{-1}$ in the inlet arm of the sample.

The locations at which the tomographies were taken are shown in Figure 5.11 and denoted as T1-T7. In the inlet and outlet arms, (locations T1, T6, T7), to visualize the parabolic profiles typical for laminar regime, the Doppler angle θ between the propagation direction of the probing radiation and the flow velocity vector (assumed parallel to the sample axis of symmetry) was set to ~102°. At the junction site (T2–T5), to visualize the components of the flow associated with the turbulent regime, the angle θ between the direction of the scan beam and the main inlet stream (flow parallel to the axis of symmetry of the samples) was set to 90°. To improve the SNR in the computed spectrograms, each measured point was averaged 20 times.

Figure 5.12 represents a set of cross-sectional velocity profiles acquired approximately 20 *mm* away from the centre of the junction at the positions T1 in the inlet arm, and T6 and T7 in the outlet arms and for the angle $\theta \approx 102°$ (see Figure 5.11). The initial flow velocity profile measured in the inlet arm was found to be steady and close to parabolic indicating the laminar regime (Figure 5.12a). Laminar regime was also restored in the outlet arms away from the junction (Figure 5.12b and c).

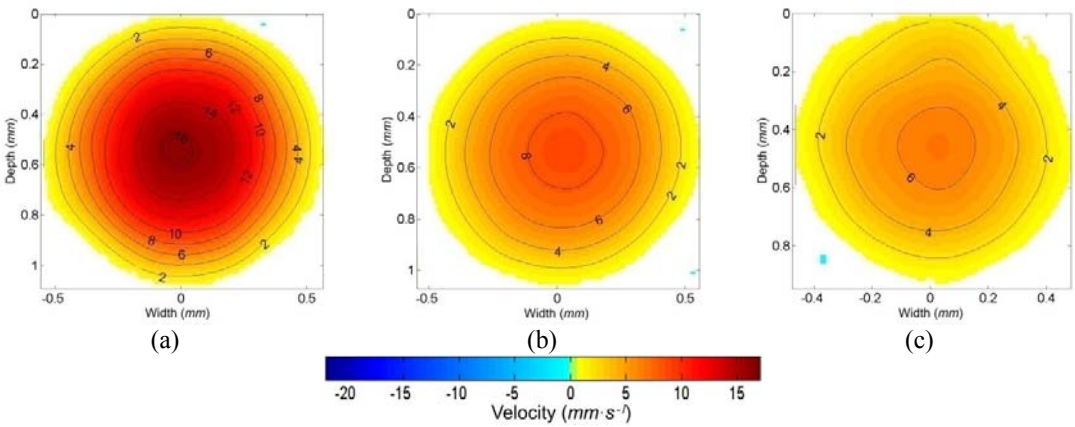

Figure 5.12. – *Velocity profiles of flow acquired across the inlet and outlet arms: (a) at the position T1, (b) T6 and (c) T7 (see Figure 5.20 for details).*

Quantitatively, the flows in both outlet arms were nearly identical due to symmetry of the sample geometry. A slight disruption of the laminarity can be associated with the complexity or irregularity of the channel's geometry (not perfectly circular cross-

section). The sum of maximum velocities observed in the outlet arms equals to the maximum velocity in the inlet arm, which, in its turn, matched well with the expected value of 78.5 $mm \cdot s^{-1} \times \cos\theta = 16.3\ mm \cdot s^{-1}$. Figure 5.13 demonstrates turbulent flow velocity profiles acquired across the Y- shaped junction at the positions indicated as T2-T5. All images have been taken close to the Y-junction with $\alpha \approx 90°$, where α indicates the angle between the probing radiation and the sample axis of symmetry. Thus, only the vertical projections, *i.e.* u_z components, of the velocity were recorded during the measurements.

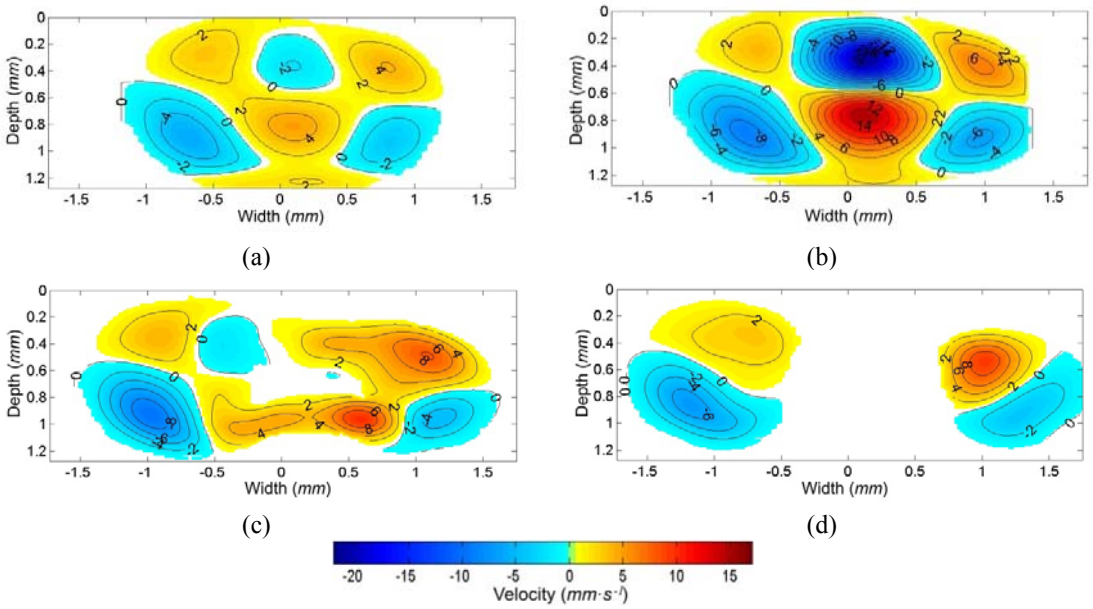

Figure 5.13. – *Turbulent flow velocity profiles acquired across the Y- shaped junction (a) at the position T2, (b) T3, (c) T4 (d) and T5 (see Figure 5.11 for details).*

As shown in Figure 5.13a, laminar regime was disrupted and turbulence has arisen at the position T2, just before the inlet arm branches into two outlet arms. In the middle of the junction, at the position marked as T3, turbulence was developed even farther (Figure 5.13b). Qualitatively, the flow pattern is similar to the one shown in Figure 5.13a. However, quantitatively, the velocity magnitudes are higher and the inversion effect is well pronounced, *i.e.* the increased magnitude of the positive and negative velocity projections in the upper and bottom parts of the vessels. The flow was subdivided at the position marked as T4 (Figure 5.13c). The middle part of the image is empty as the outlet arms joins at this point to form the apex/tip. Acquired at T5, the

image of flow pattern depicted in Figure 5.13d demonstrates turbulent regime behaviour. However, a tendency to the convergence to the laminar regime, shown in Figure 5.12b and c, is already apparent. The observed turbulence is steady and is stemmed from the geometry of the vessel, *i.e.* is the result of the junction presence in the way of flow propagation; the fact that all measurements are steady and repeatable also supports this conjecture.

To ensure consistency between adjacent measured points of the acquired data, a set of experiments was performed to check and validate the assumption of steady flow for both laminar and turbulent regimes that may develop within the complex geometry phantoms.

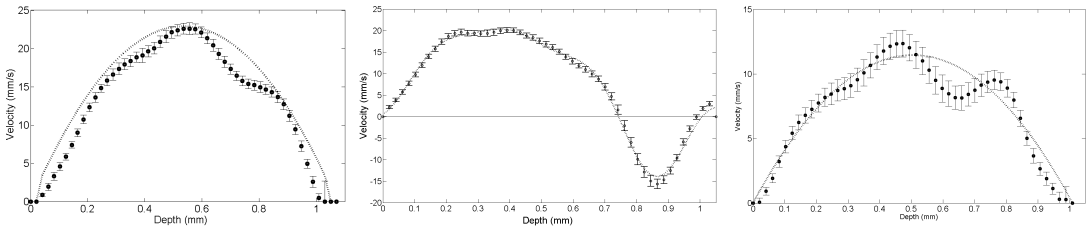

Figure 5.14 – *Flow velocity profiles acquired at the cross-sectional midpoint of the Y-shaped sample (a) at the inlet arm, about 20* mm *from the junction; (b) at the junction (c) and at the outlet left arm at about 20* mm *after the junction. The angle* α *between the scan beam and the sample was set to 80° for (a, c) and 90° for (b). The input volume flow rate was 121.67* $ml \cdot s^{-1}$. *Each plot represents the averaged flow velocity (dots) over 100 repetitions. The experimental data are compared with the calculated theoretical velocity distribution (dotted line) in (a, c), while in (b) the dotted line represents a polynomial approximation of the experimental data. Plots of the standard deviation (vertical bars) calculated for different depth positions along the scan are added.*

Figure 5.14 shows the velocity profiles acquired from the Y-shaped sample at the midpoint of the vessel cross-section (a) at the inlet arm, (b) at the junction and (c) at the left outlet arm. Each point was averaged 100 times for a total observation time of about 800 *s*. The results show that the steady property of the flow, not only in laminar regime (Figures 5.14a, 5.14c) but even in turbulent regime (Figure 5.14b). Figure 5.15 shows cross-sectional velocity profiles acquired at the end of the inlet arm (Figure 5.15a), at the junction (Figure 5.15b and 5.15c) and at the outlet left arm, just after the junction (Figure 5.15d) of the T-shaped sample. Observing the flow velocity patterns, it is well recognizable the disruption of the laminar regime in the junction area. Nevertheless, the patterns present a certain degree of symmetry related to the vessel geometry.

Figure 5.16 shows the cross-sectional velocity distribution acquired at two different positions at the junction of the Y-shaped sample, measured at two different flow rates respectively.

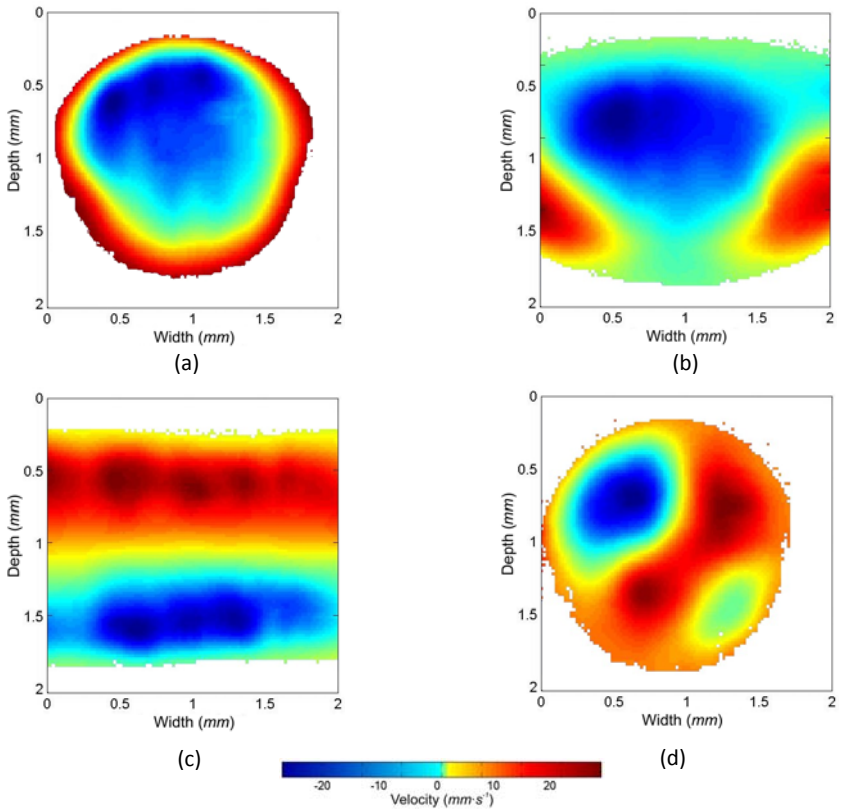

Figure 5.15 – *Cross-sectional velocity profiles taken across the junction of the T-shaped sample. The channel's diameter is 1.76* mm*. The angle between the scan beam and the sample was set to 90° and the input volume flow rate was set to 121.67* ml·s^{-1}*. Images acquired (a) at the end of the inlet arm, facing the entrance of the bifurcation; (b-c) moving across the junction (d) and after the junction, at the entrance of the left outlet arm.*

Even in this case the disruption of the laminar regime is well evident, while a certain degree of symmetry is still maintained. A change in the flow rate within the selected values on the syringe pump didn't modify the cross-sectional patterns while changing the intensity of the flow velocity.

Figure 5.17 shows the cross-sectional velocity distribution acquired at the junction of the three samples along the longitudinal direction, *i.e.* positioning the tomographic plane parallel to the flow stream. As it may be intuitive to expect, the greatest disruption of the laminar regime occurred at the end wall of the junction for the T- and Y-shaped

samples. For the Y-shaped sample with aneurism, it is interesting to notice that no significant motion of fluid was recorded inside the aneurism.

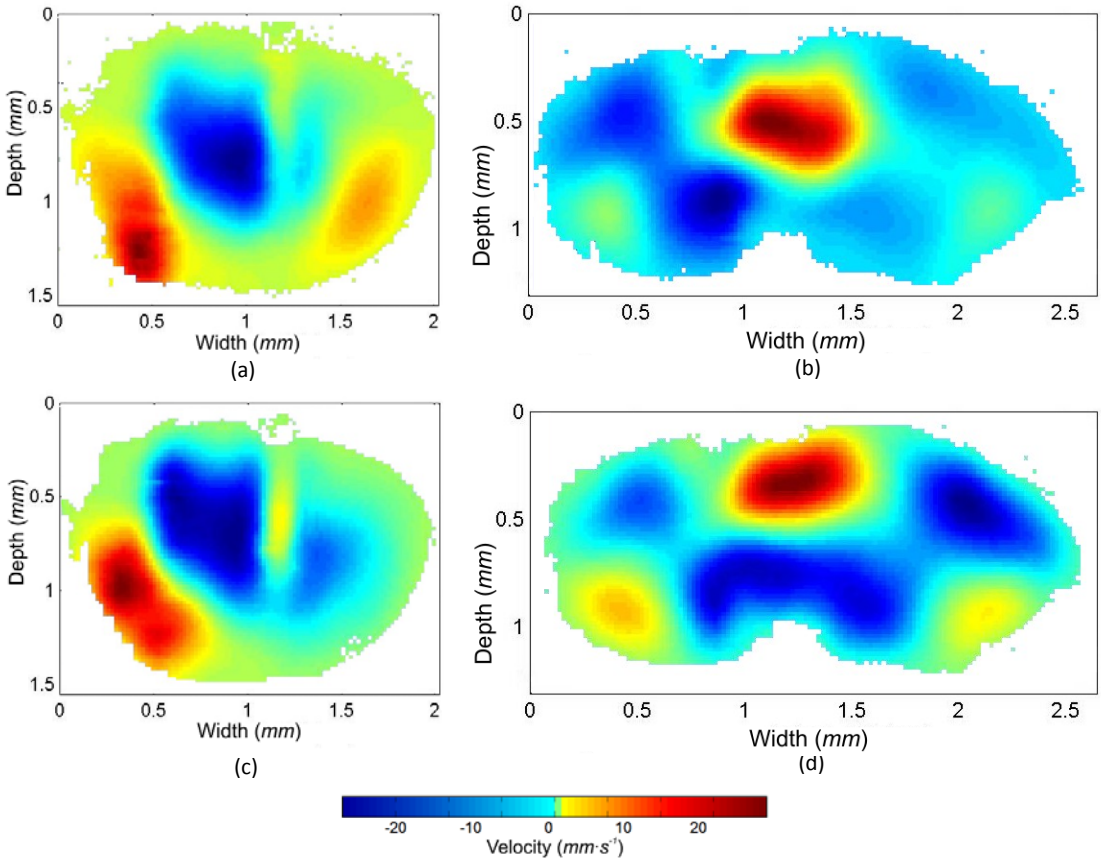

Figure 5.16 – *Cross-sectional velocity profiles taken across the junction of the Y-shaped sample. The channel's diameter is 1.76* mm. *The angle between the scan beam and the sample was set to 90° and the input volume flow rate was set to 61.67* ml·s^{-1} *(a, b) and 121.67* ml·s^{-1} *(c, d) respectively. (a, c) Images acquired at the junction, just after the end of the inlet arm. (b, d) Images acquired at the beginning of the bifurcation of the outlet arms.*

The turbulences were developed mainly at the junction in the area close to the entrance of the aneurism, similarly to the previous cases, as if the flow stream was encountering the sample wall.

The system used in the experiments employed one probe only, allowing the detection of one component of the velocity vector only. This configuration didn't allow a quantitative determination of the velocity vector, due to the uncertainty of the Doppler angle θ. However, by setting a normal incidence of the scan beam on the sample, *i.e.* α = 90°, it allowed qualitative detection and estimation of steady non-laminar flow velocity profiles through the junction, as the non-zero velocity component measured

along this direction was associated to the disruption of the laminar regime. With the selected inlet volume flow rates and the sample boundary conditions as described above, a steady non-uniform flow all along the micro channel, characterized by laminar flow in regions away from the junction, and possibly turbulent flow in the junction area was assumed.

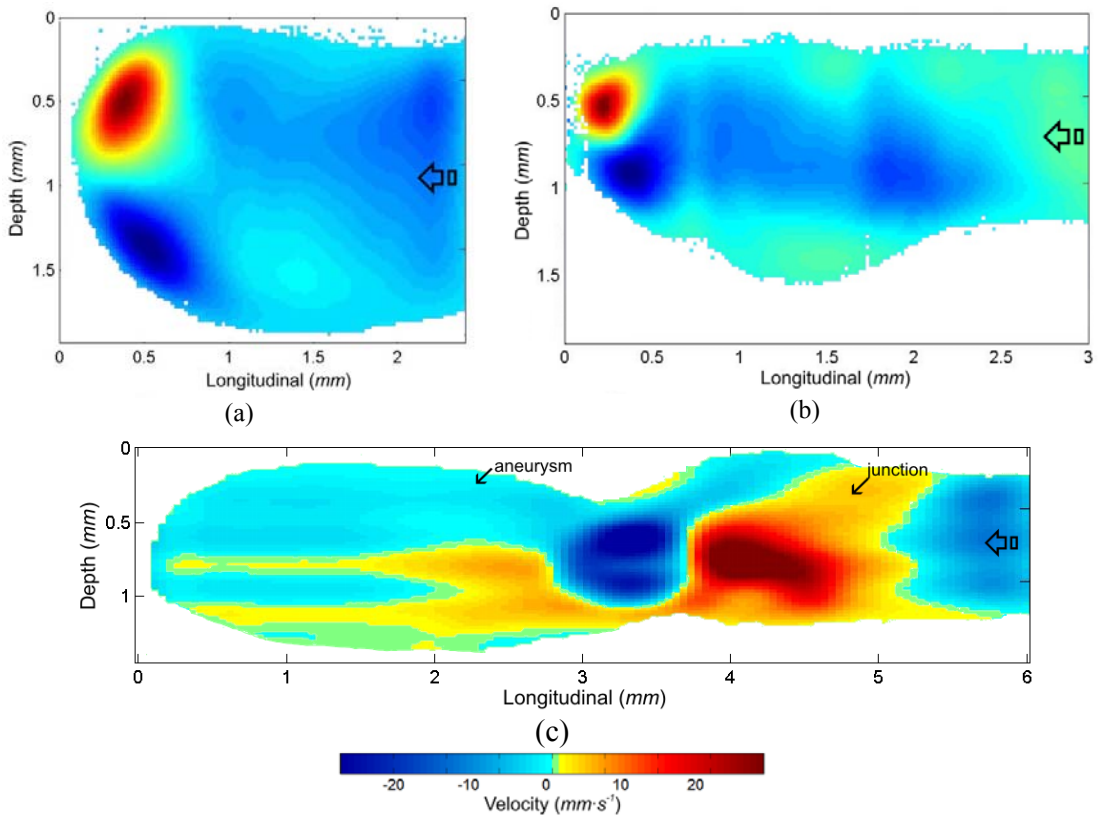

Figure 5.17 – *(a) Longitudinal cross-sectional velocity profiles acquired through the junction of the T-shaped sample, (b) Y-shaped sample (c) and Y-shaped sample with aneurism, where the small top arrows identify the aneurism and junction areas respectively along the imaged cross-section. The angle between the scan beam and the sample was set to 90° and the input volume flow rate was set to 61.67* ml·s^{-1}. *The big arrows at the right side in the three images indicate the direction of the flow entering the junctions.*

The laminar assumption was made possible evaluating the Reynolds number,

$$Re = \frac{u_{D,z} d \rho}{\eta},$$

where $u_{D,z}$ is the flow velocity component along the beam direction, in $mm \cdot s^{-1}$; d is the micro channel diameter in mm; ρ the fluid density in $g \cdot mm^{-3}$ and η the dynamic viscosity in $g \cdot mm^{-1} \cdot s^{-1}$. Given $d = 1$ mm, the low value of intralipid concentration (1%) used in the

measures allowed to consider $\rho = 0.001\ g{\cdot}mm^{-3}$ and $\eta = 0.01$ *Poise* or $\eta = 0.001\ g{\cdot}mm^{-1}{\cdot}s^{-1}$, similar to those of water at 20°*C*. With these values and with reference to the inlet highest volume flow rate used in the experiments, the calculated Reynolds number was well below 1800, indicating that the flow should be nominally laminar in the regions away from the junction. This assumption was supported by the experimental results (see Figure 5.14) as no fully developed turbulence was observed in these tracts of the phantoms. For measurement validation, comparison was made between the measured flow velocity profiles and the theoretical velocity distribution for laminar flow at a number of input volume flow rates in those tracts of the samples, *i.e.* regions away from the junction, where the flow dynamics can be numerically determined from theoretical modeling (Douglas *et al.* 2000). For this to be the case the fluid motion in the phantom had to be steady but need not be uniform all along the sample. In other words, the velocity distribution and cross-sectional area of the stream may vary from cross-section to cross-section, but, for each cross-section, they must not vary with time. This restriction arose from the necessity to have constant-in-time flow behaviour while scanning a cross-section. Each image point required 4 *s* to be measured and (at least) 60 points were needed to cover the whole channel cross-section of 1 *mm* diameter. That meant that the time needed to acquire a whole tomography was at least of 240 *s*; during this interval, the flow behaviour should not change in time. The use of the syringe pump – *i.e.* constant inlet volume flow rate with time – allowed us to take for granted that in the experiments the flow exhibited steady and laminar behaviour, at least at the inlet arm entrance and at the outlet arms exits of the samples. This assumption was confirmed by experimental results. Seven points on the phantom were chosen as test points: three at the samples extremities, located at about 20 *mm* from the junction; three in the region around the junction, located about 1 *mm* off the ideal intersection of the axis of symmetry of the sample arms and one in the middle of the junction.

The averaged measurement of each acquired scan line was repeated 100 times, with each measurement comprising the average of twenty A-scans in order to maintain a high SNR. The total observation time per point was 800 *s*. Analysis of the time-series of A-scan data indicated that the flow over this period was constant in time. Furthermore, to verify the hypothesis of laminar flow with parabolic profile at the entrance and at the

exits of the samples, full orthogonal cross-section tomographies were acquired at the entrance of the inlet arm and at the exit of the outlet arms of each sample. The measurements were repeated at two different angles α between the light beam and the sample axis of symmetry, setting α equal to 80° and 90° respectively. The former angle was chosen to detect the velocity component along the flow main direction, which was supposed to be parallel to the sample's axis of symmetry; the latter to confirm that no velocity components arose in any other direction non parallel to that axis.

These measurements were repeated for a range of different inlet flow rates, as set on the syringe pump, and the experimental results confirmed the steady laminar nature of the flow motion. Afterwards, to image flow dynamics regimes at the junction, α was set equal to 90° in order to visualize only the components of the flow velocity deviating from laminar behaviour. From each set of measurements and from each sample it was easily visible how the flow at the entrance of the inlet arm and at the exit of the outlet arms exhibited steady and laminar behaviour. As the flow approached the junction, where the boundary geometry became more complex, some irregularities in the flow behaviour arose, turning it from laminar to turbulent. After the junction, in the outlet arms, when the boundary cross-sectional geometry became regular once more, the flow tended to return to its steady and laminar behaviour.

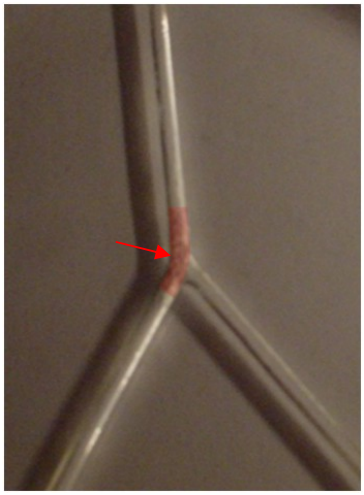

Figure 5.18 – *Y-shaped phantom with deployed stent at the junction used in the experiment. A stent was deployed at the junction (marked in red) to investigate the consequent changes in the flow dynamic at the junction area due to its presence. The diameter of the vessel was about 1.90* mm*. The red arrow indicates the position of the deployed stent.*

Figure 5.18 shows a built phantom with a deployed *stent* across the junction. A stent is a tube or metallic grid designed to be inserted into a vessel or passageway to keep it open. Stents are inserted into narrowed coronary arteries to help keep them open after balloon angioplasty. The stent then allows the normal flow of blood and oxygen to the heart. Stents placed in narrowed carotid arteries, the vessels in the front of the neck that supply blood to the brain, appear useful in treating patients at elevated risk of stroke. The need of this set of experiments was originated from a joint collaboration with Professor Hugh Barr and Dr. Nick West of Gloucestershire Royal Hospital, to perform preliminary investigation on the effect of stent deployment on flow dynamic in vessels with bifurcations. These feasibility studies aimed to investigate the accessibility of complex flow dynamic mapping using DOCT.

As for the above mentioned experiments, the fluid used in the experiment was stock solution of intralipid at 1% in volume. To estimate the changes in flow dynamic at the junction area due to the presence of the stent, a first set of measurements with no stent deployed were performed. Figures 5.19 and 5.20 illustrate the results of the acquired data.

Cross-sectional tomographies at the inlet channel, across the junction and at the outlet arm left and right respectively were acquired. As it was expected, the obtained results were comparable with the results obtained from similar artificial vessels used for flow dynamic characterization in complex geometry vessel. The inlet flow exhibit steady and laminar regime (Figures 5.19a, b). Crossing the junction, the flow maintained its steady property whilst entering in turbulent regime (Figures 5.19c, d, e, f). The developed turbulences at the junction showed a certain degree of symmetry due to the symmetry of the sample (without stent), as it was observed from similar measurements with similar samples. Figure 5.20 illustrate the results acquired from the outlet arm left (Figures 5.20a, c and e) and right (Figures 5.20b, d and f) of the sample respectively. The data are acquired just after the junction (Figures 5.20 a and b), where some turbulences are still present; after about 5 *mm* off the junction (Figures 5.20 c and d), where turbulent regime is still present with reduced intensity; and after 20 *mm* off the junction (Figures 5.20 e and f), where the laminar regime is recovered.

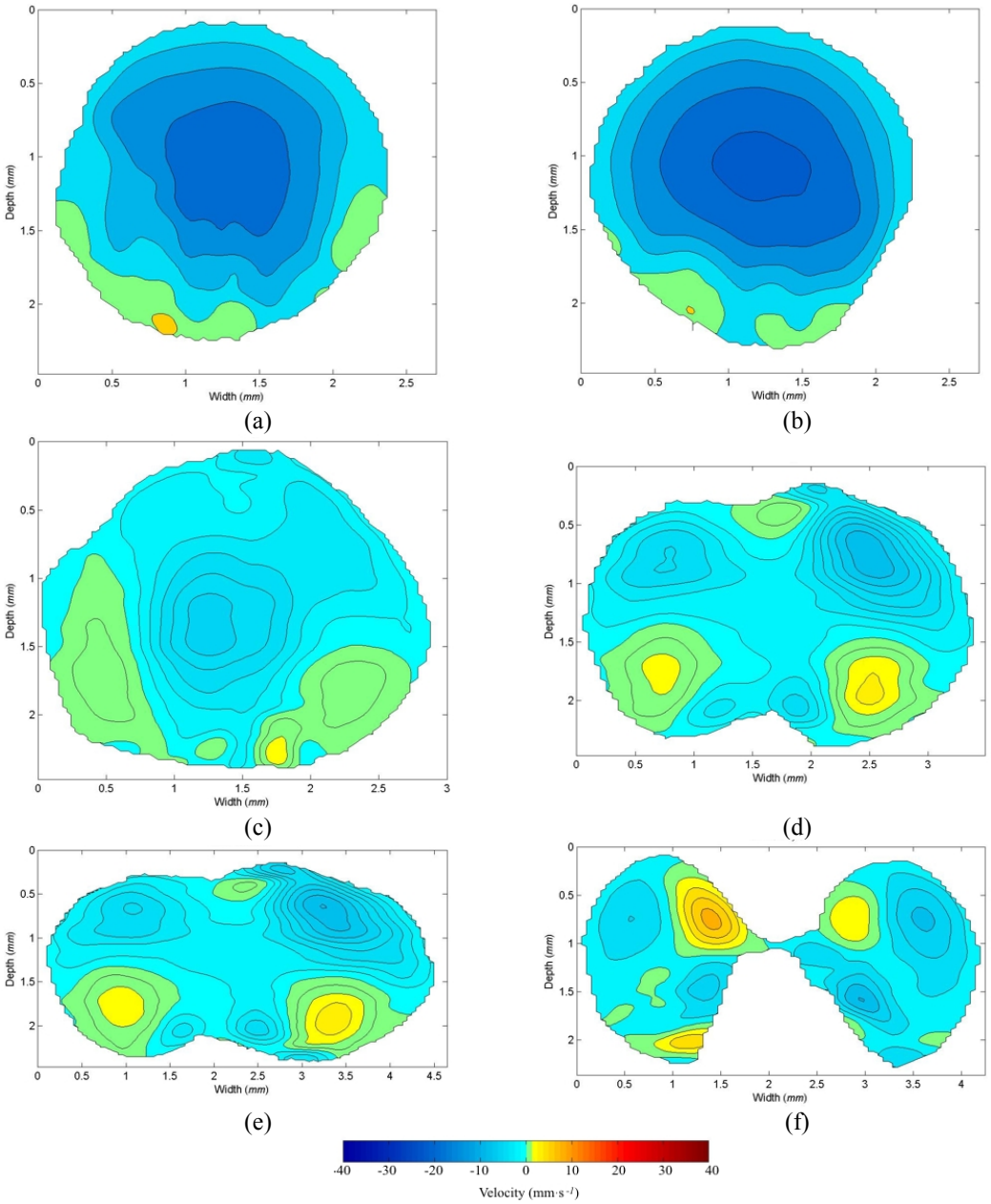

Figure 5.19 – *Cross-sectional flow velocity mapping from the Y-shaped phantom as illustrated in Figure 5.18, with no stent deployed inside the vessel. (a) Inlet arm at about 5* mm *off the junction. (b) Inlet arm just before the junction. (c-f) Across the junction. (a, b) The inlet flow regime was steady and laminar. (c-f) In crossing the junction, the flow maintained its steady property, while passing from laminar to turbulent regime. A certain degree of symmetry in the development of turbulence can be recognized in due to the sample symmetry.*

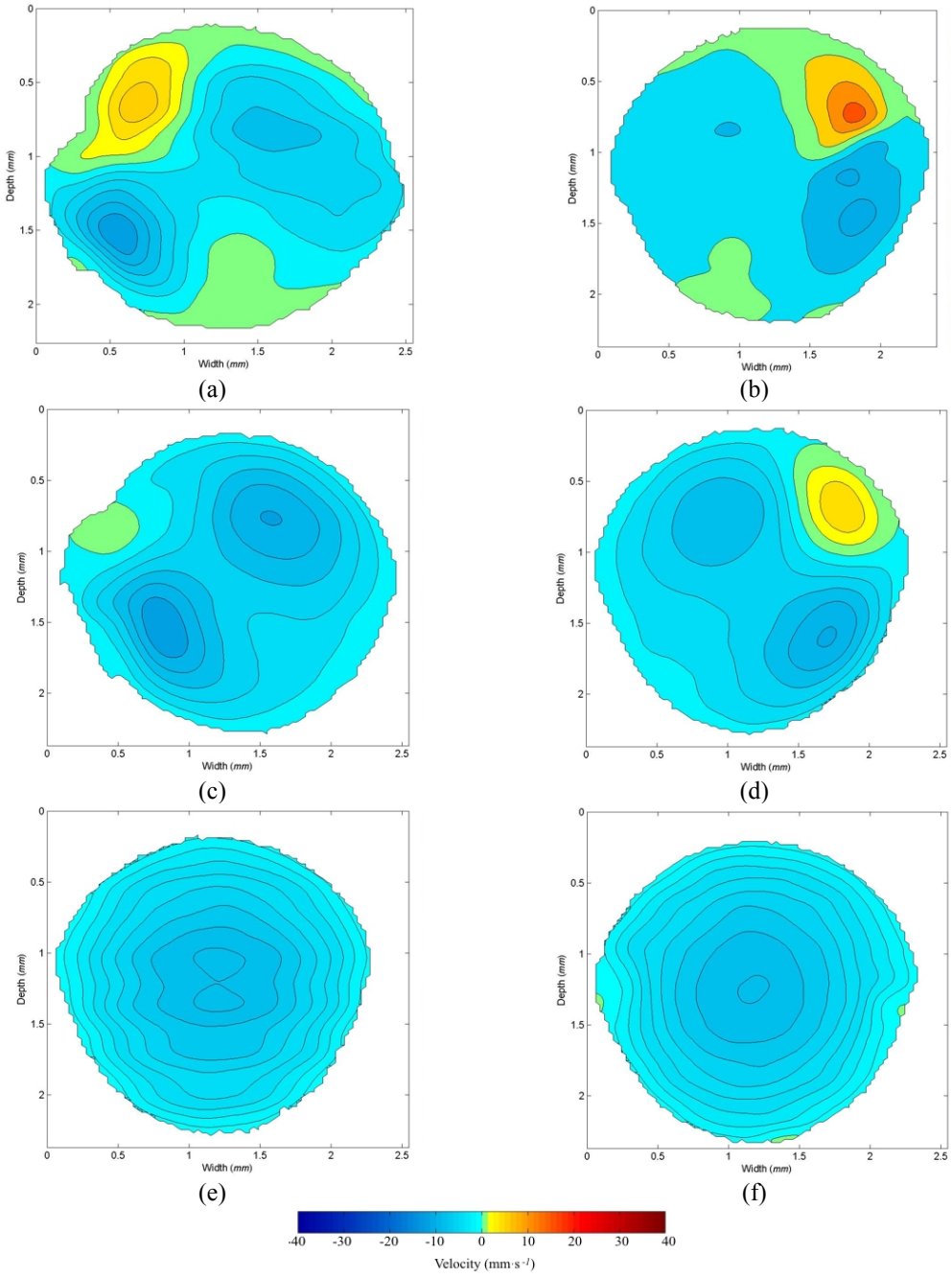

Figure 5.20 – *Cross-sectional flow velocity mapping from the Y-shaped phantom as illustrated in Figure 5.18, with no stent deployed inside the vessel. (a) Outlet arm right just after the junction, (c) after 5* mm *off the junction (e) and after 20* mm *off the junction respectively. (b) Outlet arm left just after the junction, (d) after 5* mm *off the junction (f) and after 20* mm *off the junction respectively. For both arms, it is well recognizable the presence of turbulent regime in areas close to the junction (a and b for right and left arm respectively), which tent to attenuate while moving apart from the junction (c and d for right and left arm respectively), to finally restore the laminar regime at about 20* mm *off the junction (e and f for right and left arm respectively).*

Figures 5.21, 5.22, 5.23 and 5.24 show the results acquired from the same sample with the stent deployed at the junction. The figures report cross-sectional flow velocity mapping in the left column and the associated structural OCT image on the right column, to ease the comparison of flow dynamic mapping with the position of the metallic grid composing the stent. The shadowed areas in the structural images are due to the fact that the probing radiation cannot pass through the metal of the stent. This fact must be taken into account when analyzing the flow images, which appears to show the rising of turbulences in the shadowed areas. From observing Figure 5.21a, which represents a cross-sectional tomography acquired just after the entrance of the stent, one could erroneously interpret the flow regime as turbulent, due to a substantial difference in the typical flow distribution pattern as expected in laminar regime (see for example Figure 5.12 and Figure 5.20e and f). A vertical stripe of random velocities distributed around zero appears in the flow velocity pattern (see Figure 5.21a), coincident with the shadowed area in the structural image (see Figure 5.21b). Ideally, no signal should be detected in this area of the sample, due to the fact that the probing radiation is blocked by the presence of the metallic grid of the stent. The detected Doppler shift may be originated from the detection of multiple scattered photons – and not from the ballistic ones – which can carry altered flow velocity information associated to a different position in the sample in respect the one plotted in the cross-sectional mapping. Measurement of flow dynamic occurring within the lumen of the stent revealed a regime similar to the one measured in absence of the stent, except in the areas localized around the position of the metallic grid of the stent, where some turbulence was observed. Of particular interest was the mapping of the flow dynamic developed in the *left* outlet arm, *i.e.* the outlet arm free from the stent, to monitor the possible increase of turbulence or flow rate variations due to the presence of the stent. Figures 5.23 and 5.24 illustrate the results from a set of measurements acquired along the left outlet arm, moving apart from the junction. In particular, the results in Figure 5.23c and d were acquired just after the stent; from the images it is recognizable the propagation of the perturbation in the flow.

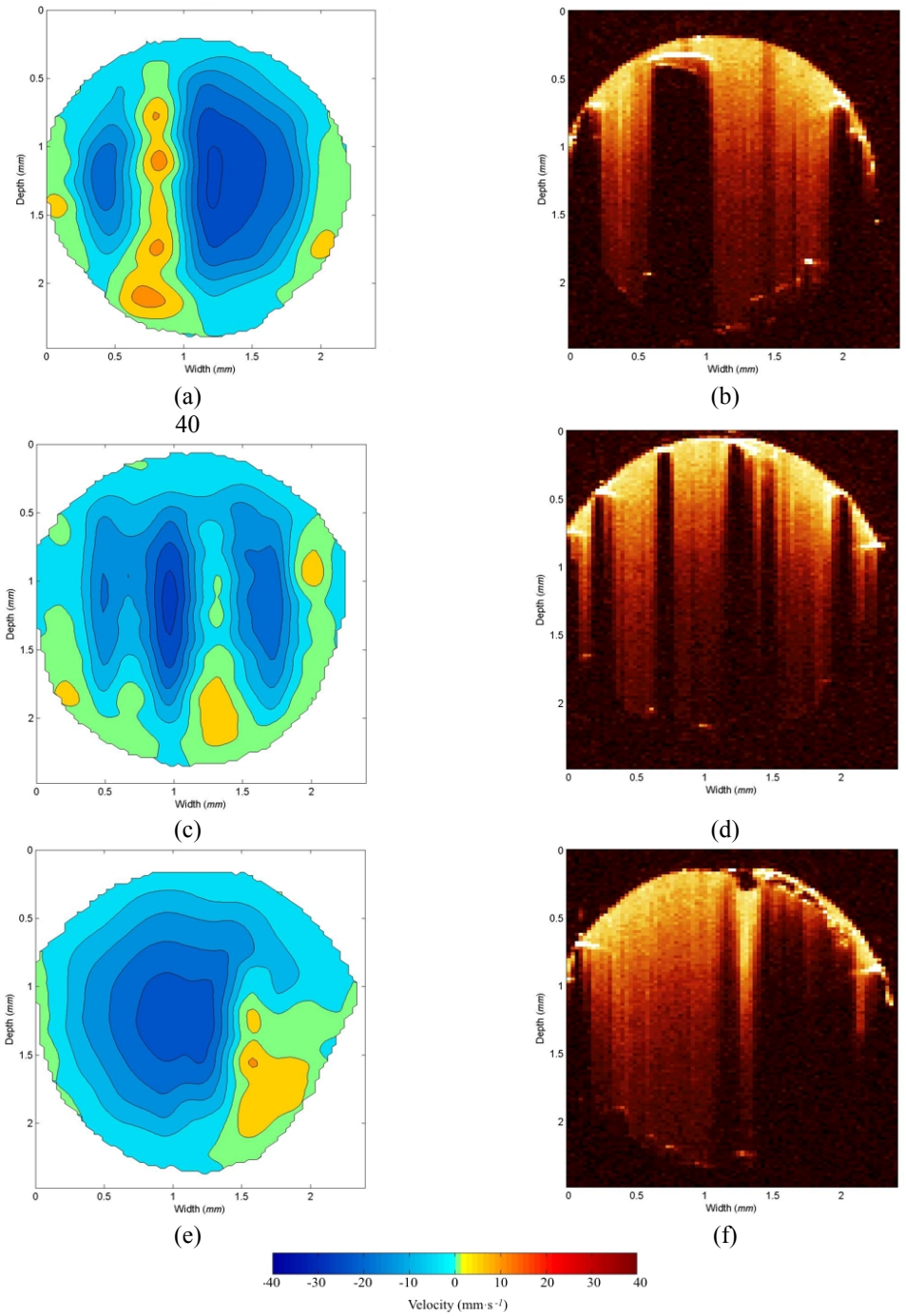

Figure 5.21 – *Cross-sectional flow velocity mapping from the Y-shaped phantom as illustrated in Figure 5.18, with stent deployed inside the vessel (left column) and associated structural OCT images (right column). (a, b) Inlet arm just after the entrance of the stent, (c, d) at midway between the entrance of the stent and the junction (e, f) and just before the junction. The flow exhibit steady regime. Laminar flow was developed towards the centre of the vessel, with probable disruption of the laminarity in regions around the metallic grid of the stent (see text for details).*

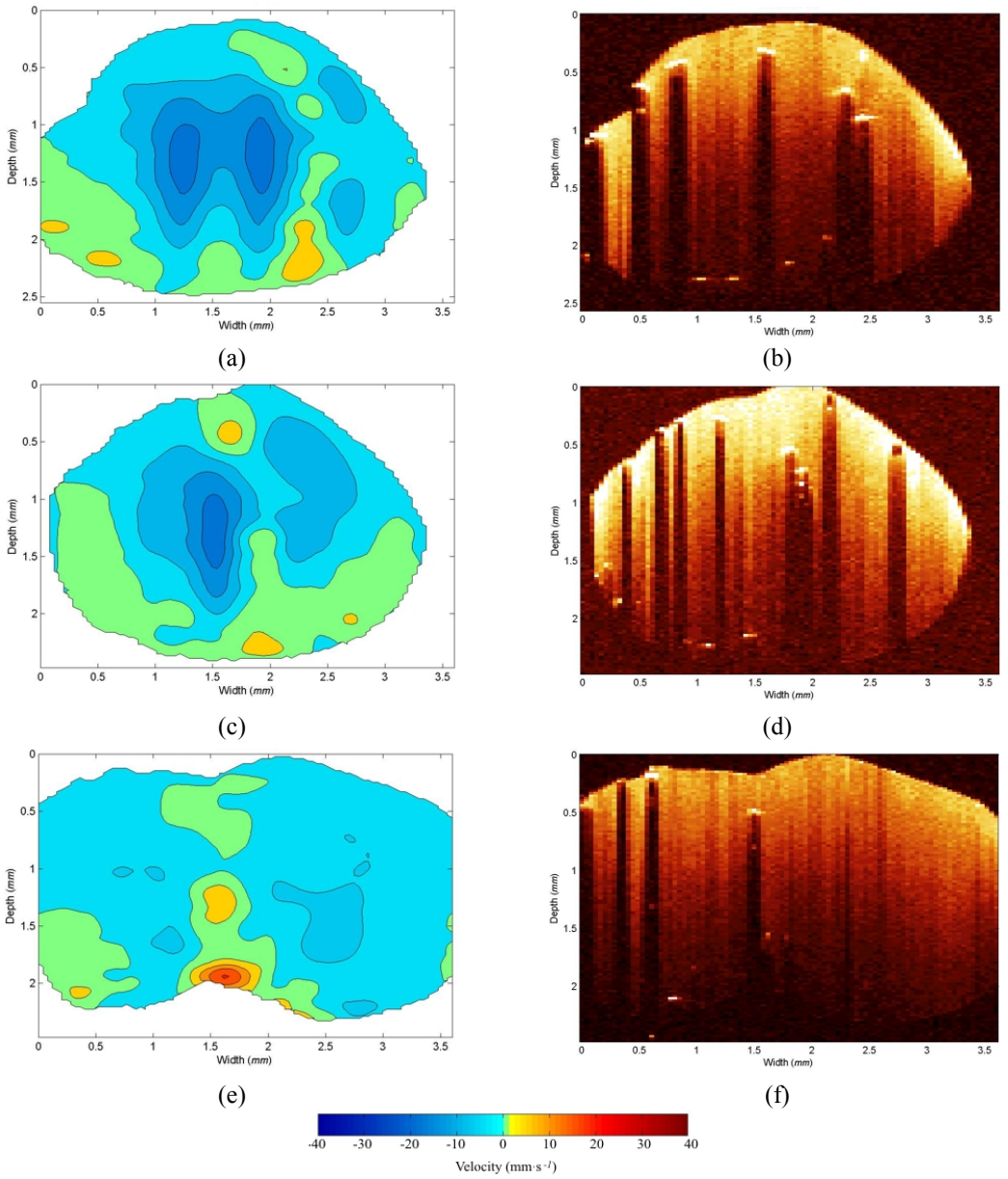

Figure 5.22 – *Cross-sectional flow velocity mapping from the Y-shaped phantom as illustrated in Figure 5.18, with stent deployed inside the vessel (left column) and associated structural OCT images (right column). The measurements were taken at the junction, where the two outlet arms begin to stem. (a, b) Beginning of the bifurcation; (c, d) at the middle of the junction and (e, f) towards the end of the junction. From this set of measurement it can be seen that turbulences tented to develop around the positions of the metallic grid of the stent, as can be evinced by comparison of flow mapping images with the associated structural image.*

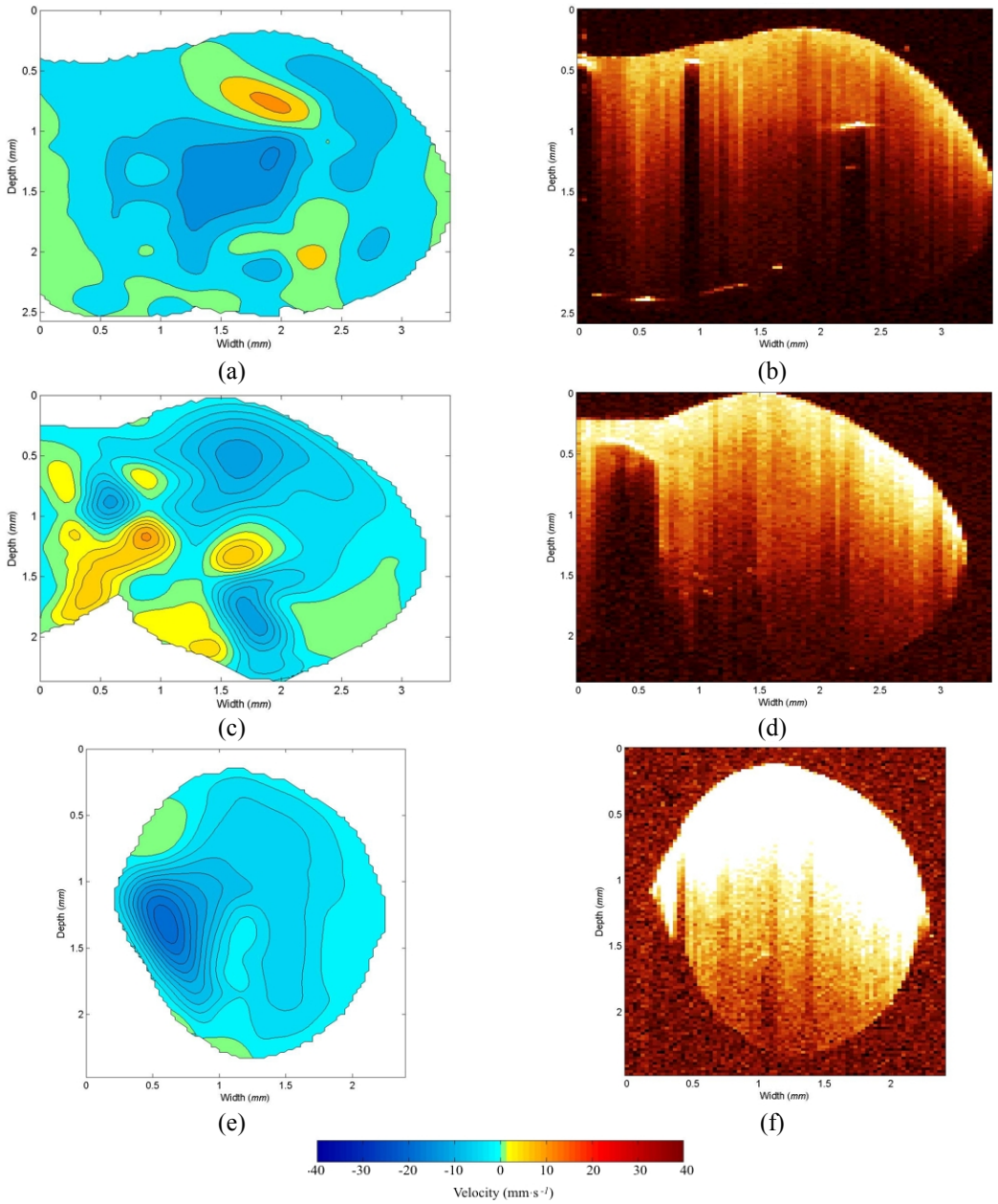

Figure 5.23 – *Cross-sectional flow velocity mapping from the Y-shaped phantom as illustrated in Figure 5.18, with stent deployed inside the vessel (left column) and associated structural OCT images (right column). The measurements were taken at the junction, where the two outlet arms begin to stem. (a, b) At the junction, where the right arm stem from the junction. (c, d) at the middle of the junction and (d, f) along the right arm, after about 10* mm *off the junction. From this set of measurement it can be seen that turbulences tented to develop around the positions of the metallic grid of the stent, as can be evinced by comparison of flow mapping images with the associated structural image.*

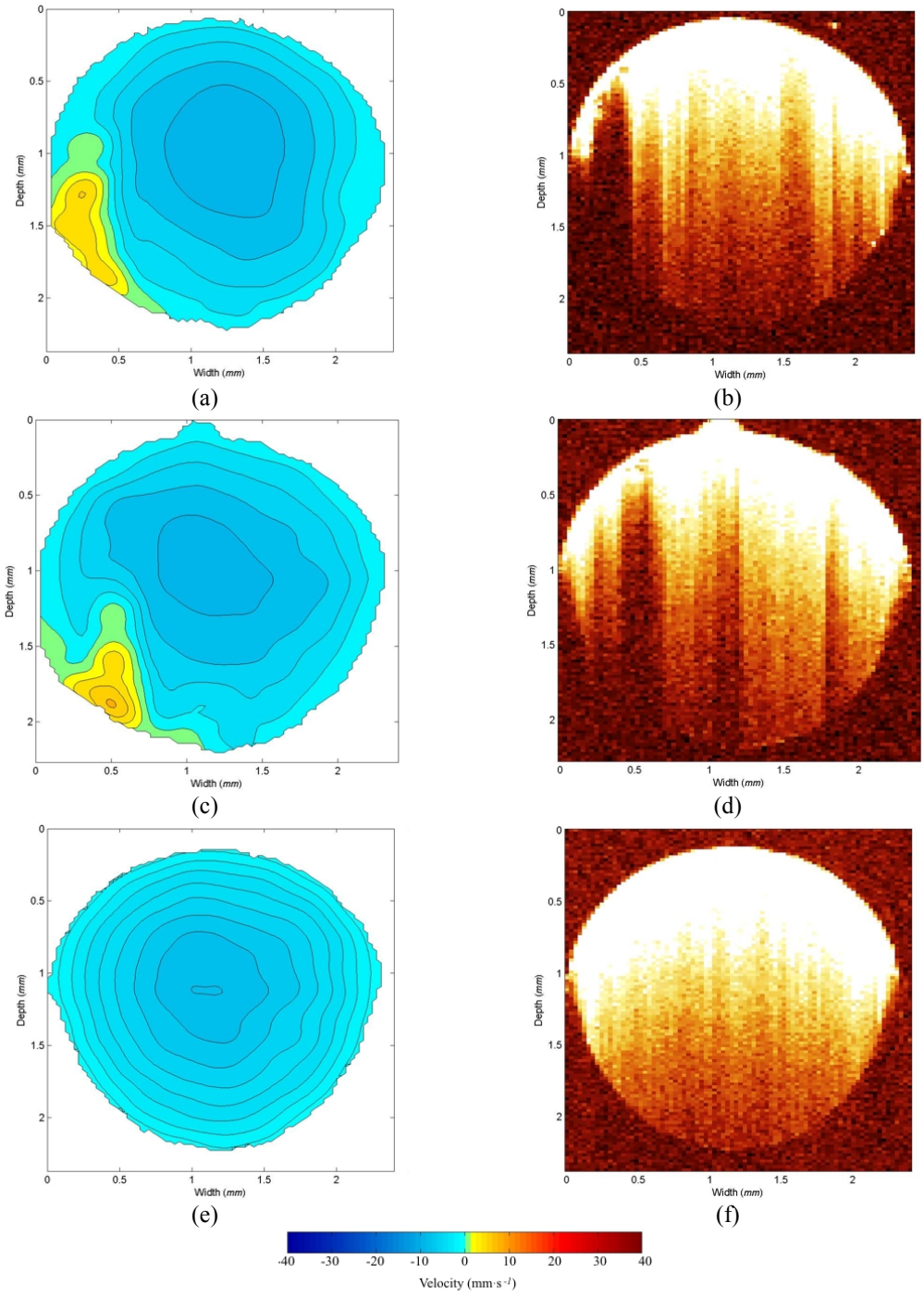

Figure 5.24 – *Cross-sectional flow velocity mapping from the Y-shaped phantom as illustrated in Figure 5.18, with stent deployed inside the vessel (left column) and associated structural OCT images (right column). The measurements were taken along the right arm (no stent). (a, b) 1 mm past the stent; (c, d) about 5* mm *off the stent and (d, f) 30* mm *off the stent. From this set of measurement it can be seen that laminar regime tented reappeared with channel geometry restoration, as can be evinced by comparison of flow mapping images with the associated structural image.*

As the distance from the junction and the stent increases, the perturbation tend to exhibit common behaviour observed from the stent-free measurements (Figure 5.22e, Figures 5.23a and c), until a fully restoration of laminar regime at about 30 *mm* off the junction (Figure 5.24e).

The last reported set of experiments involves cross-sectional flow dynamic mapping in complex geometry vessel using 11% stock solution of haemoglobin as flowing media. The sample used in the experiments consisted in a Y-shaped vessel with aneurism between outlet arms, as illustrated in Figure 4.14c. The fluid was set in motion by the syringe pump. Four set of measurements were performed for mapping cross-sectional flow velocity distributions using a non-Newtonian fluid. Two inlet volume flow rates were selected on the syringe pump, 3.7 $cc \cdot min^{-1}$ and 5.2 $cc \cdot min^{-1}$ respectively and for each chosen value, two different angles, 80° and 90° respectively, between the propagation of the probing radiation and the flow main stream were imposed. Each set of measurements was composed by three cross-sectional tomographies located at three different positions across the junctions and separated of about 1.5 *mm* from each other. The first position was located at the junction when the outlet branches begun to stem; the middle position was located at the entrance of the aneurysm and the third position was located 1.5 *mm* farther, covering the two outlet arms and the aneurism. For both Figure 5.25 and Figure 5.26, the images in the left column of the figure represent the acquired cross-sectional velocity mapping, whilst the images shown in the right column represent the associated structural OCT image. Figure 5.25 shows the results acquired imposing 3.7 $cc \cdot min^{-1}$ input volume flow rate on the syringe pump. Figures 5.25a, c and d were acquired imposing α = 90°. Figures 5.25g, i and k were acquired imposing α = 80°. Similarly, Figure 5.26 shows the results acquired imposing 5.2 $cc \cdot min^{-1}$ input volume flow rate on the syringe pump. Figures 5.26a, c and d were acquired imposing α = 90°. Figures 5.26g, i and k were acquired imposing α = 80°.

A comparison of the results obtained from the sample kept at the same angle α but with different input flow rates, *i.e.* comparing Figures 5.25a, c and e with Figures 5.25g, j and k and Figures 5.26a, c and e with Figures 5.26g, j and k, shows similar patterns at different magnitudes in the cross-sectional flow velocity mapping for the two velocities

at the entrance of the junction (Figures 5.25a and g and Figures 5.26a and g). More difficult is the interpretation of the results for the other positions, where seems that the turbulence is more developed for lower input volume flow rates (Figures 5.25c and j and Figures 5.26c and j) and where other factors, such as viscous forces within the fluid, may intervene more significantly in the formation of turbulence, rather than the mere sample geometry.

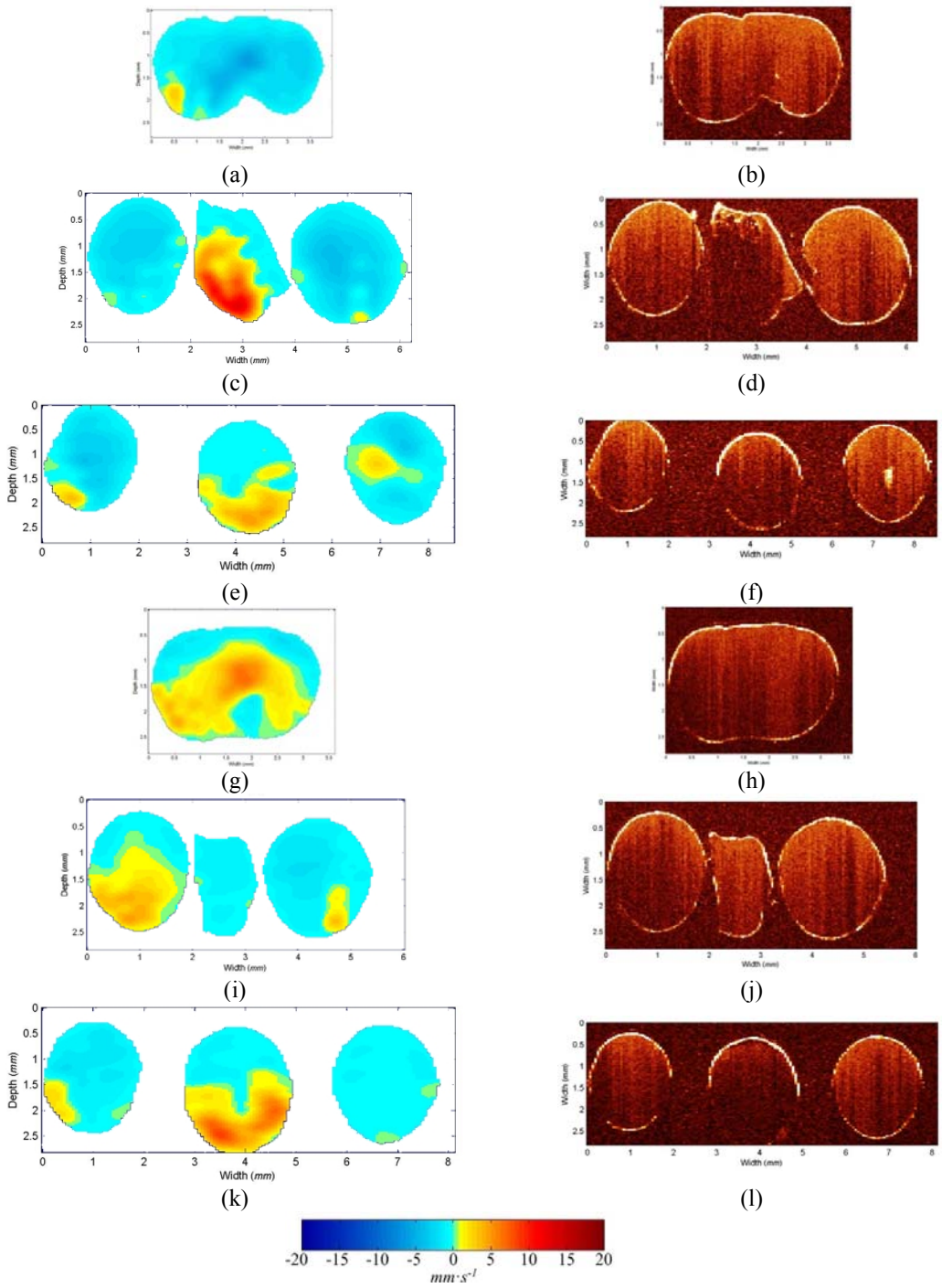

Figure 5.25– *Flow dynamic cross-sectional mapping using 11% stock bovine haemoglobin solution. The sample used in the experiments consisted in a Y-shaped junction with aneurism between outlet arm (see Figure 4.17c).The angle between the probing radiation and the sample was set to* $\alpha = 80°$ *for both* $Q_{in} = 3.7$ cc·min^{-1} *(Figures a, c, e) and* $Q_{in} = 5.2$ cc·min^{-1} *(Figures g, j, k). The images on the left represent the cross-sectional velocity mapping; the images on the right represent the associated structural OCT image.*

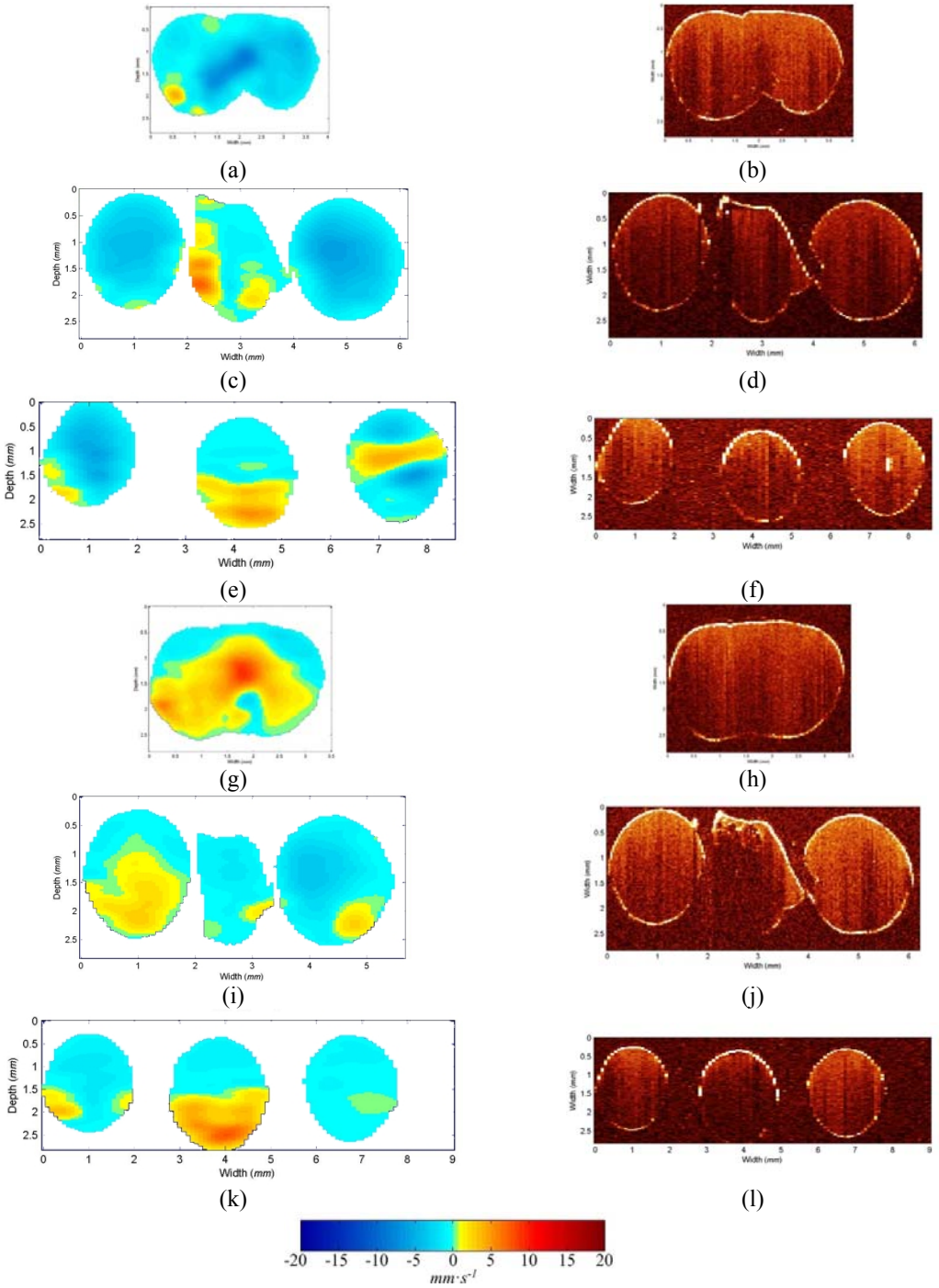

Figure 5.26 – *Flow dynamic cross-sectional mapping using 11% stock bovine haemoglobin solution. The sample used in the experiments consisted in a Y-shaped junction with aneurism between outlet arm (see Figure 4.17c).The angle between the probing radiation and the sample was set to* $\alpha = 90°$ *for both* $Q_{in} = 5.2$ cc·min^{-1} *(Figures a, c, e) and* $Q_{in} = 5.2$ cc·min^{-1} *(Figures g, j, k). The images on the left represent the cross-sectional velocity mapping; the images on the right represent the associated structural OCT image.*

5.4.2. Application for skin tissues measurements in vivo

The time domain OCT system and RSDL described in paragraph 4.6 was applied for imaging skin blood vessel at the depth of about 1.5–1.7 *mm*. The reticular dermis blood vessel forming a Y-shaped junction was visualized with the increased probing depth of ~1.5 *mm*. Figure 5.27 demonstrates the images of a human finger tip using 1.3 μm SLD and 1.5 μm SLD. The achieved probing depth for 1.5 μm SLD was approximately half of the probing depth obtained for 1.3 μm SLD. Therefore, all further results were obtained for the 1.3 μm SLD. Figure 5.27a shows the OCT image of superficial vein in human finger where the vein was barely seen by the naked eye. The frequency of the reference arm scanner was set to 80 *Hz*. Further increase of the scanning frequency degraded the image quality of the deeper layers. Beyond 100 *Hz* only upper layers of the skin could have been seen even when the carrier frequency was kept within the range of the bandpass filter.

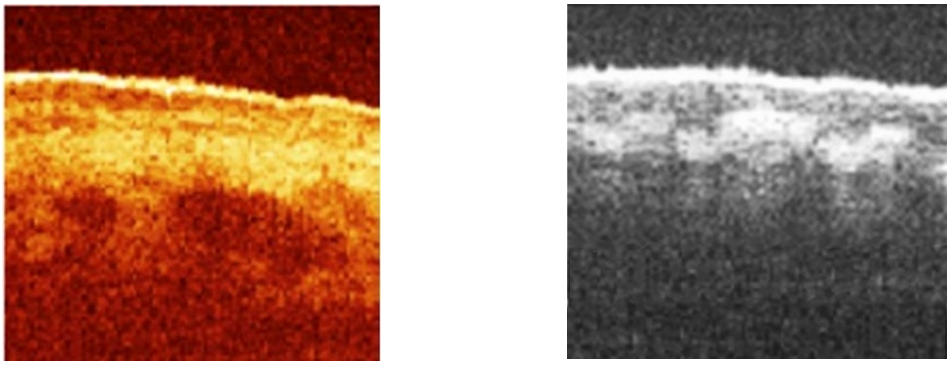

(a) (b)

Figure 5.27. – In vivo *subcutaneous blood vessels of a human finger taken close to Y-junction: (a) 1.3* µm *SLD, (b) 1.5* µm *SLD. Size of the image is 2×2* mm.

To increase the spatial resolution and the depth of imaging, glycerol as an optical clearing agent (Bashkatov *et al.* 2000) was topically administered onto the skin. Figure 5.31b shows the image of the blood vessel after 15 *min* from topical application of the optical clearing agent. To reduce system noise, averaging over 2 to 4 consecutive A-scans was performed. In this case, the scanner moved 2 to 4 times slower, corresponding an averaging over 2 to 4 lines. In addition a 0.1–0.3 *mm* pivoting point offset of the SM was introduced to perform movement of the beam across each pixel of

the image. The raster averaging increased the acquisition time proportionally up to 2–3 *s* but additionally improved SNR by 4–8 *dB*. This approach reduced speckle noise, increased contrast and allowed visualization of deeper layers of the skin (Figure 5.28c). It was also possible to detect a distinctive structural signal backscattered from blood. It appeared inside the blood vessel only after one minute of hand exercise (Figure 5.28b and c, arrows). Separated analysis of A-scans on this area confirmed the presence of the distinctive structural signal arising from within the blood vessel. The achieved RA phase stability between consecutive A-scans was about 10–20%. Therefore it was not possible to detect a reliable phase shift between consecutive interferograms and extract velocity information of the blood flow for the shown vessel. Nevertheless, the intensity signal of a structural image from faster moving particles becomes stronger due to more scattering events over probe volume for the chosen detection time.

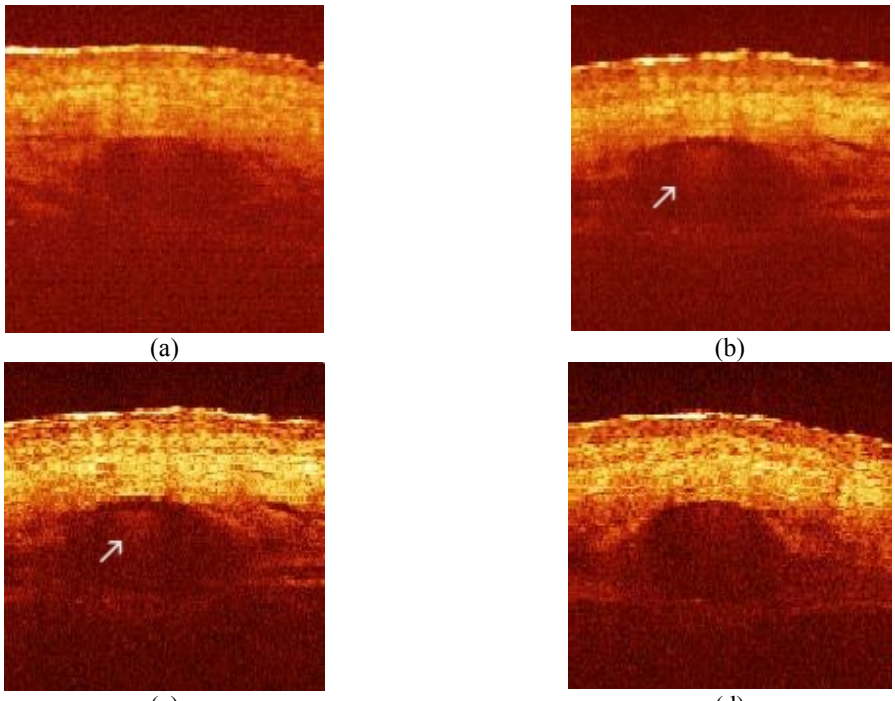

Figure 5.28 – *OCT images of superficial blood vessel of a human finger* in vivo*. (a) Normal conditions; (b) 15* min *after application of the optical clearing liquid; (c) averaging over 4 consecutive A-scans; (d) averaging and 20* min *after application of the optical clearing liquid. The arrow in (b) and (c) point to the distinctive structural signal detected from the blood flow. Size of the images is 2×2* mm*.*

Figure 5.28d shows the same vessel after 20 *min* from the beginning of the application of the optical clearing. The upper surface structures are less distinguishable, although

the structures at the depths of about 1.5–1.7 *mm* are better resolved. The shape of the vessel appears to be more rounded as a consequence of the fact that the clearing liquid penetrates into the tissue but not into the vessel. Since it was impossible to operate a conventional biopsy from the *in vivo* tissue, further investigation is needed to understand this important phenomenon. We suggest two possible explanations for the (apparent) swelling of the tissue in the OCT images: a) mechanical swelling of the tissue due to the penetration of the optical clearing agent; b) a change in the refractive index of the tissue around the lumen of the vessel, which appears like an apparent modification of tissue morphology in the OCT images. Applying different optical clearing agents makes it possible to acquire OCT images with different altered refractive index of the tissue. The analysis of the acquired OCT images may help to determine which effect is predominant. Separate A-scan calculations revealed that the upper layers were resolved with the accuracy of about 12–15 μm, which corresponds to the axial resolution L_{ax}. The deeper layers were resolved with the maximum resolution of 30–50 μm. We believe that this is due to multiply scattered photons, which are still coherent to the reference signal (Kuz'min *et al.* 2005) and are detected from the structures deeper than 0.8–1.0 *mm* (Bizheva *et al.* 1998, Berrocal *et al.* 2005). Since ballistic photons can be discriminated from the diffuse photons at a depth of about 20–25 *MFP* (Bizheva *et al.* 1998) and taking into account the range of optical properties of skin tissues (Douven and Lucassen 2000, Jaques 1996), it seems reasonable to assume that further increase of coherence probing depth up to about 2–2.5 *mm* can be achieved without excessively compromising the lateral and axial resolution.

5.5 Porous scaffolds for tissue engineering

Tissue engineering, rapidly developing branch of bioscience, is widely adopted for the purposes of the tissue growing using the substrate materials. Three-dimensional porous scaffolds possess a great opportunity for the directional growth of the cells and for the supplying them with nutrients. However, the complex porous structure of the scaffolds creates difficulties for the measurements and control of nutrient flow. Along with the rapid development of tissue engineering, seen in the last decade, the progress of the

associated techniques including active use of the new imaging and diagnostic methods is observed (Minuth *et al.* 2006). Tissue engineering involves the use of cells to regenerate the damaged tissues, leaving natural substances to restore organ activities (Langer and Vacanti 1993). Substrate materials are essentially important for the cells to maintain their tissue-specific functions (Temenoff *et al.* 2000). These substrates, so called scaffolds (Mikos and Temenoff 2000), usually serve at least one of the following: (i) allow cell attachment and migration; (ii) deliver and retain cells; (iii) enable diffusion of vital cell nutrients and products of metabolism; (iv) exert certain mechanical and biological influences (*e.g.* flow induced shear stress) to modify the speed of the cell life cycle. To achieve the goal of tissue reconstruction, scaffolds must meet some specific requirements including optimal regime of nutrients flow distribution to enhance cell growth (Lin *et al.* 1997).

The diagnostic systems, applied for the control of flow within the scaffolds, include computational modelling techniques, *e.g.* Michaelis-Menton kinetics for characterization of nutrient intakes in scaffolds, Navier-Stokes equations for modelling fluid outside the scaffold (Chung *et al.* 2007), micro-computer tomography (micro-CT) (Cioffi *et al.* 2006) and the experimental approaches, such as conventional microscopy, confocal laser scanning microscopy (CLSM) (Pawley 2006) and since recently, optical coherence tomography (Bagnaninchi *et al.* 2007). Conventional microscopy, such as upright microscopy, has been applied to describe the perfusion flow in bioreactors in situ (Stephens *et al.* 2007). CLSM is often used for the purposes of imaging of tissue, *e.g.* 3D microstructure of hydroxyapatite bone scaffold specimens (Ren *et al.* 2005) with maximum scanning depth of about 100 μm and spatial resolution of about 1 μm. The main disadvantage of these techniques lies in the difficulty of quantitative measurements of fluid flow dynamic due to the multiple scattering (Hunag *et al.* 1991, Fercher *et al.* 2003).

Conventional OCT provides cross-sectional images of tissue structure (Gelikonov and Gelikonov 2006, Larin *et al.* 2007). Major advantage of this technique is the great potential opportunity for visualizing the tissues morphology with relatively high probing depth (up to 2 *mm*) and spatial resolution (in a range of 2-15 μm) (Huang *et al.*

1991, Schmitt 1999). It was shown that OCT with the combination of optical clearing provided images of internal structures of tissue with higher resolution (Proskurin and Meglinski 2007).

DOCT allows measuring fluid flow velocity at discrete spatial locations and monitoring the turbulence and laminar multidimensional velocity profiles in complex micro-channels (Bonesi *et al.* 2007a, Bonesi *et al.* 2007b).

The DOCT system was employed to obtain conventional OCT imaging of the scaffold structure and DOCT imaging to investigate the feasibility of mapping spatial fluid flow velocity distribution within the complex scaffold structure. The scaffold used in the study was constructed from polysaccharidic material, called *chitosan* (Bagnaninchi *et al.* 2007). 2% chitosan solution was prepared by dissolving chitosan flakes (95% deacytalated, Sigma-Aldrich, UK) in 1% v/v glacial acetic acid. The resulting solution was cast in several moulds (1.5 *mm* inner diameter) which were frozen overnight and subsequently freeze dried. The resulting scaffold was rehydrated in a gradient of ethanol (100%, 70% and 50%) and stored in PBS solution. 1% of stock solution of intralipid was used as modelling fluid. Intralipid was set in motion by a syringe pump (Harward, mod.975) allowing constant input volume flow rate under laminar regime. The average inlet flow velocity was about 16.1 $mm \cdot s^{-1}$. Figure 5.29 shows the cross-sectional structural images of the scaffold acquired with the DOCT system.

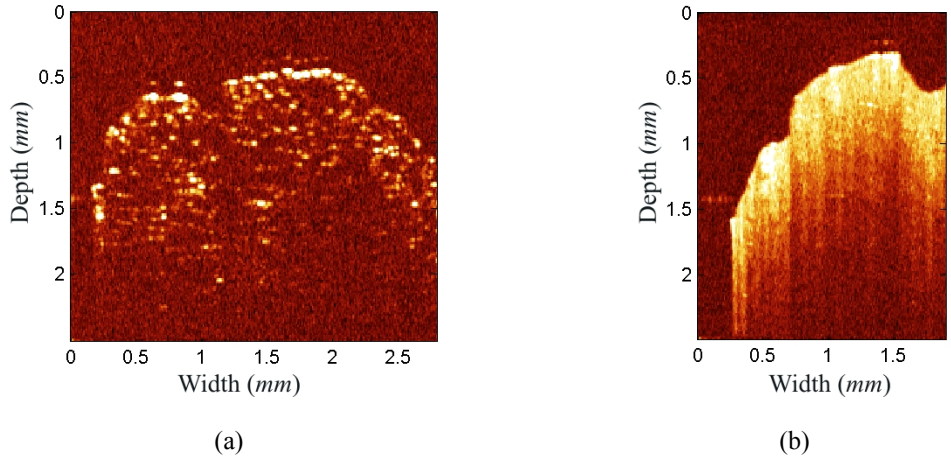

Figure 5.29 – *OCT imaging of the scaffold structure. (a) Scaffold wet with distilled water. (b) Scaffold wet with 1% stock solution of intralipid.*

Figure 5.29a illustrates the scaffold wetted with distilled water. From the image the porous structure can be recognizable. Figure 5.29b illustrates the same scaffold wet with 1% stock solution of intralipid. In this case the structural information of the porous structure of the scaffold is lost in the OCT imaging, probably due to the fact that the refractive index of the stock solution of intralipid is similar to the one of the material composing the scaffold.

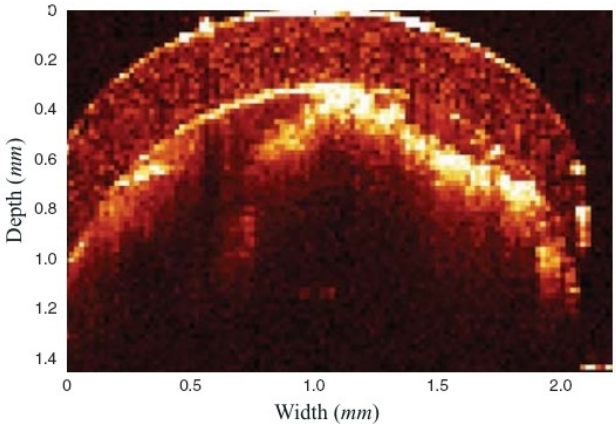

Figure 5.30 – *Image of the internal structure of scaffold embedded in plastic tube.*

Figure 5.30 illustrates a structural image of the scaffold embedded in the plastic tube used for the flow dynamic experiments. The main peculiarities of the internal structure are clearly seen, however the porous nature of the sample is unclear.

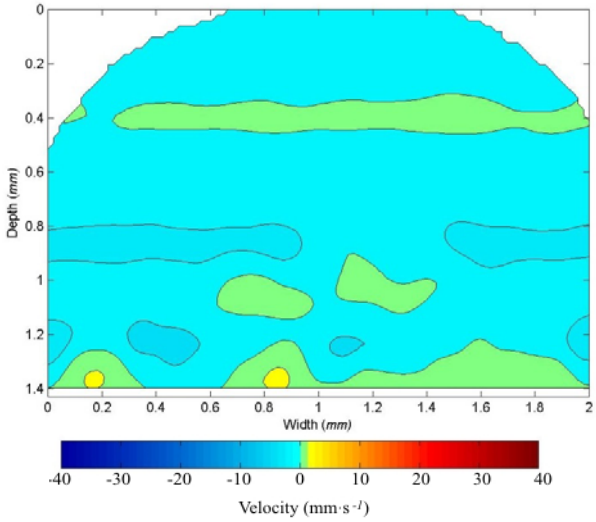

Figure 5.31 – *Cross-sectional flow velocity distribution of non-filtered 1% stock solution of intralipid through the scaffold. The averaged input flow rate was 16.17* $mm \cdot s^{-1}$.

Figure 5.29a illustrates the scaffold wetted with distilled water. From the image the porous structure can be recognizable. Figure 5.29b illustrates the same scaffold wet with 1% stock solution of intralipid. In this case the structural information of the porous structure of the scaffold is lost in the OCT imaging, probably due to the fact that the refractive index of the stock solution of intralipid is similar to the one of the material composing the scaffold.

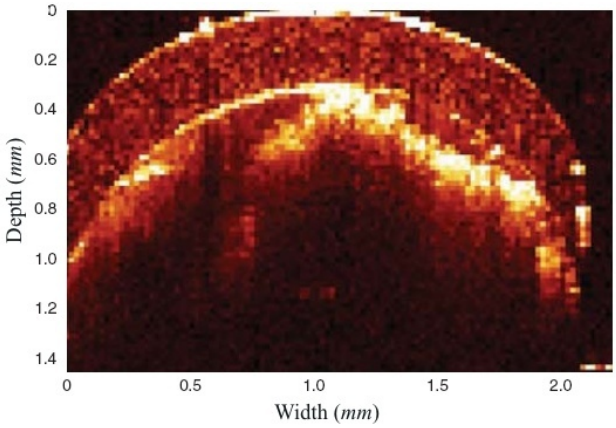

Figure 5.30 – *Image of the internal structure of scaffold embedded in plastic tube.*

Figure 5.30 illustrates a structural image of the scaffold embedded in the plastic tube used for the flow dynamic experiments. The main peculiarities of the internal structure are clearly seen, however the porous nature of the sample is unclear.

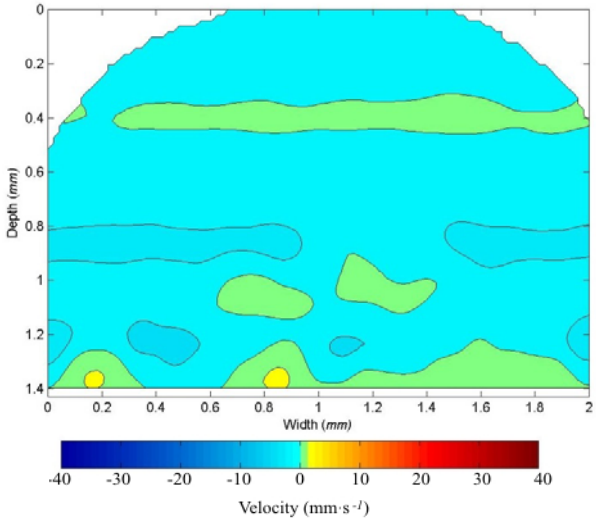

Figure 5.31 – *Cross-sectional flow velocity distribution of non-filtered 1% stock solution of intralipid through the scaffold. The averaged input flow rate was 16.17* $mm \cdot s^{-1}$.

Figure 5.31 demonstrates the flow velocity distribution within the scaffold obtained with DOCT. The results of DOCT measurements shows that some fluctuations of velocity are observed, but the average velocity tends to zero, *i.e.* there is no flow present through the scaffold structure. The possibility that large lipid particles in the solution could obstruct the pores within the scaffold was investigated using scanning electron microscope (ISI ABT-55) to evaluate the actual pores size, as the OCT didn't allow estimating the diameter of pores. The electron micrograph of the scaffold is presented in Figure 5.32.

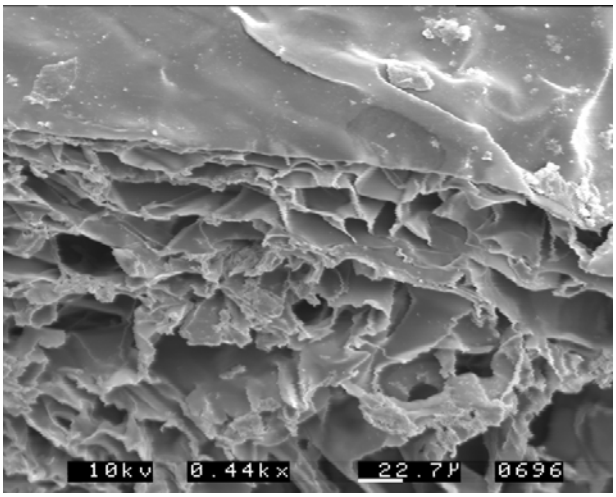

Figure 5.32 – *Microstructure of scaffold obtained with ISI ABT-55 low-vacuum scanning electron microscope.*

The average size of the pores appeared to be in a range of 20 to 40 μm with the effective diameter of about 30 μm. The 1% stock solution of intralipid was then filtered with filter paper to avoid presence of the large lipid particles that could block the flow through the pores. The flow dynamic experiment was further repeated using the filtered stock solution of intralipid. The obtained results, illustrated in Figure 5.33, demonstrate distinctive differences in the velocity distribution in comparison with the results of non-filtered stock solution of intralipid reported in Figure 5.31. It is seen that the distribution of the flow of filtered intralipid solution is not uniform and there are areas with higher velocity (up to 5 $mm \cdot s^{-1}$), compared to the overall background velocity.

Figure 5.33b shows the structural image overlapped with the representation of the cross-sectional flow velocity distribution. Thus, these results make it possible to evaluate the

shear stress within the scaffold in a particular area and optimize input flow rate consequently.

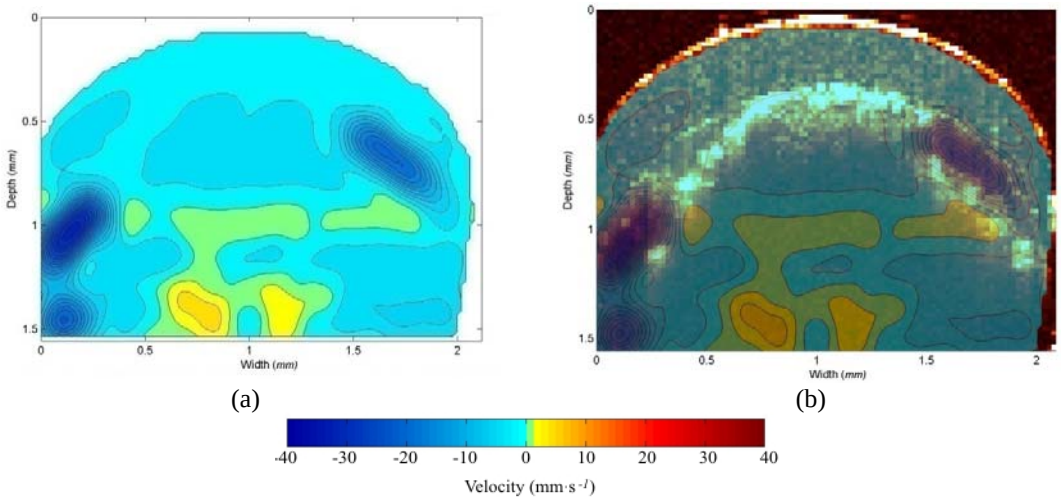

Figure 5.33 – *Cross-sectional flow velocity distribution of filtered 1% stock solution of intralipid. (a) Flow velocity mapping and (b) flow velocity mapping overlapped to the associated structural OCT image.*

5.7 Summary

A synthesis of the media and results obtained from the developed DOCT system has been reported. Optical properties of stock solutions of intralipid in distilled water at different concentrations were investigated using DOCT to determine the most suitable values to be used in the flow dynamic experiments. Optical properties of bovine haemoglobin were also investigated using the DOCT system.

The DOCT system was used for mapping flow dynamic in complex geometry vessels using Newtonian (stock solution of intralipid) and non-Newtonian (stock solution of haemoglobin) fluids. Results obtained applying the DOCT system to the developed artificial vessels consisted in Y-shaped, T-shaped, vessel with aneurism and Y-shaped with deployed stent at the junction were illustrated.

The transition from laminar to turbulent flow velocity profiles in the Y-shaped vessels with complex geometry was examined. The results clearly show laminar flows in the inlet and outlet arms at the distance of approximately 20 *mm* from the junction. We

observed the turbulence formation and the transition from laminar to turbulent behaviour of flow in the region close to the junction.

The DOCT system was extended to *in vivo* imaging of the subcutaneous human skin tissues and blood vessels. The system enabled *in vivo* DOCT imaging for two wavelengths 1.3 μm and 1.5 μm. The transcutaneous probing depth for 1.3 μm SLD was twice as much as the probing depth for 1.5 μm SLD. Using 1.3 μm SLD and topical application of optical clearing agent, enhanced OCT imaging at probing depth up to 1.5–1.7 *mm* was achieved. That allowed resolving deeper tissue structures and obtaining images of subcutaneous blood vessels (~0.2–1 *mm* in diameter) generally not detectable by conventional OCT imaging *in vivo*. The reduction of speckle noise by using optical clearing osmotic agents increased image contrast and spatial resolution and allowed visualization of deeper layers of the skin. We detected a distinctive structural signal backscattered from the blood vessels that was not previously observed by OCT. However, due to low phase stability (10–20%) of adjacent A-scans for the *in vivo* measurements, DOCT computation was not applicable in our case and it was not possible to extract the velocity information of the blood flow. However, the promising results of mapping subcutaneous blood vessel *in vivo*, in conjunction with the results obtained from the phantoms, may open the path to further investigation to achieve subcutaneous complex blood flow dynamic measurements *in vivo*, as it may be required by port wine stains blood flow investigations. Furthermore, the developed DOCT system, when used in combination with optical clearing techniques, can be also useful in evaluation of penetration depth and testing the efficiency of health care and cosmetic products entrance within the superficial skin tissue.

OCT and DOCT imaging was also applied to obtain images of the internal structure of scaffolds used in tissue engineering. DOCT was applied to feasibility studies for monitoring flow velocity distributions within the scaffold structure. The average pore diameter within the scaffolds was estimated using electron microscopy. It was demonstrated that DOCT can be potentially used to monitor the complex micro-flow and for estimation of shear stress within the scaffold. DOCT approach, coupled with computational modelling methods (Cioffi *et al.* 2006) can improve and provide new

scaffold design criteria, optimize transport of nutrients and other substance of interest to and from the cells and potentially enhance the tissue growth.

Chapter 6

Conclusions and Future Work

In this thesis, the flow dynamic in complex geometry vessel has been comprehensively investigated by means of non-contact, non-invasive, high-resolution optical technique known as Doppler optical coherence tomography. Flow dynamic measurements of complex flow are a challenging problem that can be approached with a number of solutions, each of which is applicable under different conditions to varying degree of accuracy. The use of mathematical models to simulate real situations can be very difficult to apply, *e.g.* due to the intrinsic difficulty of accurately describe the flow using the Navier-Stock equations in closed form, or very demanding in terms of computational time. Other detection techniques, such as Doppler ultrasounds, may not offer sufficient resolution for mapping flow dynamics in small vessels. To overcome some of the limitations of other existing techniques and to enable non-invasive, high-resolution flow dynamic mapping in small vessels, a DOCT system has been developed in the laboratories of Cranfield Health at Cranfield Unviersity, UK. The system was built from standard optical and electronic components and also included some custom developed electronic circuitery for signal detection and conditioning. The performances of the assembled system meet the criteria for mapping of complex flow dynamic in small vessels

The built DOCT system was used to image high-resolution ($10\times10\times10\ \mu m^3$), one-dimensional and multi-dimensional flow velocity distributions profiles in complex geometry vessels. T-shaped, Y-shaped phantoms and phantoms with aneurism were custom built to study the interaction of the flow dynamics with different channel geometries and to map the related velocity profiles at several inlet volume flow rates. Under constant boundary conditions, *i.e.* channel geometry and inlet flow rate, even using phantoms with very high irregularities in the walls geometry – as could be a human vessel – the flow revealed to be steady and non-uniform, and repeatable cross-sectional velocity profiles were acquired. Different velocity profiles were recorded in different sample positions in reproducible measures. Parabolic profiles at the entrance and exits of the samples were acquired, indicating a steady laminar regime. A variety of different velocity profiles, such as blunted, triangular or “S” shaped where also measured at the junction or in regions of the sample where the channel geometry was

irregular and/or complex. The observed shapes of the velocity profiles acquired in these areas indicated that the flow regime was steady but no longer laminar.

The study of the mutual effect and interactions of the blood flow with the surrounding vessel geometry is of great interest in biorheology and cardiology. In particular, DOCT technique could become a valid support for cardiologists as a means of simultaneous imaging of the vessel morphology and related blood flow velocity distribution, from which the shear stress acting on vessel walls can be computed. To achieve farther investigation of blood flow in human sub-cutaneous blood vessels, the original developed DOCT system was improved by implementing a RSDL in the reference arm. The extended system was used in combination with optical clearing techniques to access OCT imaging of human palm blood vessels *in vivo*.

In addition, beyond the main scope of the thesis, a number of engineering tasks were solved, including design and realization of the phantoms used in the experiments and the DOCT electronic circuitry for signal detection and conditioning and the development of the Matlab code for data analysis. During the Ph.D. activity it has also been designed and developed a PS-OCT system for investigations in tissue engineering. The system implemented custom designed electronic circuitry based on programmable microcontrollers technology to perform data acquisition with different polarization states of the probing radiation.

The real advantage of DOCT is its ability to perform non-invasive detection and measurement of flow velocity profiles of moving elements in turbid media. The technique has a great potential for use in the clinical management of patients who can benefit from micro-vascular monitoring. Information provided by DOCT could be used to detect and diagnose atherosclerotic diseases; to monitor perfusion and viability before, during and after reconstructive procedures; in the studies of the effects of blood flow dynamic in the artificial vessels and junctions resulted from a by-pass operation or to screen human skin blood flow *in vivo*. Real-time DOCT imaging can monitor the transient flow behaviour in human blood vessels due to the heartbeat and the non-Newtonian flow effects, with particular attention on the dependency of the blood viscosity on the local shear rate. Moreover, most of the cardiovascular studies rely on

the computational fluid dynamics (CFD) results to determine the role and importance of that blood flow factors that could be involved in the genesis of cardiovascular diseases. DOCT, a tool capable of directly imaging the real physical situation, can assist CFD to significantly improve the quality of new therapeutic strategies or of already established interventional methods, as for example stent design and placement.

In order to obtain a qualitative and quantitative evaluation of the dynamics of the fluid in micro channels, further studies and system developments are necessary. For example, the development of a multi-beam probe can ease the instant detection of the whole 3D flow velocity vectorial field along the measured cross-section. Increasing the speed of image acquisition would allow a more detailed characterization of pulsed flow in complex vessels such as the blood flow circulation in human vessels. The possibility to access three-dimensional reconstructions of the vessel morphology and related flow velocity distribution close to the vessel walls can provide a detailed reconstruction of the associated shear stress and consequently aid the localization of low and high shear rate regions.

To sum up, given the non-invasive nature of the measurement, high spatial resolution, simple hardware requirement and relatively compact size of the system, Doppler optical coherence tomography reveals itself as a potentially effective technique applicable in all fields where micro fluidic measurements are involved, with applications not only in biomedicine, but also in other areas where non-contact, non-invasive, high-resolution velocity mapping of moving constituents are of interest.

The presented work in this thesis has been made possible also because of partial contribution from BBSRC (project no. BBS/B/04242), EPSRC (project GR/S77370/01) and Royal Society (grant IJP-2004/R3EU).

List of publications

Journals – refereed

[1] Ugryumova N, Jacobs J, **Bonesi M** and Matcher S J 2008 Novel optical imaging technique to determine the 3D orientation of collagen fibers in cartilage: variable-incidence-angle polarization-sensitive optical coherence tomography, *Osteoarthritis and Cartilage* // (in press).

[2] **Bonesi M**, Proskurin S G, Churmakov D Y and Meglinski I V 2008 Imaging of subcutaneous blood vessels and flow velocity profiles by Optical Coherence Tomography techniques, *IOP JAP* **00**(00) 000-000 // submitted.

[3] Veksler B, Kobzev E, **Bonesi M** and Meglinski I V, 2008 Application of Doppler Optical Coherence Tomography for imaging of scaffold structure and local micro-flow characterization *Laser Phys. Lett.* **5**(3) 236-239.

[4] **Bonesi M**, Churmakov D Y and Meglinski I V 2007 Study of flow dynamics in complex vessels by using Doppler Optical Coherence Tomography *Meas. Sci. Technol.* **18**(11) 3279-3286.

[5] **Bonesi M,** Churmakov D Y, Ritchie L J and Meglinski I V 2007 Turbulent flow monitoring with Doppler Optical Coherence Tomography *Laser Phys. Lett.* **4**(4) 304-307.

Conference proceedings

[1] Ugryumova N, **Bonesi M** and Matcher S J 2008 Determination of 3D optic axis orientation in cartilage by Polarization-Sensitive Optical Coherence Tomography, in *Optics in Tissue Engineering and Regenerative Medicine II*, *Proc. SPIE*, Vol. 6858, Art. no. 68580I, pp. I8580-I8580

[2] **Bonesi M**, Churmakov D Y and Meglinski I V 2008 Imaging of flow velocity profiles within the complex geometry vessels by Doppler optical coherence tomography in: *Complex Dynamics and Fluctuations in Biomedical Photonics V*, Edited by V.V. Tuchin and L.V. Wang, *Proc. SPIE*, Vol.6855, paper 6855-12 (2008) // **Invited**

[3] Bagnaninchi P O, Churmakov D Y, **Bonesi M**, Yang Y, Phelan C, Maffulli N, Meglinski I V and El Haj A J 2008 Optical properties of human tendons characterized by PSOCT and their relation to tendinopathy: a clinical study", in: *Optical Interactions with Tissue and Cells XIX*, Edited by S.L. Jacques, W.P. Roach, *Proc. SPIE*, Vol.6854, paper 6854-51.

[4] **Bonesi M** and Meglinski I 2007 Study of flow dynamics in complex vessels using Doppler optical coherence tomography, in *Proc. of OFMC 2007: Europe's Leading Conference for Measurement of Optical Fibres and Optoelectronics*, National Physical Laboratory, Teddington, UK, 131-136 // (ISBN: 0 9780946754496)

Conference presentations

[1] **Bonesi M**, Churmakov D Y and Meglinski I V 2008 Imaging of flow velocity profiles within the complex geometry vessels by Doppler Optical Coherence Tomography, *BiOS 2008*, SPIE, San Jose, California, USA, 19th-24th *Jan.*, 2008 // **Invited**

[2] Bagnaninchi P O, Churmakov D Y, **Bonesi M**, Yang Y, Walley G, Phelan C, Maffulli N, Meglinski I V and El Haj A J 2008 Optical properties of human tendons characterized by PSOCT and their relation to tendinopathy: A clinical study, *BiOS 2008*, SPIE, San Jose, California, USA, 19th-24th *Jan.*, 2008

[3] Ugryumova N, **Bonesi M** and Matcher S J 2008 The three-dimensional orientation of cartilage collagen matrix, *BiOS 2008* at SPIE Photonics West, San Jose, California, USA, 19th-24th *Jan.*, 2008.

[4] **Bonesi M** and Meglinski I 2007 Study of flow dynamics in complex vessels using Doppler optical coherence tomography *OFMC 2007: Europe's Leading Conference for Measurement of Optical Fibres and Optoelectronics*, National Physical Laboratory, Teddington, UK, 15th-17th *Oct.*, 2007.

[5] **Bonesi M**, Proskurin S G and Meglinski I V 2007 Imaging of flow dynamics in complex micro vessels by Doppler Optical Coherence Tomography ALT'07, Advanced Laser Technologies, Levi, Finland, 3rd-7th *Sept.*, 2007.

[6] **Bonesi M** and Meglinski I V 2007 Imaging of flow dynamics in complex micro vessels by Doppler Optical Coherence Tomography, *Business Briefing: The Commercial Opportunities in OCT*, University College London, UK, 21st *Mar.*, 2007

[7] Churmakov D Y, Meglinski I V, **Bonesi M** and Ritchie L J 2006 Monte Carlo model for PS-OCT imaging in turbid birefringent media *Photon'06*, Manchester, UK, 3rd-7th *Sept.*, 2006.

[8] **Bonesi M**, Churmakov D Y, Ritchie J L, Mendel D A and Meglinski I V 2006 Application of Doppler optical coherence technique for fluid dynamic studies *Photon'06*, Manchester, UK, 3rd-7th *Sept.*, 2006.

[9] **Bonesi M**, Ritchie J L and Meglinski I V 2006 Turbulent flow monitoring with Doppler Optical Coherence Tomography, *7-th Postgraduate Research Conference*, Cranfield University, Silsoe, UK, 29th *June*, 2006.

[10] **Bonesi M**, Churmakov D Y, Ritchie J L and Meglinski I V 2006 Polarization-sensitive OCT system development and Monte Carlo modelling for turbid birefringent media, *7-th Postgraduate Research Conference*, Cranfield University, Silsoe, UK, 29th *June*, 2006.

[11] **Bonesi M** 2005 Optical Coherence Tomography technology for cardiovascular applications, *Meeting for OCT in Cardiovascular disease management*, Gloucestershire Royal Hospital, Gloucester, UK, 14th *Nov.* 2005.

[12] **Bonesi M** 2005 Review of OCT UK expertise – Cranfield University, *Mapping of the UK OCT Landscape*, National Physical Laboratory, Teddington, UK, 10th *Nov.* 2005.

[13] **Bonesi M** and Wang R K 2005 Characterization of flow dynamics in vessels bifurcation using Optical Coherence Tomography *OFMC 2005: Europe's Leading Conference for Measurement of Optical Fibres and Optoelectronics*, National Physical Laboratory, Teddington, UK, 21st-23rd *Sept.*, 2005 // **Invited**.

[14] **Bonesi M** 2005 Characterisation of flow dynamics in vessel bifurcation using coherence tomography *The Rank Price Funds, Mini-Symposium on Opto-electronics for use in the diagnostic of cancer*, Grasmere, UK, 20th *June* 2005.

[15] **Bonesi M** and Wang R K 2005 Characterization of flow dynamics in vessels bifurcation using Optical Coherence Tomography 6*th Postgraduate Research Conference*, Cranfield University, Silsoe, UK, 16th *June*, 2005.

References

Alberts B, Johnson A, Lewis J, Raff M, Roberts K and Walter P 2002 *Molecular Biology of the Cell* (New York:Garland Science).

Andreeva T and Durgin W 2002 *Ultrasonic technique in characterization of the grid-generated turbulent flow* 55th APS/DFD Meeting, Dallas, TX, USA.

Angelsky O V and Maksimyak P P 1990 Optical diagnostics of random phase objects *Appl. Opt.* **29** 2894-2898.

Angelsky O V, Maksimyak P P and Hanson S 1999 *The Use of Optical-Correlation Techniques for Characterizing Scattering Object and Media* **PM71** (Bellingham:SPIE press).

Bagnaninchi P O, Churmakov D. Y., Bonesi M., Yang Y, Phelan C., Maffulli N., Meglinski I. V. and El Haj A 2008 Optical properties of human tendons characterized by PSOCT and their relation to tendinopathy: a clinical study *Proc. SPIE* 0277-786X.

Bagnaninchi P O, Yang Y, El Haj A, Hinds M T and Wang R K 2007 Characterization of local fluid flow in 3D porous construct characterized by Fourier domain Doppler optical coherence tomography *Proc. SPIE* **6439** 64390H-1.

Bagnaninchi P O, Yang Y, Maffuli N, Wang R K and El Haj A 2006 Monitoring tissue formation and organization of engineered tendon by optical coherence tomography *Proc. SPIE Int. Soc. Opt. Eng.* **6084**, 608419.

Baker R C 2002 *An Introductiory Guide to Flow Measurement* (John Wiley and Sons)

Bankroft G N, Sikavitsas V I, van den Dolder J, Sheffield T L, Ambrose C G, Jansen J A and Mikos A G 2002 Fluid flow increases mineralized matrix deposition in 3D perfusion culture of marrow stromal osteoblasts in a dose-dependent manner *PNAS* **99**(20) 12600-12605.

Barnes D C and Puttock M J 1953 National physics laboratory interferometer *Engineer* **196** 763-769.

Barton J K, Welch A J and Izatt J A 1998 Investigating pulsed dye laser-blood vessel interaction with color Doppler optical coherence tomography *Opt. Exp.* **3**(6) 251-256.

Barton J K, Izatt J A, Kulkarni M D, Yasdanfar S and Welch A J 1999 Three-dimensional reconstruction of blood vessels from *in vivo* color Doppler optical coherence tomography images *Dermatology* **198** 355-361.

Bashkatov A N, Genina E A, Korovina I V, Kochubey V I, Sinichkin Y P and Tuchin V 2000 *In vivo* and *in vitro* study of control of rat skin optical properties by action of osmotical liquid *Proc. SPIE* **4224** 300-311.

Bau H H and Wang Y-Z 1991 Chaos: a heat transfer perspective *Ann. Rev. Heat Transf.* vol IV ed. C L Tien 1-50.

Berg S and Torp H 1998 *Volumetric blood flow estimation using dynamic three-dimensional ultrasound color flow imaging* IEEE ultrasonic symposium 1513-1516.

Bernoulli D 1738 *Hydrodynamica* (Argentorati).

Berrocal E, Churmakov D, Romanov V, Jermy M and Meglinski I 2005 Crossed source detector geometry for a novel spray diagnostic: Monte Carlo simulation and analytical results *Appl. Opt.* **44**(13) 2519-2529.

Bizheva K, Siegel A and Boas D 1998 Path-length-resolved dynamic light scattering in highly scattering random media: the transition to diffusing wave spectroscopy *Phys. Rev. E* **58**(6) 7664-7667.

Blasius H 1913 Das ähnlichkeitsgesetz bei reibungsvorgängen in flüssigkeiten *Forschg. Arb. Ing.-Wes.* **131**, Berlin.

Bonesi M, Churmakov D and Meglinski I 2007a Study of flow dynamics in complex vessels using Doppler optical coherence tomography *Meas. Sci. Technol.* **18** 3279-3286.

Bonesi M, Churmakov D and Meglinski I 2007b Turbulence monitoring with Doppler Optical Coherence Tomography *Las. Phys. Lett.* **4**(4) 304-307.

Born M and Wolf E 1999 *Principles of Optics: Electromagnetic Theory of Propagation, Interference and Diffraction of Light* (Cambridge, UK:Cambridge University Press).

Boschetti F, Raimondi M T, Migliavacca F and Dubini F 2006 Prediction of the micro-fluid dynamic environment imposted to three-dimensional engineered cell systems in bioreactors *J. Biomech.* **39** 418-425.

Bouma B E, Nelson L E, Tearney G J, Jones D J, Brezinski M E and Fujimoto J G 1998 Optical coherence tomography imaging of human tissue at 1.55 μm and 1.81 μm using Er- and Tm-doped fiber sources *J. Biomed. Opt.* **3**(1) 76-79.

Bouma B E and Tearney G J 2002 *Handbook of Optical Coherence Tomography* (New York:Marcel Dekker, Inc.)

Boyes W 2002 *Instrumentation Reference Book* (Elsevier).

Brands P J, Hoeks A P, Hofsrta L and Reneman R S 1995 A non-invasive method to estimate wall shear rate using ultrasound *Ultrasound Med. Biol.* **21** 171-185.

Brands P J, Hoeks A P G, Willigers J, Willekes C and Reneman R S and 1999 An integrated system for the non-invasive assessment of vessel wall and hemodynamic properties of large arteries by means of ultrasound *Eur. J. Ultrasound* **9** 257-266.

Brezinski M E, Tearney G J, Weissman N J, Boppart S A, Bouma B E, Hee M R, Weyman A E, Swanson E A, Southern J F and Fujimoto J G 1997 Assessing atherosclerotic plaque morphology: comparison of optical coherence tomography and high frequency intravascular ultrasound *Heart* **77** 397-404.

Brezinski M E and Fujimoto J G 1999 Optical coherence tomography: high resolution imaging in non-transparent tissue *IEEE J. Sel. Topics Quant. Electr.* **5**(4) 1185-1192.

Brezinsky M E and Fujimoto J G 2002 The use of polarization sensitive optical coherence tomography and elastography to assess connective tissue.

Brezinski M E 2006 *Optical Coherence Tomography Principles and Applications* (Elsevier).

Brush S G 1962 Theories of liquid viscosity *Chem. Rev.* **62** 513-548.

Burke A P, Ferb A, Malcom G T, Liang Y, Smialek J and Virmani R 1997 Coronary risk factors and plaque morphology in men with coronary disease who died suddenly *N. Engl. J. Med.* **336**(18) 1276-1282.

Carlier S G, Li W, Cespedes E I, van der Steen A F W, Hamburger J B, Bom B and Serruys P W 1998 Simultaneous morphological and functional assessment of a renal artery stent intervention with intravascular ultrasound *Circulation* **97** 2575-2576.

Carlino A 1999 *Books of the Body* (Chicago: University of Chicago Press).

Casaubieilh P, Ford G D, James S W and Tatam R P 2005 Optical coherence tomography with a Fizeau interferometer configuration *in: Nano- and Micro-Metrology*, Heidi Ottevaere, Peter DeWolf and Diederick Wiersma Editors, *Proc. SPIE* **5858** 139-147.

Celata G P, Cumo M, McPhail S and Zummo G 2005 Characterization of fluid dynamic behavior and channel wall effect in microtube *Int. J. Heat Fluid Flow* **27**(1) 135-143.

Cebral J R, Yim P J, Löhner R, Soto O and Choyke P L 2002 Blood flow modeling in carotid arteries with computational fluid dynamics and MR imaging *Acad. Radiol.* **9**(11) 1286-1299.

Chang C J and Hou K H 2003 High-resolution optical Doppler tomography for *in vitro* and *in vivo* fluid flow dynamics *Chang Gung Med. J.* **26** 403-411.

Chao S, Xia K-Q and Tong P 2005 Three-dimensional flow structures and dynamics of turbulent thermal convection in a cylindrical cell *Phys. Rev. E* **72** 026302 1-13.

Chen C, Lu J Q, Ding H, Jacobs K M, Du Y and Hu X-H 2006 A primary method for determination of optical parameters of turbid samples and application to intralipid between 550 and 1630 *nm Opt. Expr.* **14**(16) 7420-7435.

Chen Z, Milner T E, Wang X, Srinivas S and Nelson J S 1998 Optical Doppler tomography: imaging *in vivo* blood flow dynamics following pharmacological intervention and photodynamic therapy *Photochem. Photobiol.* **67**(1) 56-60.

Chen Z, Milner T E, Dave D and Nelson J S 1997a Optical Doppler tomographic imaging of fluid flow velocity in highly scattering media *Opt. Lett.* **22**(1) 64-66.

Chen Z, Milner T E, Srinivas S, Wang X, Malekafzali A, van Gemert J C and Nelson J S 1997b Non-invasive imaging of *in vivo* blood flow velocity using optical Doppler tomography *Opt. Lett.* **22** 1119-1121.

Cheng K C 1997 A history of flow visualization: chronology *J. Flow Visual. Imag. Process.* 4 9-27.

Cheng C P, Herfkens R J and Taylor C A 2003a Abdominal aortic hemodynamic conditions in healthy subjects aged 50-70 at rest and during lower limb exercise: *in vivo* quantification using MRI *Atherosclerosis* **168** 323-331.

Cheng C P, Herfkens R J and Taylor C A 2003b Inferior vena cava hemodynamics quantified *in vivo* at rest and during cycling exercise using magnetic resonance imaging *Am. J. Physiol. Heart Circ. Physiol.* **284** H1161-H1167.

Cheng C P, Schwandt D F, Topp E L *et al.* 2003c Dynamic exercise imaging with an MR-compatible stationary cycle within the general electric open magnet. *Magn. Reson. Med.* **49** 581-585.

Cheng C P , Herfkens R J and Taylor C A 2003d Comparison of abdominal aortic hemodynamics between men and women at rest and during lower limb exercise *J. Vasc. Surg.* **37** 118-123.

Chinn S R and Swanson E A 2002 Optical coherence tomography for high-density data storage in *Handbook of Optical Coherence Tomography* B E Bouma and G J Tearney eds. (New York:Marcel Dekker Inc.).

Choma M, Sarunic M, Yang C and Izatt J 2003 Sensitivity advantage of swept source and Fourier domain optical coherence tomography *Opt. Expr.* **11**(18) 2183-2189.

Chung C A, Chen C W, Chen C P and Tseng C S 2007 The enhancement of cell growth in tissue-engineering constructs under direct perfusion: modeling and simulation *Biotechnol. Bioeng.* **97**(6) 1603-1616.

Cioffi M, Boschetti F, Raimondi M T and Dubini 2006 Modeling evaluation of the fluid dynamic microenvironment in tissue engineered constructs: micro-CT based model *Biotechnol. Bioeng.* **93**(3) 500-510.

Coletta C, Galati A, Ricci R *et al.* 1999 Coronary flow reserve of normal left anterior descending artery in patients with ischemic heart disease: a trans-esophageal Doppler study *J. Am. Soc. Echocardiogr.* **12** 720-728.

Cummins H Z and Pike E R 1973 *Photon Correlation and Light Beating Spectroscopy* (New York:Plenum Press).

Cuypers M H M, Kasanardjo J S and Polak B C P 2000 Retinal blood flow changes in diabetic retinopathy measured with the Heidelberg scanning laser Doppler flowmeter *Graefes Arch. Clin. Exp. Ophtalmol.* **238** 935-941.

Danielson B L and Whittenberg C D 1987 Guided-wave reflectometry with micrometer resolution *Appl. Opt.* **26** 2836-2842.

Darcy H 1856 *Les Fontaines Publiques de la Ville de Dijon* (Paris:Dalmont).

de Boer J F, Milner T E, van Gemert M J C and Nelson J S 1997 Two-dimensional birefringence imaging in biological tissue by polarization-sensitive optical coherence tomography *Opt. Lett.* **22** 934-936.

Dinnar U 1981 *Cardiovascular Fluid Dynamics* (Boca Raton:CRC).

Doriot P A, Dorsaz P A, Dorsaz L *et al.* 2000 In vivo measurements of wall shear stress in human coronary arteries *Coron. Artery Dis.* **11** 495-502.

Douglas J F, Gasiorek J M and Swaffield J A 2001 *Fluid Mechanics* (Prentice Hall).

Douven L and Lucassen G 2000 Retrieval of optical properties of skin from measurement and modelling the diffuse reflectance *Proc. SPIE* **3914** 312-323.

Drakaki E, Psycharakis S, Makropoudou M and Serafetinides A A 2005 Optical properties and chromophore concentration measurements in tissue-like phantoms *Opt. Comm.* **254**(1-3) 40-51.

Drexler W 2004 Ultrahigh-resolution optical coherence tomography *J. Biomed. Opt.* **9**(1) 47-74.

Drexler W, Sattmann H, Hermann B, Ko T H, Stur M, Unterhuber A, Scholda C, Findl O, Wirtitsch M, J G Fujimoto and Fercher A F 2003 Enhanced visualization of macular pathology with the use of ultrahigh-resolution optical coherence tomography *Arch. Ophthalmol.* **121** 695-706.

Drexler W, Morgner Y, Ghanta R K, Schuman J S, Kartner F X and J G Fujimoto 2001 Ultrahigh-resolution ophthalmic optical coherence tomography *Nat. Med.* **7** 502-507.

Drikakis D and Geurts B J 2002 *Turbulent Flow Computation* (Kluwer Academic Publishers).

Driver I, Feather J W, King P R and Dawson J B 1989 The optical properties of aqueous suspensions of *Intralipid*, a fat emulsion, *Phys. Med. Biol.* **34**(12) 1927-1930.

Dunkers J P 2002 Applications of optical coherence tomography to the study of polymer matrix composition in *Handbook of Optical Coherence Tomography* B E Bouma and G J Tearney eds. (New York:Marcel Dekker Inc.)

Dunn A K, Bolay H, Moskowitz M A and Boas D A 2001 Dynamic imaging of cerebral blood flow using laser speckle *J. Cereb. Blood Flow Metab.* **21** 195-201.

Elert G 2004 *The Physics Factbook* (published online http://hypertextbook.com/facts/2004/ MichaelShmukler.shtml)

Enoch J M, Giraldez M J, Huang D, Hirose H, Knowels R, Namperumalsamy P, LaBree L and Azen S P 1995 Hyperacuity test to evaluate vision through dense cataracts: research preliminary to a clinical study in India *Opt. Eng.* **34** N.3 780-784.

Ergun E, Hermann B, Wirtitsch M, Unterhuber A, Ko T H, Sattmann H, Scholda C, J G Fujimoto, Stur M and Drexler W 2005 Assessment of central visual function in Stargardt's disease/*fundus flavimaculatus* with ultrahigh-resolution optical coherence tomography Invest. Ophthalmo. Vis. Sci. **46** 310-316.

Everett M J, Schoenenberger K, Colston B W and Da Silva L B 1998 Birefringence characterization of biological tissue by use of optical coherence tomography *Opt. Lett.* **23** 228-230.

Falk E 2006 Pathogenesis of atherosclerosis *J. Am. Coll. Cardiol.* **47** C7-C12.

Fercher A F, Drexler W, Hitzenberger C K and Lasser T 2003 Optical coherence tomography – principles and applications *Rep. Prog. Phys.* **66** 239-303.

Fercher A F 1996 Optical coherence tomography *J. Biomed. Opt.* **1** 157-173.

Fercher A F, Mengedoht K and Werner W 1988 Eye-length measurement by interferometry with partially coherent light *Opt. Lett.* **13** 186-189.

Flock S T, Jacques S L, Wilson B C, Star W M and van Gemert M J C 1992 Optical Properties of *Intralipid*: a phantom medium for light propagation studies, *Lasers Surg. Med.* **12** 510-519.

Flournoy P A, McClure R W and Wyntjes G 1972 White-light interferometric gauge *Appl. Opt.* **11** 1907-1915.

Fluerau C, Kumazaki H, Sherif S, Chang S and Mao Y 2007 Quadrature Mach-Zehnder interferometer with application in optical coherence tomography *J. Opt. A: Pure Appl. Opt.* **9** L5-L8.

Freed L E and Vunjak-Novakovic G 2000 Tissue engineering bioreactors. In *Principles of Tissue Engineering* Lanza R P, Langer R and Vacanti J eds. (San Diego:Academic Press) 143-156.

Fujimoto J G, Brezinski M E, Tearney G J, Boppart S A , Hee M R and Swanson E A 1995 Optical biopsy and imaging using optical coherence tomography *Nat. Med.* **1** 970-972.

Gadallah S, Thaker K, Kawanishi D *et al.* 1998 Comparison of intracoronary Doppler guide wire and trans-esophageal echocardiography in measurements of low velocity

and coronary flow reserve in the left anterior descending coronary artery *Am. Heart J.* **135** 38-42.

Gambichler T, Moussa G, Sand M *et al.* 2005 Applications of optical coherence tomography in dermatology *J. Dermatol. Sci.* **40** 85-94.

Gandjbakhche A H, Millis P and Snabre P 1994 Light-scattering technique for the study of orientation and deformation of red blood cells in a concentrated suspension *Appl. Opt.* **33** 1070-1078.

Gatehouse P D, Keegan J, Crow L A *et al.* 2005 Applications of phase-contrast flow and velocity imaging in cardiovascular MRI *Eur. Radio.* **15** 2172-2184.

Gelikonov V M and Gelikonov G V 2006 A new approach to cross-polarized optical coherence tomography based on orthogonal arbitrary polarized mode *Laser Phys. Lett.* **3**(9) 445-451.

Gill T. P 1965 *The Doppler Effect* (New York:Academic Press).

Gjurchinovski A 2004 Reflection of light from a uniformly moving mirror *Am. J. Phys.* **72** 1316-1324.

Gladkova N, Petrova G, Nikulin N, Radenska-Lopovok S, Snopova L, Chumakov Y, Nasonova V, Gelikonov V, Gelikonov G, Kuranov R, Sergeev A, and Feldchtein F 2000 *In vivo* optical coherence tomography imaging of human skin: norm and pathology *Skin Res. Technol.* **6** 6-16.

Gnasso A, Irace C, Carallo C *et al. In vivo* association between low wall shear stress and plaque in subjects with asymmetrical carotid atherosclerosis *Stroke* **28** 993-998.

Goldstein R J 1996 *Fluid Mechanics Measurements* (Hemisphere Publishing Corporation).

Grinstein F F 2006 *On integrating numerical and laboratory turbulent flow experiments* presented by invitation at the 36th AIAA Fluid Dynamics Conference and Exhibit 5-8

June 2006, San Francisco, California (published online http://pdf.aiaa.org/preview/CDReadyMFDC06_1188/PV2006_3048.pdf).

Hagen G H L 1839 *Poggendorffs Ann. Phys. Chem.* **46** 423.

Haiying C, Qingming L, Qian L, Qiang L, Hui G and Shaoqun Z 2004 Laser speckle imaging of blood flow in microcirculation *Phys. Med. Biol.* **49** 1347-1357.

Hale G M and Querry M R 1973 Optical constant of water in the 200 *nm* to 200 *μm* wavelength region *Appl. Opt.* **12** 555-563.

Harden J L and Viasnoff V 2001 Recent advances in DWS-based micro-rheology *Curr. Opin. Colloid In.* **6**(5-6) 438-445.

Hee M R, Huang D, Swanson E A and Fujimoto J C 1992 Polarization-sensitive low-coherence reflectometer for birefringence characterizain and ranging *J. Opt. Soc. Am. B* **9** 903-908.

Herschel W, – Translation by Herschel W of Poiseuille J 1940 Recherches expérimentales sur le movement des liquids dans les tubes de très petits diameters *Mémories Presentés par Divers Savants à LAcadémie Royal des Sciences de l'Institut de France (Rheological Memoirs 1)* E Binhgam ed. (Lancaster:Lancaster Press)

Hitzenberger C K 1992 Measurement of corneal thickness by low-coherence interferometry *Appl. Opt.* **31** 6637-6642.

Hoffman A, Goetz M, Vieth M, Galle P R, Neurath M F and Kiesslich R 2006 Confocal laser endomicroscopy: technical status and current indications *Endoscopy* **38**(12) 1275-1283.

Hong H-D and Fox M 1997 Non-invasive detection of cardiovascular pulsations by optical Doppler techniques *J. Biomed. Opt.* **2**(4) 382-390.

Hooke R 1665 *Micrographia: Or Some Physiological Descriptions of Minute Bodies Made By Magnifying Glasses: With Observations and Inquiries Thereupon* (retrieved

online on 12th July 2007 at http://digital.library.wisc.edu/1711.dl/HistSciTech.HookeMicro).

Huang D, Swanson E A, Lin C P, Schuman S J, Stinson W G, Chang W, Hee M R, Flotte T, Gregory K, Puliafito C A and Fujimoto J G 1991 Optical coherence tomography *Science* **254**(5035) 1178-1181.

Hwang J H, Cobb M J, Kimmey M B and Li X 2005 Optical coherence tomography of the pancreas: a needle-based approach *Clinic. Gastroenterol. Hepatol.* **3**(7-1) S49-S52.

Izatt J A and Kulkarni M D 1996 Doppler flow imaging using optical coherence tomography in *Conference on Lasers and Eectro-Optics* OSA Technical Digest Series 9 (Washington:OSA)

Izatt J A, Kulkarni M D, Yazdanfar S, Barton J K and Welch A J 1997 *In vivo* bidirectional color Doppler flow imaging of picoliter blood volumes using optical coherence tomography *Opt. Lett.* **22**(18) 1439-1441.

Jaap A J and Tooke J E 1995 Diabetes and the microcirculation in *Clinically Applied Microcirculation Research* JH Barker, GL Anderson and MD Menger eds. (Boca Reaton:CRC press, Inc.) 31-44.

Jacques S L 1996 Origins of tissue optical properties in the UVA, visible and NIR regions, in: *TOPS on Advances in Optical Imaging and Photon Migration*, OSA Proc. ed R R Alfano and J G Fujimoto (Optical Society of America) **2** 364-369.

Johnson R W *The Handbook of Fluid Dynamics* (CRC Press).

Jonas J B, Harazny J, Budde W M, Maradin C Y, Papastathopoulos K I and Michelson G 2003 Optic disk morphmetry correlated with confocal laser scanning Doppler flowmetry measurements in normal-pressure glaucoma *J. Glaucoma* **12** 374-380.

Kelly K M, Choi B, McFarlane S, Motosue A, Jung B, Khan M H, Ramirez-San-Juan J C and Nelson J S 2005 Description and analysis of treatments for port-wine stain birthmarks *Arch. Facial Plast. Surg.* **7** 287-294.

Kemp M 1972 Dissection and divinity in Leonardo's late anatomy *J. Warbug Courtauld Inst.* **35** 200-225.

Kemp M 1989 *Leonardo da Vinci: The Marvelous Works of Nature and Man* (London:Dent & Sons).

Keele K and Pedretti C 1979 *Leonardo da Vinci. Corpus of Anatomical Studies in the Collection of Her Majesty the Queen at Windsor Castle* (New York:Harcourt Brace Jovanovich).

Kilner P J, Yang G-Z, Wilkes A J, Mohiaddin R H, Firmin D N and Yacoub M H 2000 Asymmetric redirection of flow through the heart *Nature* **404** 759-761.

Kolmogorov A N 1941 The local structure of turbulence in incompressible viscous fluid for very large Reynolds numbers *Dokl. Akad. Nauk. SSSR* **30** 229-303. Reprinted in *Proc. Roy. Soc. A* **434**(1980) 9-13 (1991).

Korbelik M and Krosl G 1994 Cellular-levels of photosensitizers in tumors – the role of proximity to the blood-supply *Brit. J. Cancer* **70** 604-610.

Krams R, Wentzel J, Oomen J *et al.* 1997 Evaluation of endothelial shear stress and 3D geometry as factors determining the development of atherosclerosis and remodeling in human coronary arteries *in vivo*. Combining 3D reconstruction from angiography and IVUS (ANGUS) with computational fluid dynamics *Arterioscler. Thromb. Vasc. Biol.* **17** 2061-2065.

Krams R, Wentzel J J, Cespedes I *et al.* 1999 Effect of catheter placement on 3D velocity profiles in curved tubes resembling the human coronary system *Ultrasound Med. Biol.* **25** 803-810.

Kulkarni M D, van Leeuwen T G, Yazdanfar S. and Izatt J A, 1998 Velocity-estimation accuracy and frame-rate limitations in color Doppler optical coherence tomography *Opt. Lett.* **23**, 1057-1059.

Kuz'min V, Meglinski I and Churmakov D 2005 Stochastic modelling of coherent phenomena in strongly inhomogeneous media *J. Exp. Theor. Phys.* **101**(1) 22-32.

Kwong K F, Yankelevich D, Chu K C, Heritage J P and Dienes A 1993 400-*Hz* mechanical scanning optical delay line *Opt. Lett.* **18** 558-560.

Lanigan S W and Cotterill J A 1990 Reduced vasoactive responses in port wine stains *Brit. J. Dermatol.* **122**(5) 615-622.

Langer R and Vacanti J P 1993 Tissue engineering *Science* **260** 920-926.

Larin K V, Ghosn M G, Ivers S N, Tellez A and Granada J F 2007 Quantification of glucose diffusion in arterial tissues by using optical coherence tomography *Laser Phys. Lett.* **4**(4) 312-317.

Leitgeb R A, Schmetterer L, Hitzenberg C K *et al.* 2004 Real-time measurement of *in vitro* flow by Fourier-domain color Doppler optical coherence tomography *Opt. Lett.* **29** 171-173.

Leitgeb R, Hitzenberger C K and Fercher A F 2003 Performance of Fourier domain vs. time domain optical coherence tomography *Opt. Expr.* **11**(8) 889-894.

Li W 1997 *Image and Signal processing in Intravascular Ultrasound* Dissertation; Erasmus University Rotterdam

Li X, Chudoba C, Ko T, Pitris C and Fujimoto J G 2000 Imaging needle for optical coherence tomography *Opt. Lett.* **25**(20) 1520-1522.

Lin M-C, Almus-Jacobs F, Chen H H, Parry G C N, Mackman N, Shyy J Y-J and Chien S 1997 Shear stress induction of the tissue factor gene *J. Clin. Invest.* **99** 737-744.

Long Q, Xu Y X, Ariff B, Thom S A, Hughes A D and Stanton A V 2000 Reconstruction of blood flow patterns in a human carotid bifurcation: a combined CFD and MRI study *J. Magn. Res. Imag.* **11** 299-311.

Longmuir R, Andrew G L and Culver Boldt H 2008 Optical coherence tomography (OCT) in neuro-ophthalmology: a clinical perspective *Neuro-Opthalm.* **32**(3) 15-125.

Lourenko L M 1998 Characterization of turbulent flow fields using PIV *UTNL,R. (Tokyo Daigaku Daigakuin Kogakukei Kenkyuka Fuzoku Genshiryoku Kogaku Kenkyu Shisetsu)* **374** 56-70.

Lowe G. D. O. 1988 *Clinical Blood Rheology* (Boca Ration Florida: CRC Press).

Luo Q, Cheng H, Wang Z and Tuchin V V 2004 Laser speckle imaging of cerebral blood flow in *Handbook of Coherent Domain Optical Methods* VV Tuchin ed. (Kluwer Academic Press).

Lupotti F A, Mastik F, Carlier S G *et al.* 2003 Quantitative IVUS blood flow: validation *in vitro*, in animals and in patients *Ultrasound Med. Biol.* **29** 507-515.

Mackay J and Mensha G A 2004 *The Atlas of Disease and Stroke* (Geneva:World Health Organization).

Marshall I, Zhao S, Papathanasopolou P, Hoskins P and Xu X Y 2004 MRI and CFD studies of pulsatile flwo in healty and stenosed carotid bifurcation models *J. Biomech.* **37** 679-687.

Massey B S 1990 *Mechanics of Fluids* (London:Chapman and Hall Ltd.).

Matcher J S, Winlove C P and Gangnus S 2004 The collagen structure of bovine intervertebral disc studied using polarization-sensitive optical coherence tomography *Phys. Med. Biol.* **49** 1295-1306.

Mathieu J and Scott J 2000 *An Introduction to Turbulent Flow* (Cambridge University Press).

Masters B R 1999 Early development of optical low-coherence reflectometry and some recent biomedical applications *J Biomed. Opt.* **4**(2) 236-247.

Meglinski I V 2003 Diffusing wave spectroscopy and its application for monitoring of skin blood microcirculation Saratov Fall Meeting 2002: Optical Technologies in Biophysics and Medicine IV (Tuchin V V ed.) *Proc. SPIE* **5068** 163-169.

Michelson A A 1893 Comparison of the international metre with the wave-length of the light of cadmium *Astron. Astro-Phys.* **12** 556-560.

Mikos A G and Temenoff J S 2000 Formation of highly porous biodegradable scaffolds for tissue engineering *Electron. J. Biotech.* **3** 23-24.

Miller R W 1996 *Flow Measurement Engineering Handbook* (McGraw-Hill Professional)

Minuth W W, Strehl R and Schumacker K 2006 Tissue engineering, from *Cell Biology to Artificial Organs* (Berlin, DE:Wiley VCH).

Mishra L D 2002 Cerebral blood flow and anaesthesia: a review *Indian J. Anaesth.* **46**(2) 87-95.

Meyer Y 1995 *Wavelets and Operators*, Cambridge Studies in Advanced Mathematics **37** (Cambridge, UK:Cambridge University Press) ISBN-13 9780521458696.

Moger J, Matcher S J, Winlove C P and Shore A 2005 The effect of multiple scattering on velocity profiles measured using Doppler OCT *J. Phys. D: Appl. Phys.* **38** 2597-2605.

Moger J, Matcher S J, Winlove C P and Shore A 2004 Measuring red blood cell flow dynamics in a glass capillary using Doppler optical coherence tomography and Doppler amplitude optical coherence tomography *J. Biomed. Opt.* **9**(5) 982-994.

Moger J, Matcher S J, Winlove C P, Shore A C 2003 Measuring blood flow dynamics using DOCT and Doppler amplitude optical coherence tomography (DAOCT) in *Coherence Domain Optical Methods and Optical Coherence Tomography in Biomedicine, Proc. SPIE* **4956** 366-373.

Moger J 2003 Investigating blood flow dynamics using Doppler optical coherence tomography *Ph.D. dissertation* (University of Exeter, UK).

Moger J, Matcher S J and Shore A C 2002 Development of a phase-resolved Doppler optical coherence tomography system for use in cutaneous microcirculation research

in *Coherence Domain Optical Methods in Biomedical Science and Clinical Applications VI*, Valery V. Tuchin, Joseph A. Izatt and James G. Fujimoto Editors, Proc. SPIE **4619** 269-275.

Moore J E Jr., Xu C, Glagov S *et al.* 1994 Fluid wall shear stress measurements in a model of the human abdominal aorta: oscillatory behavior and relationship to atherosclerosis *Atherosclerosis* **110** 225-240.

Moreno P, Falk E, Palacios I *et al.* 1994 Macrophage infiltration in acute coronary syndromes. Implications for plaque rupture *Circulation* **90** 775-778.

Naghavi M, Libby P, Falk E *et al.* 2003 From vulnerable plaque to patient: a call for new definitions and risk assessment strategies Part I-II *Circulation* **108** 1664-1678

Ndubuizu O and LaManna J C 2007 Brain tissue oxygen concentration measurements *Antioxid. Redox Signal.* **9**(8) 1-13.

Neligan P C 1993 Monitoring techniques for the detection of flow failure in the postoperative period *Micrusurgery* **14** 162-164.

Nelson J S, Kelly K M, Yonghua Z and Zhongping C 2001 Imaging blood flow in human port-wine stain in situ and in real-time using optical Doppler tomography *Arch. Dermatol.* **137**(6) 741-744.

Niazi Z B M, Essex T J H, Papini R, Scott D, Mclean N R and Black M J M 1993 New laser-Doppler scanner, a valuable adjunct in burn depth assessment *Burns* **19** 485-489

Nikuradse J 1930 Turbulente strömungen in nicht-kreisförmigen rohren *Ing. Arch.* **1** 306-332.

Ohlidal M, Ohlidal I, Druckmuller M and Franta D 1995 A method of shearing interferometry for determining the statistical quantities of randomly rough surfaces for solids *Pure and Appl. Opt. A* **5** 599-616.

Ott E, Grebogi C and Yorke J A 1990 Controlling chaos *Phys. Rev. Lett.* **64** 1196-1199.

Oyre S, Pedersen E M, Ringgaard S *et al.* 1997 *In vivo* wall shear stress measured by magnetic resonance velocity mapping in the normal human abdominal aorta *Eur. J. Vasc. Endovasc. Surg.* **13** 263-271.

Pan Y and Farkas D 1998 Noninvasive imaging of living human skin with dual-wavelength optical coherence tomography in two and three dimensions *J. Biom. Opt.* **3** 446-455.

Papathanasopoulou P, Zhao S, Kohler U *et al.* 2003 MRI measurement of time-resolved wall shear stress vectors in a carotid bifurcation model and comparison with CFD predictions *J. Magn. Reson. Imaging* **17** 153-162

Park B, Pierce M, Cense B and de Boer J 2003 Real-time multi-functional optical coherence tomography *Opt. Express* **11** 782-793.

Pasterkamp G, Schoneveld A H, van der Wal A C *et al.* 1998 Relation of arterial geometry to luminal narrowing and histologic markers for plaque vulnerability: the remodeling paradox *J. Am. Coll. Cardiol.* **32** 655-662.

Patel N A and McGhee C N 2007 Contemporary in vivo confocal microscopy of the living human cornea using white light and laser scanning techniques: a major review *Clin. Experiment. Opthalmol.* **35**(1) 71-88.

Patel N A, Stamper D L and Brezinski M E 2005 Review of the ability of optical coherence tomography to characterize plaque, including a comparison with intravascular ultrasound *Cardiovasc. Intervent. Radiol.* **28**(1) 1-9.

Pawley J B 2006 *Handbook of Biological Confocal Microscopy* (Berlin, DE:Springer).

Pedersen C J, Yazdanfar S, Westphal V and Rollins A M 2003 Phase-referenced Doppler optical coherence tomography in *Conference on Lasers and Electo-Optics 2003*, CLEO'03 412-414

Pedersen E M, Oyre S, Agerbaek M *et al.* 1999 Distribution of early atherosclerotic lesions in the human abdominal aorta correlates with wall shear stresses measured *in vivo Eur. J. Vasc. Endovasc. Surg.* **18** 328-333.

Perktold K and Rappitsch G 1995 Computer simulation of local blood flow and vessel mechanics in a compliant carotid artery bifurcation model *J. Biomech.* **28**(7) 845-856.

Piao D and Pogue B W 2007 Rapid near-infrared diffuse tomography for hemodynamic imaging using a low-coherence wideband light source *J. Biomed. Opt.* **12**(1) 014016.1-12.

Pierce M C, Hyle Park B, Cense B, and de Boer J F 2002 Simultaneous intensity, birefringence and flow measurements with high-speed fibre-based optical coherence tomography *Opt. Lett.* **27** 1534-1536.

Pierce M C, Strasswimmer J, Hyle Park B, Cense B and de Boer J F 2004 Advances in optical coherence tomography imaging for dermatology *J. Invest. Dermatol.* **123** 458-463.

Prandtl L 1904 in *Verhandlungen Des Dritten Internationalen Mathemtiker-Kongresses in Heidelberg* A Krazer ed., Teubner, Leipzig, Germany (1905) p484. English transl. in Ackroyd J A K, Axcell P and Ruban A I 2001 *Early Developments of Modern Aerodynamics* (Oxford, UK:Butterworth-Heinemann).

Proskurin S G, Sokolova I A and Wang R K 2003a Imaging of non-parabolic velocity profiles in converging flow with optical coherence tomography *Phys.Med. Biol.* **48** 2907-2918.

Proskurin S G, He Y and Wang R K 2003b Determination of flow velocity vector based on Doppler shift and spectrum broadeining with optical coherence tomography *Opt. Lett.* **28** 1227-1229.

Proskurin S G, He Y and Wang R K 2004 Doppler optical coherence imaging of converging flow *Phys. Med. Biol.* **49** 1265-1276.

Proskurin S G and Meglinski I V 2007 Optical coherence tomography imaging depth enhancement by superficial skin optical clearing *Laser Phys. Lett.* **4**(11) 824-826.

Radchenko E Y, Akchurin G G, Bakutkin V V, Tuchin V V and Akchurin A G 1999 Measurement of retinal visual acuity in human eyes *Proc. SPIE* **4001** 228-237.

Real C, Miranda R, Vilchis C, Barron M, Hoyos L and Gonzalez J 2006 *Transient internal flow characterization of a bifurcated submerged entry nozzle* ISIJ int. **46** 1183-1191.

Regar E, Schaar J A, Mont E *et al.* 2003 Optical coherence tomography *Cardiovasc Radiat Med* **4** 198-204

Regar E, van Leeuwen T G and Serruys P W 2007 *Optical Coherence Tomography in Cardiovascular Research* (Informa healthcare).

Ren F, Smith I O, Baumann M J and Case E D 2005 3-dimensional microstructural characterizations of porous hydroxyapatite using confocal laser scanning microscopy *Int. J. Appl. Ceram. Tech.* **2**(3) 200-211.

Reneman R S, van Merode T, Hick P and Hoeks A P 1986 Cardiovascular applications of multi-gate pulsed Doppler system *Ultrasound Med. Biol.* **12** 357-370.

Reynolds O 1883 An experimental investigation of the circumstances which determine whether the motion of water shall be direct or sinuous, and of the law of resistance in parallel channels *Phil. Trans.* **174**.

Roggan A, Friebel M, Dörschel K, Hahn A and Müller G 1998 Optical properties of circulating human blood in the wavelength range 400-2500 *nm J. Biomed. Optics* **4**(1) 36-46.

Rollins A M, Yazdanfar S, Barton J K and Izatt J A 2002 Real-time *in vivo* color Doppler optical coherence tomography *J. Biomed. Opt.* **7** 123-129.

Rollins A M and Izatt J A 1999 Optimal interferometer designs for optical coherence interferometry *Opt. Lett.* **24**(21) 1484-1486.

Rollins A M, Kulkarni M D, Yazdanfar S, Ung-arunyawee R, and Izatt J A 1998 *In vivo* video rate optical coherence tomography *Opt. Expr.* **3** 219-229.

Saleh B E A 1982 Optic treatment of information and vision of man in *Applicatons of Fourier-Optics Methods* G Stark ed. (New York:Academic Press) pp412-439.

Salim A, Kurwa H and Turner R 2003 Acquired port-wine stain associated with glaucoma *Clinical Exper. Dermatol.* **28**(2) 230-231.

Sampson D D 2004 Trends and prospects for optical coherene tomography in 2nd European Workshop on Optical Fiber Sensors, Culshaw B and Lopez-Higuera J M editors, *Proc. SPIE* **5502** 51-58 (Bellingham, WA:SPIE).

Sampson D D and Hillman T R Optical coherence tomography. In Palumbo G and Pratesi R, editors 2004 *Lasers And Current Optical Techniques In Biology* pp.481-571 ESP comprehensive series in photosciences (Cambridge, UK:The Royal Society Of Chemistry).

Satomura Y, Seki J, Ooi Y *et al.* 2004 *In vivo* imaging of the rat cerebral microvessels with optical coherence tomography *Clin. Gemorheol. Microcir.* **31** 31-40.

Schaefer A W, Reynolds J J, Marks D L and Boppart S A 2004 Real-time digital signal processing-based optical coherence tomography and Doppler optical coherence tomography *IEEE Trans. Biomed. Eng.* **51** 186-190.

Schlichting H 1979 *Boundary Layer Theory* (New York:McGraw-Hill).

Schmitt J M, Kolstad D and Petersen C 2005 Intravascular optical coherence tomography – opening a window into coronary artery disease Business briefing: European cardiology 2005 (LightLab Imaging, Inc.) (published online http://www.touchbriefings.com/pdf/1231/ Lightlab_Tech.pdf).

Schmitt J M 1999 Optical Coherence Tomography (OCT): a review *IEEE J. Sel. Top. Quantum Electron.* **5**(4) 1205-1215.

Schuman J S, Puliafito C A and J G Fujimoto 2004 Optical coherence tomography of ocular disease *Slack Inc., Thorofare, New Jersey.*

Silber H A, Ouyang P, Bluemke D A *et al.* 2005 Why is flow-mediated dilation dependent on arterial size? Assessment of the shear stimulus using phase-contrast magnetic resonance imaging *Am. J. Physiol. Heart Cric. Physiol.* **288** H822-828.

Smith E D J, Zvyagin A V and Sampson D D 2002 Real-time dispersion compensation in scanning interferometry *Opt. Lett.* **27**(22) 1998-2000.

Sorin W V and Baney D M 1992 A simple intensity noise reduction technique for optical low coherence reflectometry *IEEE Photon. Technol. Lett.* **4** 1404-1406.

Splinter R and Hooper B A 2006 *An Introduction to Biomedical Optics* (CRC Press).

Stanley H E and Ostrowsky N 1988 *Random Fluctuations and Pattern Growth: Experiments and Models* (Dordrecht:Kluwer).

Steinman D A, Thomas J B, Ladak H M, Milner J S, Rutt B K and Spence J D 2002 Reconstruction of carotid bifurcation hemodynamics and wall thickness using computational fluid dynamics and MRI *Magn. Resonan. Med.* **47** 149-159.

Stephens J S, Cooper J A, Phelan F R Jr. and Dunkers J P 2007 Perfusion flow bioreactor for 3D *in situ* imaging: investigation cell-biomaterials interactions *Biotechnol. Bioeng.* **97**(4) 952-961.

Stone P H, Coskun A U, Kinlay S *et al.* 2003 Effect of endothelial shear stress on the progression of coronary artery disease, vascular remodeling and in-stent restenosis in humans: *in vivo* 6-month follow-up study *Circulation* **108** 438-444.

Sugii Y, Okuda R, Okamoto K and Madarame H 2005 Velocity measurement of both red blood cells and plasma of *in vitro* blood flow using high-speed micro PIV technique *Meas. Sci. Technol.* **16** 1126-1130.

Swanson E A, Izatt J A, Hee R, Huang D, Lin C P, Scuman J S, Puliafito C A and Fujimoto J G 1993 *In-vivo* retinal imaging by optical coherence tomography *Opt. Lett.* **18**(21) 1864-.

Taganov O K and Toporets A S 1976 Study of coherence degree of radiation passed through rough surface *Opt. Spectrosc.* **40** 878-882.

Tallitsch R B, Timmons M J and Martini F 2005 *Human Anatomy* (Benjamin-Cummings Publishing)

Tan W, Sendemir-Urkmez A, Fahrner L J, Jamison R, Leckband D and Boppart S A 2004 Structural and functional optical imaging of three-dimensional engineered tissue development *Tissue Engineer.* **10**(11-12) 1747-1756.

Tatam R P 1997 Special issue on optical flow measurement: recent advances and applications *Opt. Las. Eng.* **27**(6) 529-530.

Tearney G J, Yabushita H, Houser S L, *et al.* 2003 Quantification of macrophage content in atherosclerotic plaques by optical coherence tomography *Circulation* **107** 113-119.

Tearney G J, Bouma B E and Fujimoto J G 1997 High-speed phase- and group-delay scanning with a grating-based phase control delay line *Opt. Lett.* **22**(23) 1811-1813.

Temenoff J S, Lu L and Mikos A G 2000 in *Bone Tissue Engineering Using Synthetic Biodegradable Polymer Scaffolds* (Toronto, CA:University of Toronto) p.454.

Thige B P and Matthias S 2007 Pressure and motion of dry sand: translation of Hagen's paper from 1852 *Granul. Matter* **9**(3-4) 1434-5021.

Thorell W E, Chow M M, Prayson R A, Shure M A, Jeon S W, Huang D, Zeynalov E, Woo H H,.Rasmussen P A, Rollins A M and Masaryk T J 2005 Optical coherence tomography: a new method to assess aneurysm healing *J. Neurosurg.* **102**(2) 348-354.

Tomlins P 2007 Quantitative assessment of the physical parameters of biological material using optical coherence tomography *Ph.D. dissertation*, Cranfield University, UK.

Tomlins P H and Wang R K 2005 Theory, developments and applications of optical coherence tomography *J. Phys D:Appl. Phys.* **38** 2519-2535.

Tuchin V V 2000 *Tissue Optics: Light Scattering Methods and Instruments for Medical Diagnosis* SPIE tutorial text in optical engineering **vol. TT38** (Washington: SPIE Press Book).

Tuchin V V, Xu X and Wang R K 2002 Dynamic optical coherence tomography in optical clearing, sedimentation and aggregation study of immersed blood *Appl. Opt.* **41** 258-271.

Tuchin V V 2004 *Handbook of Coherent Domain Optical Methods* (Kluwer Academic Press).

Udupa J K and Gabor T H 1999 *3D Imaging in Medicine* (CRC Press).

Ugryumova N, Jacobs J. Bonesi M and Matcher S J 2008 Novel optical imaging technique to determine the 3D orientation of collagen fibres in cartilage: variable-incidence-angle polarization-sensitive optical coherence tomography *Osteoarthritis and cartilage* (in press).

Ugryumova N, Bonesi M. and Matcher S J 2008 Determination of 3D optical axis orientation in cartilage by polarization-sensitive optical coherence tomography *Photonics West, Optics in tissue engineering and regenerative medicine II, Art. no. 68580I, Conf. Proc.* ***6858*** *I8580-I8580.*

Ugryumova N, Attenburrow D P, Winlove C P and Matcher S J 2005 The collagen structure of equine articular cartilage, characterized using polarization-sensitive optical coherence tomography *J. Phys. D: Appl. Phys.* **38** 2612-2619.

Unterhuber A, Považay B, Bisheva K, Hermann B, Sattmann H, Stingl A, Le T, Seefeld M, Menzel R, M Preusser *et al.* 2004 Advances in broad bandwidth light sources for ultrahigh resolution optical coherence tomography *Phys. Med. Biol.* **49**(7) 1253-1246.

van der Laan P A, Reardon C A and Getz G S 2004 Site specificity of atherosclerosis: site-selective responses to atherosclerotic modulators *Arterioscler. Thromb. Vasc. Biol.* **24** 12-22.

van der Meer F J, Faber D J, Baraznji Sassoon D M *et al.* 2005a Localized measurement of optical attenuation coefficients of atherosclerotic plaque constituents by quantitative optical coherence tomography *IEEE Trans. Med. Imaging* **24** 1369-1376.

van der Meer F J, Faber D J and Perree J 2005b Quantitative optical coherence tomography of arterial wall components *Lasers Med. Sci.* **20** 45-51.

van Leeuwen T G, Kulkarni M D, Yazdanfar S, Rollins A M and Izatt J A 1999 High-flow-velocity and shear-rate imaging by use of color Doppler optical coherence tomography *Opt. Lett.* **24**(22) 1584-1586.

van Staveren H G, Moes C J M, van Marle J, Prahl S A and van Gemert M J C 1991 Light scattering in *Intralipid®10%* in the wavelength range of 400-1100 nanometers, *Appl. Opt.* **30** 4507-4514.

Virmani R, Burke A P, Farb A *et al.* 2005 Pathology of the vulnerable plaque *J. Am. Coll. Cardiol.* **47** C13-C18.

Wang L V and Wu H 2007 *Biomedical Optics: Principles and Imaging* (John Wiley & Sons).

Wang R K 2004 High-resolution visualization of fluid dynamics with Doppler optical coherence tomography *Meas. Sci. Technol.* **15** 725-733.

Wang X J, Milner T E and Nelson N J, 1995 Fluid flow velocity characterization using optical Doppler tomography *Opt. Lett.* **20** 1337-1339.

Welzel J 2001 Optical coherence tomography in dermatology: a reiview *Skin Res. Technol.* **7**(1) 1-9.

Welzel J J, Lankenau E, Birngruber R, and Engelhardt R 1997 Optical coherence tomography of the human skin *J. Am. Acad. Dermatol.* **37** 958-963.

Wentzell J J, Corti R, Fayad Z A *et al.* 2005 Does shear stress modulate both plaque progression and regression in the thoracic aorta? Human study using serial magnetic resonance imaging *J. Am. Coll. Cardiol.* **45** 846-854.

Wentzel J J, Gijsen F J H, Schuurbiers J C H, Groen H C, van der Giessen A G, van der Steen A F W and Serruys P W 2007 Why do we need flow measurements? - Role of flow and shear stress in atherosclerotic disease, in: *Optical Coherence Tomography in Cardiovascular Research* ed E Regar, P W Serruys and T G van Leeuwen (Informa Healthcare) pp 289-304.

Wilson T 1990 *Confocal Microscopy* (San Diego:Academic Press).

Wojtkowski M, Srinivasan V, Ko T, Fujimoto J G, Kowalczyk A and Duker J 2004 Ultrahigh-resolution, hich-speed, Fourier domain optical coherence tomography and methods for dispersion compensation *Opt. Expr.* **12**(11) 2404-2422.

Wojtkowski M, Leitgeb R, Kowalczyk A, Bajraszewski T and Fercher A F 2002 In vivo human retinal imaging by Fourier domain optical coherence tomography *J. Biomed. Opt.* **7** 457.

Wollstein G, Paunescu L A, Ko T H, Fujimoto J G, Kowalevicz A, Hartl I, Beaton S, Ishikawa H, Mattox C, Singh O, Duker J, Drexler W and Schuman J S 2005 Ultrahigh-resolution optical coherence tomography in glaucoma *Ophthalmology* **112** 229-237.

Wolf A 1939 *A History of Science, Technology and Philosophy in the Eighteenth Century* (New York:MacMillan).

Wong R C, Yazdanfar S, Izatt J A *et al.* 2002 Visualization of subsurface blood vessels by color Doppler optical coherence tomography in rats: before and after haemostatic therapy *Gastrointest. Endocsc.* **55** 88-95.

Yabushita H, Bouma B E, Stuart L H, Thomas Artez H, Jang I K, Schlendorf K H, Kauffman C R, Shishlov M, Kang D H, Halpern E F and Tearney G J 2002 Characterization of human atherosclerosis by optical coherence tomography *Circulation* **106** 1540-1645.

Yang W J 2001 *Handbook of Flow Visualiation* (CRC).

Yang V X, Mao Y X, Munce N *et al.* 2005 Interstitial Doppler optical coherence tomography *Opt. Lett.* **30** 1791-1793.

Yang Y, Wu L, Feng Y and Wang R K 2003 Observations of birefringence in tissues from optic-fibre-based optical coherence tomography *Meas. Sci. Technol.* **14**(1) 41-46.

Yaqoob Z, Wu J, McDowell E J, Heng X and Yang C 2006 Methods and application areas of endoscopic optical coherence tomography J. Biomed. Opt. 11(6) 1-19.

Yazdanafar S, Rollins A M and Izatt J A 2003 *In vivo* imaging of human retinal flow dynamics by color Doppler optical coherence tomography *Arch. Ophthalmol.* **121** 235-239.

Yazdanafar S, Rollins A M and Izatt J A 2000 Imaging and velocimetry of the human retina circulation with color Doppler optical coherence tomography *Opt. Lett.* **25**(19) 1448-1450.

Yazdanafar S, Kulkarni M D, Wong R C K, Sivak M V, Willis J , Barton J K, Welch A J and Izatt J A 1998 Diagnostic blood flow monitoring during therapeutic interventions using color Doppler optical coherence tomography *Proc. SPIE* **3251** 126-132.

Yazdanafar S, Kulkarni M D and Izatt J A 1997 High resolution imaging of *in vivo* cardiac dynamics using color Doppler optical coherence tomography *Opt. Exp.* **1**(13) 424-431.

Yasuno Y, Makita S, Endo T, Itoh T, Itoh M Yatagai T, Takahashi M, Katada C and Mutoh M 2004 Polarization-sensitive complex Fourier domain optical coherence

tomography for Jones matrix imaging of biological samples *Appl. Phys. Lett.* **85**(15) 3023-3025.

Youngquist R C, Carr S and Davies D E N 1987 Optical coherence-domain reflectometry: a new optical evaluation technique *Opt. Lett.* **12**(3) 158-160.

Zarins C K, Giddens D Pm, Bharadvaj B K *et al.* Carotid bifurcation atherosclerosis. Quantitative correlation of plaque localization with flow velocity profiles and wall shear stress *Circ. Res.* **53** 205-14.

Zarfati O, Harris A, Garzozi H J, Zacish M, Kagemann L, Jonescu-Cuypers C P and Martin B 2000 A review of ocular blood flow measurement techniques *Neuro-Opthalmol.* **24**(3) 401-409.

Zhang J and Chen Z 2005 In vivo blood flow imaging by a swept laser source based Fourier domain optical Doppler tomography Opt. Expr. 13(19) 7449-7457.

Zhao Y, Chen Z, Ding Z, Ren H, Nelson J S 2002 Real-time phase-resolved functional optical coherence tomography by use of optical Hilbert transformation *Opt. Lett.* **27** 1702-1704.

Zhao Y, Brecke K M, Ren H, Ding Z, Nelson J S and Chen Z 2001 Three-dimensional reconstruction of *in vivo* blood vessels in human skin using phase-resolved optical Doppler tomography *IEEE J. Selec. Topics Quant. Elec.* **7**(6) 931-935.

Zhao Y, Chen Z, Saxer C, Xiang S, de Boer J F and Nelson J S 2000a Phase-resolved optical coherence tomography and optical Doppler tomography for imaging blood flow in human skin with fast scanning speed and high velocity sensitivity *Opt. Lett.* **25** 114-116.

Zhao Y, Chen Z, Saxer C, Shen Q, Xiang S, de Boer J F and Nelson J S 2000b Doppler standard deviation imaging for clinical monitoring of in vivo human skin blood flow *Opt. Lett.* **25**(18) 1358-1360.

Zvyagin A V, FitzGerald J B, Silva K and Sampson D D 2000 Real-time detection technique for Doppler Optical Coherence Tomography *Opt. Lett.* **25** 1645-1647.

Zvyagin A V, Smith E D J and Sampson D D 2003 Delay and dispersion characteristics of a frequency-domain optical delay line for scanning interferometry *J. Opt. Soc. Am. A* **20** 333-341.

Zysk A M, Adie S G, Armstrong J J, Leigh M S, Paduch A, Samson D D, Nguyen F T and Boppart S A 2007 Needle-based refractive index measurement using low-coherence interferometry *Opt. Lett.* **32**(4) 385-387.

Bibliography

Abbott M B and Blasco D R 1989 *Computational Fluid Dynamics – An Introduction for Engineers* (Harlow:Longman).

Ambrosini D and Rastogi P K 2006 Optical methods in heat transfer and fluid flow *Opt. Las. Eng.* **44**(3-4) 155-158.

Anderson Jr. J D 1995 *Computational Fluid Dynamics* (New York:McGraw-Hill).

Bennet J M, McAllister T D and Cabe G M 1973 Albert A. Michelson, dean of American optics – life, contributions to science and influence on modern-day physics *Appl. Opt.* **12**(10) 2253-2279.

Collyer A 1988 *Rheological Measurement* (Elsevier).

Chan K P, Devaraj B, Yamada M and Inaba H 1997 Coherent detection techniques in optical imaging of tissues *Phys. Med. Biol.* **42** 855-867.

Cheng K C 1997 A history of flow visualization: chronology *J. Flow Visual. Imag. Proc.* **4** 9-27.

Douglas J F, Gasiorek J M and Swaffield J A 2001 *Fluid Mechanics* (Prentice-Hall).

Gill R W 1985 Measurement of blood flow by ultrasound: accuracy and sources of error *Ultrasound Med Biol.* **11** 625-641.

Gin R, Straatman A G and Steinman D A 1999 Numerical modelling of the diseased carotid artery bifurcation using a physiologically relevant geometrical model *7th Annual Meeting of the CFD Society of Canada*, Halifax NS, May 1999 (published online).

Goldstein R J 1983 *Fluid Mechanic Measurements* (Springler-Verlag).

Hale G M and Querry M R 1973 Optical constants of water in the 200-*nm* to 200-*μm* wavelength region *Appl. Opt.* **12** 555-563.

Halliday D and Resnick R 1970 *Fundamentals of Physics* (John Wiley & Sons).

Landau L D and Lifshitz E M 1987 *Fluid Mechanics* (Pergamon Press).

Lavoisier A L 1864-1893 *(Euvres de Lavoisier, publics par les soins du Ministre de L'Instrucion Publique)* (Paris)

Linnik V P 1933 Simple interferometer for the investigation of optical systems *C. R. Acad. Sci. USSR* **1** 208-210.

Larson R G 1999 *The Structure and Rheology of Complex Fluid* (Oxford University Press).

Plapp J E 1968 *Engineering Fluid Mechanics* (Englewood Cliffs, New Jersey:Prentice-Hall).

Smith G D 1985 *Numerical Solutions of Partial Differential Equations: Finite Difference Methods* (Oxford:Clarendon Press).

Taylor R F and Schultz J S 1996 *Chemical and Biological Sensors* (IOP Publishing).

Versteeg H K and Malalasekera W 1995 *An Introduction to Computational Flow Dynamics, the Finite Volume Method* (Harlow:Longman).

Wang R K, Hebden J C and Tuchin V V 2004 Special issue on recent developments in biomedical optics *Phys. Med. Biol.* **49**(7) (IOP Publishing).

Ward-Smith A J 1980 *Internal Fluid Flow* (Oxford:Oxford University Press).

Whorlow R W 1992 *Rheological Techniques* (Ellis Horwood Ltd.)

Zeinkiewicz O C and Taylro R L 1991 *The Finite Element Method. Volume 2: Solid and Fluid Mechanics* (New York:McGraw-Hill).